Lagrangian experimental exploration of turbulence in a rotating quantum fluid

Emeric Durozoy

THÈSE

Pour obtenir le grade de

DOCTEUR DE L'UNIVERSITE GRENOBLE ALPES

Spécialité : Physique de la Matière Condensée et du Rayonnement

Arrêté ministériel : 25 mai 2016

Présentée par

Emeric DUROZOY

Thèse dirigée par **Mathieu Gibert,** Chercheur, Université Grenoble Alpes

préparée au sein du **Laboratoire Institut Néel**
dans **l'École Doctorale Physique**

Exploration expérimentale lagrangienne de la turbulence dans un fluide quantique en rotation

Lagrangian experimental exploration of turbulence in a rotating quantum fluid

Thèse soutenue publiquement le **05 novembre 2020**,
devant le jury composé de :

Monsieur Nicolas MORDANT
Professeur des universités, Université Grenoble Alpes – LEGI UMR 5519, Président du jury

Madame Francesca CHILLA
Professeur des universités, ENS Lyon – Laboratoire de Physique UMR 5672, Rapporteur

Monsieur Joachim PEINKE
Professeur des universités, Carl-von-Ossietzky Universität Oldenburg – Institut für Physik, AG TWiSt, Rapporteur

Monsieur Gregory Paul BEWLEY
Professeur assistant, Cornell University – Sibley School of Mechanical and Aerospace Engineering, Examinateur

Monsieur Pierre-Philippe CORTET
Chargé de recherche, Université Paris-Saclay – Laboratoire FAST, CNRS UMR 7608, Examinateur

Monsieur Giorgio KRSTULOVIC
Chargé de recherche, Université Côte d'Azur – Laboratoire J. L. Lagrange CNRS UMR 7293, Examinateur

Abstract

In this thesis, we describe a new cryogenic apparatus (called CryoLEM) used to study rotating helium II (or superfluid) flows by visualization of solid deuterium particles. Rotating helium II is a canonical flow that produces an organized and regular quantum vortex array.

The CryoLEM is an experimental device whose implementation was completed during this thesis. The start-up and use protocols have been established, and the first tests in real conditions have been carried out. These tests allowed us to characterize the performance of the cryostat and to better understand the formation of solid deuterium particles. While the long term objective is to perform 3D particle motion measurements, we remained focused on performing 2D measurements in a plane containing the axis of rotation. To perform Lagrangian particle tracking, an algorithm has been entirely written based on existing techniques.

This cryostat was first used to study the transient regimes that occur during particle injections, and after the start (or stop) of the rotation of the device. The aim is to estimate the characteristic time scales of these transient regimes, and compare them to the Ekman time, and an empirical time constant obtained by Tsakadze & Tsakadze using a rotating sphere filled with helium II. After a particle injection, a time proportional to the cryostat rotation rate must elapse to recover a steady state. For the spin-up problem, we found a very good agreement with an Ekman time based on the circulation quantum. In spin-down, a qualitative agreement with the Tsakadze model is found. These results allowed us to work with stationary data.

During the stationary rotation of helium II an oscillating motion of the particles with an amplitude of the order of a millimetre is observed in the rotating frame of reference. We are not able to relate the amplitude of these oscillations to any of the physical parameters that we measured. Nevertheless, these oscillations are not observed in helium I (normal liquid), which shows the fundamentally different nature of these two fluids, and motivates further studies.

Finally, a turbulent helium II flow generated by a counter-rotating turbine in the rotating CryoLEM has been studied. We have characterized this flow, and understood the scalings of its physical parameters thanks to an energy balance between injection and dissipative mechanisms. We have defined a series of surrogates to estimate the energy dissipation rate in this quantum turbulent and anisotropic flow. They use first to third order statistical quantities of the velocity increments. All these measurements lead to a coherent scaling of the radial dissipation rate as the cube of the system rotation rate, with some discrepancies in the prefactor. The third order statistics led us to conclude that energy was being transported from the large to the small scales, while anisotropy grows with the rotation rate, in agreement with the Taylor-Proudman theorem.

This thesis ends by pointing out that some of the particles evolving in this flow show oscillations of smaller amplitude than their size. This could be compatible with a particle – quantum vortex interaction mediated by the Magnus force. This observation opens a new way to study quantum vortices dynamics.

Résumé

Dans cette thèse, nous décrivons un nouvel appareil cryogénique (appelé CryoLEM) utilisé pour étudier les écoulements d'hélium II (ou superfluide) en rotation par la visualisation de particules solides de deutérium. L'hélium II en rotation est un écoulement canonique qui produit un réseau de vortex quantiques organisé et régulier.

Le CryoLEM est un dispositif expérimental dont la mise en œuvre a été achevée au cours de cette thèse. Ainsi, les protocoles de démarrage et d'utilisation ont été établis, et les premiers tests en conditions réelles ont été réalisés. Ces tests ont permis de caractériser les performances du cryostat et de mieux comprendre la formation des particules solides de deutérium. Bien que l'objectif à long terme soit d'effectuer des mesures 3D du mouvement des particules, nous sommes restés concentrés sur la réalisation de mesures 2D dans un plan contenant l'axe de rotation. Pour effectuer le suivi lagrangien des particules, un algorithme a été entièrement écrit sur la base des techniques existantes.

Ce cryostat a d'abord été utilisé pour étudier les régimes transitoires qui se produisent pendant les injections de particules, et après le début (ou l'arrêt) de la rotation du dispositif. L'objectif est d'estimer les temps caractéristiques de ces régimes, et de les comparer au temps d'Ekman, et à une constante de temps empirique obtenue par Tsakadze & Tsakadze en utilisant une sphère remplie d'hélium II. Après une injection de particules, un temps proportionnel à la vitesse de rotation du cryostat doit s'écouler pour retrouver un état stationnaire. Les résultats de notre étude de la mise en rotation sont en très bon accord avec un temps d'Ekman basé sur le quantum de circulation. Pour l'arrêt de la rotation, un accord qualitatif avec le modèle de Tsakadze est trouvé. Cela nous a ensuite permis de travailler avec des données stationnaires.

Pendant la rotation stationnaire de l'hélium II, on observe un mouvement oscillant des particules d'une amplitude de l'ordre du millimètre dans le référentiel tournant. Nous ne sommes en mesure de relier l'amplitude de ces oscillations à aucun des paramètres physiques que nous avons mesurés. Néanmoins, ces oscillations ne sont pas observées dans l'hélium I (liquide normal), ce qui montre la nature fondamentalement différente de ces deux fluides, et motive des études plus approfondies.

Enfin, un écoulement turbulent d'hélium II généré par une turbine contrarotative dans le CryoLEM en rotation a été étudié. Nous avons caractérisé cet écoulement, et compris l'évolution de ses paramètres physiques grâce à un bilan énergétique entre les mécanismes d'injection et de dissipation. Nous avons défini une série de substituts pour estimer le taux de dissipation d'énergie dans cet écoulement anisotrope et turbulent. Ceux-ci utilisent des quantités statistiques du premier au troisième ordre des incréments de vitesse. Toutes ces mesures conduisent à une évolution cohérente du taux de dissipation d'énergie radial comme le cube de la vitesse de rotation du système, mais avec différents préfacteurs. Les statistiques du troisième ordre nous ont amenés à conclure que l'énergie était transportée de la grande à la petite échelle, tandis que l'anisotropie augmente avec la vitesse de rotation, en accord avec le théorème de Taylor-Proudman.

Cette thèse se termine en soulignant que certaines des particules évoluant dans cet écoulement présentent des oscillations d'une amplitude inférieure à leur taille. Cela pourrait être compatible avec une interaction particule - vortex quantique médiée par la force de Magnus. Cette observation ouvre une nouvelle voie pour l'étude de la dynamique des tourbillons quantiques.

Acknowledgements

First of all, I would like to acknowledge the support of the LANEF who funded this project, and the direction of the Institut Néel who allowed me to use their premises. I also acknowledge the professors of the Université Grenoble Alpes for providing high quality courses. I must also thank the jury members for their evaluation work, their availability during this pandemic period and their enthusiastic welcome of this work.

Many thanks to the different teams and services of the laboratory who helped us at one point or another: the cryogenic hub, the electronic service, the administrative hub, and the warehouse staff. Among them, we have to specially mention Gregory Garde for the technical conception, realization, and assembly of the CryoLEM, and his support throughout the project. Without his work, this thesis work could never have been done.

Thanks to the HelFA team for all our friendly interactions, especially with Panayotis Spathis, Benoit Chabaud, and Pierre-Etienne Wolf. Their help and support during tough times (such as the research of helium leaks) was highly appreciated.

Props to the few non-permanent staff of the laboratory I interacted with. Victor Doebele, Alexandre Zampa, and Jeremy Vessaire, I am always ready for a beer with you, but not for a hike, sorry.

Last but not least, many thanks to the best thesis supervisor on earth: Mathieu Gibert. Working with you was always a pleasure, as I felt like I was interacting not with a supervisor, but with a friend (maybe sometimes too much). I keep in mind that I owe you 2 barbecues (and a house move), and I will invite you back as soon as my indecent engineer salary allows me to buy a house with a garden. Take care of your health until this moment, because it may take some time for me to get it. The CryoLEM needs you to be operated properly, until the resolution of all the quantum vortices mysteries, and the future PhD students need you to know what "learning from the best" means. Now I hope I shined your shoes enough to dazzle everyone at your wedding. All the best to you and your family.

Contents

Introduction

In this thesis, we describe a new apparatus used to study rotating flows of superfluid helium through visualization. Helium is the fluid with the lowest viscosity, which makes it of peculiar interest in the study of fluid dynamics. At cryogenic temperatures ($T < 2.17K$), this element enters an unusual state of matter called liquid helium II, or more commonly superfluid helium.

This fluid behaves as a classical fluid from a macroscopic point of view, but the use of quantum mechanics is necessary to explain its microscopic behavior. Indeed, classical turbulence predicts that, when a sufficient amount of energy is supplied to a fluid, eddies of various sizes and velocities are produced, and a cascade of energy from large scales to smaller ones is used to dissipate energy through viscous friction. In a superfluid, an energy source leads to the creation of angström-sized vortices (diameter $a_0 \simeq 10^{-10}m$) whose circulation ($\kappa \simeq 10^{-7}m^2/s$) is quantified. This is why they are called quantum vortices. The rotation of liquid helium II is the canonical way to produce an organized array of regularly spaced quantum vortices. Therefore, this type of flow is the natural configuration to study these objects.

In order to study them experimentally, the most recent apparatuses use visualization methods. In order to visualize the fluid motion, particles of solid hydrogen, or deuterium can be used to seed the flow. Moreover, in 2006, it has been experimentally observed that these micron-sized particles could be trapped into the quantum vortices cores, despite a size ratio of $\frac{\text{Particle diameter}}{\text{Vortex core}} \simeq 10^4$. Particle visualization techniques are therefore among the most promising of this century in the study of superfluid helium dynamics.

Open Questions

- What are the time constants ruling the spin-up and spin-down of helium II?
- What is the effect of rotation on decaying and stationary quantum turbulence?
- What are the differences between classical and quantum turbulence in a rotating frame of reference?
- How do energy transfers take place in an anisotropic turbulent flow of quantum fluid?
- How to visualize a quantum vortex?

Chapter 1

Context of study

1.1 Classical turbulence

1.1.1 Homogeneous isotropic turbulence (HIT)

In 1823, Claude-Louis Marie Henri Navier introduced the notion of viscosity in Euler equations, and George Gabriel Stokes, in 1945, gave the final form of the Navier-Stokes equation (NS) on the conservation of fluid momentum [1]:

$$\rho\left[\frac{\partial\overrightarrow{v}}{\partial t}+(\overrightarrow{v}.\overrightarrow{\nabla})\overrightarrow{v}\right]=-\overrightarrow{\nabla}P+\mu\overrightarrow{\Delta}\overrightarrow{v}+\overrightarrow{f} \tag{1.1}$$

where $\overrightarrow{v}$ is the fluid velocity (in $m.s^{-1}$), P is the pressure (in Pa), μ is the dynamic viscosity (in $Pa.s$) and $\overrightarrow{f}$ is the external forcing per unit volume (in $N.m^{-3}$). Rewriting NS using dimensionless (noted $\square^*$) variables (e.g. $v^*=\frac{v}{V}$, $\nabla X=L\nabla X$) leads to the following expression:

$$\frac{\partial\overrightarrow{v^*}}{\partial t^*}+(\overrightarrow{v^*}.\overrightarrow{\nabla^*})\overrightarrow{v^*}=-\overrightarrow{\nabla^*}P^*+\frac{\nu}{LV}\overrightarrow{\Delta^*}\overrightarrow{v^*}+\overrightarrow{f^*} \tag{1.2}$$

where L and V are respectively some characteristic length and velocity of the system and $\nu=\frac{\mu}{\rho}$ is the kinematic viscosity of the fluid (in $m^2.s^{-1}$). In this form, the equation displays a dimensionless number used to predict the behavior of a fluid in a system. In 1908, Arnold Sommerfeld called it the Reynolds number after the works of Osborne Reynolds in the 1880s [2,3].

$$Re=\frac{\text{inertial forces}}{\text{viscous forces}}=\frac{\left[(\overrightarrow{v}\cdot\overrightarrow{\nabla})\overrightarrow{v}\right]}{\left[\nu\overrightarrow{\Delta}\overrightarrow{v}\right]}\sim\frac{LV}{\nu} \tag{1.3}$$

When the non-linear inertial forces are negligible in front of viscous forces, the Reynolds number is low and the flow is dominated by momentum diffusion. This is the laminar state, which is, for example, observable in a regular pipe when the fluid is flowing slowly, or in a calm river.

By increasing the forcing, the inertial forces will become more and more important, instabilities will appear, until the flow becomes completely chaotic. This is the turbulent state which can be observed in rapids, or large atmospheric or oceanic phenomena. The transition from laminar to turbulent flows occurs at different Reynolds numbers depending on the nature of the flow. In the case of pipe flows for example, the transition is usually observed around $Re\approx 2000$ [3].

In 1922, Richardson predicted qualitatively that turbulence is actually an energy transfer in cascade from large structures to smaller ones [4], until it reaches a scale where the energy can be dissipated by viscosity. In 1941, Kolmogorov took over this cascade theory to build a statistical description of homogeneous isotropic turbulence (K41: [5–8]) around 2 hypotheses:

- At large Reynolds numbers, and far from boundaries, the small scale eddies are homogeneous and isotropic. The statistical properties of the flow at small scales are entirely determined by the kinematic viscosity ν ($m^2.s^{-1}$) and the energy dissipation rate per unit mass ϵ ($m^2.s^{-3}$).

$$\epsilon = \nu \overline{\frac{\partial v_i}{\partial x_j}\left(\frac{\partial v_i}{\partial x_j} + \frac{\partial v_j}{\partial x_i}\right)} \tag{1.4}$$

- The flow is self-similar at intermediate scales (inertial range): the statistical properties are determined by ϵ.

Based on these hypotheses, it follows naturally that the dissipation rate ϵ is the key physical quantity. When it is known, a dimensional analysis allows the introduction of several quantities used to characterize the turbulent cascade:

- The integral length scale L is the scale of the largest structures. This is the scale at which the energy is injected in the cascade. It corresponds to the scale of velocity correlations: two points separated by a distance $r < L$ will have correlated velocities, but it will not be the case if $r > L$. L is related to the standard deviation of velocity fluctuations σ and the energy dissipation rate ϵ:

$$L = \frac{\sigma^3}{\epsilon} \tag{1.5}$$

  The integral Reynolds number can be defined using this length scale:

$$Re_L = \frac{L\sigma}{\nu} = \frac{\sigma^4}{\nu\epsilon} \tag{1.6}$$

- The Kolmogorov length scale η is the scale of the smallest eddies in the flow. This is the scale at which the kinetic energy is converted into heat by viscous friction. It is related to the dissipation rate ϵ and the fluid viscosity ν:

$$\eta = \left(\frac{\nu^3}{\epsilon}\right)^{1/4} \tag{1.7}$$

  It immediately comes out that

$$\frac{L}{\eta} \propto Re_L^{3/4} \tag{1.8}$$

  which means that the Reynolds number physically reflects the scale separation between the large and small structures. A large Reynolds number corresponds to a "long" turbulent cascade, in the separation space.

  The turnover time of a structure of scale η can also be estimated as:

$$\tau_\eta = \sqrt{\frac{\nu}{\epsilon}} = \frac{\eta^2}{\nu} \tag{1.9}$$

  Thus, in order to characterize the smallest structures, an experimental apparatus must have a time resolution below $\frac{\tau_\eta}{2}$, according to the Nyquist–Shannon sampling theorem.

In order to quantify these length scales through velocity measurements, structure functions are built. The idea is to characterize an eddy of size r through velocity differences (or increments). Let's assume an homogeneous and statistically steady flow probed with Lagrangian tracers. The position $\overrightarrow{X}$ of each tracers as a function of time t is known, so their velocity $\overrightarrow{v}(\overrightarrow{X}, t)$ can be computed. Then, for each pair of tracers separated by a vector $\overrightarrow{r}$, a velocity difference can be computed as $\overrightarrow{\delta v}(\overrightarrow{X}, \overrightarrow{r}, t) = \overrightarrow{v}(\overrightarrow{X} + \overrightarrow{r}, t) - \overrightarrow{v}(\overrightarrow{X}, t)$. Finally, the definition of structure functions is:

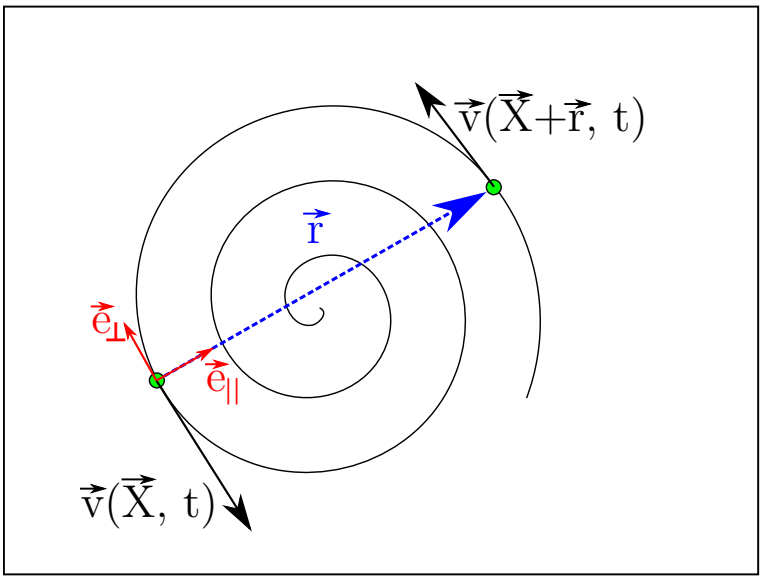

Figure 1.1: Illustration of an eddy probed by two particles following its streamlines (Lagrangian point of view), and separated by a vector $\vec{r}$.

$$S_n^{\vec{u}}(\vec{r},t) = \langle(\vec{\delta v}(\vec{X},\vec{r},t)\cdot\vec{u})^n\rangle \tag{1.10}$$

where $\langle\square\rangle$ denotes spatial and ensemble averages. As the flow is supposed statistically steady, the time dependence is usually removed by a time averaging. The unitary vector $\vec{u}$ ($||\vec{u}|| = 1$) specifies the direction along which the structure function is computed. In HIT, one often consider the vectors $\vec{u} = \vec{e_\parallel} = \frac{\vec{r}}{||\vec{r}||}$ and $\vec{u} = \vec{e_\perp}$ which is orthogonal to $\vec{e_\parallel}$ (see fig. 1.1) to compute the so called longitudinal and transverse structure functions. In the case of non-isotropic turbulence, $\vec{u}$ is chosen according to the symmetries of the system. For example, in a rotating cylindrical system, a vector along the rotation axis and the vectors of the orthogonal plane are relevant calculation directions.

These structure functions characterize the eddies of diameter $r = ||\vec{r}||$ in a homogeneous isotropic and statistically steady turbulent flow. For example, we can note that $S_2(r) = S_2^{\parallel}(r) + S_2^{\perp}(r) = S_2^x + S_2^y + S_2^z$ reflects the kinetic energy (per unit mass) of an eddy of size r. By nature, these eddies are unstable and have a lifespan which is comparable to their turnover time $\tau_r = \frac{r}{\sqrt{<(\vec{\delta v}(\vec{X},\vec{r}))^2>}} = \frac{r}{\sqrt{S_2(r)}}$. As a consequence, it takes a time τ_r to dissipate the kinetic energy E_r of an eddy of size r. Hence, the dissipation rate scales as :

$$\epsilon(r) = \frac{E_r}{\tau_r} \propto \frac{S_2(r)}{r/\sqrt{S_2(r)}} = \frac{S_2(r)^{3/2}}{r} \tag{1.11}$$

$$\Rightarrow S_2(r) \propto (\epsilon r)^{2/3} \tag{1.12}$$

The outcome is that it is experimentally possible to determine the value of ϵ through the study of velocity increments. The coefficient linking the two members of the equation 1.12 is usually noted C_2. It is the universal Kolmogorov constant [5], and its value for $S_2^{\parallel}$ has been experimentally evaluated to be $C_2^{\parallel} = 2.0$ [9]. It is also possible to show, in the transverse direction that $S_2^{\perp} = \frac{4}{3}S_2^{\parallel}$, which means that $C_2^{\perp} = 2.7$.

The previous results have been derived by dimensional analysis. However, Theodore Von Karman

and Leslie Howarth obtained, from an exact derivation of the Navier-Stokes equation in the case of homogeneous, isotropic and statistically stationary turbulence, the following equation [10]:

$$-\frac{4}{5}\epsilon r = S_3^{\parallel}(r) - 6\nu\frac{\partial S_2^{\parallel}(r)}{\partial r} \tag{1.13}$$

In the inertial range, where the influence of viscosity can be neglected, the Karman-Howarth equation (1.13) leads to the famous Kolmogorov's $4/5^{th}$ law:

$$S_3^{\parallel}(r) = -\frac{4}{5}\epsilon r \tag{1.14}$$

This result gives another way to measure ϵ. As it is a third order moment, it requires much more data than equation 1.12 to produce a converged result. However, this equation has two major advantages. The first one has already been mentioned: it is an exact result which does not rely on an experimentally evaluated constant which exact value is subject to debate. The second advantage is that a third order moment is a signed value. Therefore, it also gives an information on the direction of the energy transfers in the cascade. As $S_3(-r) \neq S_3(r) \neq 0$, the odd orders of $S_n(r)$ are not time reversible, and so is the turbulent cascade. The minus sign actually expresses the energy flow from large scales towards smaller scales, as described by Richardson.

1.1.2 Rotating turbulence: an anisotropic flow

In a flow rotating at an angular velocity Ω, the Coriolis force $\overrightarrow{f} = 2\rho\overrightarrow{\Omega} \wedge \overrightarrow{v}$ must be taken into account in the NS equation (1.1). As previously, the new equation can be normalized ($\overrightarrow{f^*} = \frac{2L\Omega}{V}\overrightarrow{\Omega^*} \wedge \overrightarrow{v^*}$) resulting in the apparition of a new dimensionless number. It is called the Rossby number, and it compares the advection term to the Coriolis force:

$$Ro = \frac{\text{inertial forces}}{\text{coriolis force}} = \frac{\left[(\overrightarrow{v}\cdot\overrightarrow{\nabla})\overrightarrow{v}\right]}{\left[2\overrightarrow{\Omega} \wedge \overrightarrow{v}\right]} \sim \frac{V}{2\Omega L} \tag{1.15}$$

When the fluid is strongly influenced by rotation, $Ro \to 0$. In this case, the Taylor-Proudman theorem [11, 12] predicts that the flow must become 2D: the dependence along the rotational axis disappears. The conclusion is clear: when a flow is significantly impacted by rotation, it becomes anisotropic. This calls into question one of the starting hypotheses of the theory detailed in section 1.1.1.

As a consequence, in the study of rotating flows, the Karman-Howarth-Monin equation (KHM) [13, 14] is the most commonly used. This is in fact an extension of the Karman-Howarth equation (1.13) to homogeneous turbulence (not necessarily isotropic). This equation connects the velocity correlation $R(\overrightarrow{r},t) = \langle \overrightarrow{v}(\overrightarrow{x},t)\cdot\overrightarrow{v}(\overrightarrow{x}+\overrightarrow{r},t)\rangle$ to the energy flux density in the space of separations $\overrightarrow{F}(\overrightarrow{r},t) = \langle \delta\overrightarrow{v}(\delta\overrightarrow{v})^2\rangle$:

$$\frac{1}{2}\frac{\partial R}{\partial t} = \frac{1}{4}\nabla\cdot\overrightarrow{F} + \nu\Delta R + \phi \tag{1.16}$$

where ϕ is a term related to the flow forcing per unit mass $\mathcal{F}$ [15]: $\phi = \frac{1}{2}\langle\overrightarrow{v}(\overrightarrow{x},t)\cdot\overrightarrow{\mathcal{F}}(\overrightarrow{x}+\overrightarrow{r},t) + \overrightarrow{\mathcal{F}}(\overrightarrow{x},t)\cdot\overrightarrow{v}(\overrightarrow{x}+\overrightarrow{r},t)\rangle$.

R can also be written as:

$$R(\overrightarrow{r},t) = \langle(\overrightarrow{v}(\overrightarrow{x},t))^2\rangle - \frac{E(\overrightarrow{r},t)}{2} \tag{1.17}$$

where E is the kinetic energy at scale $\overrightarrow{r}$:

$$E(\overrightarrow{r},t) = S_2(\overrightarrow{r},t) = \langle(\delta\overrightarrow{v}(\overrightarrow{X},\overrightarrow{r},t))^2\rangle \tag{1.18}$$

The KHM equation actually reflects the transfers of energy taking place in the space of separations in the turbulent cascade. In the case of a statistically steady flow, the term $\frac{\partial R}{\partial t}$ is equal to 0. Then, the KHM equation becomes a transport equation of R, with ϕ being the source term, $\overrightarrow{F}$ the flux of R, and $\nu\Delta R$ the dissipation (sink). In other words, ϕ represents the power (per unit mass) injected in each structure of scale r. At large scales ($r > L$), it corresponds to the forcing power (e.g. pulled grid, stirring turbine...). This power is transported by F across the whole cascade, and is dissipated at scales $r < \eta$. Thus, by energy conservation, in the inertial range we have $\phi \simeq \epsilon$. Moreover, Kolmogorov's second hypothesis allows us to neglect the term of viscous dissipation $\nu\Delta R$ in the inertial range. Therefore, in this range, the KHM equation (1.16) is reduced to:

$$\nabla\overrightarrow{F} = -4\epsilon \tag{1.19}$$

With this equation, it is now possible to determine ϵ in anisotropic turbulence. However, it requires the computation of the divergence of a third-order vector field. In other words, the amount of data required to produce converged results is staggering, and it will be very sensitive to noise. This equation has a solution in HIT: the celebrated "four-fifth law" (eq. 1.14). However, it is much more difficult to integrate it in the anisotropic case [16].

1.2 Helium[1] and quantum turbulence

1.2.1 Liquid helium: towards absolute zero

In the 1890s, James Dewar managed to liquefy several gases (such as hydrogen in 1899) for the first time. In these works, he developed processes to liquefy oxygen at industrial scales, and a container which is now widely used in our everyday lives: the dewar flask (a.k.a. Thermos of vacuum flask). This container is thermally insulated by at least two walls separated by vacuum, to cut the diffusion and convection thermal exchanges. In spite of his remarkable works, he lost the race to liquefy helium to his competitor Heike Kamerlingh Onnes in 1908 [17]. Indeed, a bit less than a decade elapsed between the liquefaction of hydrogen, and that of helium, and it involved the works of several competing research groups.

In order to liquefy helium, Onnes used large quantities of purified gaseous helium under a pressure of $100atm$, cooled down by $75L$ of liquefied air ($\sim 77K$) [17]. Then, the gas was released (Joule-Thomson effect) in a vacuumed glass dewar flask already cooled down by liquid hydrogen ($20K$). After several cycles of compression and expansion an unusually stable temperature is observed, meaning that a phase transition was occurring, and the first drops of liquid helium were observed.

Helium has the lowest boiling temperature ($4.22K$, at P_{atm}, see table 1.1) of all known chemical elements, which makes its liquid form the purest on Earth. Indeed, all other elements which could enter this fluid would solidify and settle because of the density mismatch. In Institut Néel, Grenoble, helium is liquefied using the Claude cycle with 2 turbines. This process developed by Georges Claude (founder of Air Liquide) is in fact an improvement of the liquefaction processes used by Dewar and Onnes. Basically, all the cryogenic liquefaction processes use similar principles: the Joule-Thomson effect, and heat exchangers using cryogenic fluids, such as oxygen, nitrogen, hydrogen, or gaseous helium.

This highlights the fact that the fundamentals of liquefaction technologies has not changed that much in more than a century. Once liquefied, cryogenic fluids are used in cryogenic vessels called cryostats (fig. 1.2). Indeed, if liquid nitrogen can be stored for several minutes in a regular bucket,

[1] Two isotopes of helium exist, this thesis will focus on the most common one: ^4He. If ^3He is of peculiar interest in the research on low temperature physics, its use is quite unusual in turbulence research.

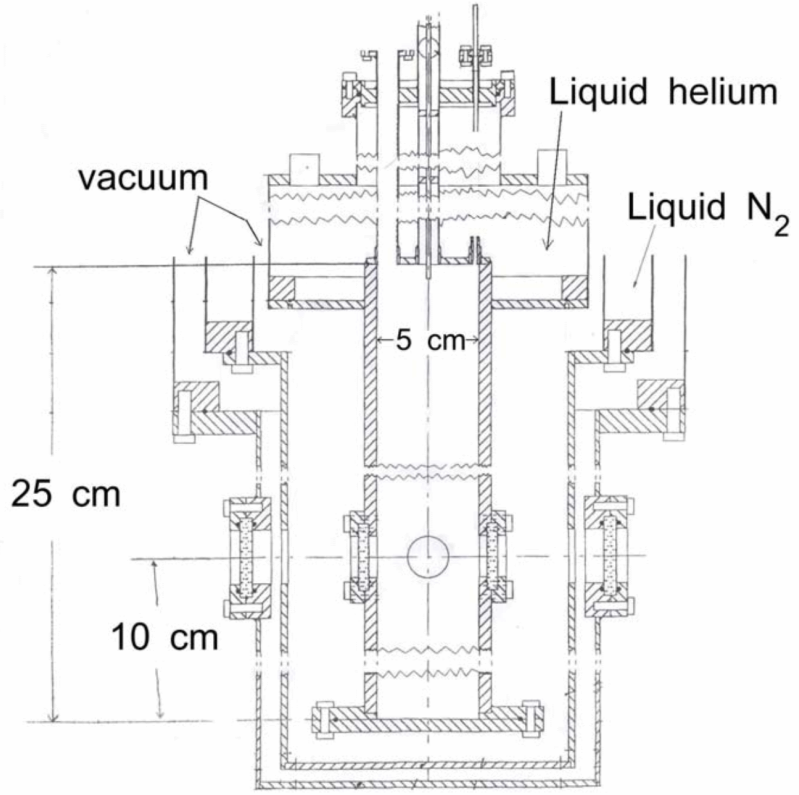

Figure 1.2: Figure taken from [18]. The drawing shows the interior of a cryostat used at Yale University (in 2006). Three concentric vessels are put one into the other, and separated by vacuum. The middle one is thermalized at $77K$ using liquid nitrogen, allowing better insulating properties than a regular dewar flask.

it is impossible to keep helium in a liquid state without special care, due to its very low latent heat ($\Delta H_{He}^{l \leftrightarrow g} = 20.7 kJ.kg^{-1}$). Cryostats can have different structures depending on their applications, but the basic principle is the same as the dewar flask. At least three insulating walls are usually necessary to keep liquid helium for several hours. To enhance the thermal insulation, it is common to use super insulator materials between the walls (in the vacuum), and/or to thermalize the middle wall with a cryogenic fluid such as nitrogen.

Liquid helium has a dynamic viscosity which is comparable to a gas, and a density between 125 and $145 kg/m^3$, leading to a very low kinematic viscosity (fig. 1.3), which is of high interest in the research on turbulence at large Reynolds numbers [20–22]. In addition, below a certain temperature noted T_λ, liquid helium displays unusual phenomena which cannot be explained by classical physics. Indeed, the use of quantum mechanics is necessary to explain them, which is why liquid helium is often called a "quantum fluid".

1.2.2 Cryogenic helium: a bridge between classical and quantum mechanics

Onnes' discovery of superconductivity in 1911 caused a real enthusiasm in the scientific community, this is probably why research on low temperature helium has slowed down until 1930. In the late 20s, Willem Keesom and his daughter tried to characterize some helium properties and discover some discontinuities around "$2.3K$", despite helium remaining a liquid. They assumed that helium could exist in two different liquid states with different properties, with a transition occurring at T_λ, close to

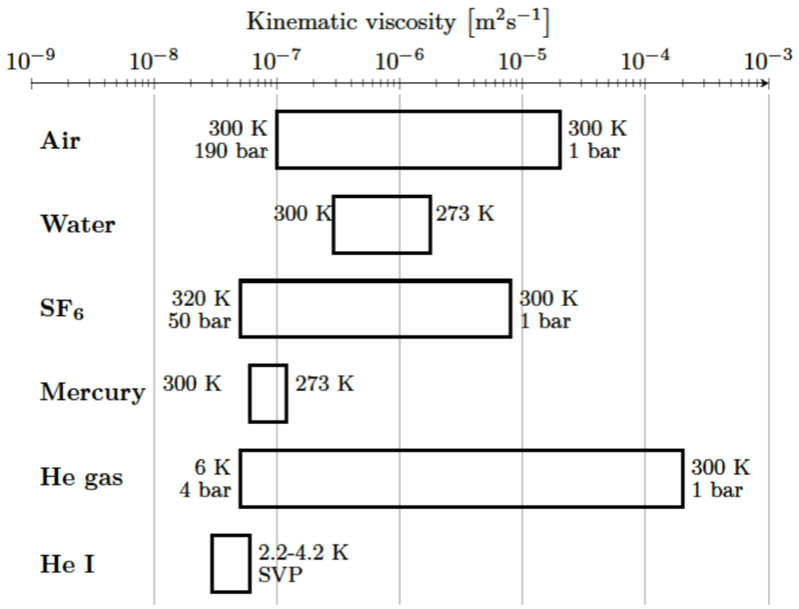

Figure 1.3: Kinematic viscosities of different fluids used in turbulence research. Image taken from [19]

$2.3K$ (actually, $T_\lambda = 2.1768K$ [23]). The name λ comes from the shape of the helium heat capacity curve (Fig. 1.4) that Keesom measured [24]. Between $4.2K$ and T_λ, the liquid is called He I, and below T_λ, the liquid is called He II. In the 1930s, many research groups discovered unusual conducts of He II:

- In 1935, J. O. Wilhelm, A. D. Misener and A. R. Clark observed that the damping of a twisting pendulum was considerably reduced in He II compared to He I. [25]
- In 1935, Keesom and his daughter found that He II was a very efficient heat conductor [24]. It has been confirmed in 1937 by J. F. Allen. [26]
- In 1938, two articles were published in the same edition of Nature: J. F. Allen explained his observations about He II flowing in capillaries with no viscous drag [27], and P. L. Kapitza described how he observed He II flowing between two optically flat disks, where He I could not flow. Based on these observations, Kapitza called He II a "superfluid", by analogy with superconductivity. [28]

The same year, several articles were published, trying to theoretically explain the above experimental observations. F. London built a bridge between superfluidity and Bose-Einstein condensation [29], and L. Tisza distinguished the condensed atoms from the non-condensed, laying the foundations of the two-fluid model [30]. L. D. Landau went back over this theory and published in 1941 what is still considered as the basis of superfluidity [31]. The construction of this theory is therefore the result of a joint effort by many researchers who have been working on the issue for several decades.

	Helium I	**Helium II**
Temperature range at P_{atm} (K)	$[2.17; 4.22]$	$[0; 2.17]$
Total density ρ (kg/m^3)	$[0.125; 0.146]$	$\simeq 0.145$
Kinematic viscosity $\nu = \frac{\mu}{\rho}$ (m^2/s)	$[1.7; 2.6] \times 10^{-8}$	$[0.8; 1.7] \times 10^{-8}$

Table 1.1: A few properties of both states of liquid helium.

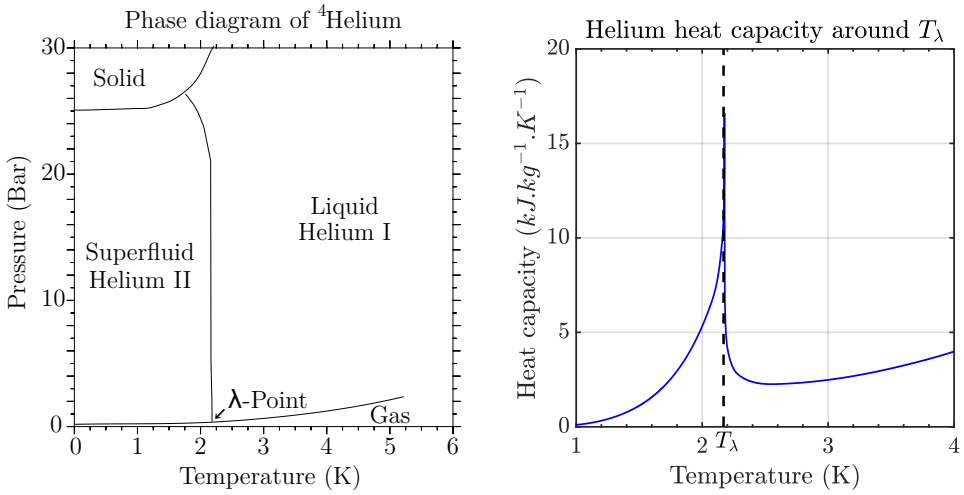

Figure 1.4: Left: Phase diagram of helium. Right: Liquid Helium (I & II) heat capacity as a function of temperature. A discontinuity at T_λ gives the curve the shape of a λ letter. Data used here comes from [23].

In this model, He II is actually a superposition of a regular viscous liquid (normal component), and a non-viscous superfluid component with zero-entropy. They act like two (almost) independent coexisting fluids, allowing us to define independent values, v_n and v_s for their velocity fields, ρ_n and ρ_s for their densities, so that:

$$\rho = \rho_n + \rho_s \tag{1.20}$$

where the subscripts n and s stand for "normal" and "superfluid".

In the limit $T \to 0$, $\rho_s \to \rho$ and $\rho_n \to 0$ (Fig. 2.5). This theory explains the phenomena observed by Allen, Misener and Kapitza: the superfluid component can flow through micro-sized capillaries without viscosity, and the normal component can damp the motion of a twisting pendulum, but less efficiently than in He I.

In the theory of superfluid helium, the fluid vorticity is contained in discontinuities which are now called “quantum vortices”. These are filaments of angström sized diameter, which can be several centimeters long. They can also be seen as holes formed by centrifugal acceleration and balanced by surface tension [32]. These vortices have a quantized circulation $\mathcal{C}$ equal to:

$$\mathcal{C} = \oint v_s.dl = n \times \frac{h}{m_{He}} = n \times \kappa \tag{1.21}$$

with h the Planck constant, m_{He} the mass of an atom of helium 4, and n an integer. The quantum of circulation $\kappa = \frac{h}{m_{He}} = 0.997 \times 10^{-7} m^2/s$ is defined. Feynman showed that a single vortex of circulation $\mathcal{C} = n\kappa$ with $n > 1$ costs more energy than a collection of quantum vortices of circulation κ (with $n = 1$) [33]. In other words, in a flow where 1 vortex should spin with a circulation $\mathcal{C} = n\kappa$, it will split into n vortices of circulation $\mathcal{C} = \kappa$.

These vortices must be connected to a wall, a free surface (vortex pinning), or to itself, forming a vortex ring. When a superfluid bulk is stirred, the number of vortices increases, forming tangles. A vortex tangle is a complex object in which the vortices can collide each other, and experience reconnections. A quantum vortex tangle is characterized by its vortex length $\mathcal{L}$ per unit volume $\mathcal{V}$:

$$\mathcal{L} = \frac{1}{\mathcal{V}} \int_{\text{along vortices} \in \mathcal{V}} dl \tag{1.22}$$

From $\mathcal{L}$ (in m^{-2}), a characteristic length can be defined for superfluid flows: the mean inter-vortex distance δ (in m).

$$\delta = \frac{1}{\sqrt{\mathcal{L}}} \tag{1.23}$$

δ is often used as a reference for the small scale of the turbulent cascade in a superfluid. Indeed, several articles report the observation of a cascade towards small scales in helium II, in good agreement with K41 theory. An inertial range with a $-\frac{5}{3}$ scaling of the energy spectra has been evidenced experimentally [34, 35], as well as numerically [36]. The validity of the four-fifth law have also been shown by Salort et al. [37]. The same group of authors showed, experimentally and numerically, that δ and κ could be used to build a relation analogous to equation 1.8 [38]:

$$\frac{\delta}{L} \simeq 0.5 Re_\kappa^{-3/4} \tag{1.24}$$

where Re_κ is a Reynolds number based on the quantum of circulation κ: $Re_\kappa = \frac{L\sigma}{\kappa}$. It is therefore possible to characterize the inertial range of the turbulent cascade in helium II, using laws analogous to K41. However, the behavior of the superfluid at scales $r < \delta$ is still subject to investigation and debate, as it significantly differs from classical turbulence [39, 40]. The dissipation mechanisms at small scales are not well understood [41]. Indeed, at these scales, one cannot consider any mean field approach: the dynamic of a collection of vortices interacting with each other must be taken into account. The most promising hypothesis would be that vortices, through reconnections, generate smaller and smaller rings [33, 42, 43], as well as undulations (kelvin waves [32]) which promote interactions between the normal fluid and the superfluid via the mutual friction force [44–47].

The mutual friction force Fns is the only link coupling the two velocity fields $\overrightarrow{v_n}$ and $\overrightarrow{v_s}$. The expression of this force in a helium II bulk rotating at Ω has been formulated by Vinen in 1957 [46]:

$$\overrightarrow{F_{ns}} = \frac{B\rho_s\rho_n}{\rho} \frac{\overrightarrow{\Omega}}{||\overrightarrow{\Omega}||} \times (\overrightarrow{\Omega} \times \overrightarrow{v_{ns}}) + \frac{B'\rho_s\rho_n}{\rho} \overrightarrow{\Omega} \times \overrightarrow{v_{ns}} \tag{1.25}$$

where $\overrightarrow{v_{ns}} = \overrightarrow{v_n} - \overrightarrow{v_s}$, and B and B' are temperature dependent coefficients [48]. When using this force in the Navier-Stokes equations applied to each component of helium II, it is possible to derive a wave equation relating $\overrightarrow{v_{ns}}$ to the temperature [49]. The complete derivation can be found in [50]. These temperature waves are called second sound [51], by analogy with the pressure wave called (first) sound.

Heat transfer is indeed something peculiar in He II. The temperature is carried by waves of v_{ns}, which means that the two fluid components are oscillating in antiphase. The second sound velocity c_2 depends on temperature, but it is about $20m/s$ between $1K$ and $1.9K$ [23]. This explains why many experiments in the early 1930s reported unprecedented thermal conductivity of He II. This is also why, when cooling down below T_λ, bubbles disappear from the bulk. Heat transfers are so fast in He II that bubbles cannot nucleate, so the fluid evaporates only from the surface. This is very convenient for visualization as bubbles would create dioptres, reflections, and interact with particles.

It is now clear that second sound is a mechanical wave that interacts with the velocity fields of both components of helium II. If a wave encounters a quantum vortex, it will act as an obstacle and scatter the second sound waves. Thus, a very common and reliable way to measure $\mathcal{L}$ is to build a resonating cavity for second sound [52]. This cavity consists of a heater at one end and a temperature sensor at the other end, separated by the distance D. If a current of frequency $f_0 = \frac{nc_2}{2D}$ $(n \in \mathbb{N})$ is supplied to the heater, a resonance of maximal amplitude a_0 occurs when the helium II bulk is quiescent (no vortices). In the presence of vortices, the resonance is damped to an amplitude $a < a_0$. By measuring this attenuation, $\mathcal{L}$ can be computed by the approximate formula [50]:

$$\mathcal{L} = \frac{6\pi\Delta f}{B\kappa} \times \left(\frac{a_0}{a} - 1\right) \tag{1.26}$$

where Δf is the width of the peak at half-maximum ($\frac{a_0}{2}$) without vortices. This method of measurement is historically the oldest measurement tool in helium II, but also the most reliable one to measure the vortex line density. Its main drawbacks are its spatial resolution and invasive character. It has been developed in 1957 by Hall and Vinen who applied this technique to another particularity of helium II: the counterflow [44], detailed here after.

When a source of heat is placed in He II, as the superfluid component has no entropy, the normal one will carry the energy away from the heater. To ensure mass conservation, the superfluid will come towards the heater, hence the name "counterflow", as He II components are moving in opposite directions. In the canonical counterflow experiment, the heater is located at the close (and insulated) end of a channel. In this case, the velocities direction is fixed by the channel's axis. Above a critical heat flux [53], quantum vortices appear, and a vortex tangle can be studied. For many decades, counterflow has been the most common experiment to study superfluid flows as it has no classical equivalent. Therefore, it is a good subject of study to reveal the differences between a classical fluid and a quantum one. It is also the easiest way to produce quantum turbulence, as it only needs a heater (and no moving parts). This is a real advantage in a cryogenic environment which is difficult to access. Furthermore, it produces well-known mean velocity fields [45]:

$$v_n = \frac{q}{\rho s T} \tag{1.27}$$

where q is the heat flux per unit area and s the entropy per unit mass. Using mass conservation (eq. 1.28), we can build equivalent relations for v_s and v_{ns} :

$$\rho_n v_n + \rho_s v_s = 0 \tag{1.28}$$

$$v_{ns} = v_n - v_s = \left(1 + \frac{\rho_n}{\rho_s}\right) v_n = \frac{q}{\rho_s s T} \tag{1.29}$$

According to Vinen's works in 1957 [46], in a steady counterflow, the vortex line density is proportional to v_{ns}^2:

$$\mathcal{L} = \gamma^2 (v_{ns} - v_{critical})^2 \tag{1.30}$$

where γ is a constant that depends on the temperature, and on the experimental apparatus, and $v_{critical}$ is the minimum velocity necessary for the apparition of the first quantum vortex, which also depends on the experimental conditions [50,54]. The validity of this law has been tested numerically [55–57] and experimentally [50, 58, 59] by several groups. The reference [50] gathers the estimations for these two parameters experimentally measured by several research groups. As an order of magnitude, it would be possible to write $\gamma \sim 100 s/cm^2$ and $v_{critical} \sim 1 cm/s$. These values also depend on the turbulent state of the counterflow. Indeed, counterflows exhibit (at least) two different turbulent states noted TI and TII [60, 61]. In the TI regime, $v_{ns} > v_{critical}$, and a tangle of quantum vortices is produced. Above a second critical velocity, turbulence is enhanced, and recent experiments [50, 61] suggest that it corresponds to the onset of the normal fluid turbulence.

If historically the experimental research on helium II has been fed by second sound measurements, and turbulence in counterflows, successive technological advances have enabled the development of other forcing and measurement tools in cryogenic environments. In opposition to counterflow, mechanically driven flows are sometimes called coflow, as both fluid components are actuated together.

For example, coflow experiments regroup the flows generated by propellers [34,62,63], a grid [35,64–66], or in a jet [67, 68].

Another widely studied coflow is the rotation of a helium II bucket. This type of flow was studied as early as 1950 [69], and experienced a revival of interest in 1955, with Feynman's prediction of an organized lattice of regularly spaced vortices [33]. Then, several other groups performed experiments of rotating helium for the next decades, leading eventually to the beautiful pictures of the vortex array by Packard's group [70]. To date, rotation is the only type of flow known to produce an organized vortex network.

1.3 Rotating helium II

1.3.1 Steady rotation

Rotating classical fluids in a cylindrical container, in steady state, are expected to rotate at the same velocity as their container. This regime is called "solid body rotation", as the fluid moves as one with its solid container. Before reaching this steady state, there is a transient state during which the energy is transmitted from the container walls to the fluid through viscosity. The duration of this transient state is characterized by the Ekman time [71]:

$$t_{Ek} = \frac{D}{\sqrt{\Omega\nu}} \tag{1.31}$$

where D is a characteristic (usually vertical) length scale, Ω the angular velocity of the container, and ν the kinematic viscosity of the fluid. In other words, the Ekman time characterizes the time needed for a classical fluid to reach the solid body rotation.

In helium II, the behavior is different, due to the potential flow of the superfluid component. In 1955, Feynman [33] predicted that, in steady state rotation, quantum vortices are organized in an hexagonal lattice which is parallel to the rotation axis, with a well-defined vortex line density:

$$\mathcal{L} = \frac{2\Omega}{\kappa} \tag{1.32}$$

The existence of this lattice has been confirmed and further studied by Hall and Vinen in 1956 [52, 72], using second sound resonators in a rotating cryostat. Vinen also highlighted the fact that the first vortex would appear only above a certain critical velocity [73]:

$$\Omega_c = \frac{\kappa}{(R^2 - r_0^2)} ln\left(\frac{R}{r_0}\right) \tag{1.33}$$

where R the radius of the helium vessel, and $r_0 \sim 10^{-10} m$ the radius of a quantum vortex. In the case of a "large" cryostat like the CryoLEM ($R = 54mm$), $\omega_c \sim 10^{-4} rad/s$, which is small enough to be ignored. As it scales as $\frac{ln(R)}{R^2}$, this critical velocity is mostly limiting small systems.

Feynman's theory seems to have generated enthusiasm in the low temperature community as many research groups of the following decades enriched the literature with articles about rotating helium II [70, 74–84]. Despite several works, the first direct observation of the lattice has been performed by Yarmchuk et al. in 1979 [70]. They used the fact that ions could be trapped in the vortex cores, and be revealed by a phosphor screen, on which they observed the hexagonal pattern of the lattice (fig. 1.5). Note that this observation is the result of several attempts (3 PhD), as the observation of a regular lattice requires a perfect mechanical stability. To overcome this problem, a small amount of ^3He has been diluted in the studied ^4He. As ^3He enters the superfluid state at a lower temperature than ^4He, it improved the stability of the system by damping the ^4He motion.

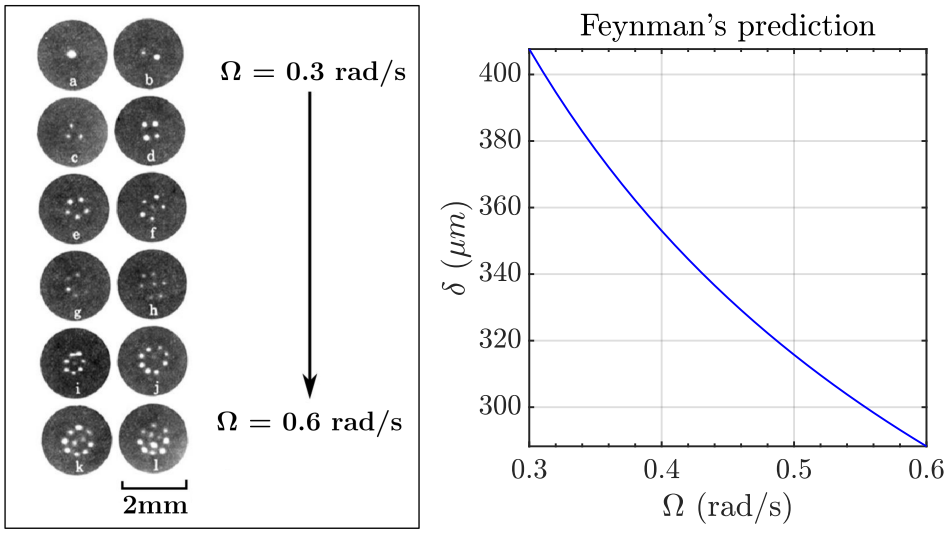

Figure 1.5: Left: Figure adapted from [70]. First images of the vortex lattice, viewed from the top, exhibiting hexagonal patterns, as predicted by Feynman. Right: Inter-vortex spacing as a function of Ω according to Feynman's rule (eq. 1.32).

Between Feynman's prediction, and Yarmchuk's observation, Tkachenko published several articles in which he mathematically demonstrated several properties of the vortex lattice, including oscillations which are now called Tkachenko waves [85]. These waves result in a periodic deformation of the lattice in the orthogonal plane. The rotating normal component of He II shears the quantum vortices, making them move away from their equilibrium position. The vortices experience a restoring force in response, and this leads to oscillations of the vortex array [86]. Ruderman gave the frequency of these waves in the case of a vessel of radius R and infinite length [87]:

$$f_{Tk} = \frac{5}{4\pi R}\sqrt{\frac{\hbar\Omega}{m_{He}}} \tag{1.34}$$

He successfully applied this model to neutron stars, whose interior matter is in superfluid state [88]. The oscillation period of several observed neutron stars was compatible with this model.

A few years later, Tsakadze and Tsakadze reported the presence of oscillations in rotating helium II, which does not occur in helium I [89, 90], proving their superfluid nature. This may be the first observation of Tkachenko waves in a laboratory. However, the frequency of their oscillations was an order of magnitude higher than Ruderman's prediction. Sonin suggested that in the case of a finite vessel, the bending of the vortices, and three dimensional effects had to be taken into account [91, 92]. These effects actually transform the Tkachenko wave into inertial waves [84] of frequency f_{IW} given by:

$$f_{IW} = \frac{\Omega}{\pi\sqrt{AH}} \tag{1.35}$$

where H is the height of fluid in the vessel, and A is a parameter related to a slip coefficient detailed in [92]. This expression is now compatible with Tsakadze's experiments.

The expressions 1.34 and 1.35 actually describe two regimes of oscillations. Two main differences can be highlighted between these two regimes: the independence of f_{IW} on the container radius, and its linear scaling with Ω. f_{IW} is also hard to evaluate due to the complexity to obtain the value of A [92]. The problem of Tsakadze's experiments is that their vessel's aspect ratio was too small to observe a Tkachenko regime disjointed from the inertial one. The existence of these waves has however been proven through their observation in Bose-Einstein condensates [85].

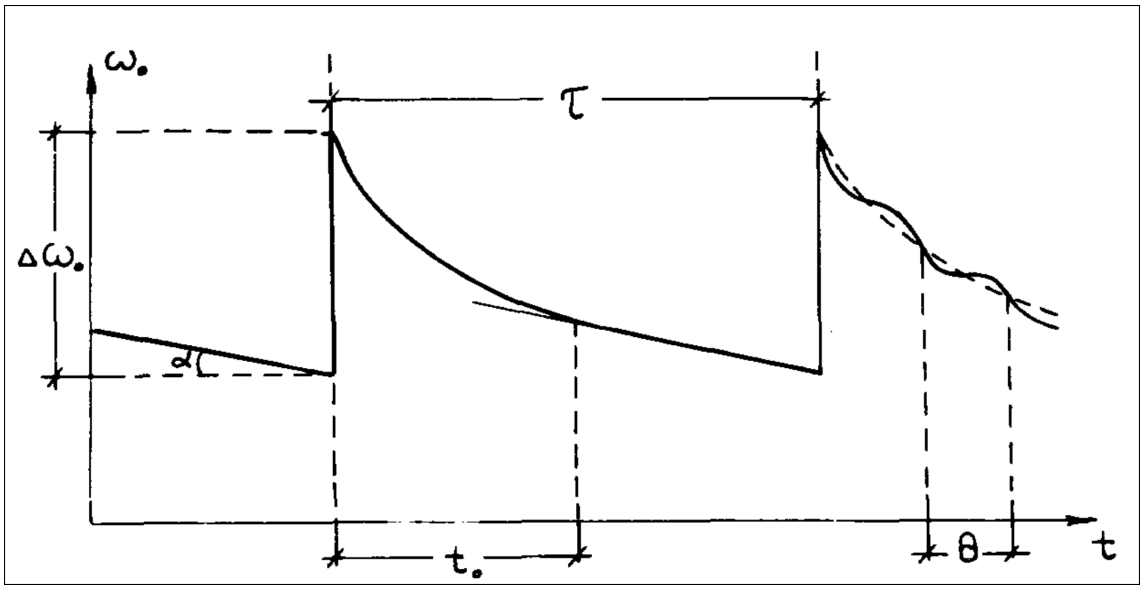

Figure 1.6: Image taken from [92]. Schematic representation of the changes in pulsar rotation velocity ω_0 with time. The diagram shows the characteristic times connected with the inner structure of neutron stars. Glitches of amplitude $\Delta\omega_0$ occur every τ. After the glitch, an exponential decay of characteristic time t_0 occurs. Some oscillations of pseudo-period θ can be observed during the decay.

If some open questions remain in the behavior of the steady lattice, even more questions remain unanswered when it comes to the transient states of the helium II rotation.

1.3.2 Transient states

The motivation for the study of rotating helium II was not only the fact that it is the only known way to produce a regular lattice. Some articles were also motivated by the prediction of superfluidity in neutron stars by Migdal [88], and the discovery of pulsars in 1967 [93]. Pulsars are neutron stars which emit an electromagnetic radiation and have a short rotational period. Thus, a distant observer (from Earth) receives a pulsating signal from this object, hence the name. A specificity of these starts is that their angular velocity is not constant, but slowly decreasing. Occasionally, pulsars experience "glitches" where the rotational frequency of the star suddenly increases [86]. After a glitch, there is a recovery process during which the angular velocity decreases quasi-exponentially while oscillating (with a period of several months) [86, 87, 89]. All these observations converged to the validation of Migdal's prediction: neutron stars actually contain superfluid matter.

A few years later, D. S. Tsakadze and S. D. Tsakadze [89] established an experimental protocol to study pulsar glitches, using rotating helium II in their laboratory. A sphere filled with helium II was set into steady rotation in vacuum. Then, the sphere is released into a free decay with low friction, and a magnetic system allows to suddenly accelerate it in order to simulate glitches. Then, an exponential decay is observed for several tens of seconds (fig. 1.6). During, and after the decay, they observed oscillations which they tried to relate to Tkachenko waves, as discussed in the previous subsection. The duration of the exponential decay has also been studied, varying the angular velocity, glitch amplitude, temperature and roughness of the sphere.

The time constant they measured was deviating from the Ekman time of classical flows. Thus, based on their observations, they built an empirical time constant for rotating He II:

$$t_0 \approx \frac{(2\pi)^{\frac{2}{5}}}{\Omega_0}\left(\frac{R^2\Omega_0}{\kappa}\right)^{\frac{2}{5}}\left(\frac{\rho}{\rho_n}\right)^{\frac{1}{4}} ln(1+5\Delta\Omega) \tag{1.36}$$

where Ω_0 is the initial angular velocity of the sphere in $rad.s^{-1}$, R the radius of the sphere in m, and $\Delta\Omega$ the amplitude of the glitch in $rad.s^{-1}$. This expression has been further discussed by Alpar who noted that, if the $\frac{2}{5}$ exponent was $\frac{1}{2}$, the first term would be nothing more than an Ekman time based on the quantum of circulation κ: $t_{Ek,\kappa} = \frac{R}{\sqrt{\Omega_0 \kappa}}$. The two other terms are empirical corrections taking into account the number of vortices [94].

Indeed, the quantum vortices are actually responsible for the unusual behavior of pulsars. When being submitted to changes of rotational velocity, it is possible to make the lattice enter a metastable state in which the amount of vortices disobeys the Feynman's rule (eq. 1.32) [89, 95]. For example, when their vessel experienced sudden velocity changes from Ω_0 to $\Omega_1 \neq 0$, they measured a delay of hundreds of seconds before observing a decay in the vortex lattice. Counterintuitively, no delay was observed when the vessel was suddenly stopped ($\Omega_1 = 0$).

Similarly, when a neutron star slows down, metastable vortices are stacked, until a threshold is reached. Then, the excess of vortices is released, transmitting their angular momentum to the vessel, and/or to the liquid, resulting in a glitch. The release of the vortices is expected to be related to their pinning force, which also depends on the roughness of the walls. A rough surface favors the nucleation and pinning of quantum vortices on it.

Therefore, the effect of the sphere roughness has been tested by sticking powder (grain size $\sim 500\mu m$) on its walls. In this case, Tsakadze and Tsakadze measured temperature-independent relaxation times of $\sim 20s$ [92]. This evidences the fact that the vortex pinning plays an important role in the relaxation time which has been significantly decreased. Moreover, the oscillations observed after the glitch kept the same frequency, but were significantly less damped, highlighting the major role of vortex pinning in the rotation decay.

This succession of articles from Tsakadze and Tsakadze, despite being subject to controversy due to the presence of mistakes and imprecision, has raised the interest of several theoreticians who tried to develop theories based on their observations [96–99]. The conclusion of these papers is the same: more experimental data is needed.

The articles of Tsakadze and Tsakadze explored several aspects of the relaxation of helium II, but the problem of the acceleration of the fluid after starting the rotation of the vessel has hardly been investigated. One of their article mention it [100], but the measurement protocol is not very clear, and they did not dig very deep in this subject. In fact, this is probably due to the fact that they could only measure the rotation rate of their vessel, but they could not measure that of the fluid in it. Thus, measurements of the fluid properties could only be done when the vessel was released, which is incompatible with an acceleration of the vessel (not considering glitches...).

Before their works, Hall [101] experienced the same problem, but gave more details on the helium II acceleration. He used torque measurements to quantify "acceleration and retardation processes" in a can filled with helium II, and containing closely spaced disks. The can is suddenly set into rotation, and the torque supplied by the motor is monitored in time. However, during acceleration, and constant rotation, oscillations due to their reduction gearing prevented them to make proper measurements without filtering, which reduced significantly the response time of the system.

Despite this problem, Hall was able to show that the acceleration and deceleration processes were not symmetric. Indeed, he observed that the acceleration process was shorter than the deceleration one, despite the initial slope of retardation being steeper than the acceleration one (fig. 1.3.2). Hall wrote that: "acceleration begins more slowly and finishes more rapidly than retardation". According to him, this is due to the fact that mutual friction force (eq. 1.25) depends on the rotation rate of the fluid. The initial fluid velocity being different in acceleration and retardation, this leads to different dynamic behaviors.

While there was already little data on helium II deceleration, technological obstacles at the time resulted in even less data on acceleration. Unfortunately, nowadays experiments on rotating helium

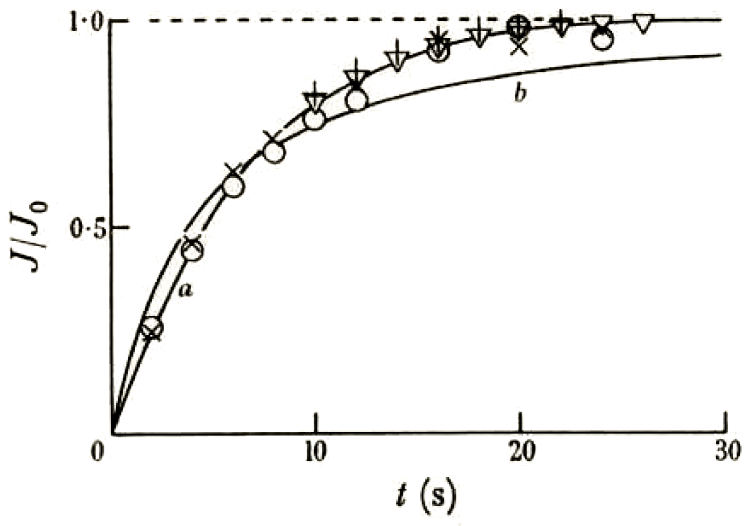

Figure 1.7: Image taken from [101]. The superfluid angular momentum as a function of time during acceleration and retardation; $\omega_0 = 0.785 rad/s$. a: mean acceleration curve; b: mean retardation curve.

II, appear less trendy than in the 1950-80s. According to Blaauwgeers et al. [102], this is due to the discoveries of other ways to generate quantum turbulence more easily, and more efficiently.

Indeed, the conception of a rotating cryostat is a real technological challenge (see chapter 2). Moreover, the pinning and depinning phenomena observed in rotating helium II play a significant role, but it is hard to study experimentally. However, rotation is still the only known forcing that produces a well organized structure of quantum vortices in helium II. Thus, it is of peculiar interest in the calibration of new sensors. For example, particles have been used to track the motion of helium II since the late 1950s [103]. But what made the particle tracking technique so popular nowadays is probably the visualization of quantum vortices by G. P. Bewley in 2006 [18], especially during rotating experiments, where particles illuminated the lattice. These relatively recent works using rotating helium II have given credibility to a (still) criticized measurement method.

During the last decade, a few new cryogenic rotating experiments have been created, in the aim of reaching lower temperatures ($< 1K$). In order to reach temperatures below 1K, the old concept of having a static cryostat in which is plunged a rotating part in contact with the outside has been abandoned. The newer facilities now use cryostats mounted on spinning frames with rotating joints for helium transport, and power supply [104–106]. However, none of them has been dedicated to the study of quantum vortices dynamics, even if ref. [104] indicates that the Manchester facility would be primarily used to investigate them (later publications from them focus on rotating solid helium [107]...).

Visualization techniques may be the key to overcome the technological issues encountered by Hall and Tsakadze. They allow a direct observation of the fluid dynamics, at different places of the bulk, in contrast to second sound resonators which measure a local vortex density. Thus, it is no longer necessary to take into account the interaction between the liquid and the vessel, and the field of observation can be located far from the walls, which would possibly remove the pinning effects. Of course, the local measurement methods have their own benefits as well, which is why using them together with a visualization technique would be of high interest.

1.4 Particles visualization in He II

In this thesis, the studied flows of helium II are probed using frozen particles. By injecting a hot mixture of gas in helium at temperatures below $4K$, we obtain a cloud of particles of different size and shape. In this section, we will first present the general concepts of particles-based measurement techniques. Then an overview of the cryogenic facilities using visualization techniques in helium II will

be presented.

1.4.1 Probing a fluid with particles

A whole field of fluid mechanics research is dedicated to the study of particle motions in their surrounding fluid. These studies are of primary interest as particles visualization techniques are now widely spread in many other fields of fluid mechanics, including turbulence. The objective of this section is to give the indicators reflecting the quality of a particle to probe a flow.

A solid particle in a fluid at rest is at equilibrium under the effect of gravity, and the upward buoyant force of Archimede's principle. In this equilibrium the difference in density between the fluid and the solid particle intervenes. Indeed, the particle will not move if it has the same density as the fluid. Thus, in order to be a faithful tracer, the particle must be as dense as the probed fluid.

Moreover, in turbulence research, the objective is to probe all the structures in the turbulent cascade, down to η: the Kolmogorov dissipative scale. A structure of size r cannot be probed by a solid particle of diameter $d_p > r$. Intuitively, we can imagine that if a large particle crosses structure, it will completely cover it. In fact, the particle will act on the fluid, by deviating the structure. However, the basis of measurements techniques is to avoid the alteration of the probed quantity. Actually, as any other sensor, a particle acts like a high-pass filter: it can only probe structures of size $r \gg d_p$. Thus, in order to probe structures as small as η, the particles must be as small as possible to fulfill $d_p \ll \eta$. In the study of He II, the small scale is the inter-vortex distance δ, which is of the order of $200\mu m$ in He II rotating around $\Omega = 15RPM$. If we consider that this value can decrease even lower in a turbulent He II flow, we need micron sized particles ($d_p \leq 10\mu m$).

Measuring a particle size

In the apparatus presented in this thesis, the objective is to work with frozen particles of deuterium, or hydrogen in helium II. A small amount of gaseous particle matter is diluted in a large amount of gaseous helium ($T = 300K$), and injected in liquid helium ($T < 4.2K$). The density of He II between $1K$ and $2.17K$ is about $145kg/m^3$, whereas the densities of solid hydrogen and deuterium are respectively $88kg/m^3$ and $206kg/m^3$. Both kind of particles are not neutrally buoyant tracers: hydrogen settles to the surface and deuterium settles to the bottom of the helium bath. As just explained, this density difference is a drawback in the production of faithful tracers. However, the quantity of available elements in He II is limited, and neutrally buoyant particles cannot be obtained (yet). Some efforts are made by the community to produce particles which density is closer to that of helium II by using deuterium hybride gas (HD) [108].

On the other hand, the size of the frozen particles is not something easy to determine, as it cannot be measured directly with a caliper. Moreover, they have irregular shape, which makes most theoretical models inaccurate to predict their size. Many ("old") publications reporting the use of "micron-sized frozen particles" do not explain how it is measured [18,67,103,109]. Recent literature on frozen particles in helium, however, report different techniques used to measure, or at least estimate, the particles size.

The first technique can give a rough estimate of the average particle size [18]. By monitoring the pressure in the reservoir containing the gaseous mixture used to produced the frozen particles, it is possible to compute the volume of matter V_p injected:

$$V_p = \frac{V_{mix}\ \Delta P\ \phi_p\ M_p}{R\ T_{mix}\ \rho_p} \tag{1.37}$$

where V_{mix} and T_{mix} are respectively the volume and temperature of the reservoir containing the injection mixture, ΔP is the difference of pressure in the reservoir before and after the injection, ϕ_p

is the quantity of diluted matter in the mixture ($\sim 1\%$), M_p is the molar mass of the diluted matter, and $R = 8.314 J.kg^{-1}.K^{-1}$ is the universal gas constant. Assuming an homogeneous seeding of N_p spherical particles of radius r_p in the whole bulk of volume V_{bulk}, and knowing the probed volume V_{FoV} and the average number of particles visible n_i, the total volume of injected particles is also:

$$V_p = N_p \times \frac{4}{3}\pi\langle r_p\rangle^3 = n_i \times \frac{V_{bulk}}{V_{FoV}} \times \frac{4}{3}\pi\langle r_p\rangle^3 \tag{1.38}$$

With equations 1.37 and 1.38, the average diameter of the particles can be estimated:

$$\langle d_p\rangle = 2\left(\frac{3V_{mix}\ \Delta P\ \phi_p\ M_p}{4\pi R\ T_{mix}\ \rho_p\ n_i\ \frac{V_{bulk}}{V_{FoV}}}\right)^{1/3} \tag{1.39}$$

This technique requires several strong hypotheses, and gives only an estimate of the mean diameter of the particle produced.

The second technique takes advantage of the density difference between He II and the particles. If a non-neutrally buoyant spherical particle is in a fluid at rest, its diameter can be computed using its settling velocity and the Stokes' law [110]:

$$\overrightarrow{v} = \frac{\frac{\rho_p}{\rho_f} - 1}{18\nu}\overrightarrow{g}\, d_p^2 \qquad \Longrightarrow \qquad d_p = \sqrt{\frac{18\nu||\overrightarrow{v}||}{|1 - \frac{\rho_p}{\rho_f}|g}} \tag{1.40}$$

where ν is the kinematic viscosity of the fluid, v the settling velocity of the particle, $\overrightarrow{g}$ the gravitational acceleration ($g = 9.8 m/s^2$), ρ_p the density of the particles, and ρ_f the density of the fluid. This model applies to spherical particles, and requires the fluid to be at rest, which is not so simple in a cryostat. Indeed, a simple particle injection in He II already stirs the fluid, and even more powerful stirring can be necessary to homogenize the flow (see section 2.3.1). Thus, by the time the fluid is at rest, most of the particles will have already settled. Only the smallest ones will remain in the field of view long enough, resulting in an underestimated result.

The third technique uses the quantity of pixels occupied by the particles on the recorded images. However, the light reflected by micron sized particles is scattered. Thus, it is necessary to apply a correction to the detected size. The light scattered by a particle of a certain size is given by the Mie scattering model [111]. This model can be applied to spherical particles, with various regimes depending on the particle size, compared to the wavelength of the lighting [112, 113]. It can also be applied to non-spherical particles (chap. 8 of [111]), but the equations become even more complex, and it requires to actually know the shape of the particles, which is not the case when working with frozen particles.

For a spherical particle of micron-sized diameter d_p, [114] gives the following approximation for its apparent diameter d_e on a camera sensor:

$$\begin{aligned} & d_e = \sqrt{M^2 d_p^2 + d_a^2} \\ \Longrightarrow \quad & d_e = \sqrt{M^2 d_p^2 + (2.44(M+1)f\#\lambda)^2} \\ \Longrightarrow \quad & d_p = \frac{\sqrt{d_e^2 - (2.44(M+1)f\#\lambda)^2}}{M} \end{aligned} \tag{1.41}$$

where M is the magnification of the camera, λ is the wavelength of the lighting, and $f\#$ is the focal length of the lens divided by the aperture diameter. The diameter d_a corresponds to the size of the first dark ring of an Airy distribution obtained when the light is diffracted by the circular aperture of the camera. In other words, this technique corrects the size of the particles as it appear on the camera sensor, taking into account the diffraction of light by the lens aperture. This last method makes it

possible to measure the size of each single particle in the seeding cloud, and it can be applied even if the fluid is not at rest. However, to be accurate, the image of the particles must be formed perfectly on the focal plane. In other words, it requires a precise optical set up.

Qualification of a particle

We already saw that deuterium and hydrogen particles do not have the same density as liquid helium (I and II). Despite the density difference, particles can produce satisfying data if the flow has enough energy to overcome the different motions induced by the density difference. The Froude number is often used to compare the influence of these quantities:

$$Fr = \frac{v_{fluid}}{v_{density}} \tag{1.42}$$

where v_{fluid} is the velocity of the probed fluid, and $v_{density}$ the terminal velocity of a particle in motion due to its density difference with the fluid. In the vertical direction, this velocity is given by the Stokes' law (eq. 1.40). In this thesis, we study particles in rotating fluid, in which inertial forces must be considered. Thus, in the radial direction, the Stokes' velocity is adapted using the centrifugal acceleration $R\Omega^2$ (Ω being the angular velocity, and R the radial position of the particle), rather than the acceleration of gravity g. Hence, in a rotating flow, it is possible to define a vertical Froude number Fr_z, and a radial one Fr_r. Furthermore, in order to study the turbulent cascade down to the smallest scales, particles should be able to probe velocities as small as $v_{fluid} = \frac{\nu}{\eta}$. As this thesis focuses on the study of He II, the small scale is considered to be the inter-vortex spacing δ, which is why we will consider the smallest fluid velocity to be $v_{fluid} = \frac{\nu}{\delta}$. Finally, we have:

$$Fr_r = \frac{18\nu^2\rho_f}{d_p^2(\rho_p - \rho_f)R\Omega^2\delta} \qquad \& \qquad Fr_z = \frac{18\nu^2\rho_f}{d_p^2(\rho_p - \rho_f)g\delta} \tag{1.43}$$

In the case of ideal tracers, we have $\rho_p = \rho_f$, and $d_p \to 0$. Thus, having a large Froude number ($Fr \gg 1$) is a good indicator of the particles ability to probe the studied flow. However, having $Fr \gg 1$ is not a sufficient condition to have "good particles".

Another quantity used to qualify particles is the Stokes number. It compares the particle response time to the characteristic time of the fluid:

$$St = \frac{\tau_{particle}}{\tau_{fluid}} \tag{1.44}$$

A low Stokes number ($St \ll 1$) describes a particle which "reacts" faster than the fluid, and will be able to follow the smallest fluctuations (fig. 1.8). The lowest fluid characteristic time is given by Kolmogorov's theory (eq. 1.9). In the case of He II, we have $\tau_{fluid} = \tau_\delta = \frac{\delta^2}{\nu}$. On the other hand, by solving the equation of motion of a settling particle submitted to its weight, buoyancy and drag force, the particle characteristic time appears: $\tau_{particle} = \frac{d^2\rho_p}{18\mu}$. Thus, the Stokes number can be expressed as:

$$St = \frac{d^2\rho_p}{18\delta^2\rho_f} \tag{1.45}$$

It is important to note that these two dimensionless numbers depend on the type of probed flow, as δ is involved. Thus, it will only characterize the ability of particles to probe a certain range of flows.

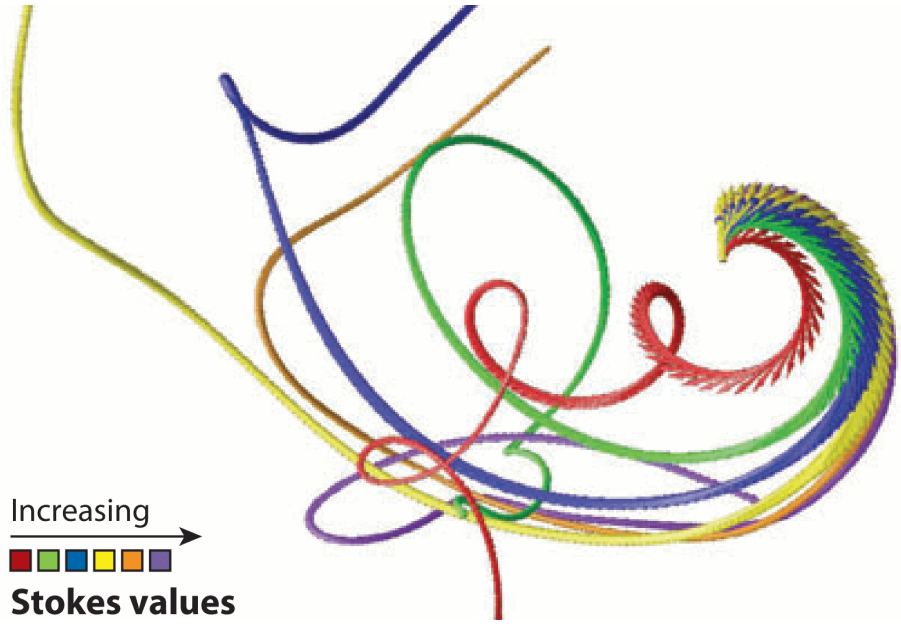

Figure 1.8: Image from [115]: Trajectories of heavy particles with different inertia. When released from within a small-scale vortex filament (matching the velocity of the underlying fluid), particles with different inertia respond to vorticity differently. Particles with large Stokes numbers are almost insensitive to the presence of the vortex. The red line represents a fluid tracer, whereas the green, blue, brown, and yellow lines correspond to increasing Stokes values, respectively.

1.4.2 Visualization in helium II

With the development of computers and CCD sensors in cameras, measurements methods using flow visualization has become more and more used. However, if tuning up any velocimetry method using particles (LDV: Laser Doppler Velocimetry, PIV: Particle Image Velocimetry or PTV: Particle Tracking Velocimetry) can require several weeks of work in classical fluids such as water, it becomes a challenge of several months (years?) in a cryogenic environment, although experiments using particles in He II can be found in the literature of the late 1950s [77, 103].

Actually, optical cryostats made of glass have been widely used in history. The first liquefaction of helium has even been done in a glass cryostat [17], so that the first drops of liquid could be seen with naked eye. Nevertheless, glass cryostats have several drawbacks. First, it is transparent to infrared radiation, so it does not completely cut heat transfers. Secondly, helium molecules are very thin, and their diffusion through solid matter can be higher than other gases (e.g. air). Therefore, peculiar attention is given to heat treatment and/or coating of the cryostats walls, in order to preserve a high insulating vacuum [116, 117]. Third, the geometry of a metallic cryogenic facility can also be better qualified due to machining technologies. Indeed, glass cryostats were often axisymmetric, with light deflections, which is not ideal for quantitative measurements of fluid motion. This is why the most recent installations are preferably made of metal rather than glass. For visualization, "small" flat optical accesses can be provided (e.g. fig. 1.2). This constitutes a good compromise between thermal insulation, and image quality.

As helium, in all its states, have a refractive index which is close to the one of vacuum, it is sometimes hard to tell if there is actually liquid in the apparatus. Thus, particles are necessary to

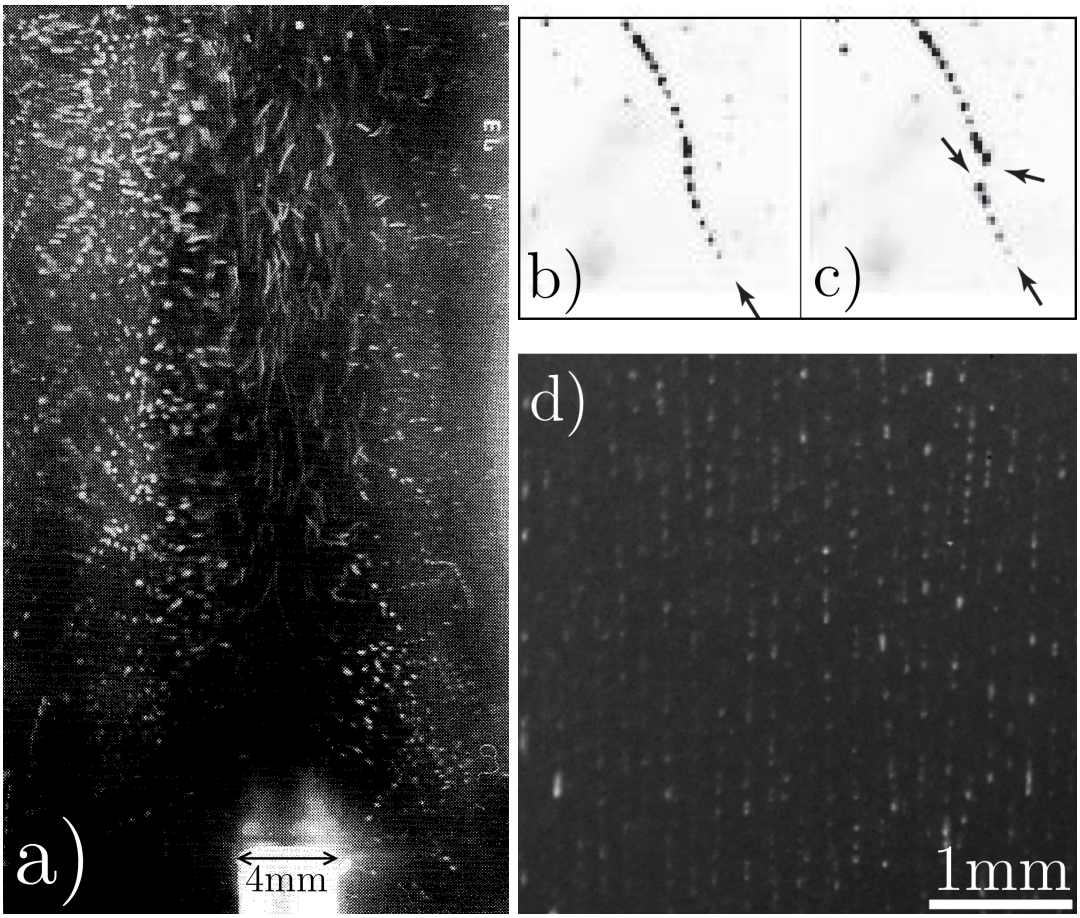

Figure 1.9: a) Image from [120]. $H_2 - D_2$ particles in a counterflow jet. b) & c) Images from [121]. H_2 particles trapped on reconnecting vortices taken at $50ms$ interval. d) Image from [18]. H_2 particles in rotating He II, illuminating the vortex lattice.

observe the fluid motion. Many kind of particles have been tested in different facilities. Historically, Chopra and Brown [103] performed the first experiments of visualization in helium II, using frozen particles made of hydrogen and deuterium (H_2 and D_2 particles). As H_2 is less dense than He II ($\rho_{H_2} = 88kg/m^3 < \rho_{HeII} \simeq 145kg/m^3$), and D_2 is denser ($\rho_{D_2} = 206kg/m^3$), the idea was to mix them in order to produce neutrally buoyant particles. They mixed both gases in a small volume at room temperature with appropriated partial pressures, and injected it in cold gaseous helium contained in their cryostat, through a heated pipe. As H_2 and D_2 have close melting points ($T_{H_2}^{l\leftrightarrow s} \simeq 14K$, $T_{D_2}^{l\leftrightarrow s} \simeq 19K$ under $1\,atm$), they can possibly aggregate together. They obtained a cloud of "particles as small as 1000 microns or less". They already observed the tendency for particles to aggregate quickly in He II, and not in He I. Particles of $1mm$ in diameter are in fact too large when it comes to probe flows in which the small length scale δ is of the order of $100\mu m$. Kitchens reports, 8 years later, the use of the same technique with which he produced "particles of $20 - 100\mu m$ in diameter" [77]. However, the method used to estimate the particles' size is not mentioned in these papers.

This method for producing frozen particles in helium II has been used by different groups working on superfluid motion [67, 77, 109]. In the late 1980s and early 1990s, several groups started to use hollow glass spheres [67, 118], which have the advantage, when sieved, of having a better-controlled size and shape, and a nominal density close to that of liquid helium [119]. However, the main drawback is that they cannot be removed from the apparatus without opening, whereas frozen particles can be evaporated just by raising the temperature above their boiling points ($\sim 25K$, see table 2.1).

In 2006, G. P. Bewley presented in his PhD thesis [18] in which he used frozen hydrogen particles and managed to observe quantum vortices. The production of these $50\mu m$ particles is a little bit different from Chopra's protocol. Bewley first dilutes H_2 in helium with a 1:10 ratio, then this mixture is injected directly in the liquid phase of He I, before cooling it down below T_λ. Once in He II, the thin cloud of hydrogen aggregates (as observed by Chopra [103]) forming small particles which can become trapped on quantum vortices cores. This has been evidenced by videos of vortex reconnections (fig. 1.9, b and c) [121], and images of the vortex lattice when the cryostat was rotating (fig. 1.9, d) [122]. This technique is now used by several groups in the small community of experimental cryogenic hydrodynamics research. It has also been adapted using other elements such as deuterium [54, 123], or air [124], and improved for direct injection in He II with smaller size [113]. Some developments are still in progress, including the use of *HD* (and not the old $H_2 - D_2$ mix) particles, which are expected to have a density very close to that of He II [108].

These particles have been used for different type of studies like rotation [18], grid turbulence [125], or reconnections quantum vortices [126]. Most of experiments used counterflow as a forcing and reported particles behavior that differs from classical turbulence. Several works report a large fraction of particles moving away from the heating source, following straight trajectories with a velocity v_p which is close to the normal fluid one v_n. A smaller fraction of particles displays erratic trajectories, which could even move against the normal fluid flow, because of the interaction between particles and quantum vortices [56, 127, 128]. Statistical studies of these flows result in a double-peaked streamwise velocity probability density function (PDF) ([127, 129, 130], and appendix D).

The velocity PDFs (in any direction) also display power-law tails when the spatial resolution of the acquisition is less than the mean inter-vortex spacing δ [54]. However, if the probed length scale is larger than δ, the PDF becomes gaussian, as it would be in a classical turbulent flow. It can be shown, by dimensional analysis, that reconnections of quantum vortices lead to velocity probabilities scaling as v^{-3} [39, 40]. Thus, the power-law tails at large velocity fluctuations are the signature of the interaction of particles with quantum vortices. These works give credibility to a still controverted technique.

Indeed, the illumination of the vortex lattice (fig. 1.9, d) observed by Bewley has not been repeated by any other group. Moreover, the reconnections and disconnections of the vortices (fig. 1.9, b and c) are rare events that have been observed only a few dozen times in the last fifteen years [124]. The controversy also comes from the following question: "How can an angstrom sized vortex trap a particle which is at least 10^4 times larger?". The explanation of a pressure gradient [131] may not satisfy the most reluctant ones, even when supported by several numerical simulations [132–134]. However, the fact that quantum vortices leave a footprint on particle motion statistics leaves no room for debate. Thus, these statistical approaches on particle motion are what constitute the most promising way to study quantum turbulence.

Chapter 2

Experimental apparatus

The first part of these three years (2017-2019) of work was to develop a new and unique cryostat: the Cryogenic Lagrangian Exploration Module (CryoLEM). The CryoLEM is a cryostat whose purpose is to observe quantum vortices using particle tracking velocimetry (PTV) in rotating helium II. It has been highly motivated by previous works detailed in section 1.4.2, especially Packard's group experiments in 1979 [70], leading to the first images of quantum vortices in rotating Helium II, and Bewley's PhD thesis [18], in which he developed a new technique to visualize them using frozen H_2 particles, opening the door to PIV (particle image velocimetry) and PTV studies of He II.

2.1 Cryogenic aspects

2.1.1 A cryostat for the visualization of rotating helium

A cryostat follows the same principle as the vacuum flasks (or Dewar flasks, in tribute to its inventor Sir James Dewar). In domestic application, they can insulate hot coffee from the colder atmosphere using vacuum in a double wall, preventing diffusive and convective heat transfers. Cryostats use the same principle, but usually feature several concentric layers with increasing (from inside to outside) regulated temperatures. As radiating transfers scale as T^4 according to Stefan-Boltzmann law, regulated low-temperature shields allow to further reduce the heating power received by the cryostat core. For example, the use of liquid nitrogen to cool a shield down to $77K$ helps reducing the radiating transfers from a room at $293K$ by a factor $\frac{293^4}{77^4} \sim 200$. These precautions are necessary, considering the low latent heat of vaporization of helium (table 2.1). It is important to note that $1L$ of liquid helium at $4.2K$ evaporates into $700L$ of gaseous helium at standard conditions of temperature and pressure. In other words, a thermal shortcut in the insulating parts of the cryostat could lead to a sudden pressure increase, and an explosion. This is why particular attention must be paid to the safety of operators, hence the extensive use of safety valves.

Originally, the CryoLEM is an orange cryostat (fig. 2.1), developed by the ILL (Grenoble) [135] and commercialized by AS Scientific Products. It follows the principle of dewar flasks, and uses liquid nitrogen as a coolant for the intermediate shield. The vacuum jacket also contains super insulator materials, increasing the insulating properties, but which can also trap some air, which is why several days of pumping are needed to reach a satisfying vacuum pressure ($\sim 10^{-7} mbar$). This cryostat also features an additional helium reservoir.

The mechanical modification of the Orange Cryostat into the CryoLEM (Fig. 2.4) lies in the addition of a modular experimental cell at the bottom, and a spinning gasket at the top, on the pumping line (see section 2.1.2). The experimental cell (fig. 2.2, a.) is encapsulated in two larger shields (fig. 2.2, b. and c.), all separated by vacuum. The intermediate one is in direct contact with

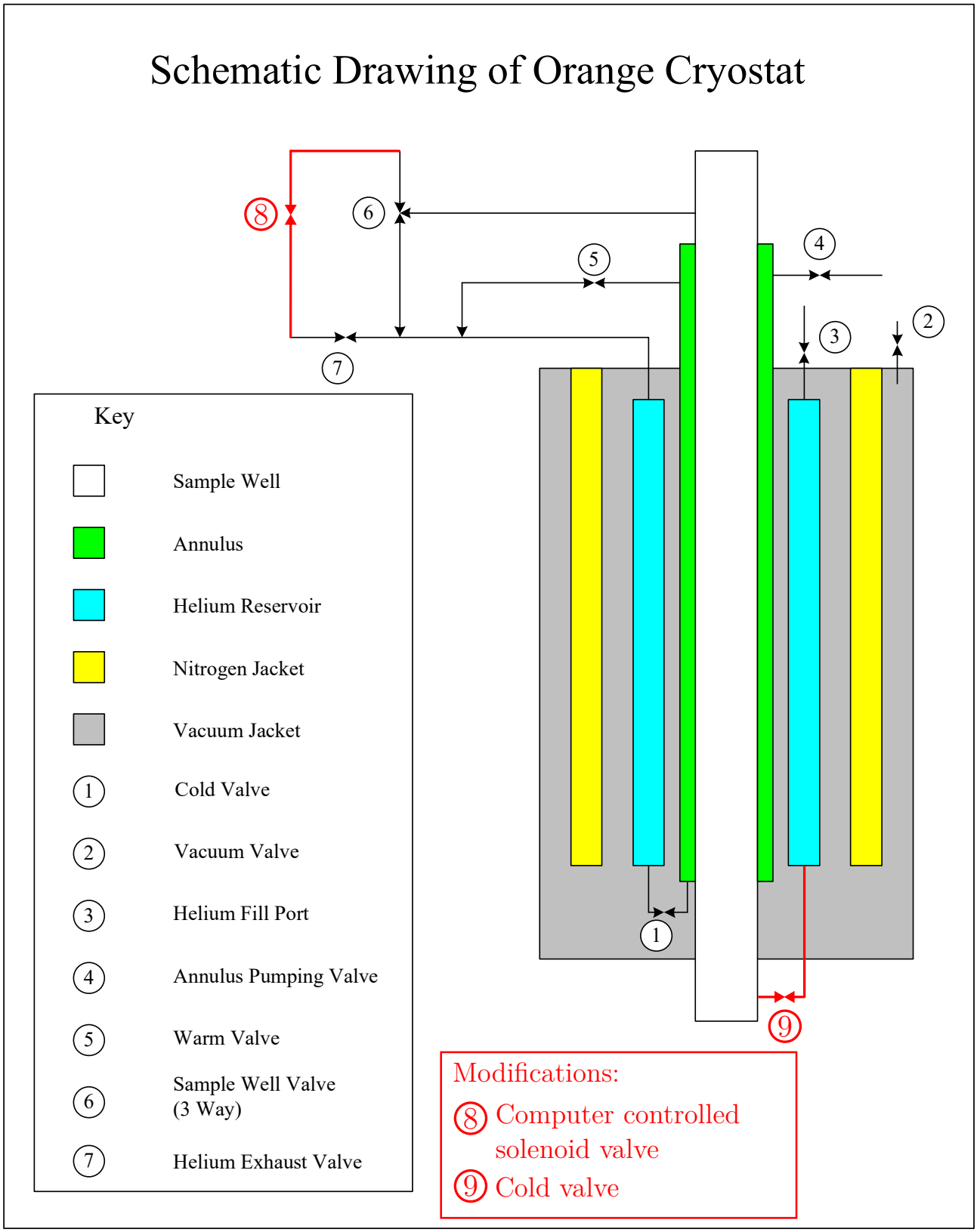

Figure 2.1: Schematic view of the orange cryostat (source: nist.gov). It has been modified by adding a cold valve (9), allowing to fill the core of the cryostat with liquid helium, and a solenoid valve (8) allowing to release the evaporated helium gas in the reservoir to the top of the pumping line.

Material	Boiling point at 1bar (K)	Latent heat of vaporization (kJ/kg)
Water (H_2O)	373.15	2265
Nitrogen (N_2)	77	200
Helium (He)	4.22	20.7
Hydrogen (H_2)	20	455
Deuterium (D_2)	23.3	322

Table 2.1: Latent heats and boiling points of chemical elements used in the CryoLEM. Water is given as a comparison. Despite its low boiling temperature, hydrogen has a latent heat which is twice larger than Nitrogen: all cryogenic fluids do not have such a low latent heat.

the original nitrogen jacket, hence thermalized to $T \gtrsim 77K$ and cutting down radiating transfers. Two other valves have also been added (in red on fig. 2.1). One of them (9) is used to fill the cell with liquid helium from the reservoir. The other is a solenoid valve controlled by the main computer in order to release the evaporated helium from the reservoir to the top of the pumping line (more details below).

As the aim of this experiment is to study the fluid through PTV, 8 optical accesses have been placed on each shield. The configuration of the windows makes it possible to study the fluid through any angle (in 2D and 3D). For example, in 2D, the particles in the fluid can be enlightened by a laser sheet which can be orthogonal to the rotational axis (horizontal), or containing it (vertical). In these cases, the optical axis of the camera must be orthogonal to the laser sheet, i.e. facing the bottom window of the cell, or a window on its side respectively. In the configuration of the figure 2.2, the bottom window has been replaced by an access for our sensors wires. This access could be exchanged with any other window if the bottom one had to be used. Moreover, this window configuration makes it possible to always have a window to let the laser beam exit the cell. This criterion is fundamental in order to avoid heating the cryogenic fluid in the cell with the powerful laser light.

The inner windows have a $25mm$ diameter, and are made of sapphire. This material has a good thermal conductivity, ensuring a uniform temperature of the window. This combined to its high transparency in the visible domain, avoid the creation of counterflow sources which could be provoked by an absorption of the laser light for example. In order to cut all the radiating transfers, the windows of the intermediate shield are made of KG3. This is a technical glass, transparent at visible wavelength, but with a transmittance of less than 1% in the infrared domain [136]. This last criterion is fundamental as the aim of this shield is to cut heat exchanges through infrared radiation. The outer windows are made of borosilicate glass, which is standard in vacuum applications. These have been covered by an anti-reflective coating to ensure the quality of the optical path.

The geometry of the experimental cell can be divided in two parts: an upper cylinder ($\varnothing 198mm$ inner diameter, $92mm$ high), and a lower elongated square cupola (Fig. 2.2), allowing flat optical accesses. The inner side of the lower part is axisymmetrical (fig. 2.3, $\varnothing 108mm$), in order to avoid any stirring due to a polygonal shape [137]. However, there are still some small recesses on the sides of the optical accesses, which cannot be avoided as they are flat. The inner volume of the experimental cell is $3.9L$.

The original $9L$ helium reservoir has been kept intact. The bottom of the reservoir is connected to the experimental cell with a capillary equipped with a "cold valve" (fig. 2.4), which can be operated manually from the top of the cryostat. Having two separated reservoirs for helium is definitely a plus. It reduces the volume of the experimental cell, making possible to evaporate helium and particles during a night, and start experiments with a clean cryostat the next day, by a simple helium transfer from the second volume (see section 2.1.3). Moreover, during experiments of several hours, a significant amount of helium can evaporate. It is convenient to be able to refill the cell quickly, with a single operator,

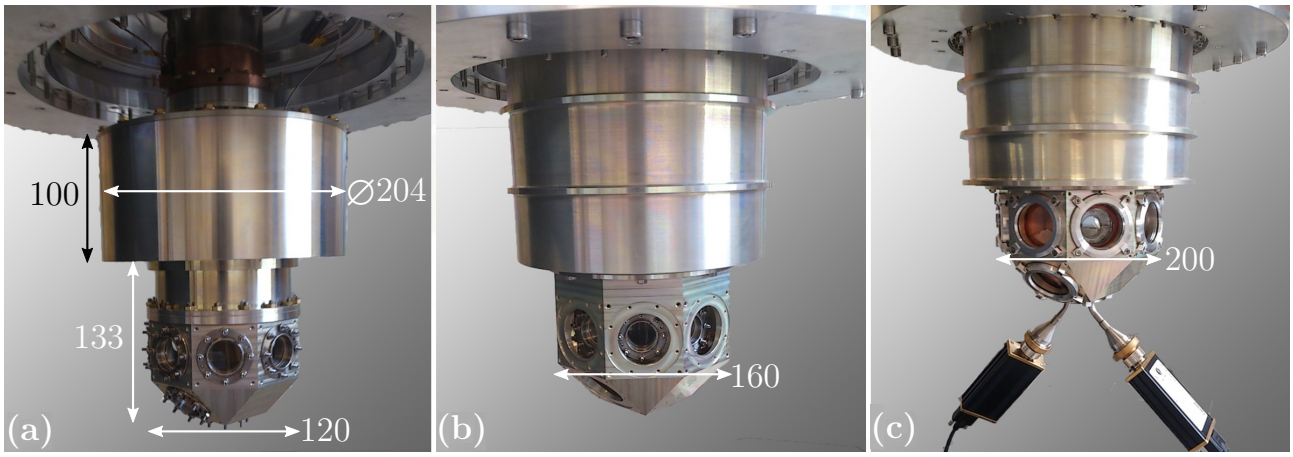

Figure 2.2: Photographs of the encapsulated shields of the cryostat. The dimensions are given in mm. **(a)** Inner part ($2K$), in contact with the superfluid. **(b)** Intermediate shield ($95K$), in contact with a liquid nitrogen bath. **(c)** Outer part ($300K$), in contact with room atmosphere.

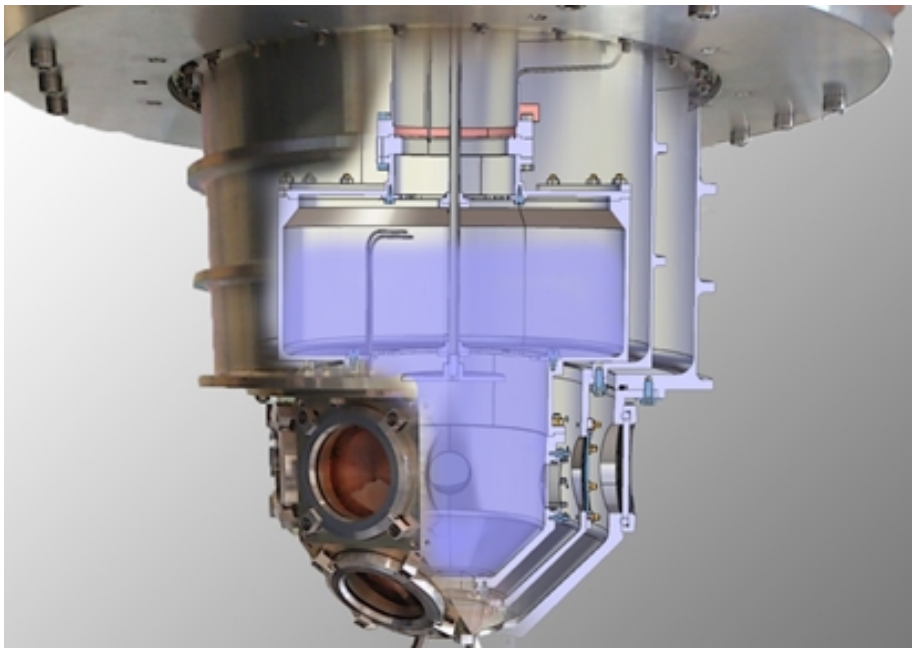

Figure 2.3: Cut view of the cryostat experimental cell. Once the three stages assembled, and cooled down to their operating temperatures, the windows' centers are aligned, allowing visualization of the inside. The inner windows have a $25mm$ diameter.

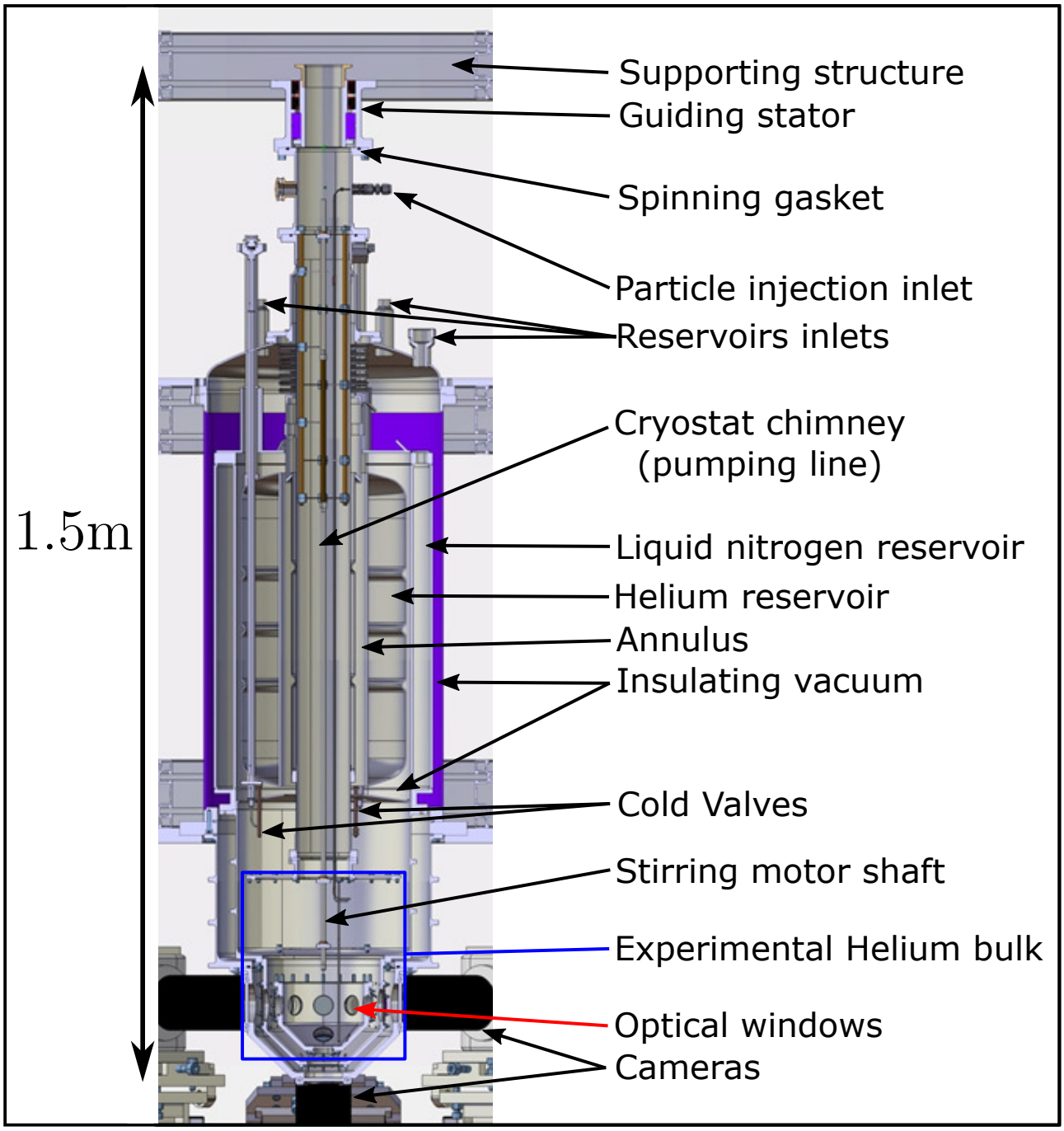

Figure 2.4: Overall labelled drawing of the cryostat

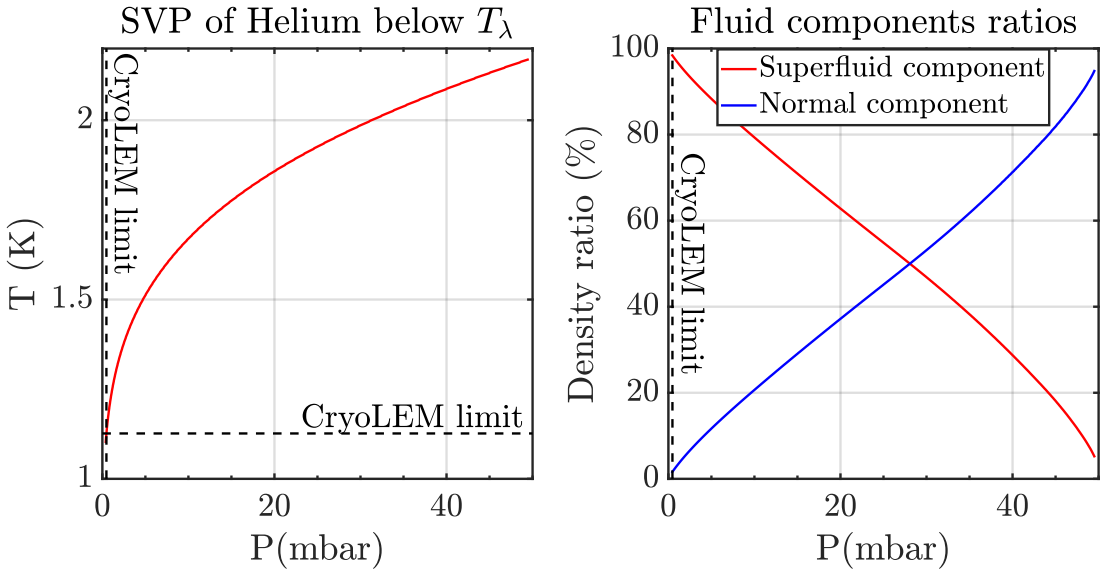

Figure 2.5: Temperature and fluid ratios of liquid helium II at SVP.

simply by opening the cold valve.

2.1.2 Pumping line

Helium is liquefied in Institut Néel in $100L$ (or more) bottles at the disposal of researchers. In these bottles, helium is stored at saturated vapor pressure (SVP), slightly above the atmospheric pressure, at $4.2K$. In order to reach the superfluid state after being transferred to the cryostat, the bath pressure is decreased along the SVP curve (fig. 2.5), allowing to reach temperatures below $T_\lambda = 2.17K$.

To decrease the temperature, a rotary vane pump SOGEVAC SV300B is connected to the cryostat through an $\sim 9m$ long pumping line. The pump has a nominal pumping rate of $280m^3/h$. The line includes pipes of various impedances which can be selected thanks to a network of manual valves (Fig. 2.6). This network of pipes whose inner diameter is between $25mm$ and $160mm$, is used in different configurations depending on the desired working temperature of the helium bath. Using the largest pipes, the minimum pressure reached in the cryostat in experimental conditions is $P_{lim} = 0.47mbar$, which is equivalent to $T_{lim} = 1.13K$, and He II composed of 98.4% of superfluid.

As the fluid is operated at SVP, pressure stability is required in order to avoid the drift of many physical properties (Fig. 2.5, and section 1.2). Thus, a regulating butterfly valve VAT 61232-KAGZ-0001 has been installed on the pumping line (Fig. 2.6). Two pressure sensors supply data to the PID-controller of the valve. One of the sensors has a range of $[0; 1000]mbar$ (Keller 33X) and the other reads pressures between 0 and $100mbar$ (Keller 41X), for a better precision in the pressure range of superfluid helium ($[0; 50]mbar$). Based on this data, the regulating valve stabilizes the pressure with fluctuations below $\pm 0.1mbar$.

However, this valve is made to operate with flow rates between 0.25 and $80L/s$, which is too high for our experiment, as thermal losses are very low ($0.1W$, see section 2.1.4). Actually, the use of a heater is necessary to increase the gaseous helium flow rate, otherwise the valve is unable to regulate the pressure properly. During most of experiments performed between February 2018 and 2019, a $0.2W$ heating power is generated by the heater located at the bottom of the experimental cell, in order to allow pressure regulation. Such low heating power is not enough to produce any fluid motion as there is no flux concentrating channel in the cryostat. Thus, it propagates in all directions, resulting in

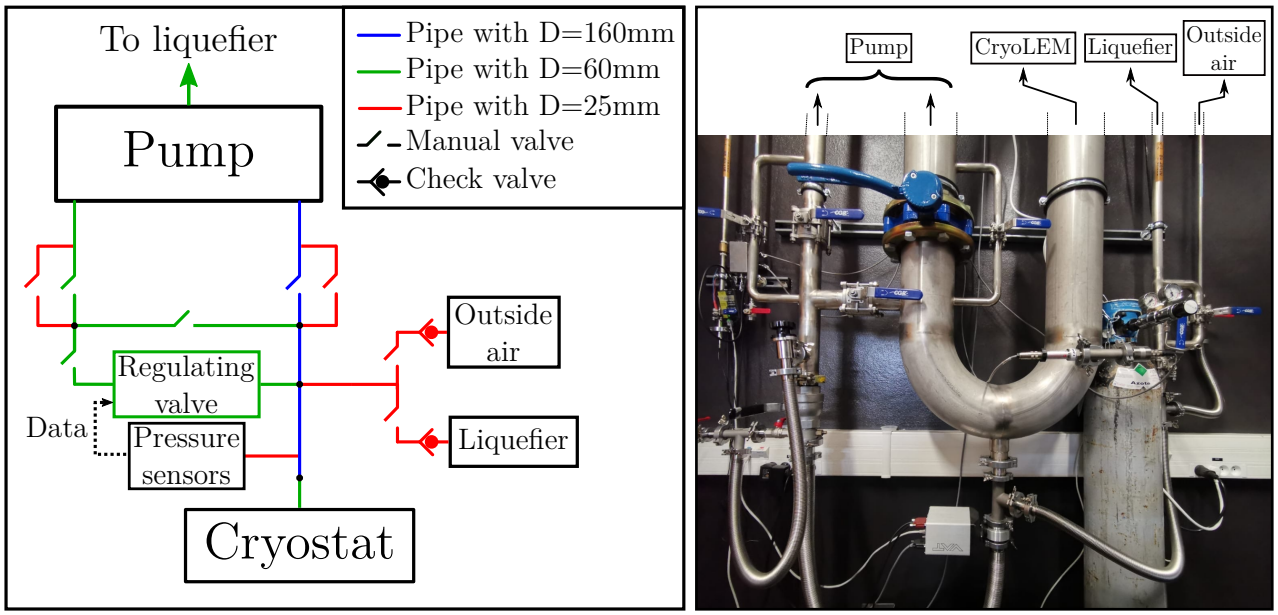

Figure 2.6: Drawing of the pumping network (left, not to scale), and photograph of the actual system in the laboratory (right). The manual valves allow different configuration, and more especially, different impedances. The pump sends gaseous helium back to the liquefier of the institute for recycling. When the cryostat is at rest with condensed helium inside, it is connected to the liquefier through a check valve. However, if the cryostat contains hydrogen or deuterium (from evaporated particles, hence in a very small amount), it has to evaporate to the outside air as they could damage turbines in the liquefying process. A regulating valve controlled by pressure sensors has been implemented to ensure pressure stability in the experimental cell.

a flux density of $q_{heat} = 2mW/cm^2$. In the working range of the cryostat, this corresponds to a value of v_{ns} between $0.17mm/s$ (around $T = 2K$) and $4mm/s$ (at $T = T_{lim} = 1.13K$). As explained in section 1.2.2, this value is below the critical velocity necessary to trigger turbulence in a counterflow of helium II. Thus, this heating allows pressure regulation, without affecting fluid motions in the probed area.

The importance of pumping condensed helium is the major obstacle to building a spinning cryostat. If rotating gaskets have already been implemented in the industry, many technologies are not compatible with cryogenic fluids, and especially helium which is the most easily leaking fluid. Historically, many rotating cryostats were used in the study of superfluidity, but they were using spinning gaskets using mercury, a toxic heavy metal which use has been progressively banned from many countries between 1990 and 2010. The CryoLEM features a new spinning gasket technology which we developed in collaboration with the cryogenic team of the Institut Néel (G. Garde). The possibility of a patent is under study, which is why it will not be detailed here.

2.1.3 Cooling down the CryoLEM

At this stage, the CryoLEM is a newly built apparatus. Before running experiments, it was necessary to establish a routine, and protocols in order to operate the system. In this subsection, we detail the experimental protocol used to set the CryoLEM in its nominal state for cryogenic experiments.

A few days before each session of experiments, the insulated vacuum is pumped for a whole weekend down to $[4:9]\times10^{-7}mbar$, which is close to the limit of our turbomolecular pump ($\sim 10^{-7}mbar$). Once the vacuum is closed and the pump removed, liquid nitrogen is injected in the dedicated reservoir. The

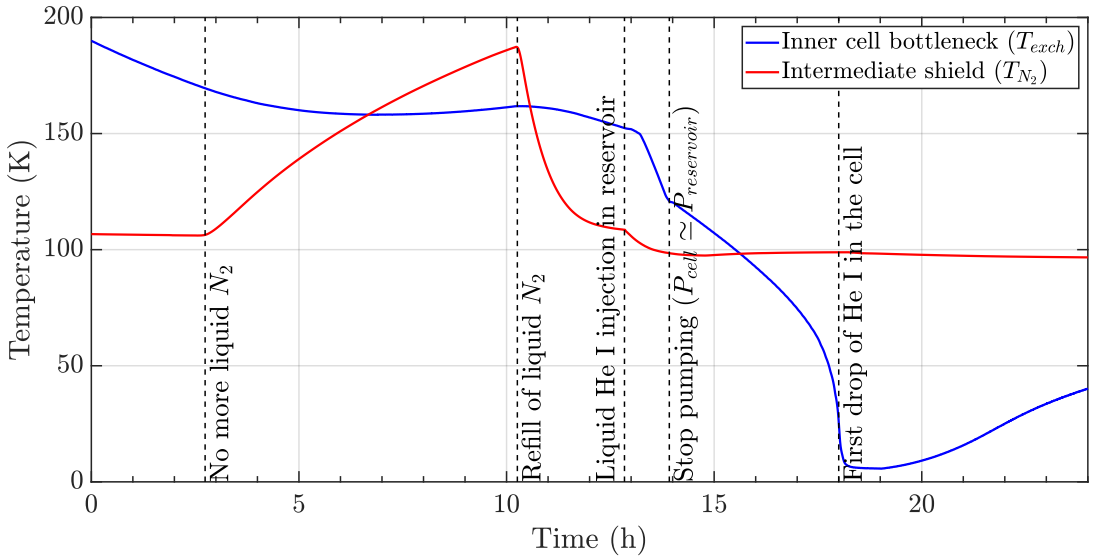

Figure 2.7: Temperature of the bottleneck between the cryostat chimney and the cell (T_{exch}), and of the nitrogen shield (T_{N_2}) on December 11^{th} 2018. The nitrogen reservoir has been filled the day before at 7PM, and is completely evaporated at 3AM. In the morning, the temperature inside the cryostat has decreased to $\sim 160K$ because of radiation. Around 1PM, the helium reservoir filling has started, making T_{N_2} decrease below $100K$.

cooling down of the intermediate screen can take up to three hours. Thanks to various PT100 sensors (see section 2.3.3) placed on its external surface, we measure a steady temperature of $T_{N_2} \sim 105K$ (fig. 2.7) which is larger than the temperature of vaporization of nitrogen ($T_{N_2}^{g \leftrightarrow l} = 77K$). This difference of temperature is due to the equilibrium between the cooling by conduction from the reservoir (at the upper end), the radiation from the room (on the whole surface), and the radiation from the inside which is hotter at this stage.

By injecting liquid nitrogen after the vacuum closure, we increase the insulating capacity of the vacuum. Once closed, the cooling down condenses several components of air, such as water and oxygen which could remain in the vacuum, hence a pressure decrease (cryopumping). Usually, the CryoLEM is left in this state for a whole day so that the inner part slowly cools down by radiant transfer from the intermediate shield. Temperatures such as $T_{exch} \simeq 150K$ can be reached inside the cryostat the next morning (Fig. 2.7). This temperature is measured on a copper heat exchanger placed on the outside (i.e. in the vacuum) of the bottleneck between the pumping line and the inner cell (see section 2.3.3 and fig. 2.24).

At this temperature, the helium transfer from the $100L$ bottle to the $9L$ reservoir can start. As this reservoir is also insulated with super insulator materials, without any optical access, it can be filled in less than 30 minutes. However, it can take more than an hour to fill the experimental cell, due to a larger amount of metal parts to cool. Moreover, both containers are connected only by a thin capillary which results in a slow transfer. Indeed, two valves connect the cell and the reservoir: a cold valve has been added to the original orange cryostat, to connect them by the bottom (in the liquid), and the 3 way valve (#6 on fig. 2.1) connects them by the top (in the gas). Thus, during transfers, the cold valve is open, and it is possible to tune the transfer speed by changing the pressure difference at both ends of the capillary. For a slow transfer (e.g. $4h$ on fig. 2.7), both volumes can be connected by the top, and the flow from a volume to another is forced by gravity only. For a quicker one (e.g. $< 1h$ on fig. 2.8), the 3 way valve is closed: the pressure in the reservoir increases due to evaporation of liquid helium. Moreover, it is possible to pump down the cell, and reach a pressure difference of $\Delta P = P_{reservoir} - P_{cell} \simeq 1bar$. On fig. 2.7, there is a clear change of slope in the cooling when the

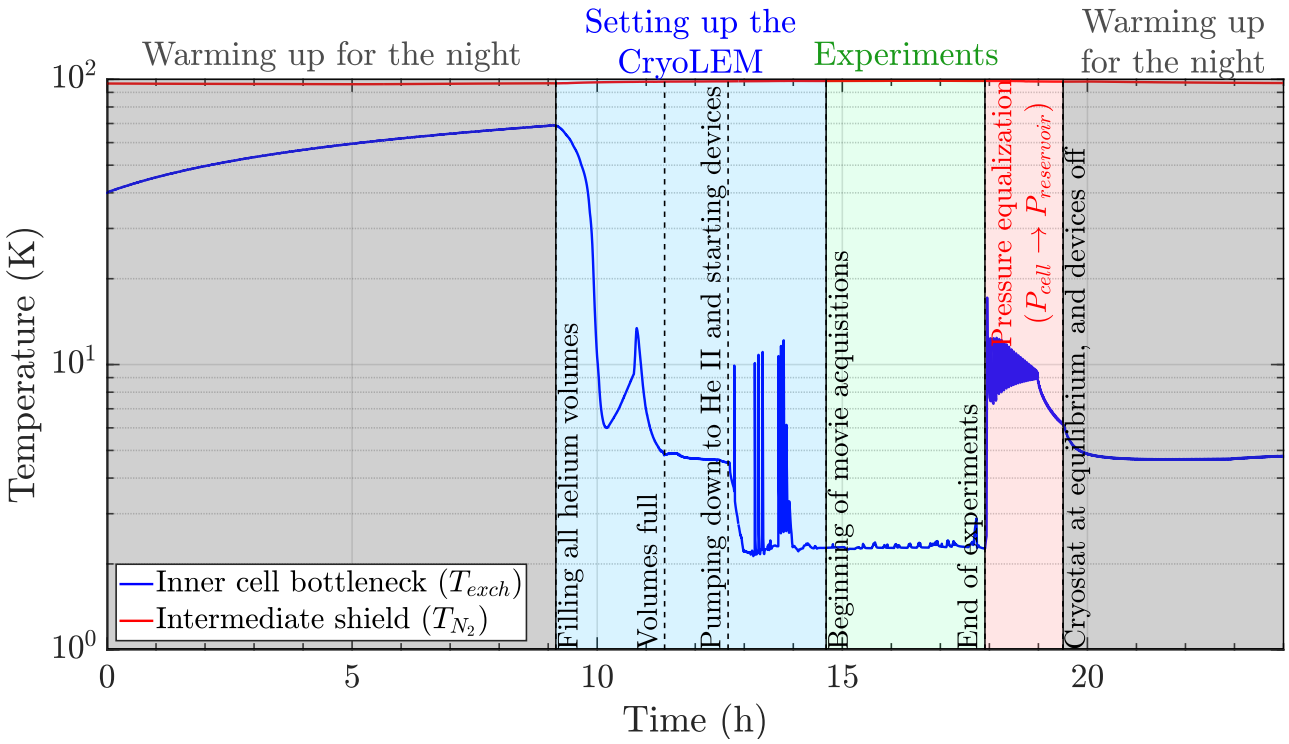

Figure 2.8: Temperature of the bottleneck between the cryostat chimney and the cell (T_{exch}), and of the nitrogen shield (T_{N_2}) on December 12^{th} 2018. This is the typical temperatures we have during experiments. When movies are acquired, we measure a stable value of $T_{exch} \simeq 2.3K$. The little fluctuations observed are due to particle injections ($300K$ gas) between the movies. Such a stable temperature is obtained thanks to pressure regulation, and the fact that the reservoir evaporates through a safety valve (see section 2.1.2). We can also note the stability of T_{N_2}, meaning that the capacity of the nitrogen tank is sufficient to keep the cryostat "cold" out of business hours.

pump is stopped (around 2PM).

Once the cell is cold ($T_{He} < 4.2K$) and filled, the actuators and acquisition systems can be started, and the particles injected for a whole day of experiments (fig. 2.8). Usually, at the end of the day, the bath is close to being empty, and the reservoir is still full (see section 2.1.4). Then, the cryostat is left evaporating to the outside air for the night. A line is dedicated to this purpose (fig. 2.6), because the injected particles must not be sent back to the liquefier, which they could damage. Thus, the low amount of liquid helium remaining in the cell at the end of the day is not recycled.

The next morning, the cryostat has warmed up to $[50; 70]K$ (fig. 2.8), which means all the helium from the bath and the particles have evaporated outside, and the outlet pipe of the cryostat can be switched back to the liquefier. The reservoir is used to refill the bath that is now cleaned from all particles, and the reservoir is refilled from a bottle of helium. This operation takes around an hour and can be repeated several days in a row for long sessions of experiments.

2.1.4 Cryostat autonomy

Even if the cryostat is well insulated, some heat flux from the outside remains, making the fluid evaporate slowly. How long can the CryoLEM be operated without external refills? According to several experimental sessions, it is now known that, when the nitrogen reservoir is full, with an intermediate shield at a constant temperature of $\sim 100K$ and the cryostat core has a temperature above $150K$, it takes around 9 hours to evaporate all the nitrogen (Fig. 2.7). In practice, we refill it every morning and every evening during experimental sessions, which is enough to keep its temperature constant below

$100K$, if the cell is cold (Fig. 2.8).

If previous experiments showed that the helium bath can be used for a whole afternoon, the surface of helium has been observed for several minutes in December 2018 to determine precisely the lifespan of a superfluid helium bath in the CryoLEM. During this experiment, the superfluid was at $2.088K$ ($40mbar$), the cryostat was spinning at $15RPM$, the laser power was set to $0.5W$ to enlighten the deuterium particles and the heater was set to $Q_{cell} = 0.2W$ in order to help regulating the pressure (mentioned in section 2.1.2). The surface of fluid was already in the middle of the image recorded by our camera when we started recording. After less than 7 minutes of movie, the surface of fluid was already below the field of view. In order to numerically follow the surface of fluid, two approaches have been tested :

- As the the laser sheet appeared brighter at the gas-superfluid interface, the intensity of each pixel row was summed. The position of the maximum was considered to be the position of the surface. This high luminosity can be due to D_2 particles trapped by surface tension, or to the low incidence angle of the laser sheet, leading to reflections.
- The particle tracking velocimetry algorithm (see chapter 3) has been applied to this movie. For each image, the maximum vertical position of the detected particles was considered to be the position of the surface.

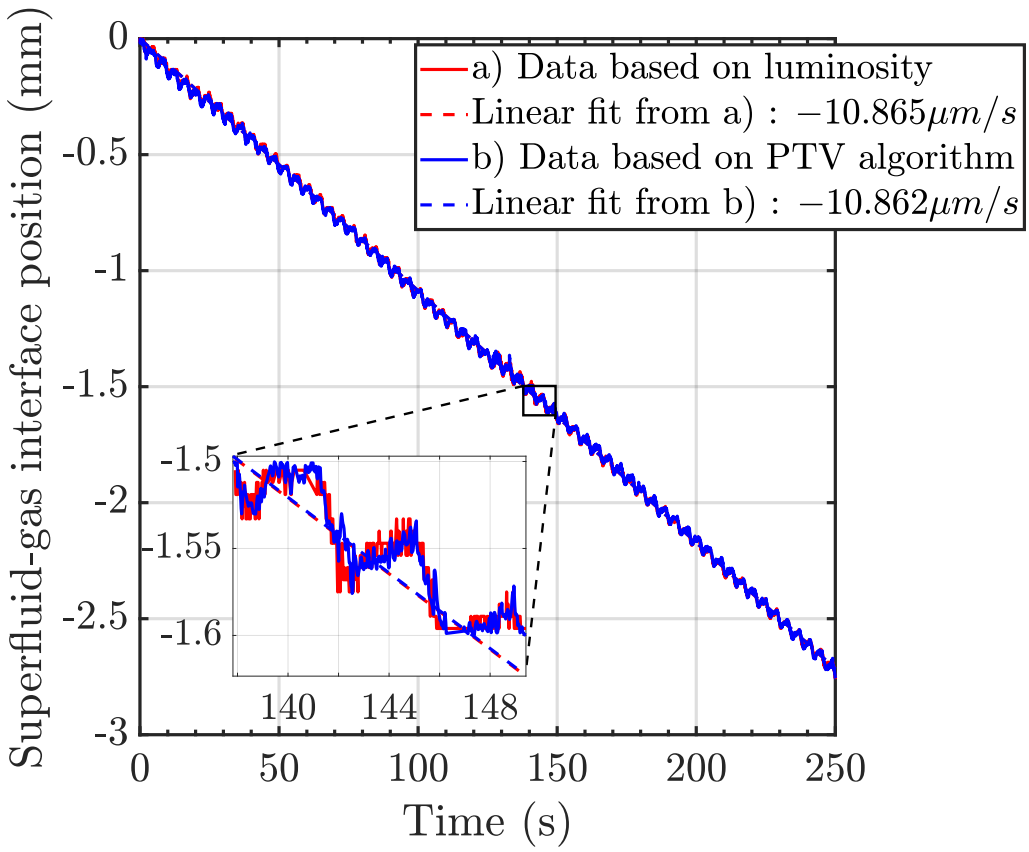

Figure 2.9: Position of the superfluid-gas interface in the CryoLEM during a movie recorded in December 2018, in usual experimental conditions. Two different methods are used to detect the interface: one uses the PTV algorithm, and the other uses the brightness of the interface (luminosity). Both give an interface velocity of $-10.9\mu m/s$. The oscillations are in phase with the cryostat rotation ($\Omega = 15RPM$). They will be further discussed in sections 2.2.1 and 4.2.1.

The results of both methods are given on figure 2.9, and they are identical. We measure a constant surface velocity equal to $-10.9\mu m/s$, or $-39.1mm/h$. Let $\mathcal{V}_{HeII}$ be the volume of the He II bulk. Considering the diameter of $108mm$ in the bottom part of the cell, this results in an evaporating flow rate equal to $\frac{d\mathcal{V}_{HeII}}{dt} = 0.36L/h = 1.0 \times 10^{-7}m^3/s$. Knowing the latent heat of liquid helium ($\Delta H_{He}^{l\to g} = 20.7kJ/kg$) and its density ($\rho_{He}(2.088K) = 145.8kg/m^3$), the heat loss of the cryostat can be estimated:

$$Q_{loss} = \Delta H_{He}^{l\to g} \times \rho_{He} \times \frac{d\mathcal{V}_{HeII}}{dt} - Q_{cell} = 0.10W \tag{2.1}$$

This value is actually a low value for such a cryostat of $1.5m$ high, but it was expected as all possible care has been given to reach it. Thus, if the $3.9L$ of the cell are completely filled, it would take $10h53$ to empty it in these experimental conditions. This autonomy is very satisfying, as it is long enough for a complete day of work, considering that it takes at least $1h30$ to fill all the volumes and start the devices in the morning. However, this is an overestimated value as we obviously cannot study He II dynamics when the fluid level is in the middle of the windows.

Actually, we would like to study He II far from its boundaries, while keeping a height of fluid as constant as possible (e.g. to compute the Ekman time (eq. 1.31)). Thus, the experiments should be done when the superfluid-gas interface is in the upper cylinder of the cell. This part has a volume of $2.84L$ ($\varnothing 198mm$, $92mm$ high), which means that its autonomy in experimental conditions is about $7h55$. While the interface is in it, its level decreases by $11.6mm/h$. Thus, during a $10min$ long movie (typical case), the He II height is reduced by $1.93mm$, which corresponds to a change of 1.6% in the worst case (liquid level at its lowest).

The autonomy of the helium reservoir has not been measured precisely as it is harder to have data about it. The superconducting gauge in it is the only source of information, but it is not calibrated and does not have a precise resolution. Moreover, its autonomy is way larger than the bath's which is enough to keep the CryoLEM cold during an entire night.

2.2 Actuators

2.2.1 Spinning table

If various optical cryostats already exist, the CryoLEM uniqueness resides in the fact that it makes possible the visualization of turbulence in He II rotating up to $120RPM$, in stable thermodynamic conditions. To our knowledge, the only experiment focused on quantum vortices in rotating ^{4}He II during the 21^{st} century is the one performed by G. P. Bewley during his PhD [122]. However, the apparatus could spin only if pumping was stopped, even though helium was evaporating, resulting in a pressure (and consequently, temperature, superfluid ratio etc.) drift. The CryoLEM, however, can rotate while being connected to the pumping line thanks to a specially developed rotating gasket which keeps sealed low temperature helium.

To enable the rotation of the system, the whole structure of the CryoLEM is mounted on an air bearing rotary table of $\varnothing 1.5m$, designed by Jena Tec. This platform, is composed of two superimposed disks (Fig. 2.10). The lower one is crossed by a compressed air line. When this line is open, the upper platform levitates $50\mu m$ above the lower one, removing dry friction between the two, and allowing the rotation of the upper one. A motor under the table is controlled by the user through a dedicated man-machine interface, allowing stable rotation of the CryoLEM up to $120RPM$ ($2Hz$), in both directions. Most of experiments have been done with an angular velocity set between -15 and $15RPM$. At these velocities, He II should display a lattice of quantum vortices regularly spaced by $\delta > 178\mu m$ (section 1.3). Consequently, the frozen particles of size $d_p < 100\mu m$ used in the He II bath will be able to probe the lattice, as they are smaller than δ (see section 2.3.1).

A helium-proof spinning gasket is used to connect the inner part of the CryoLEM to the pumping line. This gasket is mounted on a guiding stator (fig. 2.11, left) which is strongly fixed to the walls of

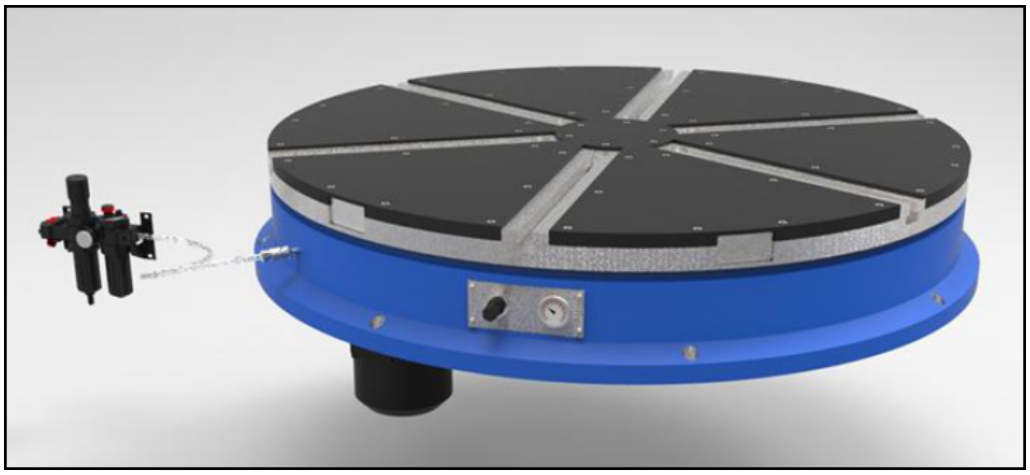

Figure 2.10: Picture of the rotating table CAD model. The blue part is the static lower disk, supplied by a compressed air line (with a regulator, on the left of the picture). The black and gray disk above levitates $50\mu m$ above the lower one, removing dry friction, and allowing rotation up to $120RPM$. The black cylinder under the table is the motor, connected to the table by a synchronous belt.

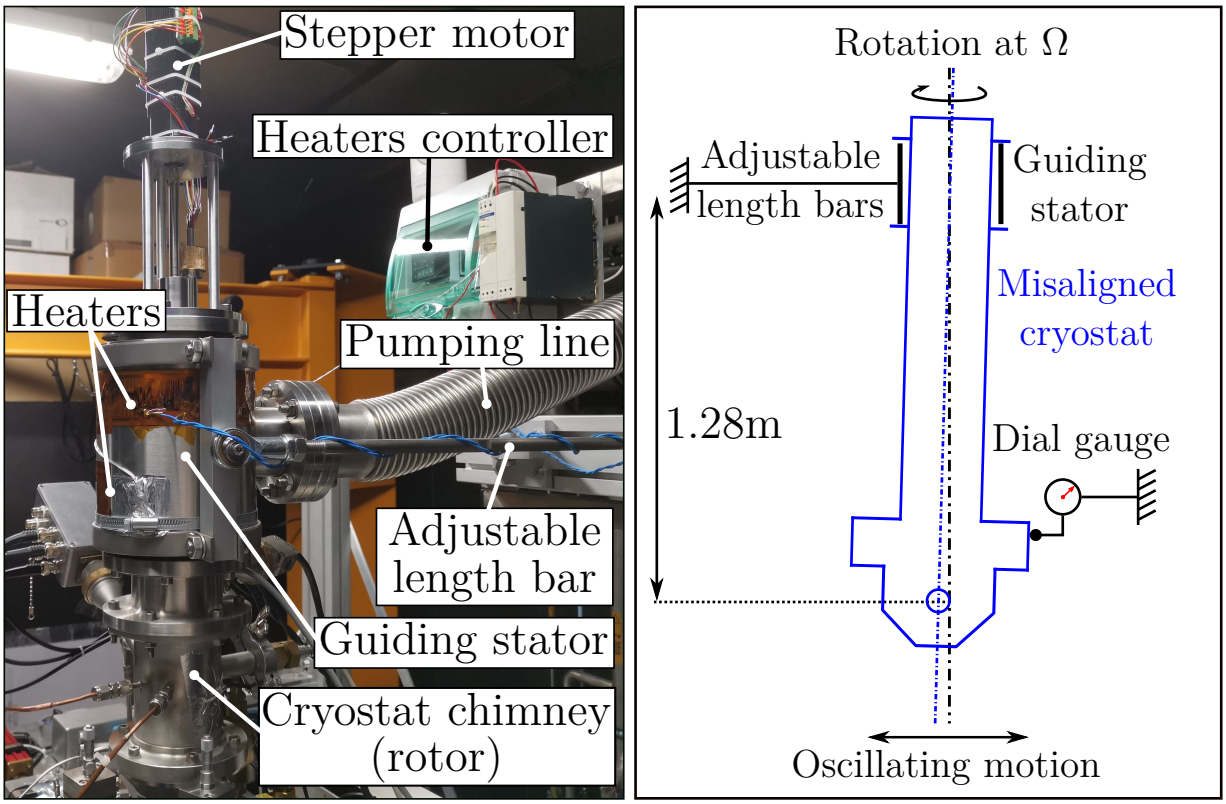

Figure 2.11: The cryostat is rigidly guided at its top by a stator. As there is a gap of $1.28m$ between the "ball joint" and the observation window, a small misalignment at the top leads to a problematic oscillating motion of the experimental cell. Thus, this motion has been measured by a dial gauge while positioning the cryostat, in order to align it carefully with the spinning axis and the guiding stator. This fine tuning was made possible thanks to bars of adjustable length.

the laboratory by rigid bars of adjustable length. The cryostat chimney passes and spins through this part. Thus, this part, the cryostat central axis of symmetry, and the rotating table axis must be finely

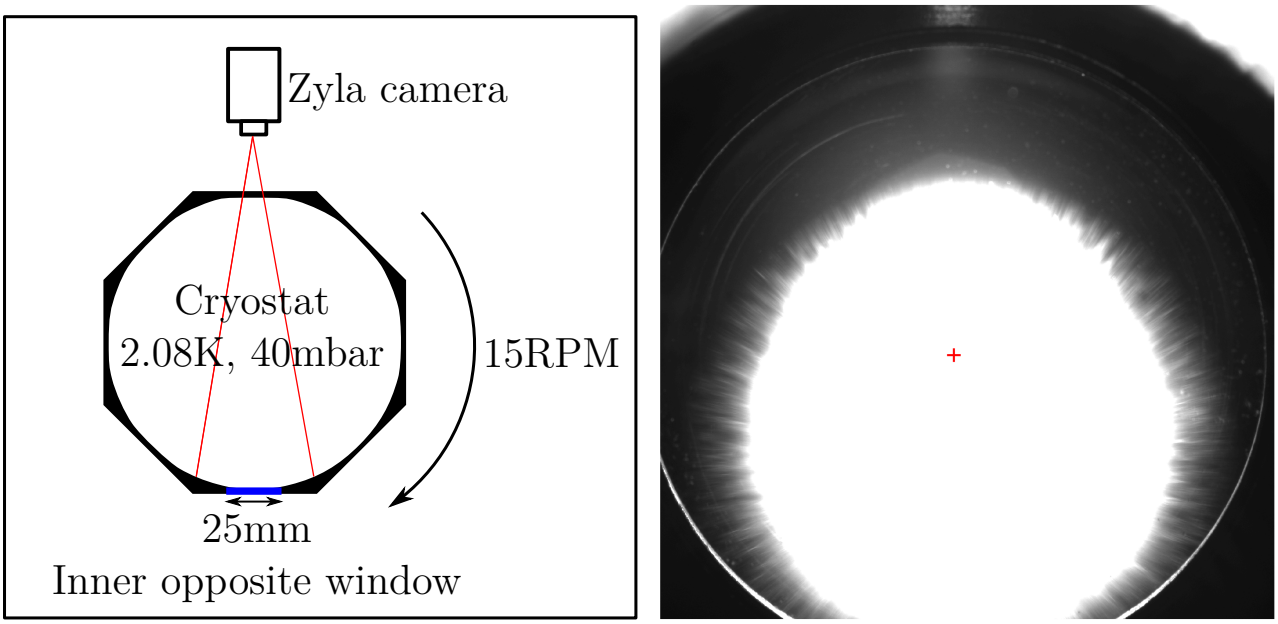

Figure 2.12: Left: Drawing of the protocol used to record the cryostat oscillations during rotation. The camera is focused on the opposite inner window (the insulating shields are not represented). The cryostat contains He II at $2.08K$ in order to see its behavior in experimental conditions. Right: An image of the opposite window. The bright area in the middle is the room light. It is reflected by the edge of the window, which is particularly visible on the bottom corners of the image. The red cross is the center of the window, detected by interpolating a circle on the visible window edges.

aligned. The cryostat has been placed on the table, and aligned using dial gauges fixed to the walls of the lab. Then, the guiding stator position has been optimized by measuring the displacement of the experimental cell with respect to the table, when rotating. If the guiding stator, which is located at the top of the cryostat, is not perfectly aligned, the experimental cell at the bottom will move like a pendulum when rotating (fig. 2.11, right). Acting on the adjustable bars length, the guide is moved until the motion of the cell becomes as close as possible to zero.

On figure 2.11 left, heaters can be noticed on the guiding stator. As large quantities of just evaporated helium can be pumped, the spinning gasket can reach temperatures below $0°C$ if nothing is done. Then, water from air could freeze on it, and stick it. As this could provoke severe damage to the spinning mechanism, heaters have been stuck on the stator. Thus, if the temperature of the gasket falls below $15°C$, the heaters are on, and when it is above $20°C$, they are off.

Despite a careful alignment, oscillations of the seeding particles were observed during experiments with superfluid and liquid helium. Using a camera fixed to the spinning structure (assumed perfectly rigid) rotating at $15RPM$, the motion of one of the inner cryostat windows has been recorded (Fig. 2.12). During these measurements, the cryostat is filled with He II, with a pressure of $40mbar$, in order to be as close as possible to experimental conditions. 6000 images have been recorded at 52Hz, corresponding to 28 table revolutions.

The edge of the window reflects the room light of the laboratory, drawing bright arcs of circle on the bottom corners of the acquired image (Fig. 2.12, right). These arcs were interpolated with a circle using a MATLAB code which gives its radius and center position. The circle radius is equal to 1250 ± 1 pixels on every image. As the actual window has a radius of $12.5mm$, the scale of the image is $1pixel = 10\mu m$. The fact that the window size variations are below 0.1% is a good indicator of the code ability to detect the window's edges. The position of the circle as a function of time is given on figure 2.13. It shows a periodic displacement of $50\mu m$ in both vertical and horizontal directions at the

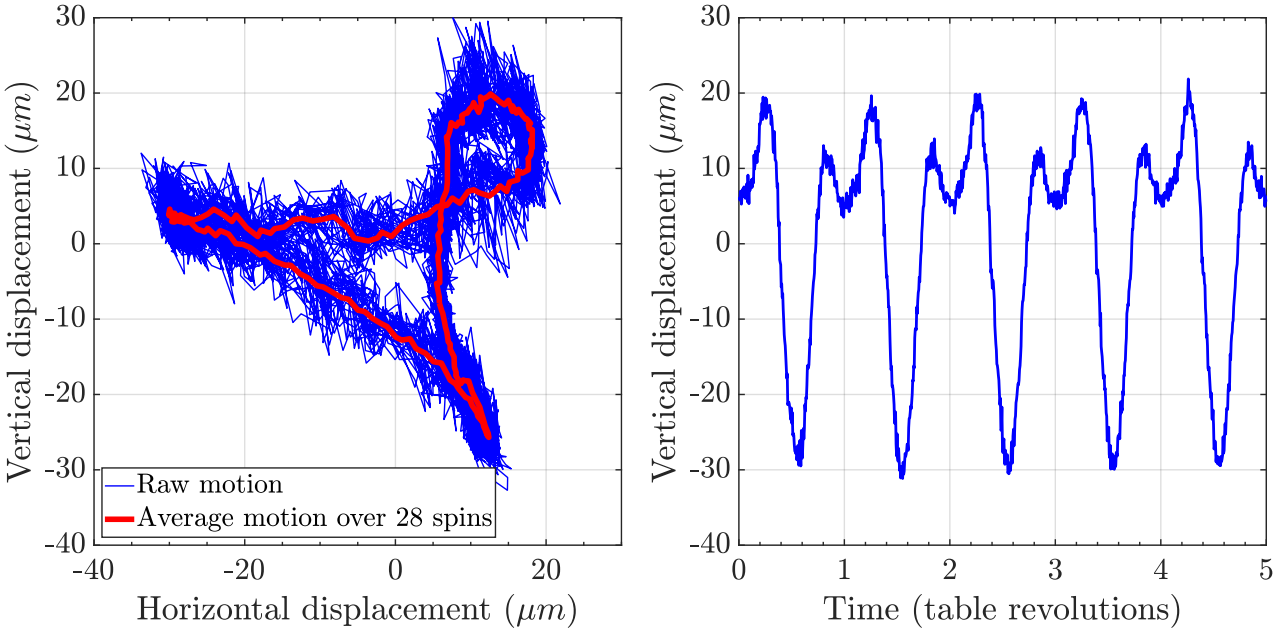

Figure 2.13: Left: 2D motion of a CryoLEM window when the apparatus containing He II at $2.08K$ is spinning at $15RPM$. This is the result of the experiment described in fig. 2.12. The cryostat oscillates with an amplitude of $\sim 50\mu m$ Right: Time dependence of the horizontal component of this motion. Only 5 revolutions have been displayed for clarity. The window motion is perfectly synchronous with the rotating table.

same frequency as the spinning structure. This motion is probably due to a misalignment of a few microns between the cryostat spinning axis and the guiding stator, resulting in a pendulum behavior of the experimental cell. Considering the difference of altitude between the window and the guide being $1.28m$, and the height of the guide being $170mm$, the misalignment should be around $1.65\mu m$. Considering the size of the apparatus, the presence of such small oscillating motion is already a success.

Oscillations of rotating He II have already been reported by Packard [138], or Bewley [18]. If Packard argues that his oscillations come from a mechanical excitation, Bewley claims that his could be the first experimental observation of Tkachenko waves. In our case, the misalignment must play a role in exciting inertial waves, as explained in section 1.3.1 and in [84]. Whatever the nature of these oscillations could be, they have only been observed in steady rotating He II, and they have been easily overcome by other turbulent forcing, such as stirring (detailed in section 4.3). In the future, the CryoLEM will be equipped with a set of six 3-axis accelerometers in different locations, in order to study this perturbing motion more extensively.

2.2.2 Stepper motor

A stepper motor is placed at the top of the cryostat, on the spinning axis, and its shaft crosses the whole cryostat chimney (fig. 2.11, left), down to the experimental helium bath. The shaft is $1.45m$ long and it passes through several guides in order to avoid its flexion, and keep its stability of rotation. This shaft is hollow, reducing the torque necessary to actuate it, and heat transfers by conduction in it.

The motor is a Haydon Kerk - Ametek LR35MH4AE-12-840. It features two independent axis: one for rotation, and one for translation, with a maximal stroke of $840mm$. The rotating axis has 200 steps per revolution, and the translating one has $25steps/mm$. Both feature adjustable microsteps, which means that motor steps can be divided by a value between 2^0 and 2^8, for improved precision

(but lower velocities). In the current configuration, speeds of the order of $200RPM$ in rotation, and $10mm/s$ in translation can be achieved.

This contributes to the modularity of the CryoLEM as different forcing can be done, without changing the whole mechanical power chain. Initially, a flat propeller has been mounted on it, and used to stir the fluid in order to homogenize the particle field (see section 2.3.1). In this case, the propeller is translated close to the field of view, set in rotation to stir the particles, and then translated back as far as possible, in order to neutralize its action on the studied flow. The translation could also be used for future experiments on grid turbulence (decaying turbulence if pulled once [64, 139], or steady state if oscillated [65, 125]), just by replacing the propeller at the tip of the shaft. Another benefit would be the calibration of 3D visualization techniques (in future works): a test pattern can be fixed at the tip of the shaft, and moved to calibrate the cameras.

The driver is a Trinamic TMCM-3110. This board is connected via RS485 port, to a brainbox ES-313, which is a serial to ethernet adapter. The brainbox is connected to the lab network, allowing communication from a distance with the main computer. The driver is provided with a software: TMCL-IDE 3.0 which can be used on a computer to communicate with the motor. The user can play with different settings, which are converted in an hexadecimal message of variable length sent to the driver which pilots the motor axes. This software contains a programmable section, in which the user can write some code in order to realize successive operations, loops, etc. For example, it is possible to program the motor to move up and down at constant velocity (trapezoidal velocity signal) in order to achieve an oscillating motion which could be applied to study grid turbulence. The software can also display graphs of the position and velocity of the motor.

However, the long shaft of the motor crossing the whole cryostat, including seals and bearings which can block it by friction. In some configurations allowing high velocities, the motor appear unable to operate continuously, because of its lack of torque. The problem is that the software do not report these unexpected stops, which means that they display a prediction of the motor motion, and not an actual measurement. Moreover, when programming an oscillating motion (trapezoidal velocity signal) some "position reach flags" have been used: it is a message sent by the motor when a certain chosen position is reached. These messages turned out to be sent too early as the software displayed a position graph of lower amplitude than expected. In short, the motor is currently open-loop controlled, and sensors must be added to adopt closed-loop control, collecting real information about its position and speed.

Up to now, the motor has only been used for simple applications, such as continuous rotation of a propeller (fig. 2.14 and section 4). In order to centralize a maximum amount of devices in a single interface, a LabVIEW code as been written in order to control the motor. This code allows the user to set all the motor parameters. To build this code, we decoded the hexadecimal messages sent by TMCL-IDE which are accessible in a log window. Then, the LabVIEW code can translate the user's commands into the corresponding hexadecimal message which would be sent by TMCL-IDE. This works perfectly for writing positive numbers, but for negative numbers and reading, the code times out. The coding of the order into an hexadecimal message has been checked with the TMCL-IDE logs, and the transmission of the message through the network has also been verified using Wireshark. The reason why these peculiar messages do not work with LabVIEW remains unknown, but they are not mandatory to run simple orders.

In conclusion, the stepper motor used in the CryoLEM is interesting because of its two independent axes which can move objects in the cryostat from outside. Simple commands can be sent with the main control LabVIEW code, but the use of the manufacturer's software TMCL-IDE is necessary for more complex ones. However, even in this case, some sensors (position, velocity, torque...) must be

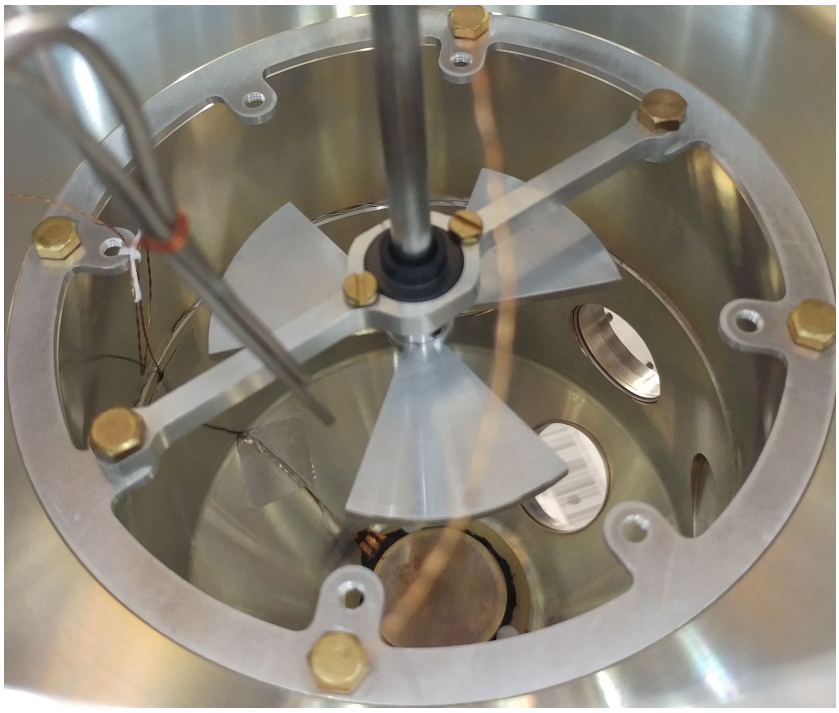

Figure 2.14: Photograph of the flat propeller in the (open) CryoLEM cell. The central part of the propeller is a cylinder of $\varnothing 10mm$ fixed at the tip of the motor shaft. The blades are $29mm$ long, so the total diameter of the propeller is $68mm$.

implemented in order to set up a closed loop control.

2.2.3 Counterflow channel

Following the enthusiasm of several experimental research groups on counterflow (see section 1.4.2), a heater has been placed in the CryoLEM during its first runs in 2017. It is a copper disk of diameter $\varnothing 32mm$ under which is placed a 34Ω resistor. This disk was placed at the center of the bottom of the inner cell (fig. 2.15, left), which is $5cm$ below the center of the field of view. However, as there was no channel to concentrate the flux, even when supplying a power of $1W$ (which is a lot in a cryogenic environment), no fluid motion was observed. Indeed, at the level of the field of view, the power is spread on the whole section of the cryostat ($\varnothing 108mm$), resulting in a heat flow rate of $q_{cell} \simeq 11mW/cm^2$. This is comparable to the lowest values experimented by Paoletti et al. [127], but without any possibility to reach higher values without risking to burn the heater. Note that, despite the inefficiency of this heater to generate counterflow, it appeared really useful to regulate the pressure of the experimental cell (see section 2.1.2), or evaporate as much helium as possible at the end of a day of experiments, in order to recycle it before switching the evacuation to outside air (see section 2.1.3).

A new counterflow channel has been developed (fig. 2.15, right). In order to avoid visualization through non-optically flat interfaces, we decided to use a square section. The heater is a square of $19mm \times 19mm$ under which are stuck two strain gauges whose resistance are equal to 120Ω. Copper has been selected for its high thermal conductivity. Despite the strain gauges being small, their heating power will spread in the whole copper square, and we can assume the heat flow rate to be homogeneous along the cross section of the channel. Furthermore, the copper square is placed on a fiberglass base. This material has been chosen for its low thermal conductivity, preventing thermal losses to the bottom.

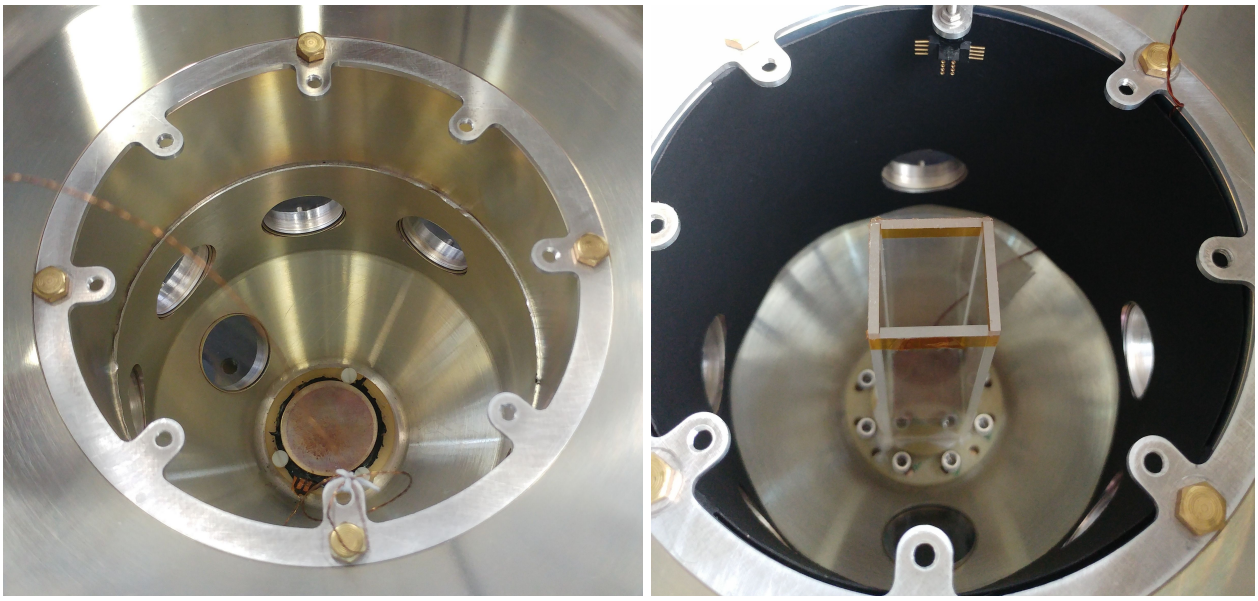

Figure 2.15: Left: "old" (2017) copper disk fixed at the bottom of the CryoLEM. Right: New (2019) counterflow channel in the CryoLEM. The walls close to the field of view have been covered by a dark sheet of paper to limit light reflections on the background of the field of view.

In other words, the heating power supplied by the resistors travels through the copper square, and is evacuated by the normal component of He II through the channel. The base is fixed at the bottom of the inner cell, in the same place as the previous copper disk. However, it is $30mm$ high, bringing the copper square only a few millimeters below the bottom of the field of view.

The walls of the channel have been machined in a $2mm$ thick commercial Plexiglas sheet. They are rectangles of $20mm$ large per $100mm$ long, fixed on the fiberglass base, $20mm$ below the heater. Thus, the resulting length of the channel is $80mm$, which corresponds to an aspect ratio of 4, the same as the channel used in Prague cryogenic facility ([140] and appendix D). For classical turbulent channel flows, the length is often chosen to be at least 25 to 40 times larger than the width, in order to observe fully developed turbulence, and avoid entrance effects [141]. In quantum turbulence, this length still needs to be determined, though it has already been shown by Hrubcová et al. [54] that the distance from the heater has an effect on the measured vortex line density. In any case, it is not possible to place a longer channel in the CryoLEM, as one of the stepper motor guides, in the upper cylinder of the inner cell, stands in the way. From this results that the channel length cannot exceed the height of the lower elongated square cupola of the inner cell ($\sim 120mm$).

2.3 Data acquisition

2.3.1 Particle seeding system

Production of frozen particles

As helium is transparent, with a refractive index of 1.03 around $2K$ [142], tracers are used to visualize the fluid motion. In a cryogenic environment, the use of “regular” solid spherical particles of controlled density is not convenient. There are several obstacles to the use of solid (in atmospheric conditions) particles, and the highest one is the fact that particles cannot be removed from the cryostat without opening it. Therefore, several research groups have used frozen particles made of hydrogen or deuterium to observe cryogenic flows (see section 1.4.2).

Hydrogen and deuterium become solid respectively at $14K$ and $19K$. Consequently, if this gas was simply injected in He II, it would become solid before entering the superfluid bath ($T < 2.17K$), and block their injection pipe. Thus, a small amount of one of these elements is diluted in room temperature gaseous helium before injection, according to the protocol described by G. P. Bewley in 2006 [18]. This way, pipe blocking is avoided, and a cloud of small particles illuminates the experimental helium bath. After a day of experiments, warming up the cryostat vessel above the boiling temperature of the particles ($21K$ for H_2 and $25K$ for D_2) allows to restart experiments the next day with a clean vessel (see section 2.1.3).

The density of superfluid helium between $1K$ and $2.17K$ is between 145 and $146kg/m^3$, whereas the density of solid hydrogen and deuterium are respectively $88kg/m^3$ and $206kg/m^3$. Both kind of particles are not neutrally buoyant: hydrogen settles to the surface and deuterium settles to the bottom of the helium bath. This can be seen as an advantage, as the shape of the particles is not precisely controlled. Thus, if a very large particle appears in the field of view, it will settle quicker than small ones, according to Stokes' law (section 1.4.1).

In order to produce these particles, two tanks of $1L$ of gas (limited to $4bar$ of pressure) are embedded on the spinning structure (Fig. 2.16). During the preparation of the gaseous mixture, a movable cart is connected to the embedded injection system. All the valves of these two equipment are solenoid valves. They are computer controlled by two dedicated programmable logic controllers (PLC) to ensure the reliability and repeatability of the process.

First, the whole system is pumped down to be as clean as possible from air, or previous gas mixtures. Then, the reservoir V_2 is filled with deuterium (or hydrogen), up to a certain pressure, and completed with pure helium up to $3.5bar$. The partial pressure of seeding gas can be adjusted in order to change the mixture ratio, but it is usually set to $52.5mbar$, corresponding to 1.5% of seeding gas. Once this mixture is ready, V_2 is closed, and the pipes are pumped again to vacuum. The reservoir V_3 is filled with pure helium up to $3.5bar$.

Both reservoirs are connected to the helium vessel by two capillaries of $\varnothing 0.5mm$ and $\varnothing 1.5mm$ inner diameter, and $\sim 1.5m$ long. These capillaries are made of a cupronickel alloy. Only one of them is used at a time, but one can still be used if the other is blocked. Indeed, as the capillaries are thin, the repetition of several injections could lead to particles stuck on its walls, and eventually a complete obstruction. This is why V_3 has been filled with pure gaseous helium: this gas is injected after each injection in order to rinse the capillaries. By choosing the diameter of the capillary used, it is also possible to adapt the injection flow rate which is a key parameter of the particle shaping (see section 2.3.1).

Another way to change the flow rate is to change the difference of pressure between both ends of the injection capillary (see further, with eq. 2.2). Thus, in addition to the solenoid valve, a pressure regulator has been implemented on each injection line in 2018. The solenoid valves allow to remotely prepare the mixture and inject the particles, and the regulators keep the injection pressure constant. Thus, even after several injections reducing the pressure in the reservoirs V_2 and V_3, the flow rate remains the same in the capillaries. Moreover, the injection pressure can be manually adjusted between 0 and $3bars$ (absolute). This setting can be read on the manometer of the pressure regulator with a resolution of $50mbar$.

Several groups working with frozen particles in superfluid helium report injections in the normal state (above T_λ), before cooling down to the superfluid state [43, 143]. That way, the particle cloud is thinner, even if aggregation is enhanced once the superfluid state is reached. The problem of this protocol is that most particles had already settled out of the field of view during the time needed to cool down to superfluidity with a stable pressure. Thus, a way to create a thin particle cloud with an injection below T_λ is of high interest in the research on superfluid flows. In 2016, Fonda et al. described a way to produce sub-micron particles below T_λ by controlling a small leak of air in the

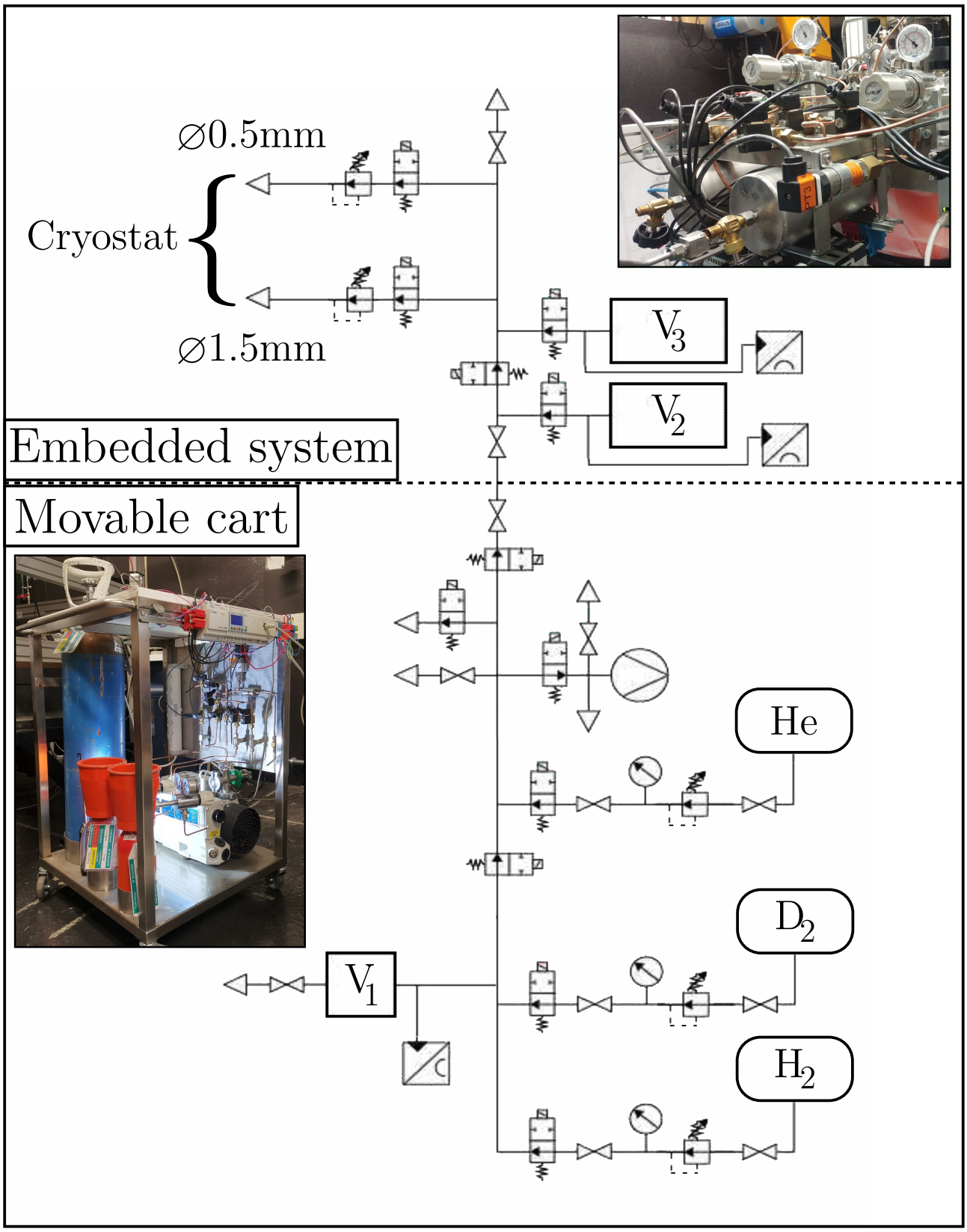

Figure 2.16: Pneumatic circuit diagram of the particle injection system. The cart includes a pump, bottles of hydrogen, deuterium and helium. The reservoir V_1 is used to prepare the mixture with a precise partial pressure of the seeding component. V_2 usually contains pure helium and V_3 the gas mixture. All the valves are solenoid valves controlled using a dedicated PLC.

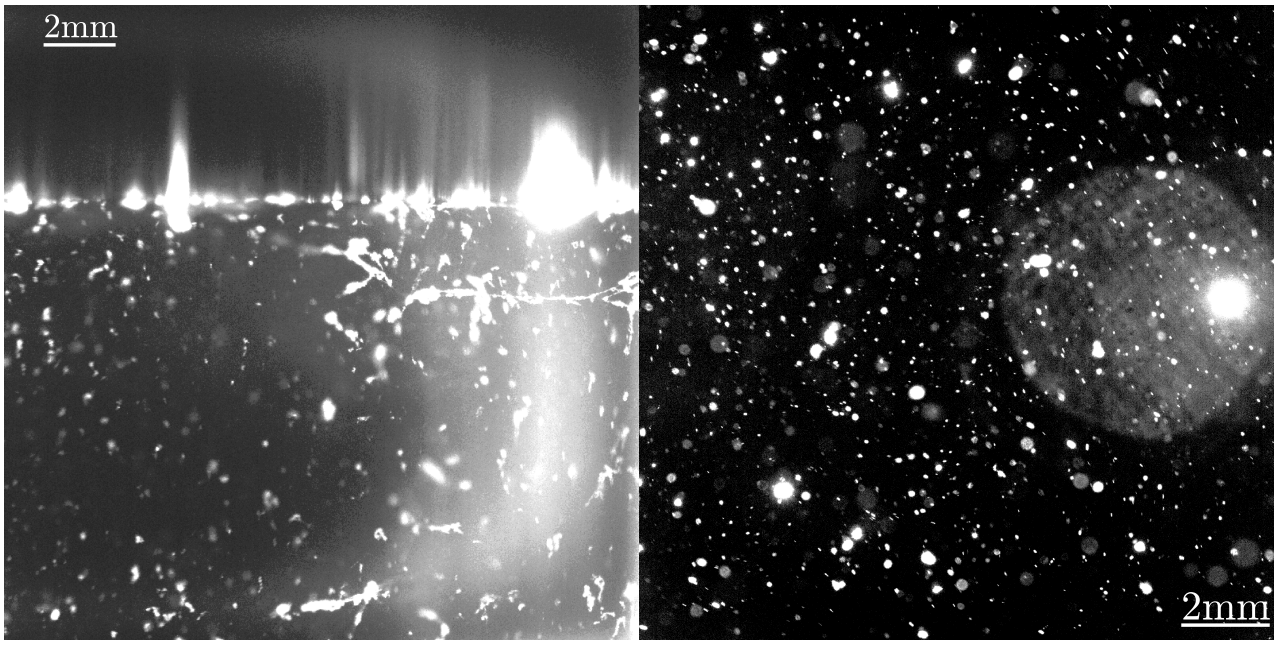

Figure 2.17: Left: Picture of hydrogen particles injected in the CryoLEM in rotation below T_λ, acquired with a Phantom v311 (cropped). The liquid-gas interface is visible at the top, where particle stack due to their low density. These particle stacks reflect a lot of light, provoking bright areas in the background. Hydrogen particles aggregate as filaments as seen in [43, 144]. Right: Picture of deuterium particles injected in the CryoLEM in rotation below T_λ, acquired with a Zyla SCMOS camera (background subtracted). As the pressure has not been regulated, some large particles appear a few seconds after the injection. These large particles create unusually bright areas which affect the particle detection algorithm, and could even blind the camera.

cryostat [113]. This describes in fact a way to reduce the injection flow rate, even if this is not clearly said, nor quantified in the paper.

Particle injection protocol

The purpose of our injection system is to be able to produce a cloud of thin particles (micron-sized), which is dense enough to produce converged statistics, but suitable for PTV. Based on the different features of our injection system, experiments with different injection parameters have been performed, in order to study their influence on the particle field properties. According to our observations, the shape of the particle cloud is influenced by the following physical quantities:

- The nature of particles (H_2 or D_2) and the mixture ratio
- The liquid helium amount in the vessel
- The diameter of the injection capillary
- The pressure difference between both ends of the capillary

In helium II, frozen particles have been reported to aggregate with time. This is something that we also observed in the CryoLEM, with both kind of particles. However, hydrogen particles aggregate forming filaments [43, 144], whereas deuterium simply forms larger and larger blocks (Fig. 2.17). As most theoretical models focus on spherical particles, staying as close as possible to this shape is beneficial. This is why most of our experiments have been done with deuterium, rather than hydrogen.

Moreover, deuterium has the advantage to be denser than helium, allowing the resuspension of particles by blowing pure gaseous helium at the bottom of the superfluid bath. As the end of injection capillaries are submerged and oriented downwards, it is not possible to do the same with hydrogen which is less dense than helium, and consequently settles to the top.

The seeding gas dilution ratio is something that has been tested by almost every visualizing helium research groups, as reported in the literature of the last 20 years. Bewley suggested, in 2009 [43], that the mixture ratio should be set to 2% of seeding gas. He also noted that particles' size increases for ratios above 20%, and becomes "vanishingly small for mixtures more dilute than 0.2%". In the CryoLEM, ratios between 0.75% and 5% have been tested. In this range, the mixture ratio does not have a clearly visible impact on the particle shape. However, below 1% the amount of visible particles was too small to produce enough statistics. Above 3%, the smallest capillary ($\varnothing 0.5mm$) was blocked after a few injections. This is why a ratio of 1.5% of seeding gas has been used in most experiments.

The helium level in the cryostat also plays a role, as the particles were smaller when the helium level was lower. A "smoke" of deuterium could also be produced when the helium level was so low that the capillaries' end were above the condensed helium surface. These effects are due to thermal exchanges between the hot gas and the cryogenic helium, through the walls of the capillaries during the injection.

When the helium level is high, the temperature gradient in the pipe is higher, leading to abrupt temperature changes, quicker condensation, and higher risk of pipe blocking. However, due to the difficulty of measuring precisely the helium level in the cell, the dependency is still not well understood. Many publications describing apparatuses for superfluid visualization report the use of a resisting wire wrapped around the injection pipe, in order to heat it during injections, and limit the temperature gradient [18, 103]. This is something that will be improved in the future, but which has not been implemented yet in the CryoLEM.

The capillary diameter and the pressure difference actually refer to the flow rate in a pipe according to the Hagen-Poiseuille equation:

$$Q_{inj} = \frac{\pi r_c^4 (P_{reg} - P_{cryo})}{8 \mu L_c} \tag{2.2}$$

where Q_{inj} is the mixture flow rate in the capillary, r_c is the capillary radius, P_{reg} is the pressure set by the regulator, P_{cryo} the pressure in the cryostat, μ is the dynamic viscosity of the mixture flowing in the capillary, and L_c is the length of the capillary. Actually, even without pressure regulation, the small capillary ($\varnothing 0.5mm$) could already produce a very thin particle cloud. The problem is that this capillary was often blocked by frozen particles after a few injections, forcing the use of the larger one ($\varnothing 1.5mm$).

Before using regulators to study the influence of the pressure difference, we used the protocol developed by G.P Bewley [18, 43], with injections above T_λ. Without regulators, injections in the superfluid state produce larger particles of various shapes. Some particles could even reach a diameter of $350\mu m$ (Fig. 2.17), which is ~ 100 times larger than the average particle size when injected in liquid helium I. These anomalously large particles could blind the camera during acquisitions due to their brightness, and they are too big to resolve the intervortex spacing of our studied flows (in a simple rotation at $\Omega = 5RPM$, $\delta = 320\mu m$).

The addition of regulators on the injection lines has several benefits. Firstly, the pressure difference between both ends of the injection capillary remains constant, for a better repeatability of particles formation. Secondly, this makes it possible to produce micron-sized particles directly in He II ($T < T_\lambda$).

Thus, we avoid several pressure changes, and keep a better stability of the system. Thirdly, the injection process has been shortened considerably, leaving less time for particle settling, therefore keeping more of them in the field of view.

The injection pressure is read on the dial gauge of the manometer of the regulator. Its resolution is $50mbar$, for measurements between $+2bar$ and $-1bar$ of relative pressure. Thus, we directly measure $\Delta P_{inj} = P_{reg} - P_{cryo}$. Usually, the duration of injections is set to 2 seconds, which means that the pressure has to be read within this small time interval. In other words, our pressure measurements are not very precise, and the uncertainty is about $\pm 25mbar$.

Lowering the injection pressure from $\Delta P_{inj} = 1bar$ to $\Delta P_{inj} \sim 500mbar$ did not have a clear impact on the particle size. Below $250mbar$, it was hard to say if the particles were actually injected in the cryostat, because nothing was visible. Between 250 and $400mbar$, the size of the particles, and the density of the cloud was changing significantly. By lowering the pressure, the size of the particles was decreasing, the size distribution was narrowing, but the particle amount was diminishing as well (fig. 2.18). The blinding largest particles completely disappeared, and the particle size is comparable to the one obtained by injecting above T_λ, following Bewley's protocol.

To overcome the lessening of the particle amount, several (or longer) injections can be done, until the operator considers there are enough tracers. However, reducing the flow rate also reduced the inertia of the particles when they reach the fluid. Consequently, when the fluid is at rest (or lightly stirred), they stay clustered close to the capillary's end, and do not come to the field of view. This is why a propeller has been often used to stir the fluid during injections, leading to a transient state which is not wanted during our experiments. A study of the propeller effects on the velocity fluctuations of

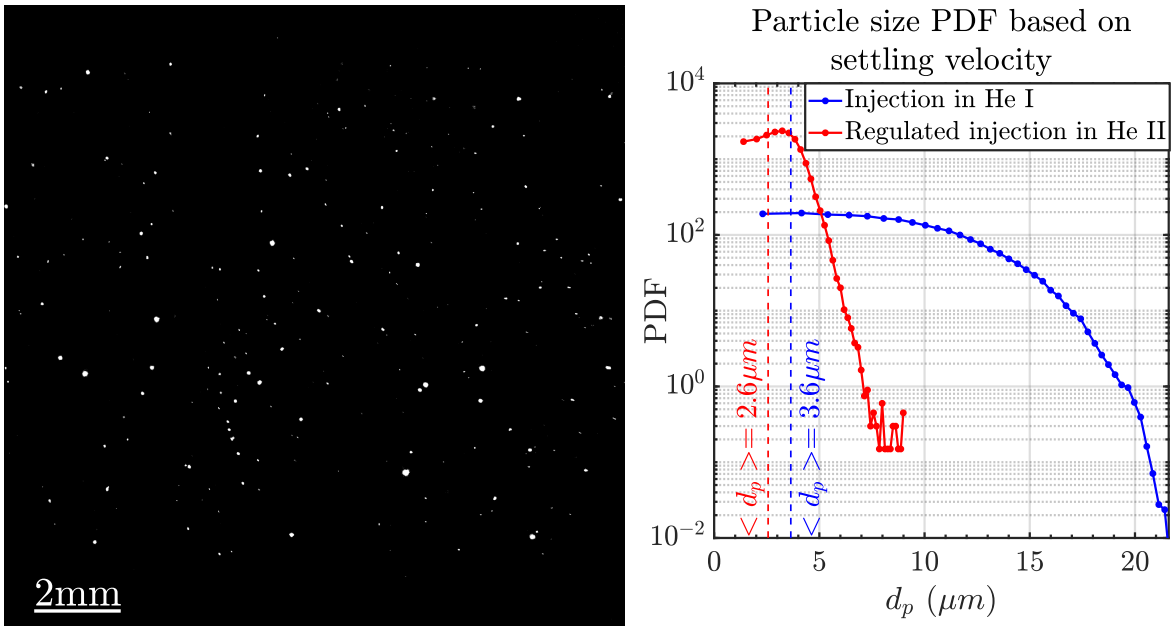

Figure 2.18: Left: Picture of deuterium particles suspended in helium II, injected below T_λ using the protocol described in the text. The background of the picture has been darken by removing the median luminosity of a hundred images of this sequence (see chapter 3). Right: Particle size PDF of the movie from which the picture on the left has been extracted (red), and of a movie in which the particles have been injected above T_λ, following Bewley's protocol (blue). These PDF are computed using the vertical velocity of the particles, and the Stokes' law (eq. 1.40). Some velocities were positive (upward), despite deuterium being denser than helium, meaning that the fluid was not completely at rest. This resulted in negative diameters which are not displayed, but the computed mean take them into account, explaining the small value.

the particles in the fluid led us to assume that the propeller effects vanished after $200s$, regardless of the pressure and temperature in the cell (see section 4.1.1).

In conclusion, the injection parameters which will be used in our experiments are the following:

- Mixture of gaseous helium (98.5%) and deuterium (1.5%) at $300K$.
- Injection directly in superfluid through a $1.5mm$ diameter capillary.
- The pressure difference between the injection line and the cryostat is $\Delta P_{inj} \sim 300mbar$.
- A propeller stirs the fluid in order to make the seeding homogeneous.
- A $200s$ wait is needed to avoid propeller effects, and let the largest particles settle.

Particle qualification

The particle size is a fundamental quantity to know the quality of the measurements which will be carried out in the CryoLEM. In the subsection 1.4.1, three methods to estimate the particles size have been given:

- 1) Using the quantity of gaseous mixture released in the cryostat, and compare it with the quantity of visible particles (eq. 1.39).
- 2) Using their settling velocity and the Stokes' law (eq. 1.40).
- 3) Using the size of the particles directly measured by the camera, and rescaling it with an approximated law of light scattering (eq. 1.41).

The first technique (1) only gives an estimate of the mean particle size. It requires to monitor the pressure in the mixture reservoir, and to know the volume of liquid helium in the cryostat cell V_{bulk}. These two quantities are not precisely known in the CryoLEM, but for a rough estimation, we will use $V_{bulk} = 3L$, and $\Delta P = 0.2bar = 2 \times 10^4 Pa$ (the difference of pressure before and after the injection). The volume of the reservoir containing the mixture is $V_{mix} = 1L = 10^{-3}m^3$, and its temperature is assumed to be equal to the room temperature: $T_{mix} = 293K$. In most movies studied in this thesis, the particles are made of deuterium D_2, which molar mass is $M_{D_2} = 2 \times 10^{-3}kg/mol$, and density $\rho_{D_2} = 206kg/m^3$. In the previous section, we chose a mixture containing $\phi_p = 1.5\%$ of deuterium. Moreover, the Zyla camera is used, with a field of view of $14.3 \times 14.3mm^2$. The width of the laser sheet has been experimentally determined (see section 4.3): $e = 2.6mm$. This leads to a probed volume equal to $V_{FoV} = 5.3 \times 10^{-7}m^3$. In this volume, we usually observe at least a hundred particles a few seconds after the injection ($n_i \simeq 100$). With all these parameters, the mean particle diameter is estimated:

$$\langle d_p \rangle = 2 \left(\frac{3 V_{mix}\ \Delta P\ \phi_p\ M_{D_2}}{4\pi R\ T_{mix}\ \rho_{D_2}\ n_i\ \frac{V_{bulk}}{V_{FoV}}} \right)^{1/3} = 16\mu m \tag{2.3}$$

This value is close to the objective of $10\mu m$. Particles of this size are indeed an order of magnitude smaller than the inter-vortex distance in helium II rotating at $\Omega = 15RPM$. Moreover, they might reach their limit when probing a turbulent flow. However, this remain an estimation, supposing for example that the seeding is homogeneous in the whole bulk. We know that it is not the case, as we must use a stirring turbine to homogenize it. To refine this estimate, the other two techniques have been used.

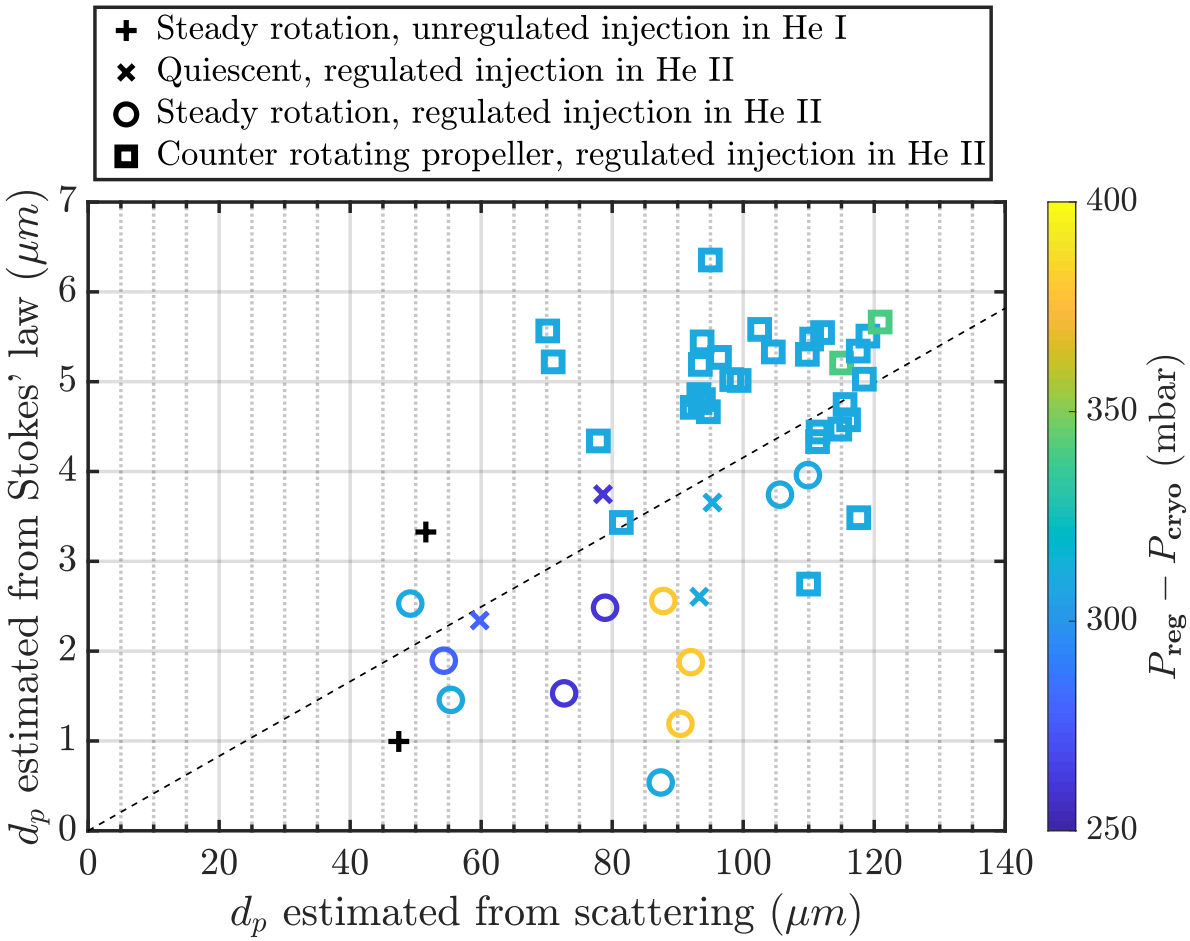

Figure 2.19: Mean particle size computed using the Stokes settling velocity, and the light scattered on the camera sensor, for 52 steady state movies (those reported in tables A.4, and A.6). The marker shapes indicate the type of flow in which the measurements have been done, and the color indicate the difference of pressure between the cryostat and the injection regulator (if regulated). Both measurements methods do not give the same results, but a linear trend can be observed (slope 1/24). The large particle size found by the optical technique can be attributed to out-of-focus particles which appear larger than they are. The fastest particles can also appear larger if their displacement between two frames is larger than the pixel size.

The figure 2.19 reports the mean particle sizes measured in 52 different acquisitions. 16 of them were recorded during the steady rotation of the cryostat (table A.4), 4 without forcing, and 32 in the rotating cryostat, containing a counter-rotating propeller (table A.6, and section 4.3). Except in the latter case, the Stokes' law should apply, because in steady rotation, the fluid can be considered at rest in the rotating frame of reference. Based on the fact that the rotating propeller is flat, hence generating a purely radial flow, and that the mean vertical velocity measured in these flows was independent on the forcing ($v_z \simeq -0.5mm/s$, see section 4.3 and figure 4.23), we decided to apply the Stokes' law to these movies as well.

The settling velocity technique returns a particle size $d_p \in [1 : 6]\mu m$. This value is in good agreement with the particle sizes reported by other groups working with cryogenic frozen particles [43, 66, 129]. Note that most of them used this technique to estimate their particles' size. This result fulfills the objective of having particles smaller than $10\mu m$. However, the light scattering technique returns a particle size $d_p \in [47 : 120]\mu m$, which is significantly larger than the other two techniques.

On average, the size of the particles obtained with the optical technique are 24 times larger than with the settling velocity (black dashed line on fig. 2.19). Actually, an increasing trend can be guessed which means that both techniques give similarly scaling results.

Let's focus on the acquisitions made in quiescent helium II ($\times$ symbols on fig. 2.19). In these conditions, the hypotheses of both the light scattering and Stokes' law are valid. The minimum size measured with the scattering technique is $60\mu m$ in this case. If the particles actually had this size, their settling velocity would be $-68mm/s$. The field of view is $14.3mm$ high, which means that, on average, particles could not stay longer than $0.21s$ (11 frames) in the field of view. However, the average length of a track in this movie is $2.36s$ (124 frames). It comes out that the particles cannot be this large.

Actually, the optical technique has several limits in our configuration. First of all, the thickness of our laser sheet being $2.6mm$, it is possible to have out of focus particles, hence having a larger apparent size. Moreover, all the movies have been acquired with a frame rate of $52.3Hz$, and a maximum exposure time. The velocities measured are of the order of $\sim 1mm/s$ which corresponds to a particle displacement of $\sim 20\mu m \simeq 3$ pixels between two frames. Consequently, even if our particles were spherical they would appear elongated in the direction of their velocity vector. A particle of 1 pixel in diameter moving at $1mm/s$ will create a bright area of 4 pixels on our frames. The figure 2.19 has been plotted again taking this phenomenon into account. We used the velocity vector and the orientation of elongation of each particle to decrease their apparent diameter. The result has not been displayed here as it is similar to fig. 2.19, with optically estimated diameters which are 25% smaller on average. The average factor between the Stokes and the optical techniques becomes 20 instead of 24, which is still very large. Based on all these inconsistencies in the optical technique, we decided to consider the size resulting from the settling velocity measurements to be the real one, and keep $d_p \in [1:6]\mu m$, in agreement with the literature.

On the figure 2.19, the impact of the injection pressure on the particle size can also be observed. The two injections in liquid He I resulted in the smallest particle sizes according to light scattering. They are also in the lowest half according to the settling technique. By reducing the injection flow rate, we managed to produce particles of similar size, even if no trend relating pressure and size appear on this figure. There is indeed a problem of repeatability in the particle production. This may be due to difficulties to read the exact pressure setting on the regulator manometer. One thing is certain though: lowering the injection pressure produces smaller and more homogeneous particles, as shown by the apparent size of particles visible on figures 2.17, and 2.18. It comes out that the particle formation follows complex laws, which will not be studied here thoroughly. However, we found that the flow rate was a parameter significantly impacting this phenomenon, and reducing its value allowed us to produce particles of satisfactory size.

Using this particle size, it is possible to compute Froude and Stokes numbers (eq. 1.43 & 1.45). As a reminder, these quantities reflect the particles' ability to faithfully trace the fluid streamlines. Quality particles have a Stokes number $St \ll 1$ and a Froude number $Fr \gg 1$. In section 1.4.1, we defined a radial and an axial (vertical) Froude numbers in rotating flows. The axial ones compares the velocity of the fluid small scale to gravity settling velocity, while the radial one compares it to centrifugation velocity.

In this thesis, most experiments have been done with D_2 particles, under a pressure of $P_{cryo} = 40mbar$. In these conditions, the particle density is $\rho_p = 206kg/m^3$ and the apparent kinematic viscosity of helium II is $\nu = 1.19 \times 10^{-8} m^2/s$. Moreover, in our experiments, the cryostat was spinning at $\Omega \in [3:15]RPM$. Considering the most unfavourable case (i.e. minimized Fr_r) we will use $\Omega = 15RPM$ to compute Fr_r. As the spinning axis is in the middle of the field of view, the maximum distance between it and a particle is $R = 8.6mm$. With these values, the figure 2.20 has been computed.

This figure is a logarithmic representation of the three dimensionless numbers, using the just mentioned parameters, as a function of the inter-vortex spacing δ and the particle diameter d_p. A

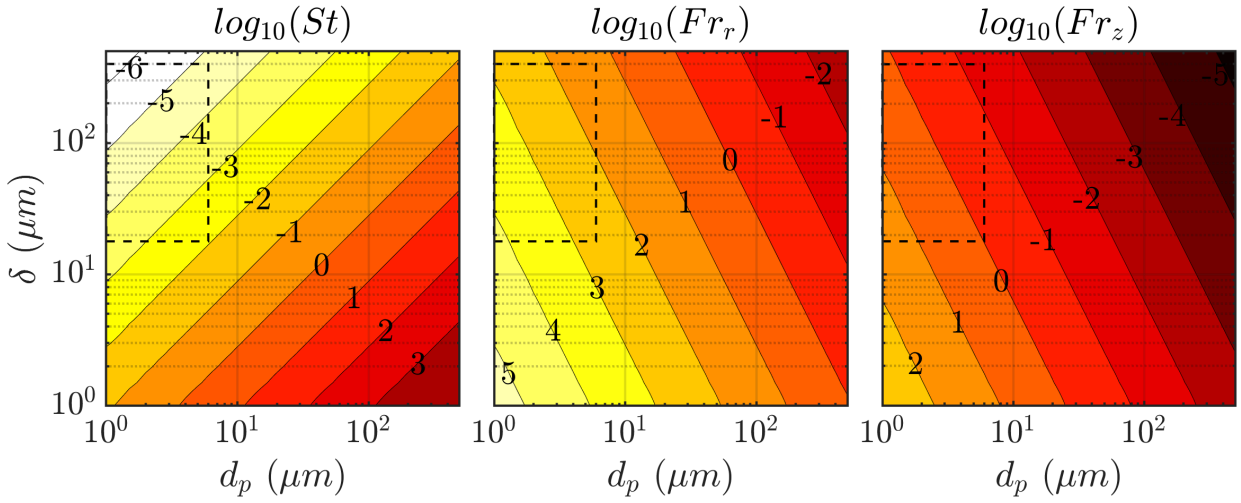

Figure 2.20: Evolution of the Stokes and Froude numbers as a function of the particle diameter d_p and inter-vortex spacing δ. The scales are logarithmic, so that each contour line represents a decade, indicated by the number on the line. The space of study of this thesis is shown by the black dashed rectangle: $d_p \in [1:6]\mu m$ and $\delta \in [\delta(3RPM) : \frac{\delta(15RPM)}{10}] \simeq [18:400]\mu m$.

dashed black rectangle has been drawn, showing the parameter space used in this thesis. In this rectangle, we have $d_p \in [1:6]\mu m$, according to our particle size estimation using the Stokes' law. The upper bound for δ has been computed applying the Feynman's rule (eq. 1.32) with an angular velocity $\Omega = 3RPM$. The lower bound is more difficult to estimate, as we also performed turbulent experiments in which the Feynman's rule does not apply (e.g. counter-rotating propeller in rotating He II in section 4.3). Thus, we estimated it to be a tenth of the value of δ given by the Feynman's rule with $\Omega = 15RPM$. Finally, the interval of study for δ is $[\delta(3RPM) : \frac{\delta(15RPM)}{10}] \simeq [18:400]\mu m$.

According to figure 2.20, we will work with Stokes numbers in the interval $St \in [10^{-6} : 10^{-2}]$, which fulfills the $St \ll 1$ criterion. The radial Froude number can vary between 10 and 10^4, which also fulfill the criterion $Fr_r \gg 1$. However, in the vertical direction, we have $Fr_z \in [10^{-1} : 10]$, which is of the order of 1. In other words, even with a strong forcing, gravity will play a significant role in the vertical motion of the particles. This was indeed expected, as the density difference between the particles and the fluid have already been mentioned several times.

To sum up, our injection protocol allows us to produce micron-sized deuterium particles. The Froude and Stokes numbers indicate that these particles are faithful tracers, allowing to acquire reliable data on He II dynamics. It is however necessary to be careful with the vertical velocities which are significantly impacted by the density difference between the particles and the fluid.

2.3.2 Image acquisition

Particles are enlightened by a light sheet generated by a continuous wave laser ALS-GREEN-10-SF whose power is adjustable up to a maximum of $10W$. In this thesis, the power used has always been $0.5W$, but higher powers will be needed in 3D, and with higher frame rates (implying shorter exposure times). The beam wavelength is $\lambda = 532nm$, and it has a gaussian intensity (beam quality factor $M^2 < 1.1$, and 94% roundness). The whole laser system is composed by 6 different blocks that must be embedded on the spinning table. Several of these blocks are connected together with optical fibers. This setup inevitably leads to positioning constraints, forcing the laser beam to travel more than $2m$, and be reflected by 4 mirrors before encountering the lenses that transform the beam into

a sheet (Fig. 2.21). This can also be seen as an advantage, as long distances allow for more precise alignments.

The sheet is generated by two cylindrical plano-convex lenses whose respective focal length are $3.9mm$ and $50mm$, resulting in a $33mm$ high and $2.6mm$ thick laser sheet (this value will be precised in section 4.3). Even though the cryostat has been carefully designed and positioned, some small parallelism errors remain ($< 1°$, Fig. 2.22). As the laser sheet crosses 3 to 4 interfaces (depending on the experimental sessions) with non-zero reflectance before reaching the area of interest, it is a bit distorted. This effect can be observed when the laser sheet exits the cryostat. At this point, the distortion is even worse because the sheet has crossed 6 to 8 interfaces. However, these deviations do not significantly impact the data. As the sheet is inevitably distorted, the four criteria used to validate the positioning of the lenses were:

- 1) Minimize the distortion, i.e. having the flattest sheet possible
- 2) Having the same height at the entrance and at the exit of the cryostat
- 3) The bottom of the exiting sheet must be located at the same altitude as the bottom of the incoming one
- 4) Make sure that the laser sheet does not hits anything other than the window.

In other words, the laser sheet must be a rectangle which is parallel to the floor, and smaller than the inner window size ($< 25mm$). The criterion 4 is specific to cryogenic systems. For example, if the laser hit a metallic part at the edge of the window, it could become a heating source in the helium bath, leading to accelerated evaporation, and counterflow. In order to avoid this with our $33mm$ high laser sheet, a shutter has been placed before the cryostat entrance window. It makes it possible to adjust the sheet height, which is usually set to $\sim 20mm$.

Two different cameras have been used during our experiments. The first one is an Andor Zyla 5.5 sCMOS, and it has been used between February 2018 and 2019. This camera can record movies up to 52images/s, with a resolution of 2048×2048 pixels^2, written in 16 $bits$, and whose pixel size is $6.5\mu m$. Thanks to a compatible data acquisition card supplied by the manufacturer, the images can be sent to a computer at bit rates that can reach $3.5Gbit/s$. The computer is equipped with two RAID0 solid state drives (SSD) of respectively $800GB$ and $1600GB$.

The other type of camera is a CMOS Phantom v311 made by Vision Research. It can record movies up to 3250 $images/s$ at full resolution (1280×800), written in $8bits$, and whose pixel size is $20\mu m$. The data is written on an internal $8GB$ high-speed memory, which is equivalent to 8000 images at full resolution. Three of these cameras are available in the laboratory as their initial purpose is to record 3D particle motion. In that case, the frame rate must be as high as possible as the amount of particles on each image would be very large. However, 3D particle tracking velocimetry will not be detailed in this thesis as it has not been implemented yet.

In order to capture the motion of micron-sized particles, macro lenses are used. All the available lenses are monofocal ($50mm$ or $100mm$ focal length) in order to minimize distortion. They also feature adjustable aperture, so that the luminosity and depth of field can be adjusted (for example, a deeper field of view will be recorded when 3D will be implemented).

The Phantom camera makes is possible to record particle motion with a high time resolution, but only for a few seconds ($\sim 2.5s$ at maximum frame rate), after which a transfer of data to a computer has to be done for several minutes ($\lesssim 4min$). The Zyla camera, on the other hand, can send the recorded images to a computer in real time, but the frame rate is limited to $52Hz$. The use of the Phantom camera is more tedious because the operator spends most of his time waiting for the data transfer, but a high frame rate can be necessary to observe highly turbulent flow such as counterflow.

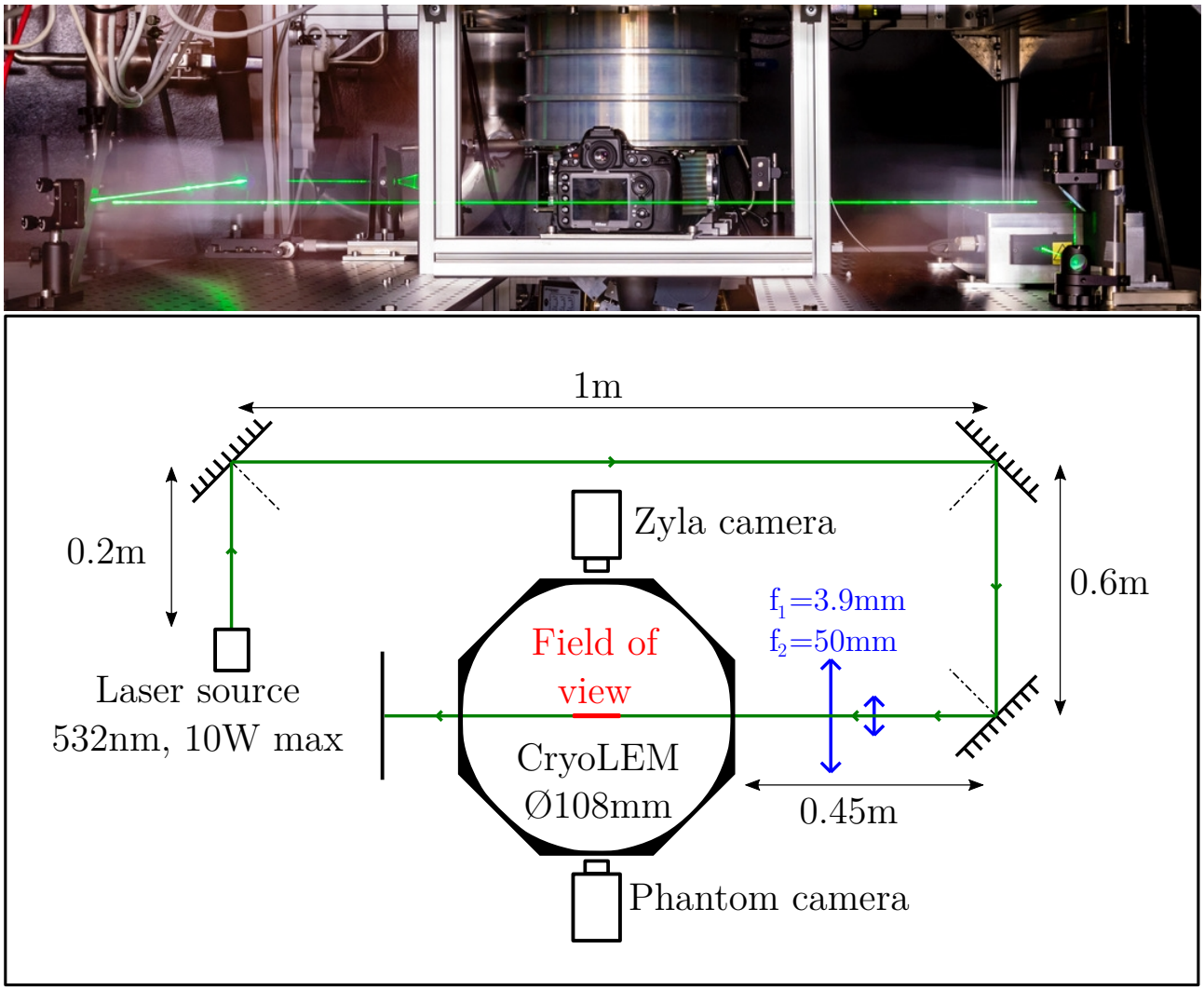

Figure 2.21: Top: Photograph of the optical system. Exceptionally, the Zyla camera was replaced by a Nikon DSLR. Bottom: Schematic view of the optical system from the top of the cryostat.

In this thesis, we will focus on moderately turbulent flows, which is why a high frame rate is not mandatory. Thus, all of the movies used in the chapter 4, and listed in the appendix A have been recorded with the Zyla camera. Most of the movies recorded are 30000 images long, and recorded at maximum frame rate, corresponding to a duration of $9min$ $33s$. Each movie recorded in these conditions represents $250GB$ of data. Thus, he cumulative memory available in the computer can store 9 movies, corresponding to $1h30$ of particle dynamics in He II. This is the usual amount of data we produce each day of experiment ($2.4TB/day$), due to several hours of transfer from the acquisition computer to the laboratory network attached storage (NAS).

This NAS storage is divided in two volumes of respectively $16TB$ (RAID10) and $70TB$ (RAID6). The RAID10 disk allows higher read and write speeds, which is why it is used to store processed (or being processed) data, while RAID6 is used to store the large raw images. For now, it is enough to store all the data acquired. With the future implementation of 3D PTV, it may become full very quickly. However, an efficient production of 3D PTV data will only be possible if a technical solution allows us to transfer data from the camera to a computer in real time. This solution could be to use embedded field-programmable gate arrays (FPGA) on each camera, to extract the positions of the particles in real time. Thus, the data transferred to the acquisition computer would no longer be a heavy image, but a lighter array containing coordinates.

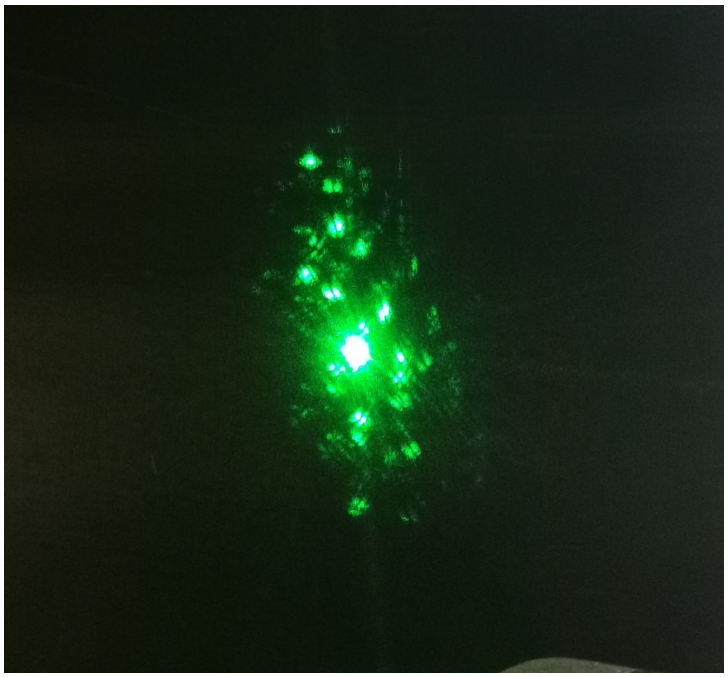

Figure 2.22: Laser beam and reflections after crossing the cryostat. The maximum distance between two laser beam images (dots) is about $4cm$. Considering that ~ 15 points are visible, and that each point results from a reflection on each of the 6 windows crossed, we can assume that the beam travelled 5 times back and forth in the cryostat, corresponding to a traveling distance of $2m$. We can conclude that the parallelism error between the cryostat layers is about $0.5°$.

Beyond data management, the Zyla camera has other advantages over the Phantom. Indeed, the images of the first are encoded in 16 bits (against 8 for the latter), so the distinction between the particles and the background is easier to make. Indeed, the inner surface of the CryoLEM is reflecting visible light as it is made of aluminium. Thus the contrast between the particles and the background can be weak. A black sheet of paper has been added to cover the inner walls of the cell in 2019 (see fig. 2.15, right). Furthermore, the pixel size is reduced from $20\mu m$ to $6.5\mu m$, increasing the spatial resolution of the measurements for a better understanding of the particles formation.

In order to calibrate this camera, a picture of the turbine at the tip of the stepper motor's shaft is taken before each experimental session. The central cylindrical part of the propeller has a known diameter of $10mm$. The apparent diameter of the cylinder is compared to this value in order to have the calibration (fig. 2.23). This method is not the most precise, but it is easy to apply, especially in a hard-to-reach environment, while giving a satisfying precision.

2.3.3 Sensors

The CryoLEM is equipped with several sensors that can be separated in 4 main categories :

- The cameras which were just detailed in section 2.3.2
- 8 temperature sensors
- 3 pressure sensors
- 3 liquid level sensors

Several temperature sensors are set in different places of the cryostat. Three temperature dependent resistors (Cernox®) are placed on the external face of the helium bath (R^{1K}), at different

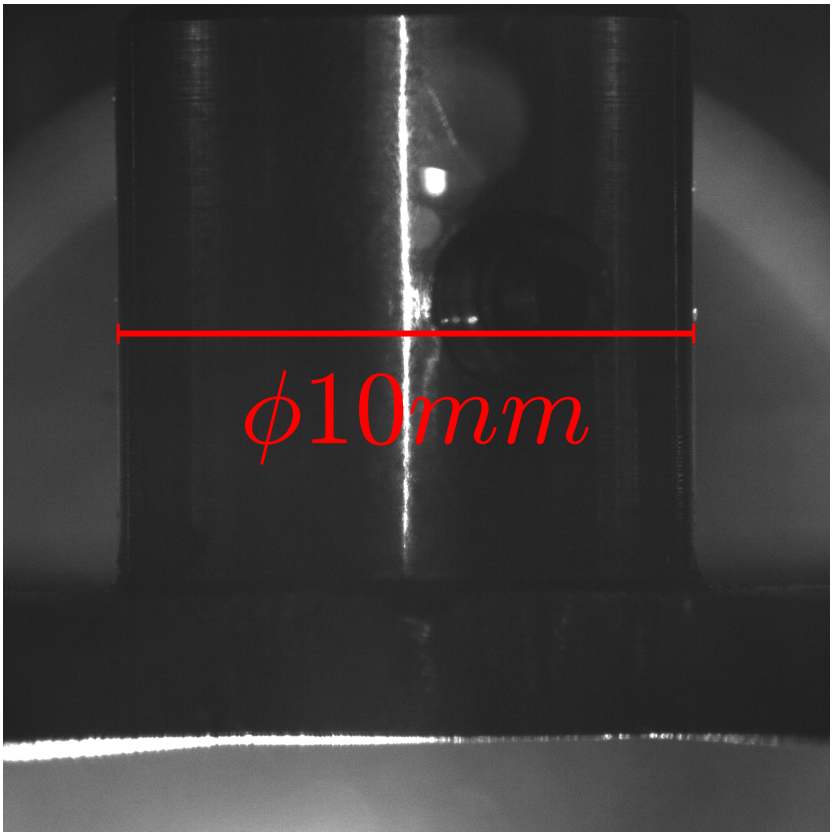

Figure 2.23: Image of the propeller in the cryostat. It is used to calibrate the spatial scale of the camera, knowing that the central cylindrical part of the propeller has a diameter of $\varnothing 10mm$. This picture gives a calibration of $7\mu m$/pixel.

altitudes ("Top", "Mid", "Bot", fig. 2.24). These gauges are made to operate between $1.4K$ and $325K$. Only the one at the top (R_{top}^{1K}) is calibrated, and the two others only give a trend of the temperature variations. For example, when some liquid helium appears at the bottom of the cryostat, R_{bot}^{1K} becomes constant. The calibrated one has a resistance of 85Ω at $320K$, increasing to $47k\Omega$ at $1.4K$.

Another Cernox® is placed in the insulating vacuum, on a copper exchanger stuck at the beginning of the pumping line (R_{exch}). This one is calibrated too, and has never been displaced in several years, which makes it the most reliable and predictable low temperature sensor during experiments. For example, during helium filling of the cell, when this sensor indicates 4.2K, it means that the helium level has reached the extreme top of the cell.

Three Pt100 are on the external face of the liquid nitrogen jacket (T_{N_2}). They are placed in a similar way as the ones on the inner cell: one at the top, one in the middle, and one at the bottom. Usually, T_{N_2} is used to know when the intermediate screen has reached its temperature limit ($\sim 100K$), allowing the beginning of the helium injection to cool down the inner part of the cryostat. During experiments, when the inner cell has reached its lower temperature, the liquid nitrogen jacket temperature is measured to be between $90K$ and $95K$ depending on the altitude. As Pt100 can operate down to $73K$, which is below the temperature of boiling nitrogen ($77K$) these sensors provide accurate enough measurements, with a simple and standard calibration law.

The last temperature sensor is another Pt100, placed on the spinning gasket, which has to remain at room temperature. When cooling down the cryostat, a large amount of cold ($< 200K$) gaseous helium can be pumped. This can lead to water condensation and freezing on the pumping line, at the top of the cryostat. Thus, it is necessary to control the temperature of the spinning gasket so that it does not stick and break because of ice. This last sensor is connected to a thermal regulator

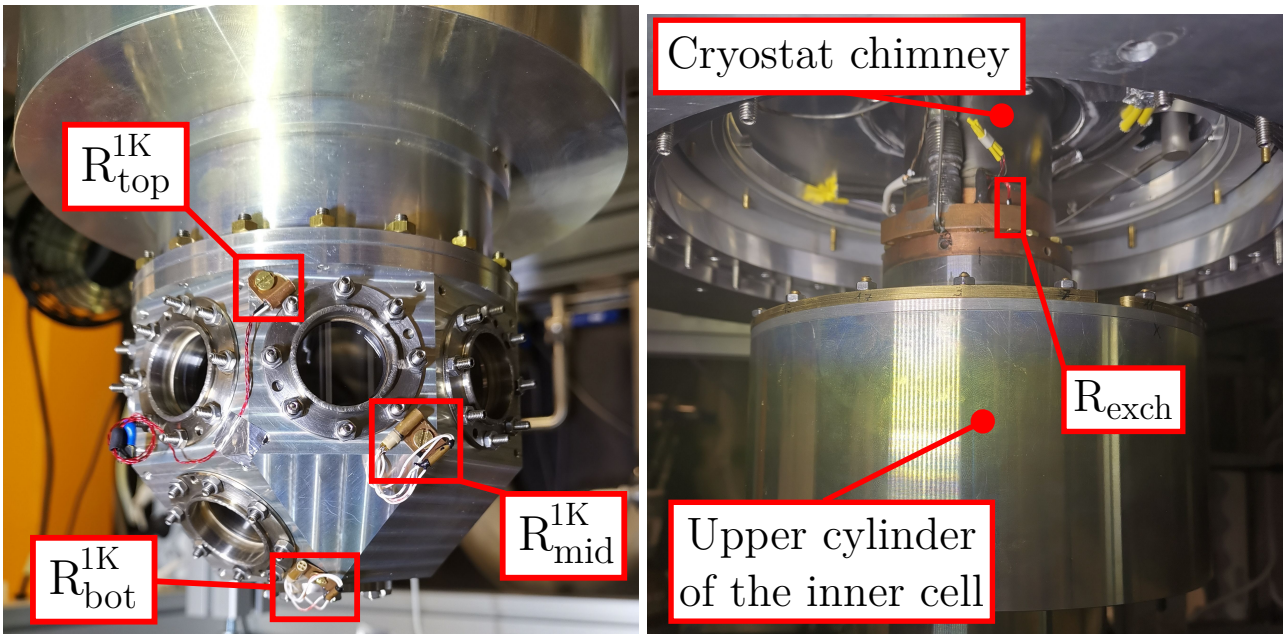

Figure 2.24: Photographs of the inner cell of the cryostat. The three temperature sensors Cernox® are highlighted. R^{1K}_{top} and R_{exch} are the only calibrated ones, which means that the two others only give a resistance which follows a similar trend as the temperature.

which controls heaters stuck on the spinning gasket (fig. 2.11, left). When the temperature reaches $15°C = 288K$, the heaters are activated until the temperature rises above $20°C = 293K$.

All these sensors are wired using thin ($\varnothing 100\mu m$) constantan wires ($\sim 50\Omega/m$) in order to avoid heat transfers from the laboratory room. In the case of the R^{1K} sensors, a thermalisation coil ($77K$) has been implemented on the intermediate shield. The resistances are measured using an AC 4-wire measurements to avoid thermo-electrical biases and discard the wires resistances. We typically use a polarisation current of $\sim 1\mu A$ which leads to a power dissipated in the resistance of the order of $\sim 1pW$, to avoid overheating the area we want to probe. All this is made possible thanks to three MMR3 (Resistance Measurement Module, featuring 3 channels) devices, developed in the Institut Néel and commercialized by Cryoconcept.

The pressure sensors are also crucial. As mentioned in section 2.1.2, the superfluid helium is operated at saturated vapor pressure. In other words, the helium in the bath and in the reservoir are constantly evaporating, and we can control the superfluid temperature by pumping on it. However, the helium reservoir should not be pumped below the atmospheric pressure as it is poorly sealed due to the cable gland of the helium injection inlet. That is why it is isolated from the bath during experiments by closing the cold valve, and the three way valve (fig. 2.1). In that case, its pressure is released to the room air through a safety valve.

Therefore, three numerical pressure sensors are used. One of them (Keller PAA-33X) has a pressure range of $[0; 1]bar$, and is strain gauge based. It is connected to the reservoir, allowing the observation of a constant pressure when helium is confined, evaporating slowly through the safety valve. If the pressure increases too much, this is a sign of the safety valve being inoperative (stuck by ice for example), and this could lead to the explosion of the cryostat. The pressure in the cell is monitored by two other sensors connected to the pumping line. One is the same as the one used in the reservoir, and the other (Keller PAA-44X) has a pressure range of $[0; 100]mbar$, and uses the capacitive technology. This low pressure probe is essential as helium is operated at saturated vapor

pressure. The temperature of the helium bath is directly related to the pressure in the cell (Fig. 2.5), and He II is obtained for pressures below $SVP(T_\lambda) = 50.4mbar$. Thus, the range of this sensor is ideal for precise pressure measurements in the CryoLEM cell. Moreover, in order to keep our system as stable as possible during experiments, the low pressure sensor is used to control the regulating valve mentioned in section 2.1.2.

At last, the cryostat is equipped with 3 liquid level sensors : one in the helium bath, one in the helium reservoir, and one in the nitrogen reservoir. The first two are superconducting gauges made of niobium-titanium (Nb-Ti). The part of this gauge that is immersed in liquid helium ($T < 4.2K$) becomes superconducting, while the rest stays resistive. Thus, the total resistance of the gauge gives the helium level: the resistance varies between 120Ω (empty) and 60Ω (full). However, these gauges have not been calibrated, and the one in the experimental bath only covers the upper cylinder in order to avoid alterations of the experiments made in the lower part. This is why T_{exch} is often used to know when the experimental cell is filled, as mentioned above.

In order to measure the resistance of these gauges, a current of $\sim 80mA$ is supplied, resulting in a global heating of the sensor. During experiments, the usual resistance of the gauge is about $\sim 80\Omega$, so the heating power injected is $512mW$, which is a large value in a cryostat at $2K$. This heat is only dissipated in the gaseous helium above the liquid bulk, as the immersed part is in superconducting state. Despite this, our temperature sensors on the walls of the cell measured an increase of $\sim 5mK$ during the measurements. If the temperature of the liquid helium II bulk instantly comes back to equilibrium when the measurement stops, the walls of the cell have an inertia. Thus, the difference of temperature between the walls and the superfluid produces a counterflow which is visible on the particle motion. This is why the liquid helium level measurement (LHLM) sensors are not used during image acquisitions. This is actually favorable, as less heat is injected in the cryostat, resulting in a longer lifespan of the liquid helium.

The temperature of liquid nitrogen being too high to reach superconductivity of Nb-Ti wires ($T_{N_2}^{g\leftrightarrow l} = 77K > T_{crit}(Nb-Ti) \simeq 10K$), a homemade sensor have been experimented. This gauge is made out using a sealing joint for electronic boxes. To ensure their mass continuity this rubber bond is loaded with graphite. The temperature affects the resistance of this "wire" and gives a continuous image of the liquid nitrogen level. The resistance of this gauge between $3k\Omega$, when the cryostat is empty at room temperature, and 5150Ω when it is full, just after the nitrogen transfer. This sensor is not calibrated either, and highly non-linear. Consequently, it only gives us a rough idea of the liquid nitrogen level. In practise, the nitrogen reservoir is full when it overflows, and empty when the temperature of the jacket, measured by the Pt100 mentioned above, starts to increase.

2.4 Conclusion of this section

This section presents the first big part of the work presented in this thesis. In 2017, the basis of the CryoLEM was already in place: the modified orange cryostat was fixed (and carefully centered) on the spinning table, and the pumping line (including the spinning gasket, and the pump itself) was connected to it. The work accomplished made it possible to move from an innovative cryostat concept to a concrete and functional system (visible on fig. 2.25).

During this thesis, the cryostat cell has been closed, and its functionality and autonomy have been tested, and validated. The protocols to cool it down, and the routine to perform experiments for several days have been established. The system has also received several improvements on many aspects: a PID-controlled valve for pressure regulation, a rigidly fixed optical system, two pressure regulators for the particles injection, and a counterflow channel for future experiments. All these devices are remotely controlled through the laboratory's local area network. For this purpose, some LabVIEW user interfaces have been developed, allowing to monitor and control the whole system.

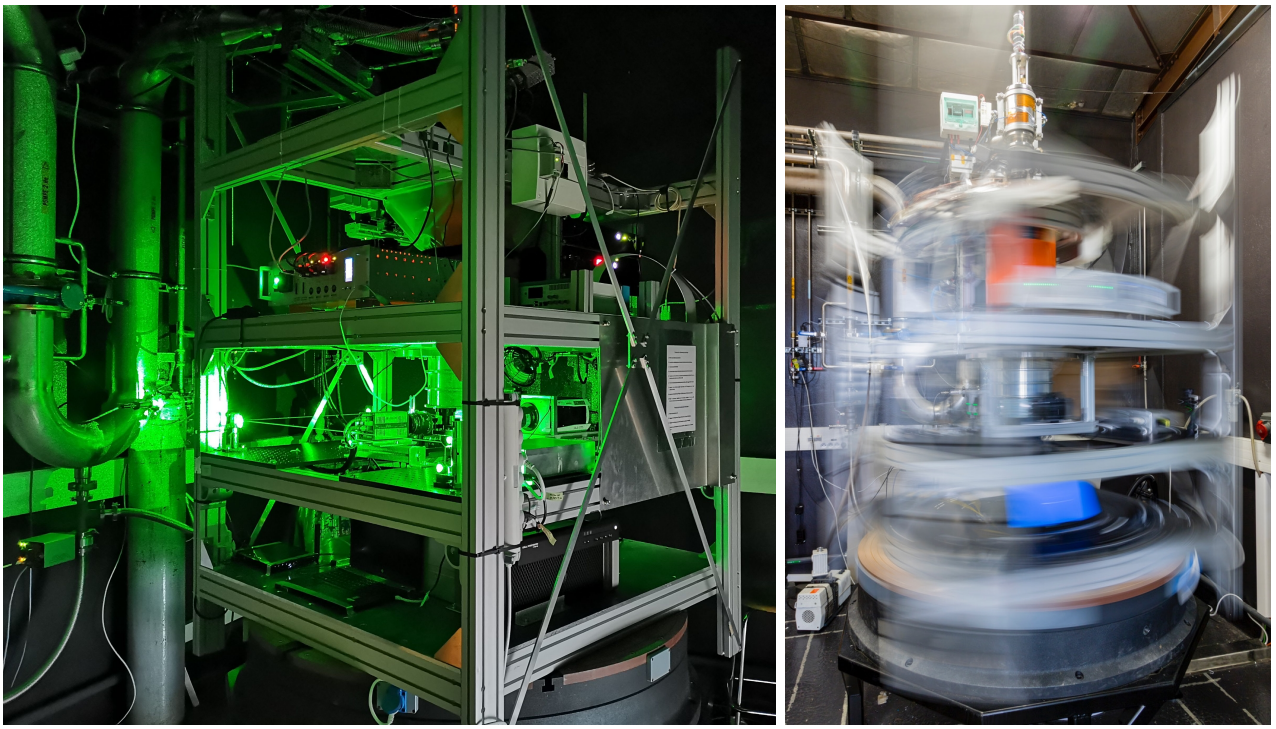

Figure 2.25: Left: Photograph of the system during an experimental session. The lights have been switched off to minimize optical perturbations in the system. Note that all the devices are rigidly fixed to the spinning structure. The parts at the top are hidden here, but they have already been shown on figure 2.11. Right: Long exposure photograph of the system while spinning. It highlights the rotating and static parts.

Preliminary experimental sessions have also been carried out, and were focused on studying the formation of frozen deuterium particles by injecting a hot ($300K$) gaseous mixture directly in helium II ($< 2.17K$). By regulating the injection pressure, it is possible to reduce the injection flow rate, and the size of the particles. The dependence of the particle size on the flow rate has not been thoroughly answered, and some questions remain on the particle formation. However, we showed that the current (convenient) injection protocol allows the production of micron-sized particles that can reliably trace the movement of the fluid, hence producing quality data.

This new apparatus mixes the new cryogenic technologies and measurement methods of the 21^{th} century, with one of the most canonical experiments on liquid He II: the rotation. The modularity of the CryoLEM allows the installation of different types of forcing, for a deeper exploration of the properties of quantum turbulence, with or without global rotation. The CryoLEM is expected to operate for the next decades, and help answering modern problems on quantum and classical turbulence.

Chapter 3

Particle tracking velocimetry

This chapter describes the MATLAB code, developed during this PhD thesis, used to process the recorded images. This code takes as input the images of particles in a fluid recorded by a single camera. The result is a structure containing 2D trajectories of the particles in the plane delimited by a laser sheet.

3.1 Particle Detection

The first step of our tracking program is to detect the particles on the raw images. The particles are enlightened by the (left) side of the image and reflect the laser light. Consequently, they are recorded as bright objects on a darker background. However, the background is not completely black due to particles scattering light on the walls of the CryoLEM. Some pre-processing is done to darken it and obtain contrasting particles. A first approach could be to take a single shot of the background before injecting particles. However, the presence of particles provokes additional reflections. Thus, the first hundred images of each acquisition sequence are used to compute a median image. The median of each pixel of these images is computed and the result is subtracted on all the images of the aforesaid sequence (Fig. 3.1). This relies on the hypothesis of a low particle number density: most of the time, each pixel records the background, and sometimes a particle passes in front of it. The median has the advantage of being less subject to variations due to extreme events (in our case: bright particles) than the mean, resulting in a more accurate background, even in the presence of particles. As shown in fig. 3.1 on the right, this simple and quick pre-processing can remove an heterogeneous background efficiently. On the luminosity profile, it is clear that the background is no longer brighter on the edges, and is set to 0. The 4 peaks correspond to the particles on this row.

This median computation may be more efficient if it was done using the whole sequence of images instead of the first hundred. But in that case, the process was unnecessarily long, and could lead to RAM overload due to the large amount of heavy images. It is also imaginable to compute a median for each image using for example the 50 preceding and succeeding images (time sliding median). Indeed, in some sequences, the density of particles is way higher in the beginning than in the end, resulting in a decrease of the background brightness. This time sliding median method has not been done due to computational costs. When subtracting the median of the first 100 images was not fully effective, some bright areas could sometimes remain, especially in the corners of the images. In these cases, a simple mask was applied to remove them at the cost of the loss of all data in these areas. This is a conservative approach to obtain quality data.

Once the pre-processing is done, the detection of the particles can start. MATLAB features a native function called "regionprops[1]", which can measure different properties of image regions. This works with binary (black and white) images, or with gray-scale images if the regions are explicitly

[1] https://fr.mathworks.com/help/images/ref/regionprops.html

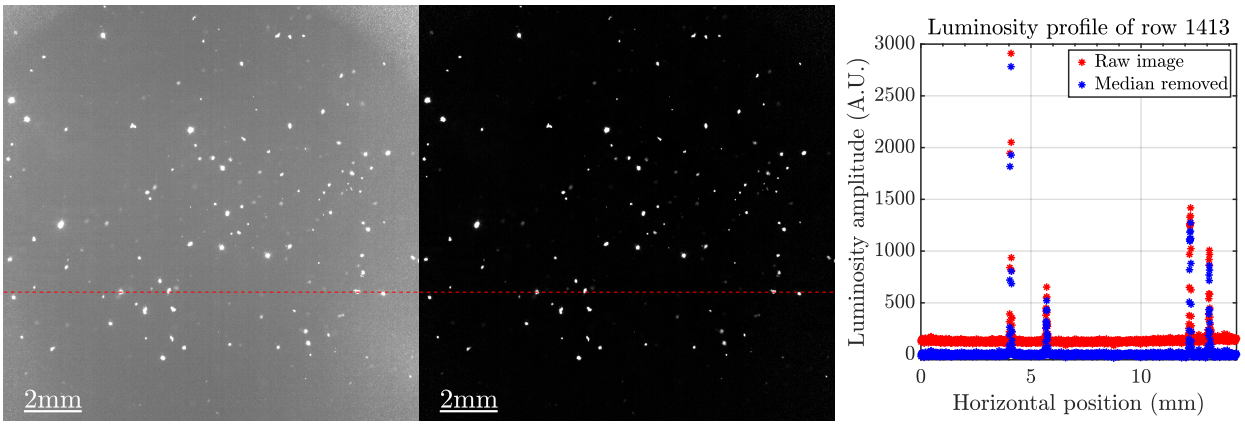

Figure 3.1: Left: Image #67 of a sequence recorded by the Zyla camera (raw). The red line highlights the row which is used to display the profiles on the right image. Middle: Same image, but the median of the first 100 images has been subtracted. Right: Profile of the row 1413 of both images.

specified (by a binary image). Thus, a threshold is applied to our pre-processed image in order to extract the bright regions corresponding to particles. This threshold is the first and most important input parameter of our detection algorithm, and is carefully determined by a "manual" investigation of a few images of each sequence.

This thresholding gives us a binary image which will be used to specify the regions of interest when using "regionprops". However, as the particles have irregular shapes, the light is not equally reflected on their surface. Thus, it often happens that some parts of the particles are darker than others, and in that case, it is imaginable that a single particle could be detected as two. In order to avoid that, we proceed to a dilatation of the binary image by a circle of radius 1. Thus, two regions which are close enough to each other (minimum distance < 2 pixels) can be reconnected into one. Then, the native function "imfill[2]" is used. It consists in filling a region of interest if there is a black spot in the middle of it. At last, the image is eroded by the same structuring element as the dilatation (circle of radius 1) in order to preserve the size of the particles.

After all these morphological operations, the function "regionprops" is used, returning several interesting outputs:

- Centroids: this is the position of the geometric center of each region.
- Area: the number of pixels of each region.
- Weighted centroid: this is the position of the geometric center weightened by the luminosity of the pre-processed image of each region.
- Mean intensity: the mean luminosity of the pre-processed image in each region.
- Eccentricity: this is the eccentricity of the ellipse of which has the same second-moments as the region.
- Orientation: this is the angle (in °) between the major axis of the just mentioned ellipse, and the horizontal axis. This angle is given in the interval $[-90 : 90]$.

The first two outputs can be computed only with the binary image, but the two latter use the luminosity, which is why the grayscale image has to be input. In practice, the unweighted centroids are unused, and the coordinates of the particles along their tracks will be based on the weighted centroids

[2]https://fr.mathworks.com/help/images/ref/imfill.html

(simply referred to as centroids thereafter). The area can be used to estimate the size of the particles. The last two parameters are used to characterize the elongation of the regions. For example, if the orientation of a particle is the same as the orientation of its velocity vector, this can be the sign of a too long exposure time, compared to the time needed for a moving particle to cross several pixels. The orientation and eccentricity have both been used in section 2.3.1 in order to discuss the impact of the exposure time on the particle size.

3.2 Tracking particles

3.2.1 Trajectories construction

Several tracking algorithms have already been developed many years ago, and some works to improve them are still ongoing, following the recent enthusiasm around artificial intelligence. During this thesis, we wrote our own tracking codes based on the existing 3 frames minimum acceleration mentioned in [145]. This technique can be considered as a standard technique nowadays, even though it is not the most accurate one. Considering the low number density we are working with, the performance of this algorithm is sufficient. Indeed, fig. 9 in [145] gives the tracking error as a function of $\xi = \frac{\Delta r}{\Delta 0}$, where $\Delta r \simeq \frac{\langle v \rangle}{f_{acq}}$ is the mean distance travelled by particles moving with a mean velocity $\langle v \rangle$ between two frames acquired at a frame rate f_{acq}, and $\Delta 0$ is the average separation between a particle and its closest neighbor on the same frame. $\Delta 0$ can be computed as $\sqrt{\frac{A_{FOV}}{N_p}}$, where A_{FOV} is the image area (2048×2048 pixels^2 in our case), and N_p is the average number of particles on each image. Considering the most unfavourable case we had during our experiments ($\Delta r \sim 5$ pixels, $\Delta 0 \sim 150$ pixels, ξ does not exceed 0.033. Thus, the tracking error we have in this case does not exceed 1%.

An illustration of the main part of the algorithm is shown on figure 3.2. The algorithm proceeds frame by frame. Let's describe the building of the track k, already containing n points, at image number i. The 3 frames minimum acceleration algorithm estimates the position of the particle on the

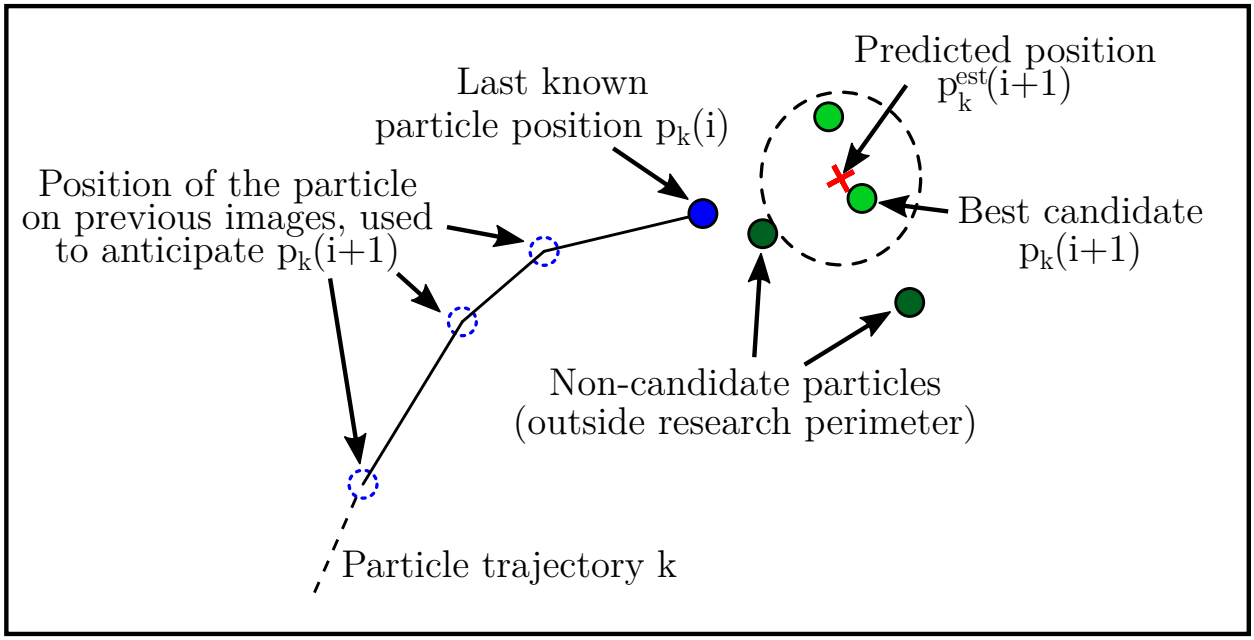

Figure 3.2: Illustration of the tracking algorithm. Knowing the past positions of a particle, the next position is estimated, and possible candidates are found in a research perimeter (dashed circle). The closest to the estimated position is saved in the track k for the image i+1.

image $i+1$ from the positions of the particle on images i and $i-1$. In our algorithm, we chose to estimate the velocity with more points (if available) in order to be less sensitive to noise. The maximum amount of points used to predict the next position is an input parameter called n_{Vest} chosen by the user, and usually set between 2 and 8. Using the predicted position, we define a research area which is defined by a second input parameter called r_{srch}. If there are particles in this area, the closest one is fit in the track k, which stays in the list of the tracks under construction.

The last input parameter is t_{skip} and allows the code to keep a track under construction if a particle has been found less than $t_{skip}+1$ images ago. In other words, we consider the possibility for a particle luminosity to go below the threshold for a maximum duration of t_{skip} frames, then come back above and be reconnected to its track. Usually, this parameter is set to 1. Thus, if no particle is found in the area of research on image $i+1$, the track can stay under construction and try to find a matching particle on image $i+2$. In this case, the predicted location of the particle is moved, using the same velocity estimation, but with a twice larger time interval. If a matching particle is found on image $i+2$, then the track is filled at $i+1$ by linear interpolation between i and $i+2$. A flag is set on these these "invented data points" in order not to take them into account in the velocity statistics.

As just explained, a track is definitely closed when matching particles are missing for more than t_{skip} images. But on the other hand, after processing all the tracks under construction, some "orphan" particles remain. They are used to create new tracks which will be processed at the next iteration (image $i+2$). As these tracks contain only one point, it will not be possible to estimate the velocity of the particle to predict the position of the second point. Then, the research area for matching particles will be centered on the particle position at i (zero velocity).

All images of a sequence are processed this way, and the resulting tracks are stored in a MATLAB structure. Each row of this structure contains a track, and this track contains data of time and position, and the data resulting from the "regionprops" function (mentioned in the previous section), such as area and luminosity of the followed particle. At this stage, velocity and acceleration have not been computed yet, and another remaining question is the choice of the input parameters by the user. These topics are covered by the two following subsections.

3.2.2 Tuning the tracking input parameters

First of all, let's recapitulate the input parameters and their impact on the algorithm:

- r_{srch} is the radius of the circle in which the next position of a tracked particle will be searched.
- n_{Vest} is the number of (past) points used to estimate the displacement of a particle between two frames.
- t_{skip} is the time (in frames) allowed for a particle to go out of the laser sheet without being disconnected from her track.

The latter is by far the easiest one to tune as it has always been fixed to 1. This parameter is made to allow the formation of long tracks, even if a particle is misdetected by artificially creating a fake point. As we trust our detection protocol, the use of this trick must remain marginal. Moreover, the fake points are not taken into account in the statistical studies, which is why the benefit of a reconnection between two small tracks is limited. In fact, the main benefit of a reconnection is to limit the number of small tracks that disappear in the filtering process detailed in subsection 3.2.3.

The choice of r_{srch} and n_{Vest} is more complicated as the tuning of these parameters should depend on the experimental conditions. Indeed, in the case of a perfectly laminar flow seeded with perfect tracers and a zero-noise optical detection system, $r_{srch} \ll 1$ and $n_{Vest} = 1$ would be sufficient to observe smooth streamlines. However, the turbulent flows studied in the CryoLEM are less predictable, because of the fluctuations of the fluid dynamics, the irregular particles shape, and the imperfections of the acquisition system.

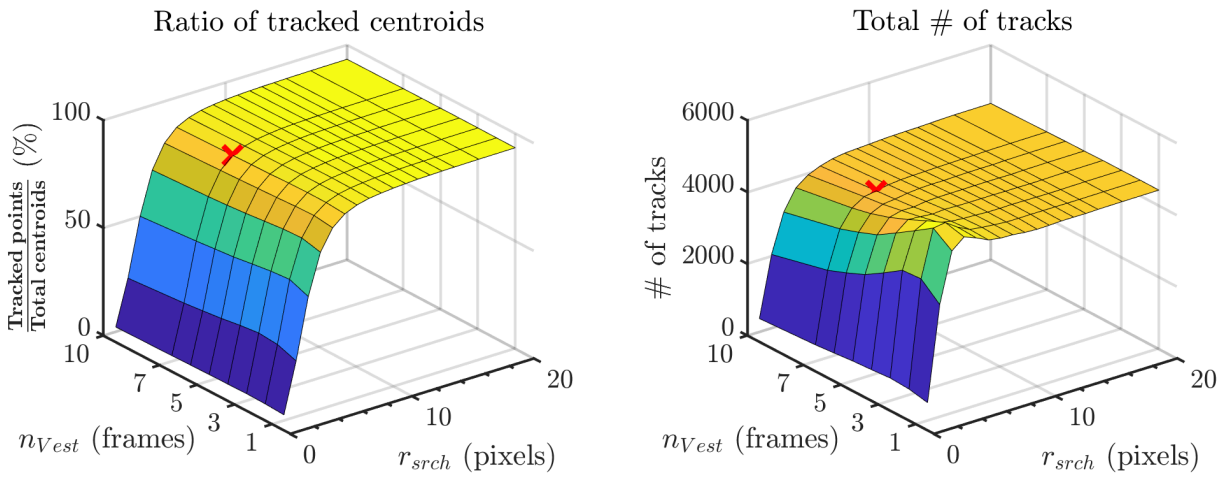

Figure 3.3: The different indicators used to characterize the tracking quality of the algorithm, based on the input parameters. The objective is to maximize the amount of quality data for future statistical studies of the particle dynamics. Thus, the best values for the parameters will maximize the number of tracked points while minimizing the amount of tracks. The selected values are indicated by the red cross (×): $r_{srch} = 6$ and $n_{Vest} = 7$.

Therefore, r_{srch} and n_{Vest} are tuned experimentally. The tracking of the centroids for each movie is repeated for several values of r_{srch} and n_{Vest} (fig. 3.3). In order to limit the computational cost, this test is not performed on the complete movie, but only a few thousands of frames. For example, on the figure 3.3, the frames 6000 to 9000 out of 15000 have been tested with 17 values of r_{srch} and 8 values of n_{Vest}. The movie used to generate this figure is an observation of particles of deuterium stirred by a turbine rotating at $6RPM$ (in the frame of the laboratory), in the CryoLEM counter-rotating at $6RPM$ (movie #40 in table A.6, more details in section 4.3). It has been recorded long enough after the start of the actuators to be considered stationary, hence the use of a sub-interval of time. Two quantities are observed as indicators of the tracking quality:

- The amount of centroids which found their place in a track of more than 10 points. This parameter actually reflects the tracking efficiency: the more tracked centroids, the better are the parameters.
- The total number of tracks. A large amount of tracks often corresponds to short tracks. By maximizing the number of tracked centroids, while minimizing the number of tracks, we make sure to have long and reliable tracks.

The figure 3.3 shows the typical trends observed for a large majority of the movies. On the left, the ratio of tracked points compared to the initial amount of detected centroids is shown. There is a strong influence of r_{srch} up to a certain value, but the influence of n_{Vest} is less pronounced. The number of tracked points increase with r_{srch} up to a certain value (linked to $\Delta 0$), after which a plateau is observed. This is due to the fact that if there is at least one particle in the research radius, then it is paired with the track. Thus, after a certain value of r_{srch}, the tracking algorithm will converge to a stable configuration of tracks. In this case, the only reason why the construction of a track would stop is if there are less points on image $i+1$ than on image i. Otherwise, the tracks will keep growing as they will always find a matching particle on the following frame. Actually, the flat part of these graphs is attributed to "wrong connections" in the tracking process: independent tracks are mistakenly connected together because r_{srch} is too large.

On the right hand side graph, a bump is visible and it coincides with low track length values (not shown here). This bump often appears at low values of r_{srch} and n_{Vest}, and it shows that the parameters are too restrictive to produce good connections between the tracks. The final values of

Tracked interval (frames)	r_{srch}	n_{Vest}	Tracked centroids	Points per frame	Mean tracks length	Number of tracks
[6000; 9000]	6	7	87%	84	60	4225
[1; 15000]	6	7	86%	98	57	26090

Table 3.1: Results of the tracking algorithm with different parameters. The movie used to generate these tracks is the same as the one used in figure 3.3. The tracking algorithm with the parameters obtained from the study of a sub-sequence is applied to the whole movie. The results are consistent, showing the good representativeness of the sub-sequence, and the steadiness of the data.

the parameters will not be chosen in this region, because the objective is to minimize the number of tracks, in order to have the longest ones.

To sum up, in order to maximize the data quality, we need to avoid the plateau corresponding to wrong reconnections, and the bump in which the tracks are too short, while maximizing the number of tracked centroids, and minimizing the number of tracks. Thus, on figure 3.3, r_{srch} is selected at the slope change on the left hand side graph. We choose $r_{srch} = 6$ to have the maximum amount of data, while keeping the quality.

Once r_{srch} has been selected, n_{Vest} is selected by minimizing the number of tracks. Sometimes, this quantity is minimized for the supremum of the investigated n_{Vest} (as on figure 3.3, right). This means that the real minimum, if it exists, would be located out of the bounds. As previously mentioned, n_{Vest} acts like a smoothing filter. A large n_{Vest} could lead to a track loss if the particle abruptly accelerates. This is why n_{Vest} never exceeds 8. This value has been decided base on the typical values of the smoothing kernel size which will be discussed in section 3.2.3. In this case, we chose $n_{Vest} = 7$. The selected values of r_{srch} and n_{Vest} are indicated by the red cross ($\times$) on each graph of fig. 3.3.

With these selected parameters, the entire movie has been tracked, expanding the process tested on our interval of 3000 images. The values of the tracking quality indicators are shown in the table 3.1 for the studied sub sequence (images 6000 to 9000), and the whole movie. There is a good agreement between them, showing the good representativeness of the sub-sequence, and the steadiness of the data. The largest deviation is observed for the number of particles per frame. Indeed, the only unsteady quantity is the amount of particles, because non neutrally buoyant tracer particles (D_2) are used. Thus, the number of visible particles decays over the movie, which is unavoidable.

However, some of our experimental sessions were focusing on decaying flows for example (section 4.1), and in this case, the results of the tracking tests could be completely different depending on the interval of time used. In these cases, the tracking tests were done right after the disturbance, where the particles have the largest velocities. This results in "permissive" (high) values of r_{srch} and n_{Vest}, which could lead to wrong connections (in minority) in the steady part of the movie, but allowing a faithful study of the unsteady part.

3.2.3 Velocity computation and filtering

Velocity and acceleration are key measurements in the study of turbulence. In our data processing routine, these values are computed as time derivatives of the position. This results in an amplification of the experimental noise, and requires high acquisition frequencies. As our camera is limited to $52Hz$, acceleration signals were too noisy to be useful, which is why we focused our analysis on the velocity statistics. Acceleration is, of course, a very interesting quantity, but new measurements with higher frame rates (using the Phantom v311 camera) are necessary to go beyond the results presented in this thesis.

In order to reduce the impact of noise on the data, the position signals (horizontal and vertical) of each track are convoluted with a gaussian kernel [146]:

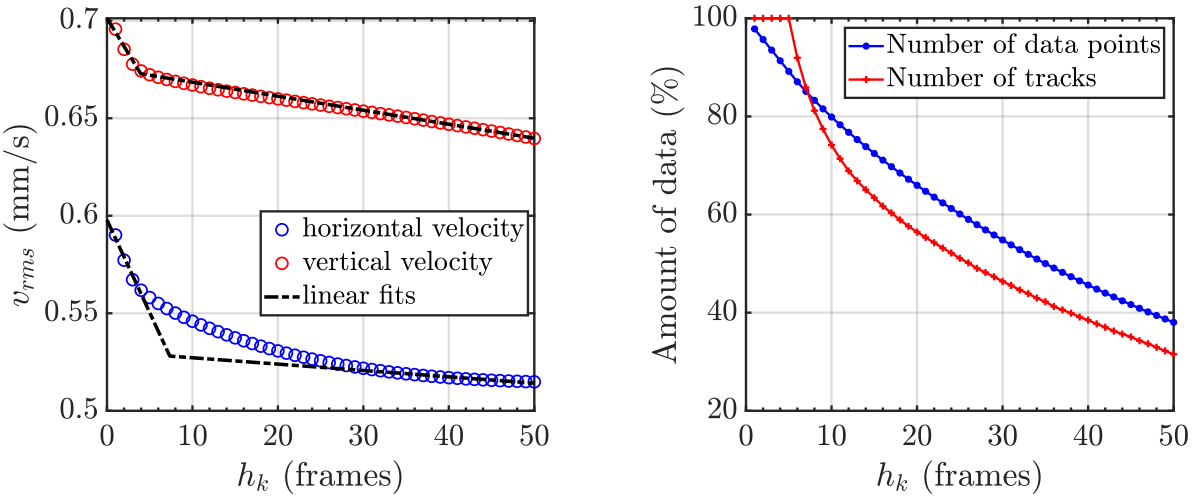

Figure 3.4: Impact of gaussian kernel smoothing on the root mean square velocity and on the amount of available data of a data set. This data set has been collected at $f_{acq} = 52.34Hz$ using deuterium particles in helium II at $2.087K$. A propeller is stirring the fluid at $3RPM$ in the cryostat counter-rotating at $3RPM$ (movie #40 in table A.6).

$$G_0(t) = \frac{1}{S_0} exp\left(-\frac{t^2}{2\sigma_k^2\tau^2}\right) \tag{3.1}$$

S_0 is a normalization factor (which depends on σ_k and τ), and $\tau = \frac{1}{f_{acq}}$ is the time interval between two frames. Note that, in practice, t is a discrete time corresponding to the time at which a frame is acquired. This kernel has a width characterized by its standard deviation σ_k, and a length l_k which corresponds to the interval of $\frac{t}{\tau}$ (which is an integer) for which the gaussian is computed. In order to simplify this two-parameter problem, we set $l_k = 6\sigma_k$, by analogy with the 99% confidence interval (three sigma) of the normal distribution. The velocity is obtained by convolution with the derivative of G_0:

$$G_1(t) = -\frac{t}{\sigma_k^2\tau^2} G_0(t) \tag{3.2}$$

In practice, l_k is forced to be odd so that the central point of the gaussian is always included in the discretization. Thus, l_k can be written as $l_k = 2h_k + 1$. During the convolution process, the h_k first and last points of each track are lost. Consequently, all tracks containing $2h_k$ points or less disappear. It is clear that h_k must be chosen high enough to remove noise from the data, but low enough to save as much information as possible.

In order to determine the best value of h_k, tracks have been smoothed multiple times with different kernel size and the influence on the velocity fluctuations ($v_{rms} = \sqrt{< v^2 >}$) are observed [147]. The example shown in fig. 3.4 is a movie in which particles of deuterium are stirred by a turbine rotating at $3RPM$ (in the frame of the laboratory), in the CryoLEM counter-rotating at $3RPM$ (movie #39 in table A.6, more details in section 4.3). The convolution process used here is a low pass filter: the velocity fluctuations (high frequency) are more and more damped with increasing h_k, which is why the root mean square velocity decreases. The typical shape of this graph is a succession of two slopes [65]. The first slope corresponds to the filtering of the high frequency experimental noise, which we want to remove. The second slope corresponds to the effect of the filtering on the actual signal, which we want to preserve. Thus, it seems reasonable to keep a value of h_k close to the junction of these slopes. However, the crossing of the slopes for the horizontal and vertical velocity do not always occur for the same h_k (respectively 4 and 7 in this example). In this case, h_k will be taken equal to 7, in order for

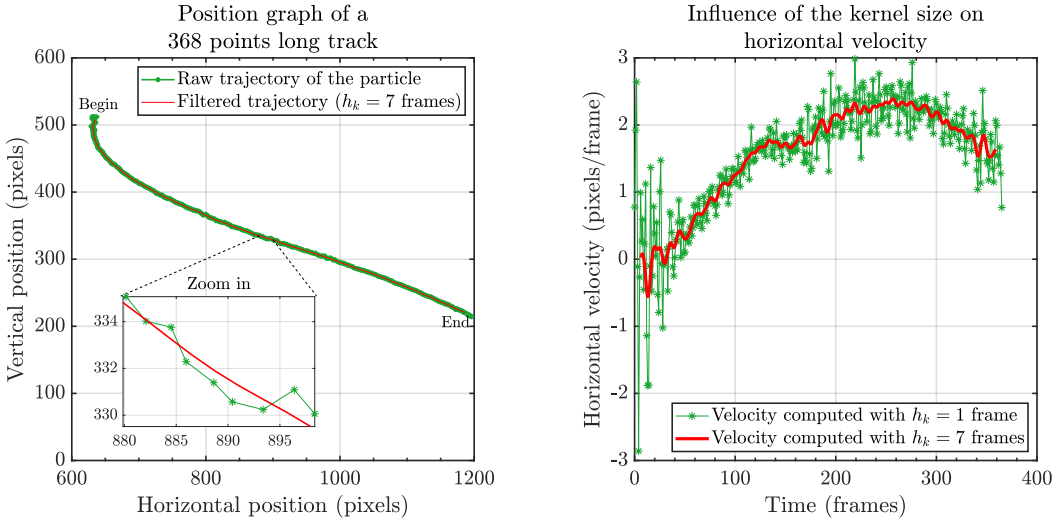

Figure 3.5: Impact of gaussian kernel smoothing on a track extracted from the data set mentioned in fig. 3.4.

both values to be free from noise. With this value, more than 80% of the data remains (fig. 3.4, right). The effect of the smoothing on a single track of this data set, with $h_k = 7$ frames is shown in fig. 3.5. This process is applied to all of our data sets.

3.3 Possible improvements

As the development of these algorithms have been done by non-specialized programmers, it would be presumptuous to say that they are perfect. Several improvements can be found at each stage of the process. For example, we already mentioned the possibility to compute a background on several sub-sequences of the movie, instead of the first 100 images, in order to take into account the luminosity change due to the settling of particles.

The most important problem of this tracking process is that it requires two interventions of the user: the threshold for particle detection is manually selected, and so are the parameters r_{srch} and n_{Vest}. This results in a loss of a time, a tedious task for the user, and a non-deterministic selection of the parameters, as the human judgement is involved. Thus, it is worth considering the automation of these two steps. The selection of r_{srch} can be automated quite easily, as it mostly consists in finding a change of slope in the graphs depicted in figure 3.3. The choice of n_{Vest} follows directly as the only requirement is to maximize the tracking quality indicators (fig. 3.3). In order to find the threshold for particle detection, the use of peak detection functions can be imagined, such as the "findpeaks[3]" native MATLAB function. In that case, it is also possible to have a non-constant threshold, varying in time and space.

Many improvements can be done in the tracking process. For example, when a track k is being built, and found a matching particle on the image $i + 1$, this particle can already be attributed to another track j. In this case, the particle can be attributed to k if the particle is closer to the expected position of k at $i + 1$ than the one of j. Otherwise, the particle stays attributed to j, and k is not matched with any particle. Instead of this, it would be interesting to test the possibility of a match with the second nearest particle. A nice improvement would also be to give priority to the tracks which have not skipped the last frame (use of t_{skip}). In fact, this issue of pairing a group of tracks with a group of particles can be linked with a field of applied mathematics focusing on stable matching. A reference in this field is the algorithm of Gale and Shapley [148] which allows to find a stable

[3]Details here: https://fr.mathworks.com/help/signal/ref/findpeaks.html

solution which matches students and their future college, based on the preferences of both groups. An implementation of this algorithm is perfectly conceivable in the tracking process, and could give better matching between tracks and particles.

In general, the different algorithms could run faster with the use of parallel computing. Despite a few attempts, we did not manage to implement it yet, as it requires independence between iterations of the for loops. This seems reasonably easy to do for the image processing which extracts the centroids as all images are independent. However, our tracks are built in a sequential way, and the list of tracks in construction changes at each iteration (frame). Thus, it seems hard to compute the tracks in parallel without changing the whole structure of the algorithm.

Heavier implementations are also possible using other more efficient tracking algorithms like the ones listed in [145]. It seems that the key to further improve our tracking algorithm is to start looking further in the future, i.e. taking into account acceleration changes by looking at image $i + 2$. This would obviously increase the algorithm complexity, but it could solve some (rare) observed issues. In several data sets, if we give a closer look to the tracks containing extreme accelerations, we realize that they are often due to tracking errors. For example, if two particles have crossing trajectories, the code can exchange the tracks, leading to a suddenly high acceleration at the crossing point.

In conclusion, our tracking algorithm will never be perfect as long as technological improvements will occur in computer science. Particle tracking algorithms are improved every day by dedicated researchers [149]. However, the important point is to have a tracking solution which gives good results in our experimental conditions (2D, low seeding, cryogenic environment...). In a cryogenic environment, the development of particle tracking algorithms appear secondary regarding all the other improvements which can be done, such as better seeding particles, implementation of 3D visualization, thermal insulation with powerful lighting...

Chapter 4

Experiments

In the following, the reduced 2D cylindrical coordinates $(r.\overrightarrow{e_r}, z.\overrightarrow{e_z})$ are used. $\overrightarrow{e_r}$ is the unit vector of the horizontal axis, and $\overrightarrow{e_z}$ is the one of the vertical axis (parallel to the rotation axis). The velocity of a particle is noted $\overrightarrow{v} = v_r.\overrightarrow{e_r} + v_z.\overrightarrow{e_z}$. In some figures, the notation v_i is used to denote v_r or v_z (specified in the legend). Besides, $< X >$ denotes spatial and ensemble averages, and $\overline{X}$ denotes a temporal average of the variable X.

4.1 Characterization of transient states

The objective of the CryoLEM is to study turbulent flows of superfluid helium through visualization. As the data obtained from these methods is heavy, the duration of an observation cannot exceed a few minutes. In that case, the question of stationarity is raised. How can we be sure that our measurements contain statistically stationary data? The transient states can come from three main sources:

- The particle injection: at first, particles were injected without pressure regulation, leading to high flow rates in the injecting pipes. Therefore, particles had a large residual velocity when reaching the field of view. Once pressure regulation has been implemented, the residual velocity of the particles was not sufficient to produce an homogeneous seeding. Thus, the fluid was stirred by a flat propeller (see fig. 2.14), which was stopped once the seeding was considered homogeneous, according to the protocol described in section 2.3.1. In that case, the recording of the data could not start before the decay of the stirring.

- The forcing: in the case of a continuous forcing, it takes some time for the whole fluid bulk to be set in motion. For example, the Ekman time introduced in 1.3 characterizes the time needed for a fluid in a rotating bucket to reach the solid body rotation regime.

- Other perturbations. In the case of the CryoLEM, it has been often produced by the liquid helium level measurement gauge. In order to measure its resistance, an intense current is supplied, leading to a heating which is dissipated in the gas above the liquid. This heating was provoking anomalous vigorous particle motion. To avoid this, no measurement were done during data recording.

During this Phd thesis, two kinds of forcing were used: the rotation of the system, and the rotation of a propeller. The objective of this section is to compare the time constants of both of these flows, measured through visualization, with the Ekman time constant (eq. 1.31), and the empirical time constant proposed by Tsakadze and Tsakadze (eq. 1.36). These time constants will be determined for different angular velocities, and different pressures corresponding to different viscosities (as explained in section 2.1.2). The transient states will be investigated in three different setups:

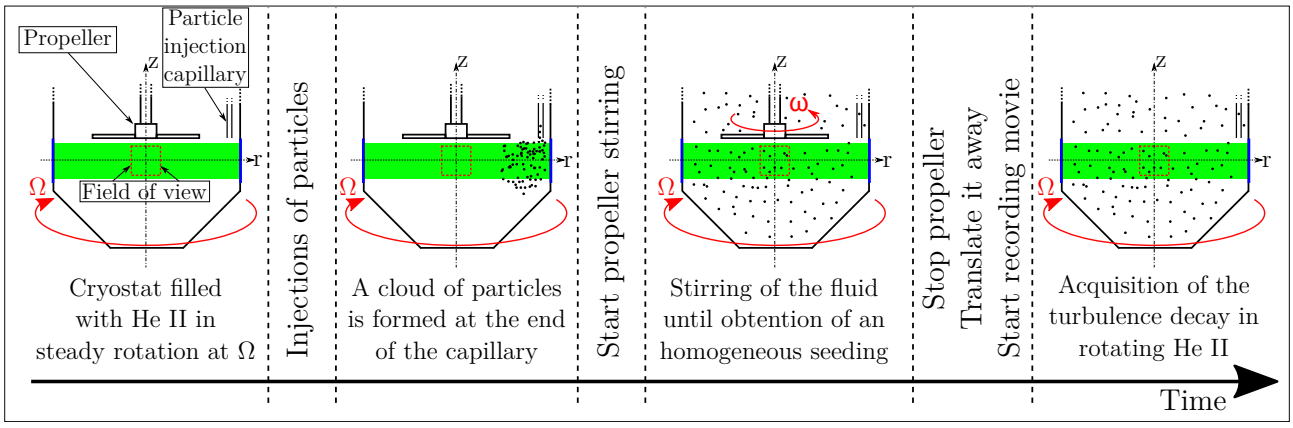

Figure 4.1: Description of the protocol used to study the stirring propeller decay. Note that the propeller is fixed to the rotating frame, which means that when $\omega = 0$, it actually rotates at $\omega = \Omega$ in the laboratory frame. Particles are injected in solid rotating He II. Then, the propeller is set in rotation at $\omega = 0.95Hz = 57RPM$. When the seeding is homogeneous, the propeller is stopped, and translated away from the field of view, and the acquisition starts for 30000 images at 52 frames per second.

- The cryostat has been constantly rotating for a long time (stationary), and the flow has been seeded with particles while the stirring turbine was on. The stirring turbine is stopped, and the acquisition starts (decay from a turbulent flow to rigid body rotation).
- The cryostat has been constantly rotating for a long time (stationary), and the flow is seeded with particles. The rotation is suddenly stopped and the acquisition starts (decay from rigid body rotation to rest: spin down).
- The cryostat is at rest and seeded with particles. The rotation is suddenly started and the acquisition starts (development from rest to rigid body rotation: spin up).

4.1.1 Decay of the stirring turbine

Here is developed the study of the decay of particles' motion after stopping a stirring turbine controlled by a stepper motor (detailed in section 2.2.2) in the CryoLEM spinning at a rate Ω (fig. 4.1). During particle injection, the turbine is set in rotation at $\omega = 0.95Hz = 57RPM$ in the rotating frame of reference. Then, the motor is stopped, the propeller is translated $\sim 6cm$ above the field of view, and the camera starts recording right after ($t = 0$). This experiment has been done 21 times with Ω set between 0 and $15RPM$. The influence of the superfluid ratio will also be investigated as the pressure has been changed on four movies. An overview of the experimental conditions of all movies is available in the table A.1 of the appendix.

This experiment corresponds to the decay of the turbulent flow produced by the propeller, in a rotating frame of reference. Similar experiments have been done in water tanks. For example, in [150, 151], they study the decay of the turbulent flow generated by a pulled grid in rotating water tanks. In [151], they identified two decay regimes. In the first one, the mean square velocity decays as t^{-n}, with $n = 1.22 \pm 0.05$. This is in very good agreement with the $n = 6/5$ exponent predicted by Saffman for an isotropic and unbounded decaying turbulence [152]. After 0.4 tank rotation, the contribution of the rotation dominates the contribution of the grid (low Rossby number): the flow becomes anisotropic, and the decay law becomes slower, with an $\Omega^{3/5}t^{-3/5}$ decay law, as proposed by Squires et al. [153].

The processing used in [151] has been applied to our data, using a normalization suitable to a propeller forcing. As the propeller used is flat, the forcing is purely radial, and we expect a strong

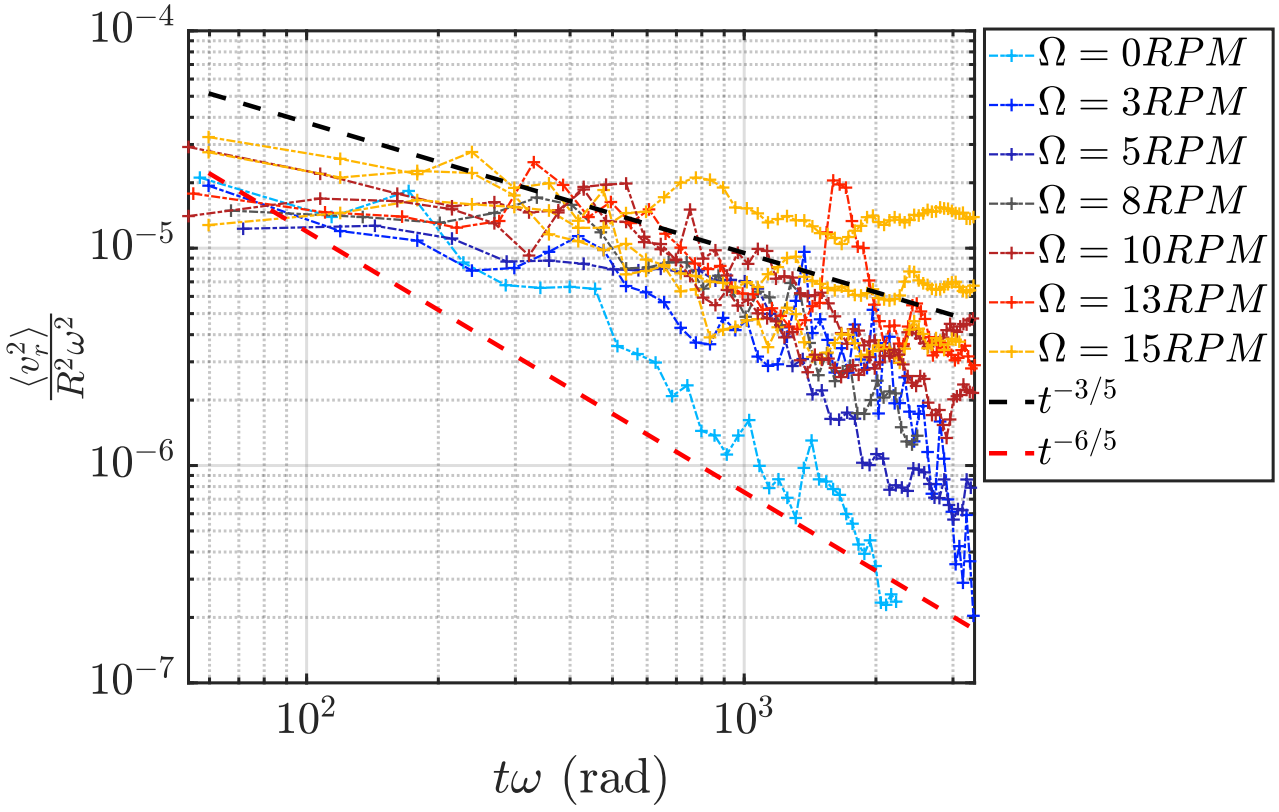

Figure 4.2: Decay of the horizontal mean square velocity as a function of time, with different angular velocities of the spinning structure. The end-of-blade square velocity of the propeller is used to normalize the vertical axis. Its radius R is $34mm$, and its angular velocity ω is always equal to $0.95Hz \simeq 6rad/s$. According to [151], a $t^{-6/5}$ scaling, followed by a $t^{-3/5}$ one should be observed.

anisotropy, leading to a $n = 3/5$ scaling. However, this is not observed, as shown on figure 4.2. Moreover, the decay in [151] was slowing down (reduction of n), whereas in our case, it accelerates. Indeed, for small values of $t\omega$, the slope is decaying with an exponent $n < 3/5$. After $t\omega \simeq 100$ various exponents are observed, but none of them follow a 3/5 nor 6/5 exponent scaling. Moreover, the $\Omega = 15RPM$ curve of fig. 4.2 with the largest final value almost does not decay because of the presence of large amplitude oscillations at the end. These oscillations are the cause of the discrepancies in the final values, and they will be further discussed in the section 4.2.1 dedicated to the steady rotation of helium II.

Different exponents ($n \in [1:2]$) depending on the angular velocity of the tank were also observed in [150] and attributed to confinement effects. These effects are expected to show up in the CryoLEM, leading to a non-conventional scaling. Moreover, the use of a pull grid produces fairly homogeneous isotropic turbulence, which is not the case with our propeller. Our forcing creates an anticyclonic flow (the turbine spins against the cryostat) known to be unstable [151]. In addition, the final value of the mean square velocity is also affected by an oscillating motion of the particles. Thus, a precise study of the turbulence decay laws is not possible with our data. Nevertheless, the objective of the data sets presented here is to determine the time needed for the CryoLEM to return to a steady state after a particle injection. This is why a simpler approach using exponential fits will be used to determine the characteristic time of the transient state.

In this study, each data set is divided into sub-sequences. In each of these sub-sequences, the mean

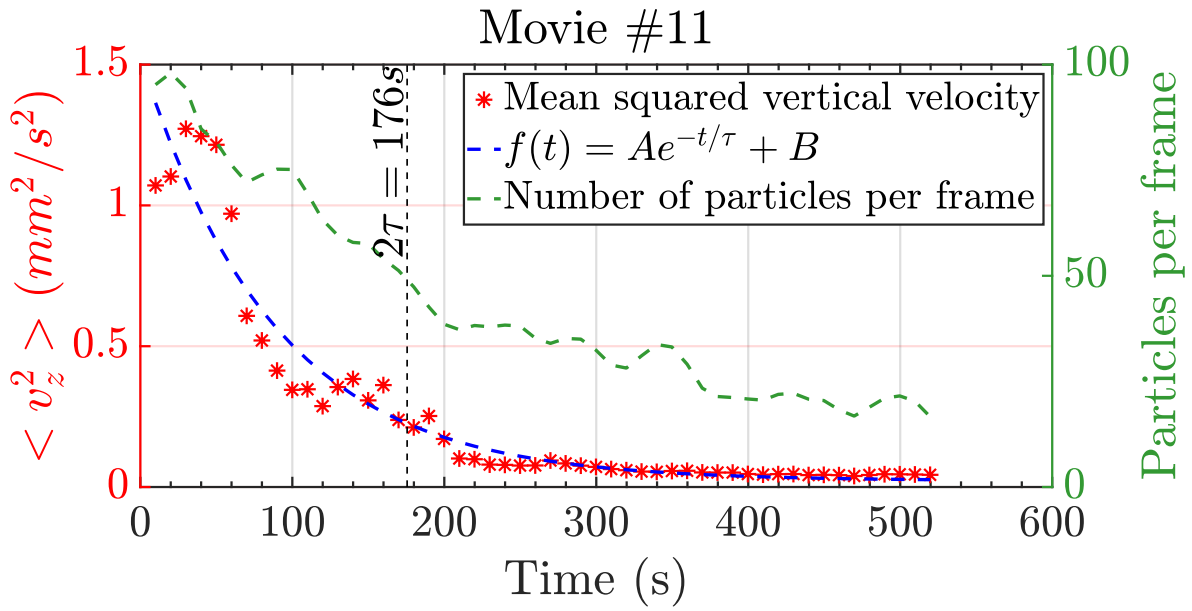

Figure 4.3: Evolution of the mean square vertical velocity during movie #11. In each sub-sequence of movie, the mean square vertical velocity is computed (*). Then, an exponential function is fitted to it (- -), and the time constant τ is extracted. The steady state is considered established after 2τ. The average number of tracked particles per image as a function of time can be read on the right axis.

square of the vertical velocity of the particles is computed. The vertical velocity component is used to avoid the contribution of the horizontal oscillations of the particles. The sub-sequences must be large enough to contain statistically converged data, and small enough to preserve a good time resolution and be considered quasi-steady. Moreover, they must contain an integer number of table revolutions, in order to avoid fluctuations of the result due to a difference between the sampling frequency and the rotation rate. In this study, the sub-sequences are $18s$ to $24s$ long, depending on the rotation rate Ω. Moreover, in order to have a smoother result, the sub-sequences are overlapping, having half their width in common with their closest neighbour. In other words, the first half of the sub-sequence k is the same as the second half of sub-sequence $k-1$, and so on. Each sub-sequence is represented by its median time on the graphs.

The evolution of the mean squared vertical velocity during the movie #11 (cf. table A.1) is displayed on figure 4.3. A clear decay is observed, followed by a steady state of constant mean square vertical velocity. In order to extract a time-constant, an exponential function $f(t) = Ae^{-\frac{t}{\tau}} + B$ ($(A, B, \tau) \in \mathbb{R}^3$) is fitted to the computed data. The stationarity is assumed to be reached after 2τ.

The time constants ($t_0 = 2\tau$) of the different movies are reported on fig. 4.4. The movie recorded with $\Omega = 8RPM$ displays an abnormal value, because no steady-state is observed in the time-window of the movie, affecting the quality of the exponential fit. In fact, its time constant is larger than the movie duration. Omitting this case and the non-rotating ones, an increasing trend is found. The second regime observed in [151], in which the mean square velocity decays as $\Omega^{3/5}t^{-3/5}$ is compatible with the result presented here. Indeed, in a scaling law of the type $(\Omega/t)^n$, the time constant is proportional to Ω. Thus, a linear fit has been done on the data. Of course, due to the method used to compute the time constants, the fit is not perfect, but the trends are comparable.

The influence of the pressure, hence the viscosity and quantity of superfluid, have also been investigated with a few movies. This parameter does not impact the result, but more points are necessary to clarify this conclusion. Overall, 80% of the acquisitions are in steady state after $200s$. This time is twice lower than the settling time $t_{settle} = 422s$ of a $d_p = 5\mu m$ deuterium particle falling from an altitude $H = 20cm$ (black dashed line of fig. 4.4). The value of t_{settle} is actually

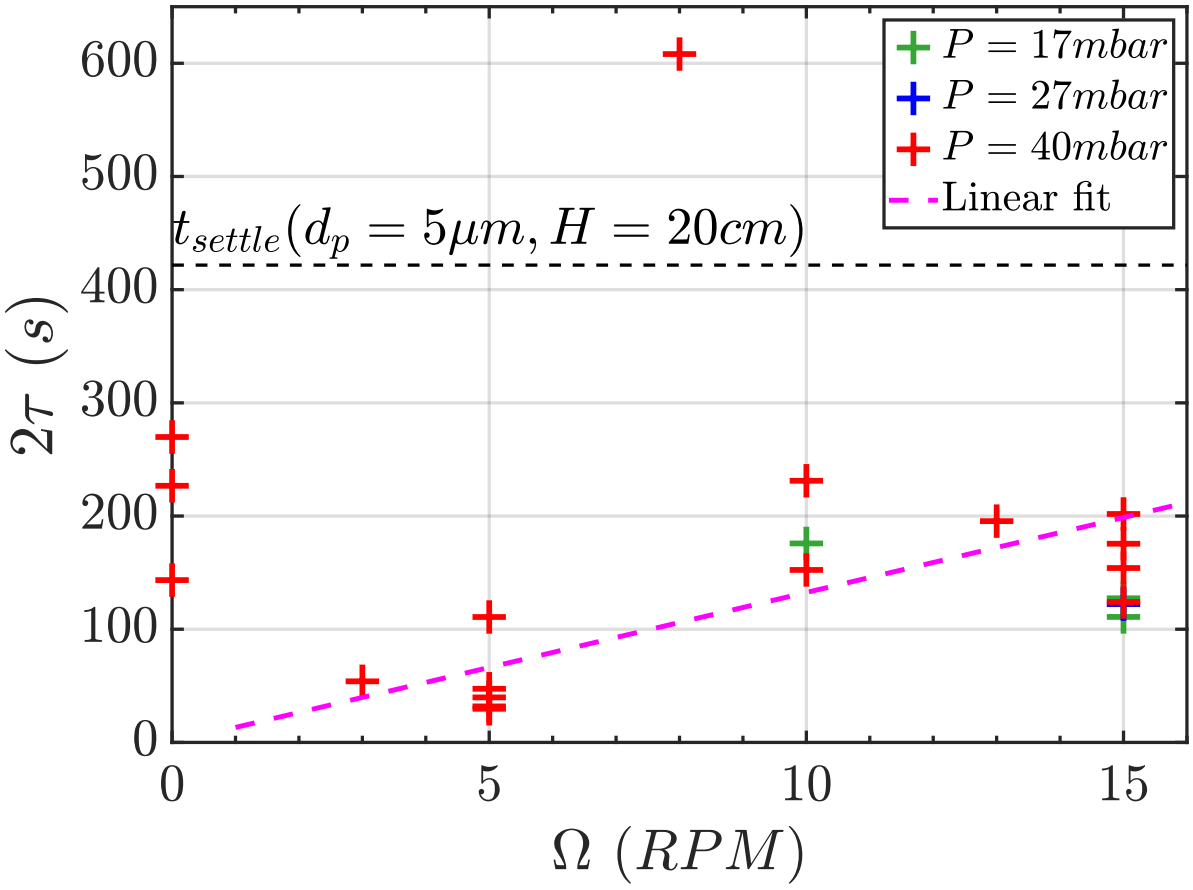

Figure 4.4: Duration of the transient states in all of the configurations listed in table A.1. The displayed value is twice the time constant of the exponential fit of each movie, as shown in fig. 4.3 ($t_0 = 2\tau$). The movie #16 ($8RPM$) has an unusually high time constant because the steady state was not recorded long enough to fit an exponential function. The fit returns $\tau = 304s$, which means that $t_0 = 608s$ is not recorded in this $438s$ long movie. The pink dashed line is a linear fit on the time constants of the rotating cases ($\Omega \neq 0$). As a reference, the settling time of a $d_p = 5\mu m$ spherical deuterium particle falling from an altitude $H = 20cm$ is shown (black dashed line).

underestimated here, because it corresponds to the settling of a particle in a fluid at rest, which is not the case in decaying turbulence. Moreover, $5\mu m$ is an average, which means that smaller particles can stay suspended longer. Thus, if a $200s$ wait takes place before each acquisition, it can last significantly more than $222s$.

Some discrepancies occur however between movies recorded in the same experimental conditions. For instance, at $5RPM$ and $40mbar$ the time constants can vary between 30 and $110s$. This difference cannot only be explained by the poor time resolution. In rotating flows, several characteristic time scales (e.g. Ekman time) are affected, not by the radius of the rotating bucket, but by the height of fluid. In our case, this height is not well known, because the level measurement has to be switched off during experiments, and because the gauge has not been calibrated in the CryoLEM. The variation of the level of fluid can explain some discrepancies but not all of them. For example, the movies #15 and #20 have been recorded in the same conditions, the same day, $\sim 1h45$ apart. Knowing the thermal losses of the CryoLEM being equal to $0.1W$ (section 2.1.4), the difference of fluid height between these two experiments is about $7mm$. Considering our temperature recordings this day, the helium level was above $14cm$ at the end of the movie #20. Then, in the worst case, the change of fluid height could not

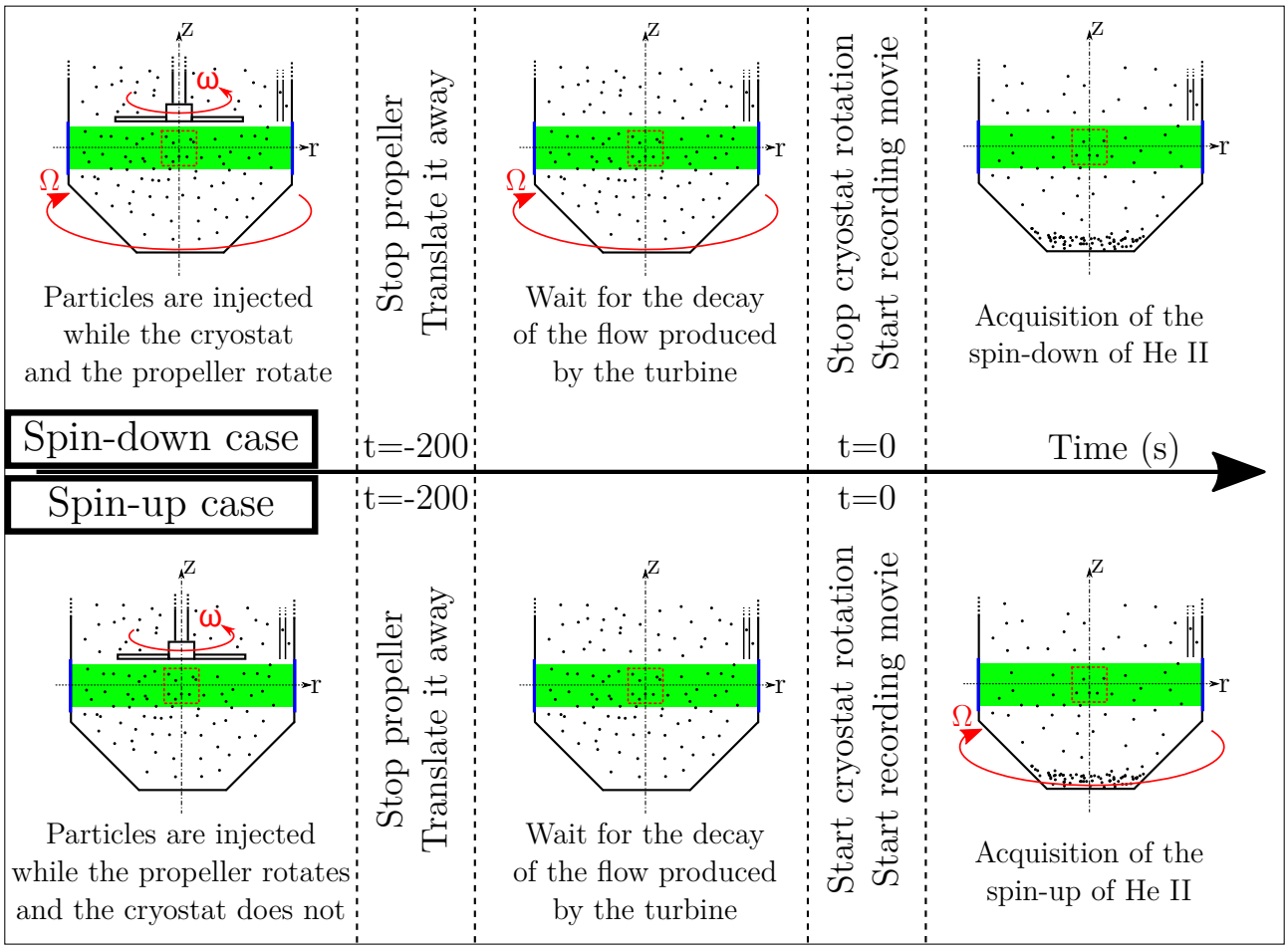

Figure 4.5: Schematic description of the experimental protocols used in section 4.1.2.

exceed 5%, and yet the time constant was changed by a factor 2.3 ($2\tau_{\#15} = 111s, 2\tau_{\#20} = 48s$).

Another impacting factor is the initial value of the mean square vertical velocity. This value is twice lower in the movie #15 than in #20 (respectively 0.6 and $1.3mm^2/s^2$). Therefore, the initial slope of the exponential fit is steeper in the latter case, resulting in a smaller time constant. This does not explains everything however, because the movies #4 and #5 which have been recorded consecutively in the same conditions, have close time constants (30 and $32s$ respectively) despite a large gap between their initial values (3 and $8mm^2/s^2$). Thus, it appears that the initial values can play a role if they are not high enough compared to the steady state values, by extending the time constants. The cause of the differences between the initial values of the movies recorded in the same conditions is unclear though...

In conclusion, these measurements do not contribute to answering the question of the turbulence decay in rotating helium II, but they give us an order of magnitude, and a trend ($\tau \propto \Omega$) of the time needed between a particle injection and the beginning of the recording of stationary movies. Thus, in future experiments, $200s$ will elapse between the particles injection, and the beginning of the acquisitions. This will be long enough to allow stationarity to be established in most cases, and short enough to keep a reasonable amount of particles on screen (avoiding settling).

4.1.2 Spin-up and spin-down of superfluid helium

In this subsection, the transient states of the cryostat rotation are investigated. These transient states happen when the rotation starts (spin-up) and when it stops (spin-down). Just like previously,

the time constants t_0 will be extracted following the same post-processing of the data, and compared with Tsakadze & Tsakadze's model, and the Ekman time constant. The protocol is the following:

Time	**Spin-down**	**Spin-up**
$t - 200s$	- The cryostat rotates at Ω - The propeller is set to $0.95Hz$ - Particles are injected	- The propeller is set to $0.95Hz$ - Particles are injected
$t = -200s$	The propeller is stopped and moved up	The propeller is stopped and moved up
$t = 0$	- The recording starts - The rotation is stopped	- The recording starts - The rotation is set to Ω
$t = t_{end}$	- The recording stops - Repeat the protocol	- The recording stops - The rotation is stopped - Repeat the protocol

Two tables recapitulating all the movies studied in this subsection are available in the appendix (spin-up in table A.2 and spin-down in table A.3). The $200s$ wait before recording has been determined in the previous subsection. It ensures that the system is initially steady. However, this waiting leaves a long window of time during which the deuterium particles settle to the bottom of the cell, out of the field of view. This degrades the quality of the statistics at the end of the recorded movies, sometimes resulting to abnormal results.

In this protocol, two parameters appear: Ω and t_{end}. The pressure was set to $40mbar$, so the influence of the viscosity has not been studied, and the focus was set on the cryostat revolution speed Ω. Usually, the duration of an acquisition is set to $573s$, corresponding to 30000 frames acquired at the maximum frequency of the camera. This value enables the observation of a transient state, followed by a well established steady state. However, the spin-down movies have been recorded before studying the time constants of the particles stirring. Thus, in order to be sure that the steady state was established, the cryostat was rotating during the first half of these movies (except #36), and stopped in the middle of the acquisition. In these cases, the stationarity can be checked in the beginning, but sometimes, the 15000 remaining images are not sufficient to observe a complete transient state (e.g. movie #33, on fig. 4.6, right). In this section, the time $t = 0$ has been shifted to correspond to the moment at which the cryostat was stopped. Hence the reduction of t_{end} from $573s$ to $273s$ in the table A.3 (appendix). Note that it takes around $\tau_{acc} \simeq 5s$ for the system to be in steady rotation (or stop) after sending the command.

The number of particles is not very high in these movies, because of the $200s$ wait between the particle injection and the beginning of the movies. At the end of some movies, there are less than 10 particles (fig. 4.6, right), because ~ 13 minutes have elapsed since the injection. According to Stokes' law and our measurements in section 2.3.1, a $5\mu m$ particle of deuterium at the top of the helium II bulk ($H \simeq 200mm$) should reach the bottom in $\sim 7min$. Therefore, having such a low number of particles at the end of the movie is expected. In theory, the remaining particles after $13min$ have a diameter of $d_p \leq 3.6\mu m$.

The same processing routine as in subsection 4.1.1 has been used. However, in these data sets, the observed value is the mean square of the velocity norm $\langle v^2 \rangle = \langle v_r^2 + v_z^2 \rangle$. Focusing on the vertical velocity did not produce satisfying results in these experimental conditions: no clear "jump" was observed after the perturbation. This is especially true in the spin-up case. A closer look at the movies show that the vertical velocity of the particles is not drastically changed when starting the rotation. The most striking effect is the apparition of trajectories describing a cylinder around the center of the image, due to the difference of velocity between the laser sheet which spins at Ω, and the fluid in the center of the bucket which slowly accelerates from rest. This out of plane velocity is qualitatively observable due to the thickness of the laser sheet (more details in section 4.3, with figures 4.25 & 4.27). When projected on the camera sensor, this velocity is reported on the radial component v_r. Thus, computing

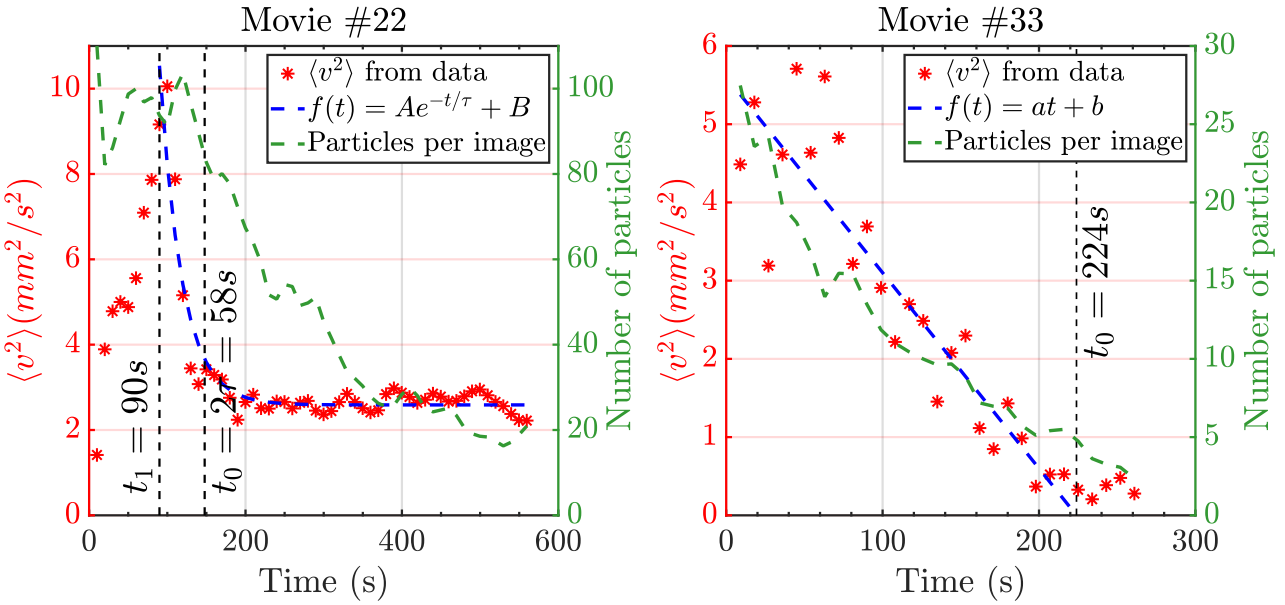

Figure 4.6: Evolution of the mean square velocity norm as a function of time in the movies #22 (spin-up) and #33 (spin-down). An exponential fit is done on the first one, from which is extracted a time constant τ. We consider the steady state established after $t_0 = 2\tau$. In the spin-up case, a delay t_1 is observed at the beginning, and the beginning of the exponential fit is shifted accordingly. On the right, no steady state is observed, which is why a linear fit has been done. The time constant is obtained when the slope crosses the zero axis: $t_0 = -\frac{b}{a}$. On this movie, the amount of particles is also very low (right axis).

$\langle v^2 \rangle$ instead of $\langle v_z^2 \rangle$ allows the observation of a jump in the beginning, followed by a decay. At the end of the movie, the usual horizontal oscillations are still observed in the spin-up case, hence the non-zero value of $\langle v^2 \rangle$.

The observed patterns are similar to the ones in the previous subsection (fig. 4.6), except for some of the "short" spin-down movies in which no steady state could be observed ($t_0 > t_{end}$). For instance, the figure 4.6 (right) shows the graph of the movie #33, in which an exponential fit could not be applied. Then, a linear fit has been done, and the time constant is the time at which the fitted line crosses the horizontal axis. With this method, the time constant is overestimated as it supposes that the steady state is reached when $\langle v^2 \rangle = 0$. In practice, there is always a residual value in steady state, due to the fluid oscillations, as it is the case in the movie #22 (fig. 4.6, left). Actually, most of the movies display a pattern similar to the movie #22, compatible with an exponential fit.

At the beginning of each acquisition, the rotation of the system abruptly changes, and the velocity of the particles suddenly increases. In the spin-down case, the particles' mean square velocity reach a maximum in less than $10s$. This time is comparable to the time necessary for the system to actually stop after receiving the command ($\tau_{dec} = \tau_{acc} \simeq 5s$). However, in the spin-up case, $\langle v^2 \rangle$ can increase for more than a minute. On the movie #22 a delay $t_1 = 90s$ is observed before the exponential decay, despite the spin-up actually starting at $t = 0$. Thus, the exponential fit has been manually adjusted to start at the maximum of the peak, without taking the first increasing points into account. At low rotation rates ($< 5RPM$), it is sometimes hard to estimate the beginning of the decay as the peak induced by the perturbation is not very well marked.

As in the previous section, when the exponential fit was possible, the stationarity is considered reached after a time $t_0 = 2\tau$, without taking the delay t_1 into account. These time constants are reported in fig. 4.7, for the 7 movies of spin-up and 8 movies of spin-down. The Ekman time $t_{Ek}^{(\kappa)}$ based on the quantum of circulation κ and on the cell radius $R = 54mm$, and the Tsakadze time t_{Tk} are also

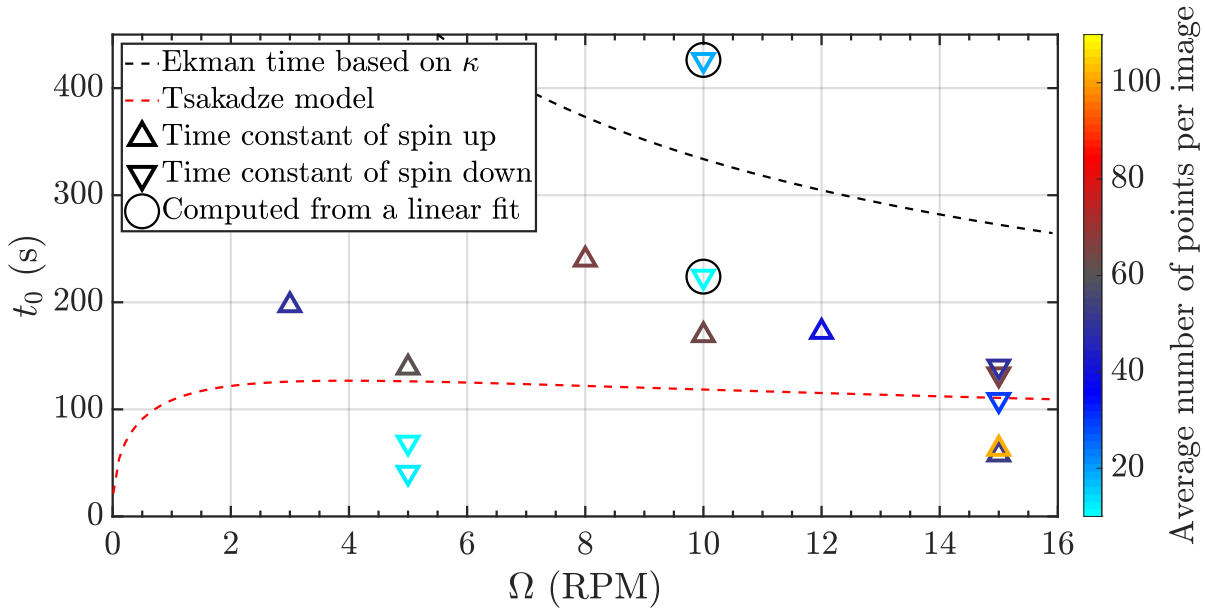

Figure 4.7: Time constants evaluated with an exponential fit ($f(t) = A\ exp(-\frac{t}{\tau})$, $(A, \tau) \in \mathbb{R}^2$) on the mean square velocity. The value displayed in this graph is twice the time constant of the exponential fits ($t_0 = 2\tau$). When no steady state could be observed after the decay, t_0 has been estimated with a linear fit ($f(t) = at + b$, $(a, b) \in \mathbb{R}^2$). In this case, $t_0 = -\frac{b}{a}$ is the zero crossing time.

displayed. The Tsakadze model has been computed using a perturbation $\Delta\Omega = |\Omega|$:

$$t_{Ek}^{(\kappa)} = \frac{2R}{\sqrt{\Omega\kappa}} \qquad t_{Tk} = \frac{(2\pi)^{\frac{2}{5}}}{\Omega}\left(\frac{R^2\Omega}{\kappa}\right)^{\frac{2}{5}}\left(\frac{\rho}{\rho_n}\right)^{\frac{1}{4}} ln(1+5\Omega) \tag{4.1}$$

where ρ is the total density of He II and ρ_n is the density of the normal component ($\frac{\rho}{\rho_n}(P = 40mbar) = 0.71$).

The points computed from our data are colored according to the average number of points on each image of the movie. As with the propeller stirring decay, some discrepancies appear between movies acquired in the same conditions. This is especially the case for the data acquired at 5 and $10RPM$ in which the amount of particles was low. These data sets include the only two cases for which we had to use a linear fit, leading to an overestimation of the measured characteristic time. Considering only the movies in which the average number of particles per image was above 40, the values found are of the same order as the Tsakadze model. The movies recorded at $15RPM$ are the most consistent in terms of repeatability. It is also clear that the time constants t_0 associated to the spin-down cases are longer than the spin-up cases. However, it is important to remember that the delay t_1 has been ignored in the spin-up cases.

This delay can be related to the asymmetry between spin-up and spin-down observed by Hall [101], and discussed in section 1.3. According to him, the time constants in spin-down should be larger than in spin-up, but the initial decay should be faster in spin-down. The time constants in spin-down at 10 and $15RPM$ are actually larger than in spin-up (but not at $5RPM$). Thus, if we only compare the results at $15RPM$, in which the number of points per frame is above 40, the results are in agreement with Hall's observations. However, if we take into account the delay t_1 in the spin-up cases, this assessment is no longer valid.

The delays observed in the spin-up cases are reported on fig. 4.8. At $8RPM$ and above, there is a very good agreement between the values of the delay t_1 and the Tsakadze time, even if they are not supposed to describe the same phenomenon. At low RPM, the computed values diverge from

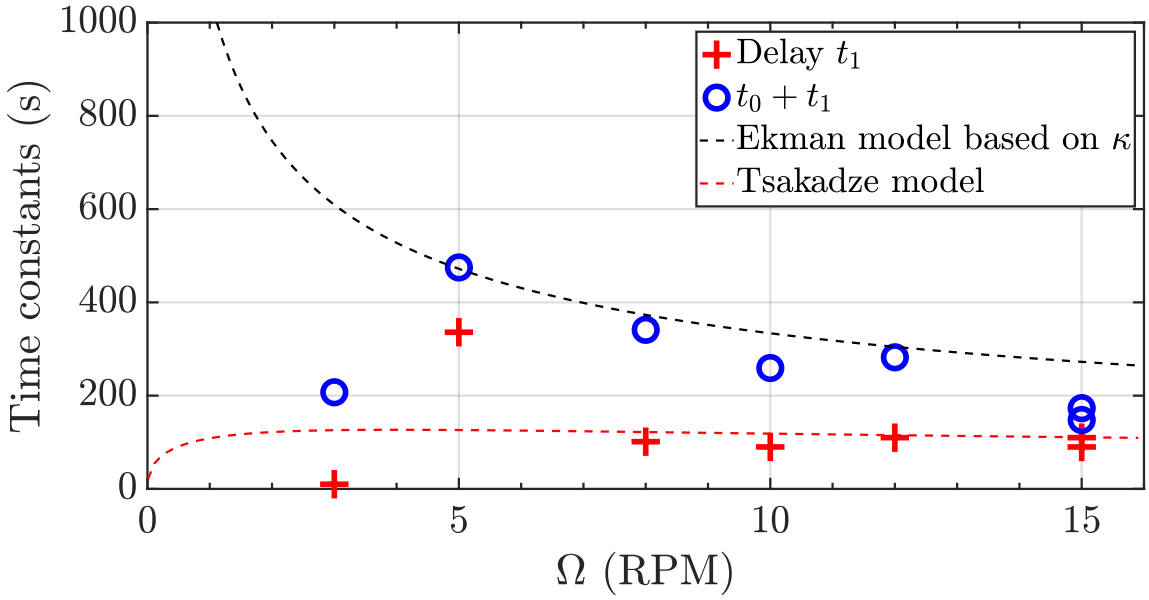

Figure 4.8: Delay between the start up of the cryostat rotation, and the beginning of the particles mean square velocity decay (+). The duration of the decay obtained in fig. 4.7 is added to this value to obtain the total amount of time between the perturbation and the steady state (∘).

Tsakadze's predictions (but t_1 is harder to estimate in these cases). The total duration of the transient state is in good agreement with $t_{Ek}^{(\kappa)}$ between 5 and $12RPM$. At $15RPM$, the sum of the delay t_1 and the time constant t_0 returns a total time of the same order as the spin-down time constants ($\sim 150s$). In Hall's article however (fig. 1.3.2), the total duration of the transient state was significantly longer in the spin-down case.

To conclude, it is hard to extract a general law from these results, even if some qualitative agreements with previous works can be found. The problem of the consistency of the results can be raised. The acquisition of more data could be profitable in several ways. First, increasing the duration of data recording would allow to observe longer steady states. Thus, it will be possible to estimate properly the time constants with exponential fits, and get rid of the linear ones. Second, the new data sets will take advantage of the works on particle injection, and contain more statistics, for more reliability. Third, it would be interesting to increase the range of investigation by setting Ω above $15RPM$. Indeed, low angular velocities are hard to investigate, because the amplitude of the perturbation is not very high, compared to the value of the steady state. For instance, the movies recorded at $15RPM$ give the most consistent results. On the other hand, studying the low revolution speeds are, of course, of higher interest as this is where the Tsakadze and Ekman models diverge most.

Finally, we have clearly identified an asymmetry between the spin-up and spin-down processes. In the spin-up case, there is a first time window t_1 during which the mean squared velocity of the particles in the rotating frame increases. This time window is compatible with the Tsakadze model. It is followed by a regime where the particles' mean square velocity decrease towards its stationary value. In the spin-down case, we only observed the second regime. All the phenomena observed in this subsection could be better characterized using a second sound resonator (see section 1.2). This kind of probe can measure the local vorticity of helium II, which could complement the particle imaging technique.

4.2 Steady rotation of the CryoLEM

4.2.1 Simple rotation of the system: the case of helium II

Once the transient states have been investigated, it is now possible to focus on the steady states. As described in section 1.3, rotating helium II produces a lattice of quantum vortices regularly spaced. According to Bewley's PhD thesis, it is possible to illuminate the lattice for direct observation using frozen particles of hydrogen [122]. Despite working at various temperatures, with several rotating velocities, using particles of hydrogen, deuterium, or air, the lattice has never been directly visualized in the CryoLEM. This may be due to the (micron sized) misalignment of the cryostat with its rotational axis (section 2.2.1) which causes mechanical disturbances affecting the lattice stability, as reported in [70]. This section presents the main characteristics of the flow produced by this canonical forcing.

Particles oscillations

When the cryostat is filled with seeded He II and steadily rotating, the particles oscillate horizontally, all together, in phase with the cryostat rotation. The figure 4.9 shows the position of the particles present in this frame (circles) together with their past trajectories (solid lines), in the cryostat rotating at $\Omega = 15RPM$. Both images have been taken using the same experimental parameters, but during different sessions. The amplitude of the oscillations is very different between these two. On the left image, the particles are slowly falling (almost) straight down with an horizontal oscillation of $\sim 0.8mm$ in amplitude. On the right, the oscillations are larger ($\sim 2.5mm$). This motion is recorded by a camera fixed on the rotating frame. In the laboratory frame, it corresponds to elliptic (or circular) trajectories, off-centred with respect to the axis of rotation, when observed from the top.

The behavior of these oscillations is different when the temperature is above T_λ. This case will be detailed in the next subsection 4.2.2. This could be a sign that superfluidity plays a role in this oscillatory motion. However, as the observed motion is exactly in phase with the forcing, we doubt that

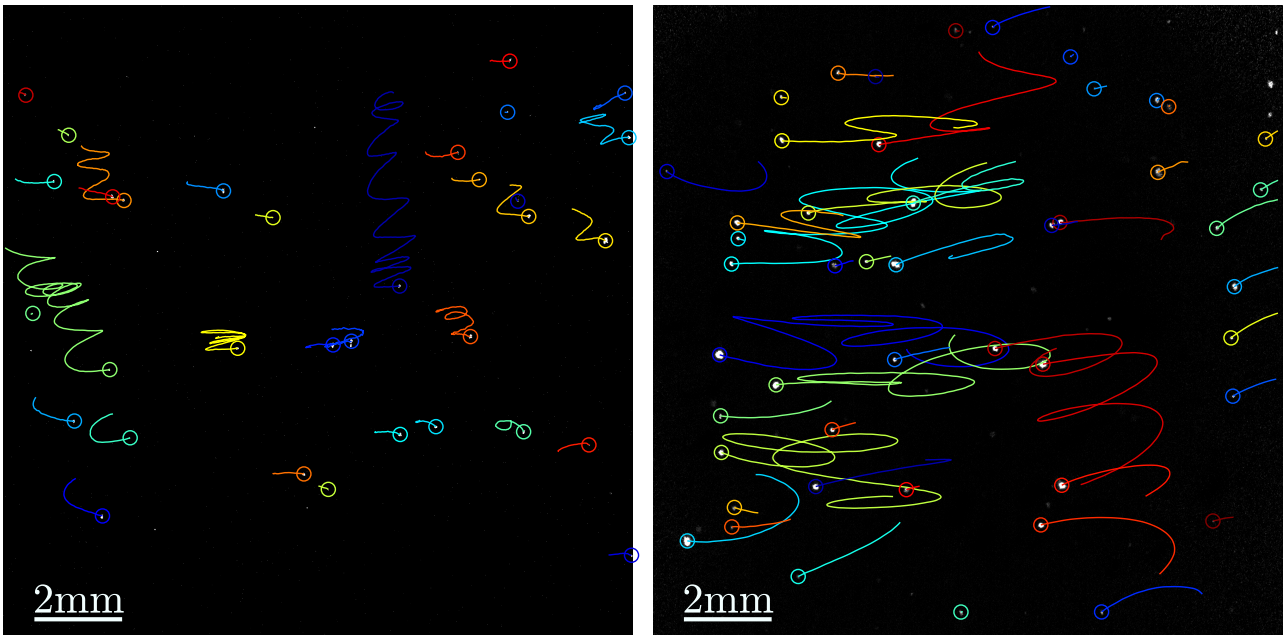

Figure 4.9: Left: Deuterium particles in helium II rotating at $15RPM$ during the July 2018 experimental session (Movie #11). The circles highlights the "present" position of the particles, and the lines represent their past position (trajectories). A color is randomly attributed to each track. Right: Particles acquired in the same conditions in December 2018 (Movie #22).

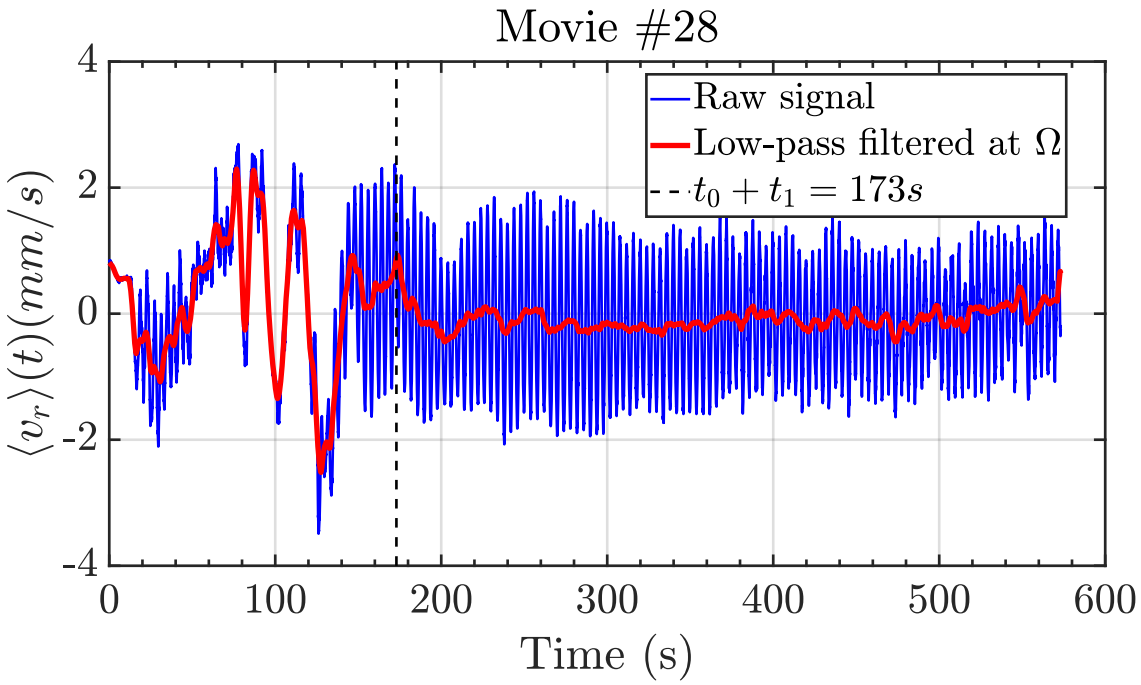

Figure 4.10: On each frame, the average of the horizontal velocity of all the tracked particles is computed: $\langle v_r \rangle(t)$. The first $173s$ of this data set have been recorded during a transient state, hence the irregular shame of the signal. After these $173s$, the particles oscillate all together in phase with the cryostat rotation. When using a filter which cuts off frequencies above Ω, the red signal is obtained. Its constancy indicates that no frequencies below Ω are excited in the steady state, allowing phase detection for the figure 4.12.

this could be a direct observation of Tkachenko waves, or anything related to the vortex lattice. Indeed, the frequency of oscillations discussed in section 1.3 are either proportional to $\sqrt{\Omega}$ (eq. 1.34), or to Ω (eq. 1.35), but not exactly equal to Ω. Moreover, our oscillations are one order of magnitude larger than the inter-vortex spacing δ given by the Feynman's rule (eq. 1.32). This is why, the most probable explanation would be an excitation of classical inertial waves by small mechanical disturbances. In order to clarify it, the possible parameters affecting the oscillations shape will be investigated.

The observation of this regular oscillatory motion leads us to the computation of phase averaged quantities. In order to detect the phases, the average horizontal velocity of all the particles on each frame is computed. The movie #28 (spin-up followed by steady rotation) is taken as an example on the figure 4.10. The result is a signal $\langle v_r \rangle(t)$ oscillating at Ω (blue line). Then, a low-pass filter with a cutoff frequency equal to Ω is applied to the signal (red line). This filtered signal is approximately constant to 0 during the steady state (reached after $173s$ in movie #28). The positive half-phase is detected when the blue signal is higher than the red, and vice versa. In order to verify this detection, the mean length of the half-phases during the steady state is computed, and we check that this value is equal to half the period of the cryostat rotation (verified within 0.2%).

Before using any phase averaging process, it may be interesting to use the temporal signal $\langle v_r \rangle(t)$ to check if other frequencies are excited. As the transient state has been kept for now, the continuous wavelet transform (cwt) function from Matlab[1] is used on each raw $\langle v_r \rangle(t)$ signal, to observe the evolution of the signal in the time-frequency domain (fig. 4.11). In the movie #28, after $\sim 150s$, a clear line appears at Ω and eclipses all the other frequencies. This indicates that the steady state flow is completely driven by the horizontal Ω-oscillations. Before $150s$, various frequencies between $0.03Hz$

[1]Details available online: https://fr.mathworks.com/help/wavelet/ref/cwt.html

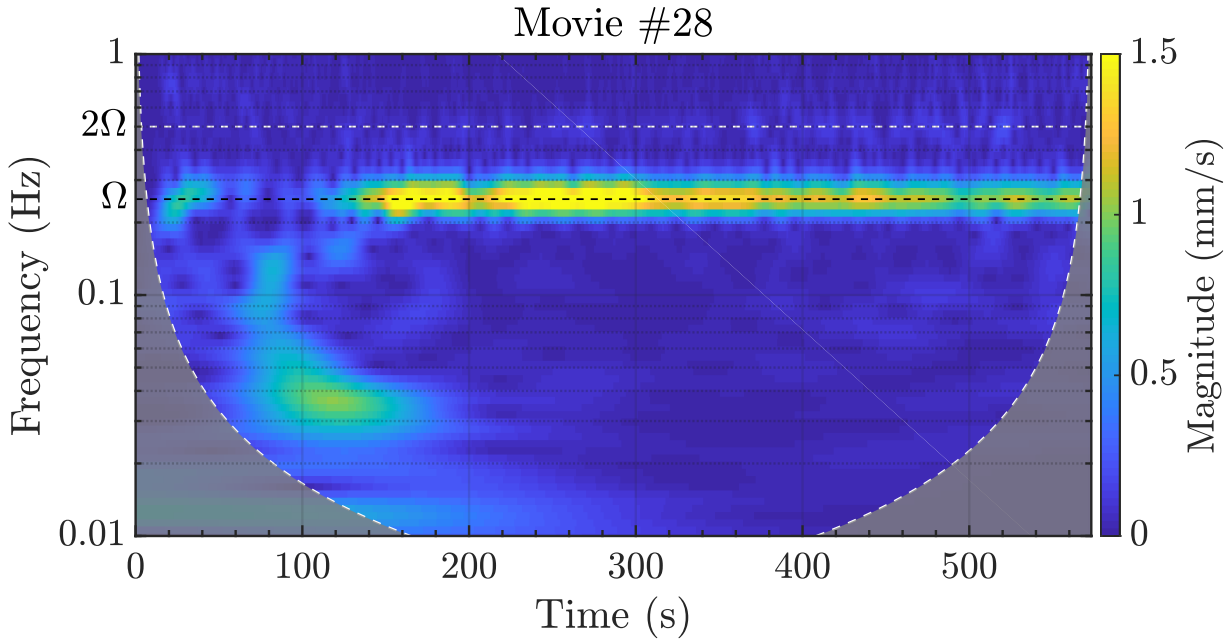

Figure 4.11: Evolution of the spatio-temporal spectrum of the raw $\langle v_r \rangle(t)$ signal (figs. 4.10 blue line) in the movie #28 (spin-up from 0 to $\Omega = 15RPM$). The grayed areas are subject to inaccurate results due to edges effects.

and Ω are excited. These frequencies should depend on the field of view, and the spatial variations of the velocity field. Indeed, during the transient state, the particles are not moving all together, hence the irregular shape of the averaged signal in this time window. This graph also allows to determine the duration of the transient state. The value of $173s$ found in the previous section is compatible with the $\sim 150s$ observed here.

As the phases are correctly detected, and the time-dependence of the signal is characterized, the focus will now be placed on the phase average of the steady state. The data set is split in two parts : the positive half-phases detected with the figure 4.10 are grouped together, and so are the negative ones. In order to measure the amplitude and shape of the oscillations, the space is divided into bins, and the mean velocity of all the particles passing by each bin is computed. In other words, for each movie, two velocity maps are obtained: one during the positive half-phases, and another during the negative ones (fig. 4.12).

The resulting maps display clear oscillating patterns. The movie #22 shows horizontal ones, in good agreement with the trajectories on figure 4.9. A descending vertical velocity is also visible, which is due to the particles settling. The oscillations in the movie #28 are u-shaped, like a pendulum. On the maps of the movie #22, the top corners also display small non-horizontal oscillations, which may correspond to the side of a u-shaped oscillation larger than the field of view. The movie #23 recorded right after #22 at $\Omega = 10RPM$ also shows similar maps. Thus, it is possible that the different shapes observed are due to a change of curvature of the "U" shape. However, this hypothesis has not been checked as these experiments have not been done again with a wider field of view. The movie #37 is another particular case, as the oscillations are not clearly visible when simply looking at the movie. This is due to the presence of a mean flow, and low frequency variations. Despite this, our process reveals the presence of horizontal Ω oscillations, even if the amplitude is smaller than on other movies.

The first pattern with horizontal oscillations is the most common one, as only 2 data sets do not display it clearly: the movies #28 and #37. These two have been recorded the same day in July 2018 with $\Omega = 15RPM$. A good indicator of the presence of horizontal oscillations is the horizontal velocity PDF. The PDF of several movies recorded at 5 and $15RPM$ are compared on fig. 4.13. At $5RPM$,

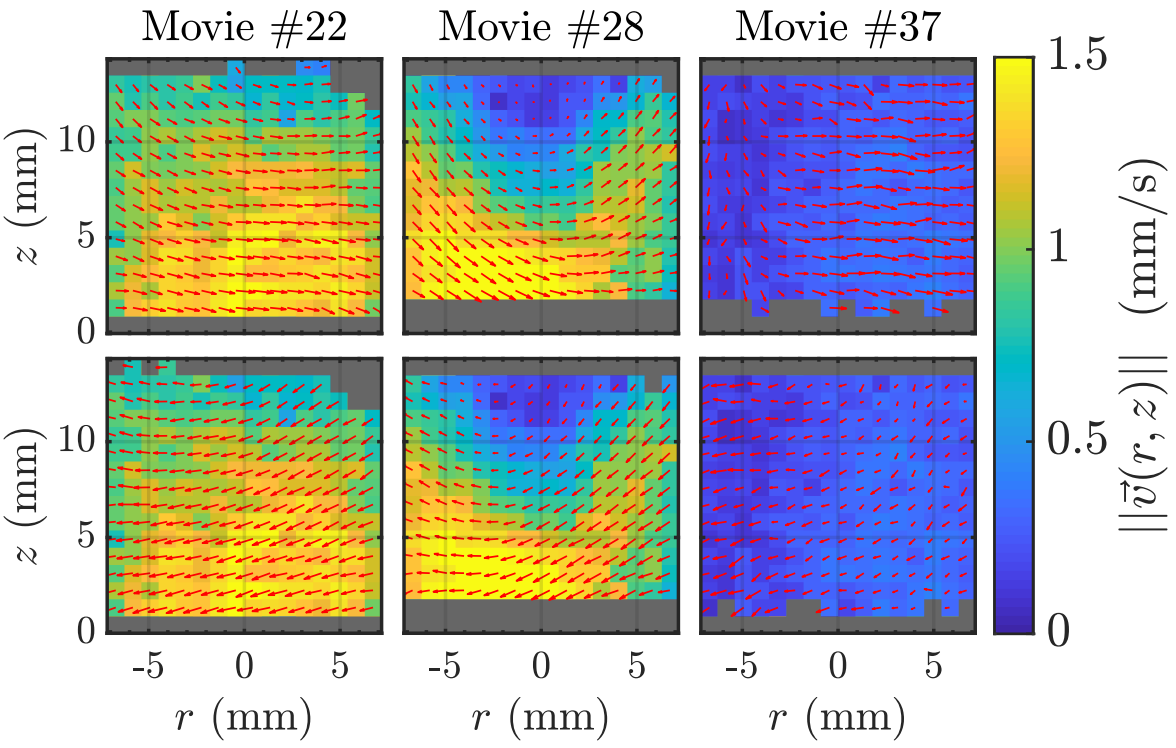

Figure 4.12: Velocity fields for each half-phase (top and bottom) of several movies recorded at $15RPM$. The color reflects the amplitude, and the arrows the direction of the velocity field (the arrows scales change from one graph to the other). Despite being recorded in the same experimental conditions the amplitude of the oscillations can be very different, in agreement with fig. 4.9. The shape of the oscillations is strikingly different in the movie #28. The grayed areas are bins in which the amount of data was not considered sufficient to reflect converged data.

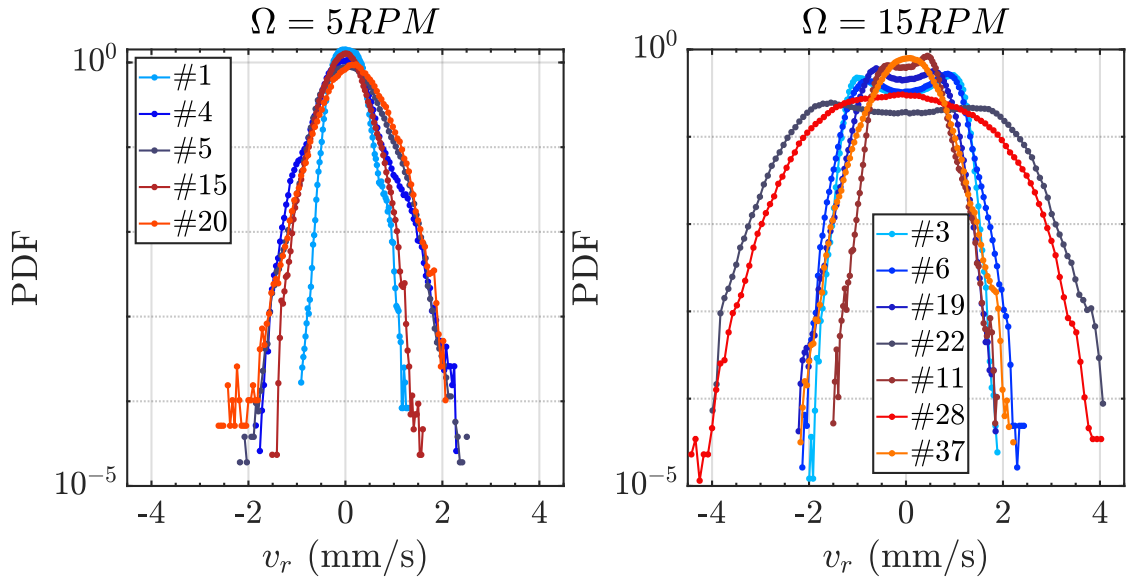

Figure 4.13: Horizontal velocity (v_r) PDF of the different data sets recorded under a steady rotation of $\Omega = 5RPM$ (left) and $\Omega = 15RPM$ (right).

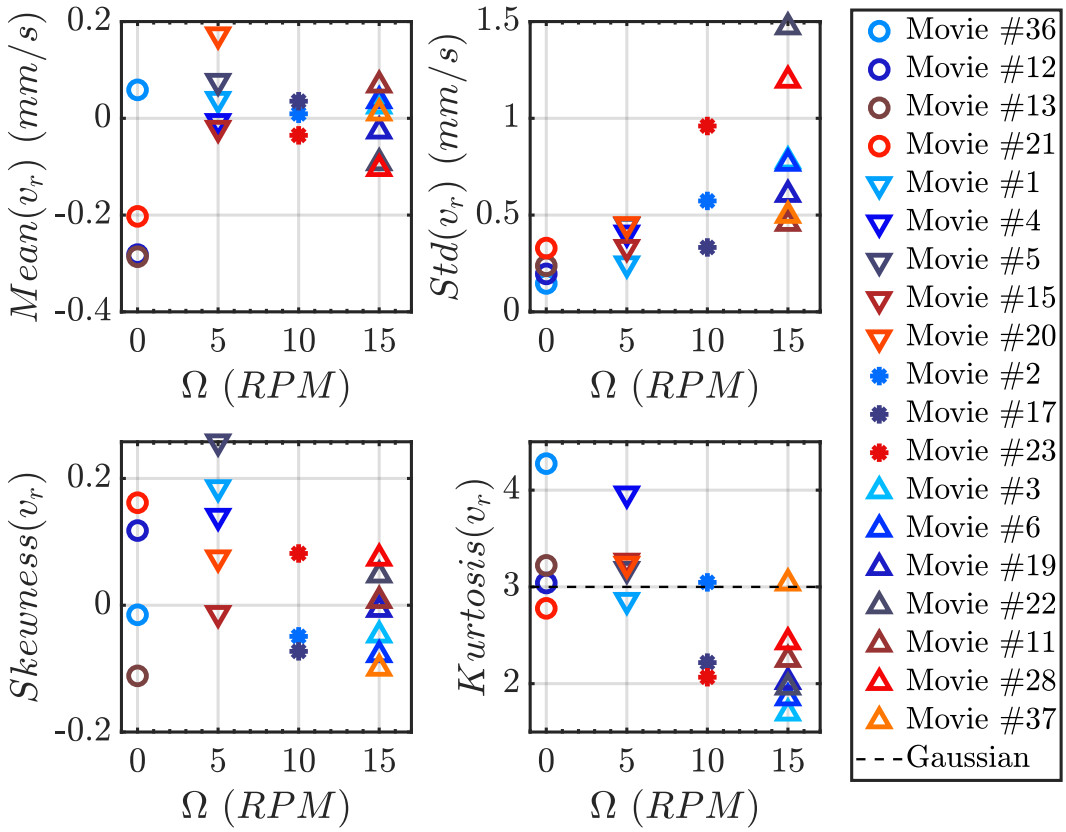

Figure 4.14: Statistical values computed from each data set. The symbols are different for each value of Ω. The color does not reflect any physical property, but they are kept the same in the different figures of this section.

there are already differences of width between the distributions, but they are small compared to the large discrepancies between the PDF obtained at $15RPM$. At this rotation rate, the oscillations cause some bumps on both sides of the mean value. The movies #28 and #37 do not display these bumps due to the different shape of their oscillations. The bumps do not appear on the PDF at $5RPM$ either, because of the small amplitude of the oscillations, but their presence has been verified using the half-phase maps. Therefore, even if no bump appears, the oscillations influence the shape of the PDF, especially their standard deviation. Because of these differences, it is not possible to merge the data sets acquired in the same experimental conditions. In order to have an overview of all the steady movies, the distributions are reduced to their mean, standard deviation, skewness and kurtosis on figure 4.14.

First, all the mean values can be considered equal to 0 as they are 5 to 60 times smaller than the standard deviation. The standard deviation grows with Ω, but the values are spreading out more and more as well. The values of skewness are distributed around 0, meaning that the distribution is symmetric, as expected in a rotating laminar flow. The kurtosis is evenly distributed around 3 (gaussian) at $5RPM$, but it decreases with Ω as the bumps appear on the PDF. Indeed, at $15RPM$ the movies #28 and #37, which do not have bumps, are the closest to 3. However, it is unclear why the movie #2 has a kurtosis of 3.05, despite the bumps on its PDF.

A linear scaling of the standard deviation was actually expected in the case of an oscillatory motion. The horizontal position of the particles on each frame can be modeled by a function of the form $r = A_f cos(\Omega t)$, where A_f is the amplitude of the fluid motion. Then, the horizontal velocity standard deviation is $std(v_r) = \frac{A_f \Omega}{\sqrt{2}}$. If these oscillations are only due to the cryostat misalignment, it

is still unclear how these disturbances of $A_c = 50\mu m$ in amplitude (see figure 2.13) could lead to $1mm$ oscillations of the particles. If all the kinetic energy of the oscillating cryostat is transmitted to the fluid, then we have:

$$\frac{A_f^2}{A_c^2} = \frac{m_c}{m_f} \tag{4.2}$$

where m_f and m_c are the respective mass of the fluid and the cryostat. In the present case, the ratio $\frac{A_f^2}{A_c^2}$ is above 400, then the mass of the moving parts of the cryostat should be at least 400 times larger than the mass of liquid in it. Depending on the amount of liquid inside, we would have $m_c \in [40 : 215]kg$, which is too large for a dewar made of aluminium. The mass of the moving parts is estimated to be around $10 \sim 20kg$. More importantly, under these assumptions, the amplitude of the oscillations decreases when the amount of fluid increases. Based on the temperature measurements taken during the movies #11 and #22, there is no doubt that there is more liquid in the latter and yet the oscillations of the particles are larger (fig. 4.9).

This simple approach is not effective for explaining the different amplitudes of oscillations observed, but the problem can come from the value of A_c. The $50\mu m$ cryostat displacement measured in section 2.2.1 have been recorded in July 2018, in the same experimental session as the movie #11, but it has not been measured again at any time. The movie #22 has been recorded in December, so it is possible that the lower temperatures in winter cause the rotating gasket to be more tightened, due to thermal expansion. Thus, it would change the play between the parts, causing a different oscillation amplitude of the cryostat cell. This is why it is necessary to permanently equip the system with accelerometers at different places, and check the stability of the cryostat rotation.

The figure 4.15 reports the amplitude of the oscillations as a function of the temperature measured using a PT100 stuck on the external wall of the guiding stator. The temperature of the gasket is $295 \pm 11K$, which means that the diameter of the external wall of the stator, made of stainless steel, can vary by up to $40\mu m$. Of course, this part is not the only one submitted to temperature variations, so this value is different from the variations of the play. However, as we observe window motions of the same order ($50\mu m$), located $1.5m$ below the gasket, this difference must have a significant impact. Actually, the complex geometry of the system, and the presence of high temperature gradients in the parts makes the impact of thermal expansion hard to predict.

This complexity is clearly depicted on figure 4.15, where no monotonic trend appears, which means that simply measuring the temperature outside of the guiding stator is not sufficient. Moreover, we know that when the pressure in the cryostat changes, large quantities of "cold" gaseous helium pass through the whole chimney, favoring heat transfers by convection and increasing the temperature gradients in the cryostat parts. This phenomenon is clearly observed during experiments when the top of the cryostat is freezing, due to the presence of water in the ambient air. Thus, frequently changing the pressure in the cryostat must significantly change the plays between the parts, and affect the stability of the rotation. In most of the movies studied in this section, the pressure has been set to $40mbar$, and stabilized at this value during the whole day, but this was not the case for movies #28 and #37. These movies were recorded during a session in which several movies in normal fluid have been shot (see section 4.2.2). The movies in normal fluid require several pressure changes in order to improve the quality of the visualization. Therefore, the numerous transfers of cold gaseous helium which took place this day may be (partly) responsible of the unusual shape of the oscillations in movies #28 and #37.

In a nutshell, the oscillations of the particles observed in rotating helium II prevent us from seeing the vortex lattice. Their most probable source of excitation is a very small ($\sim 3\mu m$) mechanical misalignment in a complex geometry, affected by large thermal gradients. In the current set up, a

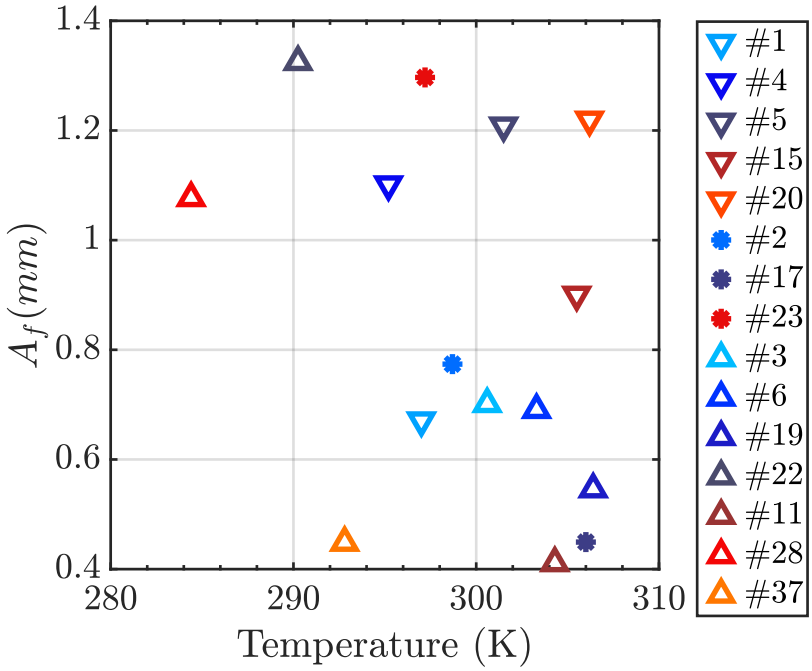

Figure 4.15: Amplitude of horizontal oscillations as a function of the temperature measured by a PT100 placed on the rotating gasket. The amplitude of the oscillations is computed from the standard deviation of the horizontal (radial) velocity: $std(v_r) = \frac{A_f \Omega}{\sqrt{2}}$. No monotonic trend appears, which means that the temperature of the gasket is not sufficient to explain the different amplitudes of oscillation.

better alignment is not achievable. However, a more flexible mounting of the guiding stator of the spinning gasket could be considered, so that it can follow the spinning axis.

Anisotropy produced by rotation of the apparatus

In the first chapter of this manuscript, we discussed the Taylor-Proudman theorem (section 1.1.2), predicting that, under the effect of rotation, a classical fluid flow becomes 2D: the dependence along the rotational axis weakens (see section 1.1.2). In order to study it in rotating helium II, the velocity structure functions will be used. Considering a pair of particles separated by a distance vector $\overrightarrow{ds} = dr\overrightarrow{e_r} + dz\overrightarrow{e_z}$, the energy distribution and the flux density between scales can be expressed as [14]:

$$E(\overrightarrow{ds}, t) = \langle (\delta \overrightarrow{v})^2 \rangle \text{ and } \overrightarrow{F}(\overrightarrow{ds}, t) = \langle \delta \overrightarrow{v} (\delta \overrightarrow{v})^2 \rangle \tag{4.3}$$

where $\overrightarrow{v}(\overrightarrow{X}, t)$ is the turbulent velocity and $\delta \overrightarrow{v} = \overrightarrow{v}(\overrightarrow{X} + \overrightarrow{ds}, t) - \overrightarrow{v}(\overrightarrow{X}, t)$ is the velocity vector increment over $\overrightarrow{ds}$. As it is not possible to merge our data sets due to their discrepancies, it will not be possible to compute a converged $\overrightarrow{F}$ which is a third order moment requiring a tow of data. Moreover, as in reference [14], since we do not measure the out of plane velocity component v_θ, we cannot compute a rigorous value of $E(\overrightarrow{ds}, t)$ in space, hence the following approximation:

$$E(dr, dz, t) = < \delta v_r^2 + \delta v_z^2 > \tag{4.4}$$

Finally, as this study focuses on stationary data, E does not depend on time, and all the frames are averaged together, resulting in the maps displayed on figure 4.16. Despite being recorded at the same angular velocity, these three maps display different patterns and amplitudes. The amplitudes are directly linked to the oscillations and the velocity standard deviation, the discrepancies of which have already been mentioned. Moreover, when $dr = dz = 0$, the difference of velocity in the fluid,

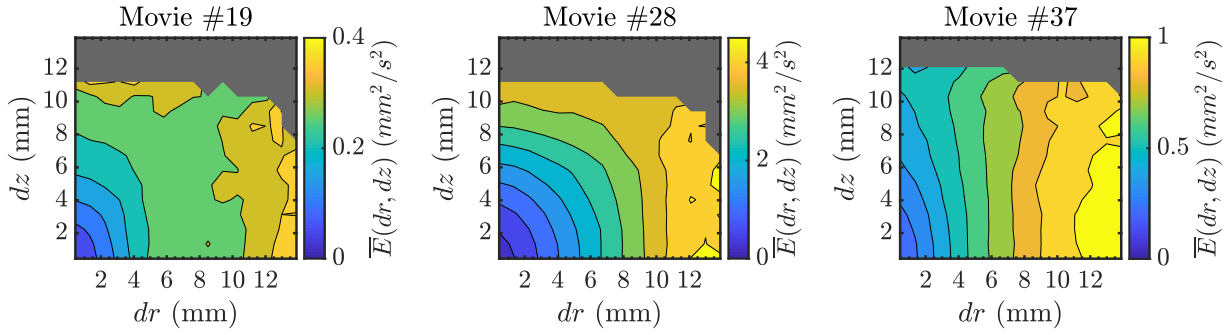

Figure 4.16: Example of time averaged energy distributions for movies #19, #28 and #37 ($\Omega = 15RPM$). If the first two display circle shaped contour lines, the latter display lines, showing a high anisotropy. The coefficient $I_{rz} = \frac{\overline{E}(dr=8mm,0)-\overline{E}(dr=2.6mm,0)}{\overline{E}(0,dz=8mm)-\overline{E}(0,dz=2.6mm)}$ is the horizontal to vertical energy ratio.

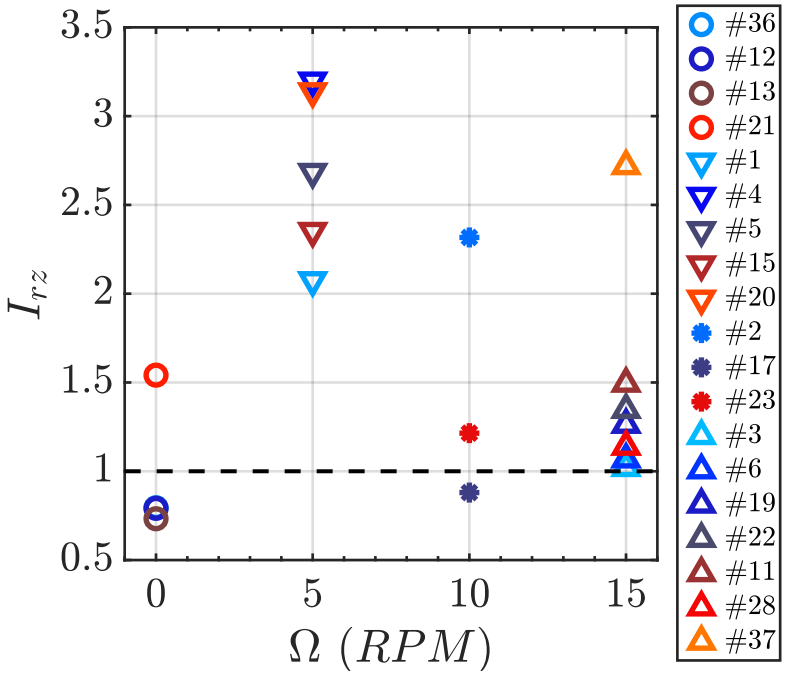

Figure 4.17: Vertical to horizontal energy ratio I_{rz} as a function of the cryostat rotation rate Ω in steady state. A value of I_{rz} above 1 means that anisotropy is induced by rotation: the dependence of E on dz is weakened.

hence $E(0,0)$, is expected to be 0. However, we often find a residual value which is due to the non zero thickness of the laser sheet ($2e \sim 2.6mm$, measured in section 4.3). Indeed, even if $dr = dz = 0$, the particles can be spaced by up to $2e$ in the third spatial component, hence the different velocities. The effect of the laser thickness on these results is further studied in the appendix B. The outcome is that the results become accurate when the separation is larger than the thickness of the laser sheet.

The graph depicting the movie #37 displays clear vertical lines, which are the sign that $\overline{E}$ varies more by increasing dr than dz. In other words, this is the sign of a strong anisotropy, in agreement with the Taylor-Proudmann theorem.

In order to quantify the isotropy levels for all movies, the vertical to horizontal energy ratio $I_{rz} = \frac{\overline{E}(dr=8mm,0)-\overline{E}(dr=2.6mm,0)}{\overline{E}(0,dz=8mm)-\overline{E}(0,dz=2.6mm)}$ is defined. This is an adaptation of the horizontal-to-vertical energy

ratio used in [14]: $\frac{\overline{E}(0,10mm)}{\overline{E}(10mm,0)}$, which corresponds to the ratio of the mean slopes of the energy for separations between 0 and $10mm$. As we know that our results are inaccurate for separations below $2.6mm$, we adapted I_{rz} to compute the slope over a valid interval. Thus, in the isotropic case, the energy distribution displays circles, since $E(\overrightarrow{ds}) = E(|\overrightarrow{ds}|)$, in which case I_{rz} is equal to 1. As the rotation along the vertical axis should decrease the dependence of E on dz, I_{rz} is expected to increase with Ω.

The figure 4.17 reports the isotropy coefficients of all movies studied in this section. The result is mitigated, and linked to the oscillations. At $0RPM$, the coefficients are well distributed around 1 ± 0.4, as expected. At $5RPM$ the values significantly increase and spread over a wide range between 1.7 and 3.1. This is the first figure that displays such large discrepancies at $5RPM$, reflecting the sensitivity of this technique. Beyond $\Omega = 5RPM$, I_{rz} do not increase as it should, and the results are more and more spread out. At $15RPM$, the movie #37, which does not display clear particle oscillations, stands out once again. It is then possible to conclude that oscillations hide anisotropy, because, at each instant t, the particles on the whole image are moving together, so the velocity differences are similar (and close to 0) in every direction. This means that the integral length scale of the observed flow is larger than the field of view. Thus, if the field of view was wider, complete structures could be observed, changing the isotropy coefficient. The reason why the movie #2 ($10RPM$) stands out is unclear, and may be related to its unexpected kurtosis value (fig. 4.14).

In conclusion, in the current set up of the CryoLEM, it is hard to study rotation alone, due to the presence of prominent oscillations. They may be responsible for the particle inability to illuminate the quantum vortices lattice. The stability of the lattice may be questioned as well. They also hide the other contributions of the rotation, such as anisotropy, making several of our observations inconsistent with the theory. The consistency of the oscillations themselves is a problem as several amplitudes have been observed in cases that should be identical. Therefore, it is necessary to add sensors on the cryostat in order to identify precisely the source of the oscillations, and its amplitude. Nevertheless, this preliminary work has enabled us to draw up paths for the future, and to introduce tools for data processing.

Two other kind of flows have been investigated. A few movies of steady rotation have been recorded in helium I (section 4.2.2), in order to see if the particles behavior changes. The other approach is to overcome the oscillations by injecting more energy in the system using the propeller (section 4.3). The cryostat filled with helium II will rotate at Ω, while the propeller inside rotates at $-\Omega$, with respect to the laboratory frame of reference.

4.2.2 Simple rotation of the system: the case of helium I

This subsection focuses on the rotation of the CryoLEM filled with classical liquid helium (He I). These data are harder to obtain due to the presence of bubbles in helium I at SVP, which is not the case in helium II (see section 1.2). Thus, in order to remove them, the pressure is slowly decreased below the λ transition by pumping. Then, a pressure of $1bar$ is suddenly restored in the cryostat using a gaseous helium bottle, removing the helium I bulk from the SVP curve. The field of view is cleared from bubbles for several tens of minutes.

This protocol has several drawbacks. First, it is heavy for such a short time window for experiments. Second, the multiple and sudden pressure changes may affect the mechanical parts due to thermal expansion and gradients. And third, cooling down the cryostat through pumping consumes a significant amount of liquid. Thus, if several time windows are necessary to acquire the desired data, it is necessary to pump several times. This operation can consume so much liquid that it would be necessary to reinject helium from the reservoir to the cell. This protocol can, of course, be improved in several ways. However, the main purpose of the CryoLEM is to study superfluidity, so the priority

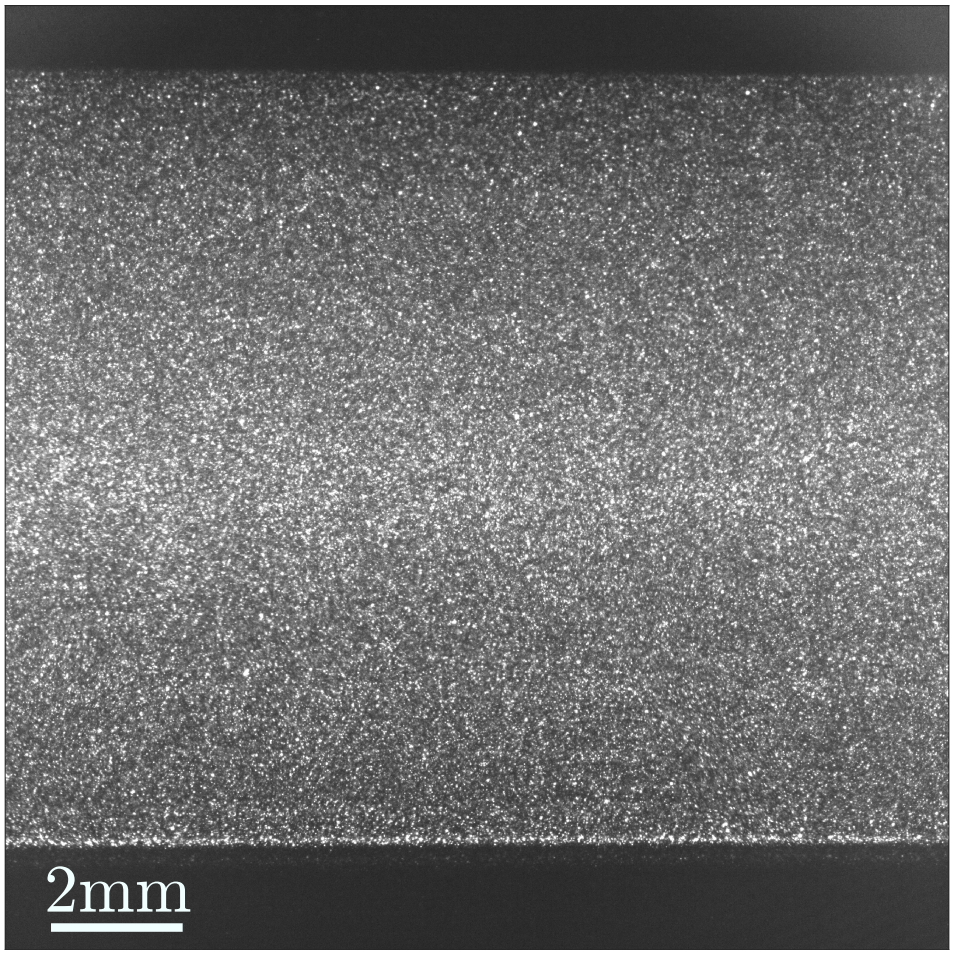

Figure 4.18: Cloud of air particles obtained after repressurizing the cryostat in order to study a normal fluid bulk free from bubbles. This image is taken from a movie, recorded in July 2018, which has been used for PIV studies in collaboration with the FAST (Orsay, France).

has been given to helium II, and helium I remains upstage, as a point of comparison, hence the small quantity of data on it (see table A.5).

The line connecting the bottle to the cryostat by their top (i.e. in the gas) was not airtight, which is why repressurizing the cryostat resulted in a helium I bulk seeded with air particles. Thus, the amount, shape and nature of the particles injected are not well controlled. By chance, the resulting seeding is a very dense cloud of thin particles, ideal for PIV studies (fig. 4.18). With the help of our colleagues P.-P. Cortet and M. Brunet from FAST (Orsay, France), a few movies have been processed, and one of them will be presented here.

In the movie #38, the cryostat was spinning at $15RPM$, while the liquid helium I was under a pressure of $1bar$, and seeded with air particles. It has been recorded around 15min before the movie #28 presented in the previous section. One of the velocity fields obtained from the PIV processing is displayed on figure 4.19. This velocity field is completely different from the regular oscillations observed in helium II. Structures of different sizes appear, and the velocity of the particles is significantly higher than in subsection 4.2.1. This observation is surprising though, because helium I is a classical fluid. Thus, it is expected to follow Ekman's laws and reach a steady state of rigid body rotation in less than $15min$ when $\Omega = 15RPM$. In our case, the rotation has started around $20min$ before the beginning of the acquisition, which is why the particles are expected to settle slowly to the bottom of the cell.

In order to confirm the steadiness of the flow, the spectrum of the velocity has been plotted for several 1000 frames long subsequences taken along the movie #38 (fig. 4.20). The spectra are

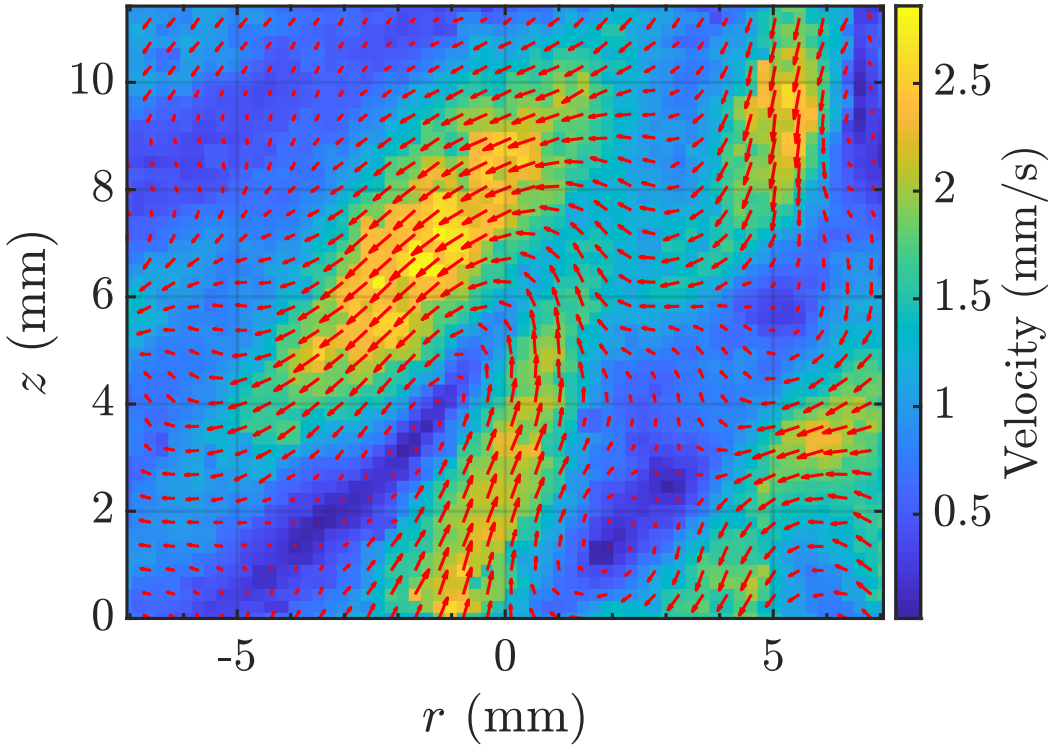

Figure 4.19: A velocity field extracted from the middle of the movie #38, resulting from a PIV study processed by our colleagues from FAST. This field shows structures of various sizes, which are very different from the regular oscillations observed in helium II (e.g. fig. 4.9).

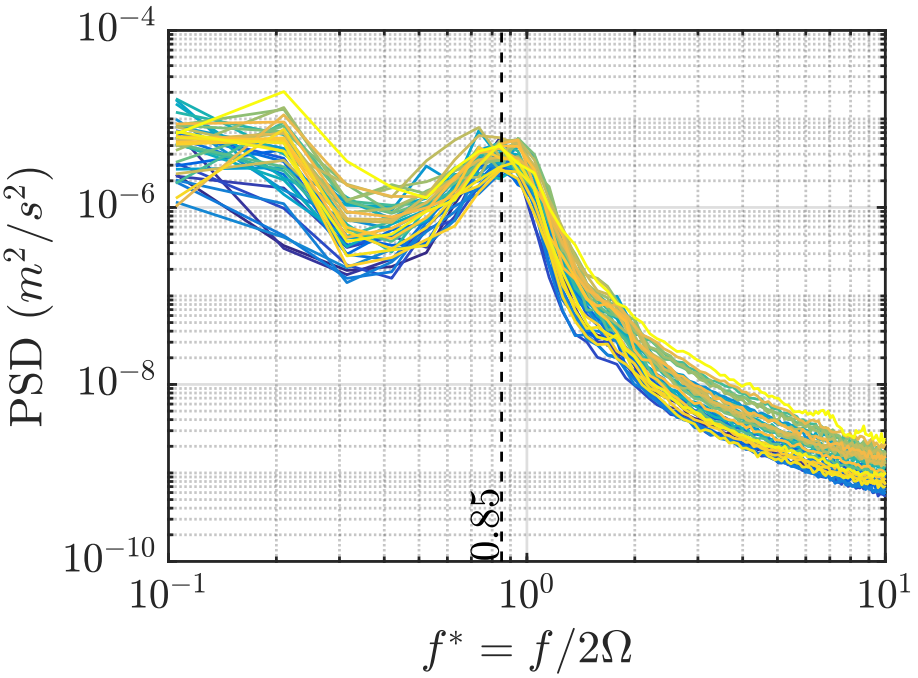

Figure 4.20: Energy spectra obtained at different time-windows (1000 frames) along the movie #38. The dark blue lines are plotted at the beginning of the movie, and the bright yellow ones at the end. The spectra are overlaid on each other, meaning that the flow is stationary. A peak is observed around $f = 1.7\Omega$, which is different from the Ω oscillation observed in helium II.

superimposed, which means that the flow is indeed stationary. They also display a peak at a frequency $f = 1.7\Omega$, which is very different from the Ω oscillations observed in helium II. These two figures show that, for the same forcing (rotation at $\Omega = 15RPM$), the flow is completely different in helium I and in helium II. At the moment, we do not have any conclusive explanation on this phenomena, but it encourages us to perform other experiments in normal fluid.

Nevertheless, a first conclusion is that the Ω oscillations observed in helium II are related to, or at least amplified by superfluidity. Several articles report the observation of oscillations in rotating helium II which are not observed in helium I [18,84]. It has sometimes been attributed to oscillations of the vortex lattice (Tkachenko waves), because the presence of quantum vortices is the main difference between the dynamics of helium I and II. However, in our case, the hypothesis of the Tkachenko waves can be rejected, because the amplitude of the oscillation can be 10 times larger than the inter-vortex distance ($\delta = 178\mu m$ when $\Omega = 15RPM$) predicted by Feynman's rule (equation 1.32). Another possibility could be that the inertial waves excited by the cryostat pendulum motion are still present, but more damped in helium I, due to the difference of viscosity.

In order to better understand the differences and similarities between both states of liquid helium, some improvements have been made in the cell. An attempt of acquisition with a wider field of view ($32.5 \times 32.5mm^2$ obtained with a 100mm lens) has been done in order to better understand the large structures of the flow observed in helium I. However, they were unusable due to the large amount of particles scattering light on the aluminium walls of the cell. Thus, a black sheet of paper has been added in order to improve the quality of the background of the images.

For a better control of the particles, the line used to repressurize the cryostat has been changed for an airtight one. Thus, when pumping down to helium II before repressurizing the cell to obtain a bulk of helium I free of bubbles, we do not inject air anymore. In order to seed the fluid with particles, the embedded reservoirs can be used with the usual mixture of deuterium and helium. This way, it will be possible to tune the amount of particles, and their size. As already mentioned in literature (e.g. [18], [112]), we observed that the particles aggregate quickly in helium II. Thus, even a dense cloud suitable for PIV, like the one shown on fig. 4.18, can aggregate in a less dense cloud of larger particles suitable for PTV. In future normal fluid studies, the protocol used to generate the particles will have to take into account the kind of processing we want to apply to measure the fluid dynamics. An injection before cooling down to helium II will result in an aggregated cloud suitable for PTV, while an injection after the repressurization will be compatible with PIV studies. For an accurate comparison of both liquid states, using the same processing may be preferable, but comparing the results given by both methods can be interesting too.

The objective of this section was to compare the rotating flows of helium II to those of helium I. The answer is clear: they are strikingly different. The observed flow is far from a solid body rotation, and the oscillations of helium II are not observed in helium I. The energy spectra showed a prominent peak around $f = 1.7\Omega$. Studying helium I is not a priority to us, as the CryoLEM is made to investigate quantum turbulence in helium II before anything else. However, the results shown here are motivating to conduct other studies, in order to understand the causes of this unexpected helium I flow. In this case, it is necessary to give a special care to the experimental protocols. Both PIV or PTV processing could be used, but the protocol must be adapted depending on the phenomenon we want to study.

4.3 Counter-rotating propeller in rotating He II

This section focuses on experiments using a propeller as a forcing in rotating helium II. The experimental set up is depicted on figure 4.21. A total of 31 data sets of 15000 frames each have been recorded in January 2019.

Once the experimental cell has been filled with helium II, and stabilized at $40mbar$ $(2.087K)$, the experimental protocol is the following:

- In the frame of the laboratory, the rotation of the CryoLEM is set to $\Omega \in \pm\{3; 6; 9; 12; 15\}$, and that of the motor is set to $\omega = -\Omega$. Thus, in the rotating frame, we have $\omega = -2\Omega$.
- Particles of deuterium are injected.
- After a $200s$ wait, the recording of the movie starts.
- When 15000 frames are acquired, the recording stops, and this protocol is repeated.

This protocol is repeated several times for each value of $\Omega < 0$ (clockwise) and $\Omega > 0$. In total, 32 movies have been recorded: 21 clockwise and 11 anticlockwise. The table A.6 summarizes all the data used in this section.

The $200s$ wait ensures the steadiness of the acquired data (see section 4.1). In order to check if it is possible to merge the data sets acquired in each experimental condition, the steadiness of the data will be quantified, and so will be the comparability of the general statistics.

As in the previous sections, the standard deviation of the velocity is used to measure the steadiness. If there is a transient state in these movies, it will be due to the propeller stirring, and therefore

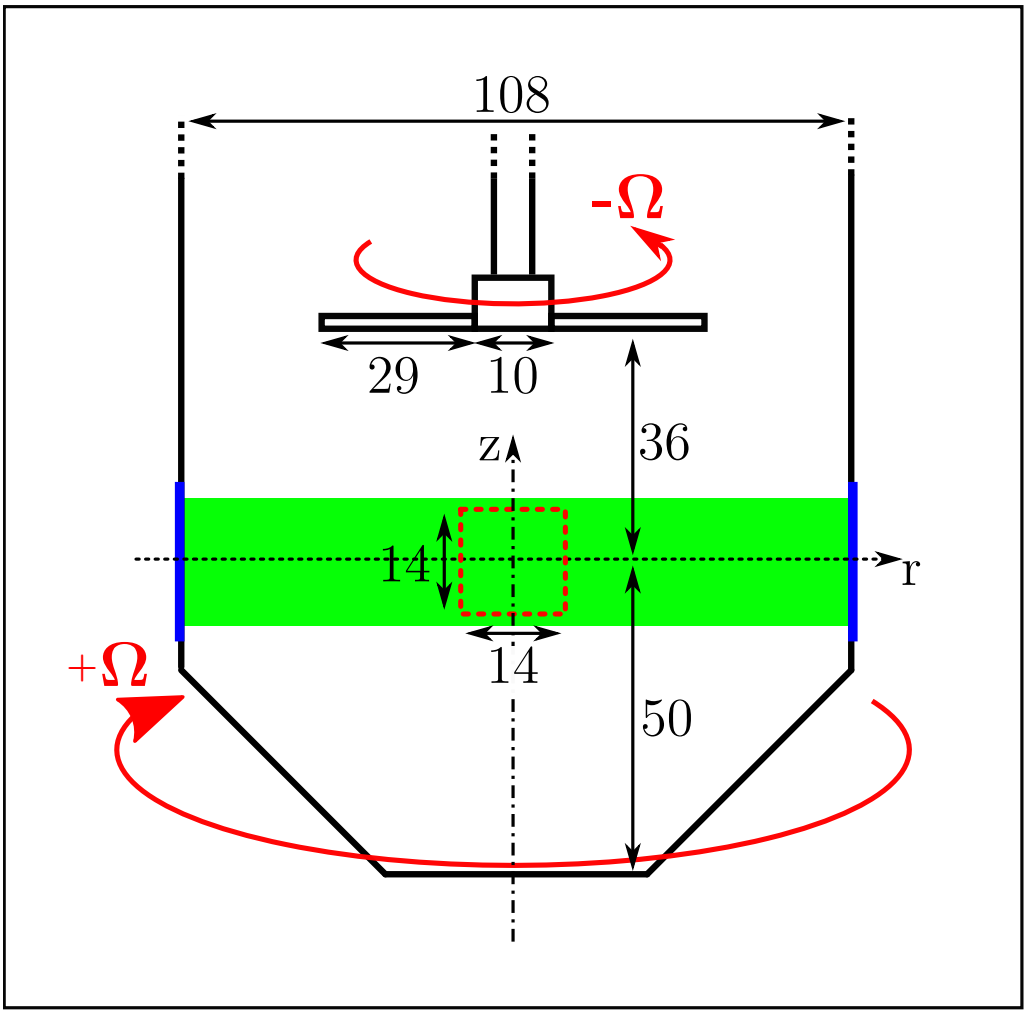

Figure 4.21: Schematic $(\vec{r}, \vec{z})$ view of the experimental setup for section 4.3. The dimensions are in mm. The propeller is the flat one shown on figure 2.14.

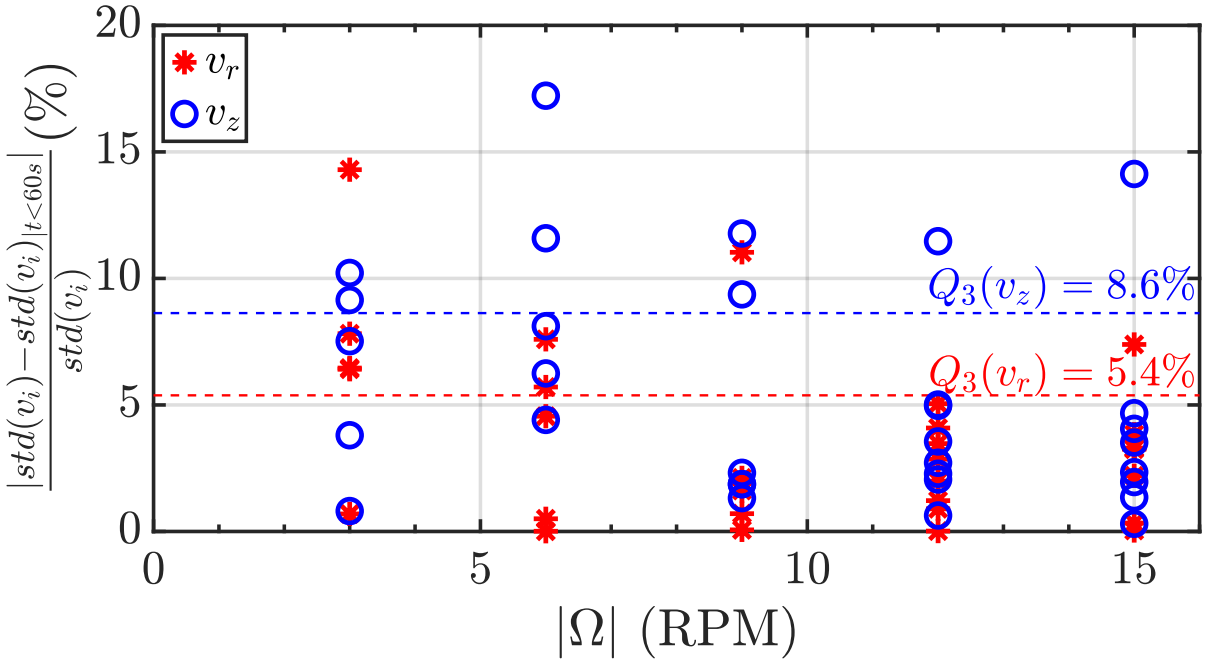

Figure 4.22: For each acquisition, we compute the difference of velocity standard deviation between the first $60s$ and the complete movie. This has been done for both velocity components ($\mathbf{v_r}$ and $\mathbf{v_z}$). The third quartile of each distribution is represented by the dashed line. In 75% (= 24/32) of the acquisitions, the difference of horizontal velocity standard deviation between the beginning, and the whole movie is below 5.4%.

located at the beginning. In the figure 4.22, the standard deviation (std) of all the particles' velocities recorded during the first $60s$ is compared to the one of the whole movie. This has been done for both the horizontal and vertical components, and the third quartile of each distribution is shown.

The std differences found can be up to 15% in the horizontal case, and 17% in the vertical one. However, considering the third quartiles, we notice that 75% of the movies have a horizontal velocity std difference of less than 5.4%, which is very satisfying. In the vertical direction, this value increases to 8.6% as the differences are more scattered. This scattering also increases when Ω decreases. Indeed, the value of the velocity std decreases with the forcing intensity. Therefore, a small perturbation produces larger relative differences at low Ω. This is also why the differences are larger with the vertical std, as it is smaller than the horizontal one.

As the steadiness of the data is satisfying, the repeatability of the experiments will now be verified. For this purpose, the velocity PDF of each acquisition has been computed. For clarity, they will be reduced to their first two moments: the mean and the standard deviation (fig. 4.23, top).

On the figure 4.23, the error bars are estimated using the different movies. They are equal to the std of the different values obtained at each Ω. The mean vertical velocity is always negative, and without dependence on Ω: $\langle v_z \rangle \simeq -0.45 mm/s$. This negative value is due to the density difference between the solid deuterium particles and liquid helium II. It is weakly affected by the forcing, because of its radial nature (the propeller being flat). It corresponds to particles of diameter $\langle d_p \rangle = 4.9 \mu m$, as discussed in section 2.3.1. On the other hand, the mean horizontal velocity is mostly positive, with different values. The reason for these positive means is unclear as the forcing is axisymmetric. We could assume that the field of view and/or the laser sheet are not centered on the rotational axis, but in this case the sign of the mean would change with the sign of Ω, which is not the case. Above $9RPM$, the values are very high, and widely scattered. In order to overcome this problem, the mean flow has

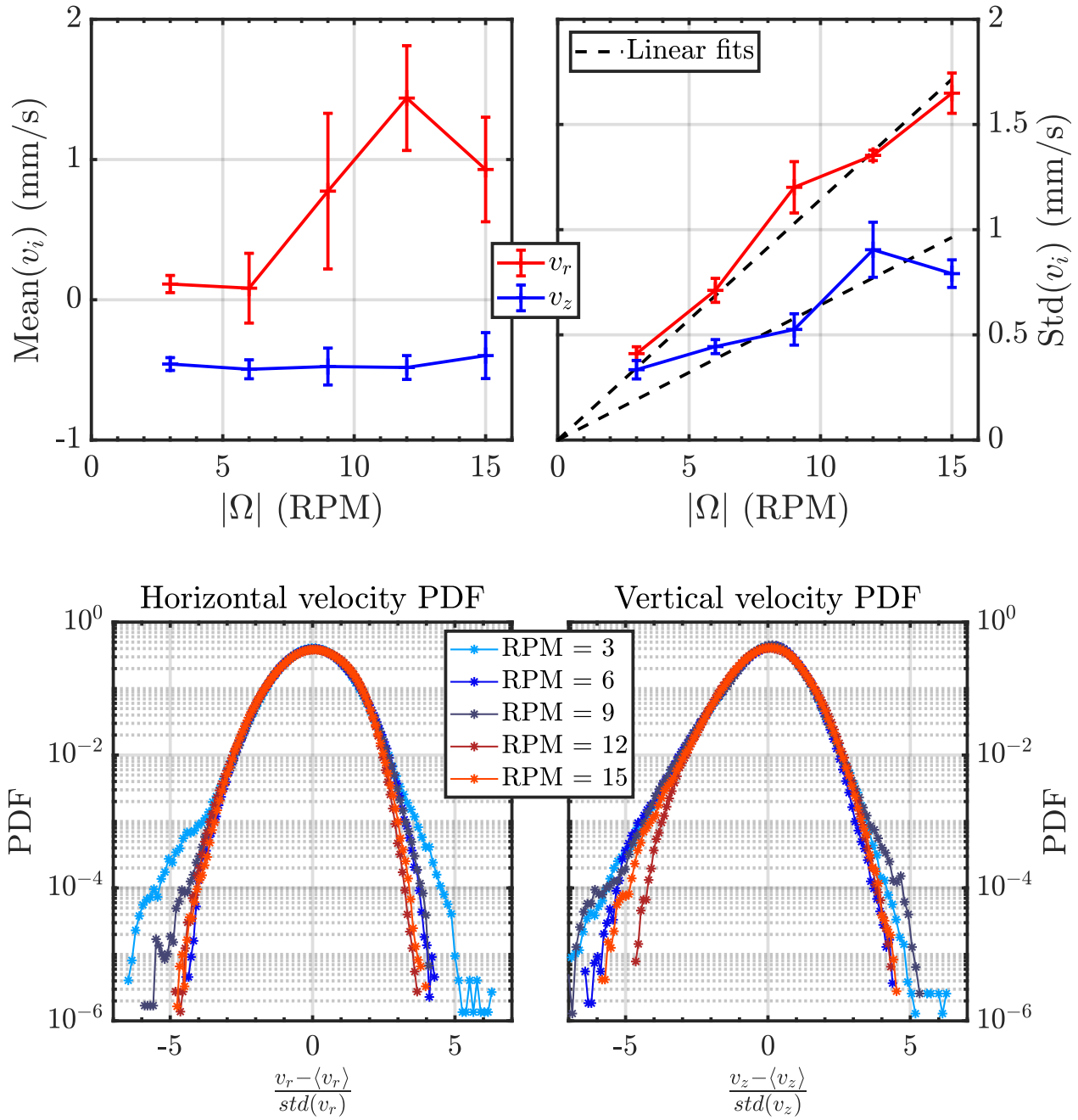

Figure 4.23: Top left: Evolution of the mean of each velocity distribution as a function of Ω. The displayed value is the mean velocity computed using all the movies acquired at each Ω. Then, the mean velocity of each single acquisition is computed, and the standard deviation of the results is used to generate the error bars. Top right: Evolution of the standard deviation (Std) of each velocity distribution as a function of Ω. The points and error bars are obtained by the same process as for the mean. A clear linear trend is observed for v_r and v_z. Bottom: Probability density functions of velocity components of the merged data sets. The mean flow has been removed, hence the zero mean. The abscissa axis has been normalized by the velocity standard deviation, resulting in perfectly superimposed PDF.

been removed in all the data. In each acquisition, the mean Eulerian map $\overrightarrow{\overline{v}(r,z)}$ is computed, and subtracted using a bilinear interpolation from all the points, resulting in mean values on the order of a $\mu m/s$.

The results of the standard deviation are more constant from one movie to another. In the horizontal direction, the relative differences between movies with the same forcing is between 2% at $12RPM$ and 12.5% at $9PRM$. As for the steadiness, these gaps are larger in the vertical direction. They are between 9% at $15RPM$ and 17% at $9RPM$. This is partly due to the lower values of the vertical standard deviation, compared to the horizontal one. The largest discrepancies occur at $9RPM$ on the two top graphs of the figure 4.23, and with both components. At this rotation rate, the standard deviation is different when $\Omega < 0$ or $\Omega > 0$. The sign of Ω cannot be the cause of a different standard deviation, but these two groups were not recorded the same day. Thus, as in the section 4.2.1, the discrepancies can be attributed to a change of play in the rotating parts of the cryostat. Overall, the repeatability of the experiment is satisfying and the merged centered and reduced velocity PDF are shown on fig. 4.23, bottom. Their cores are perfectly superimposed, but some small discrepancies can be observed in the tails, especially at $\Omega = 3RPM$. Overall, they all display a gaussian behavior, which is commonly observed in a turbulent flow.

The standard deviation also displays a clear linear trend in the horizontal direction. The linear fit in the vertical direction is less convincing, as it seem to collapse at $15RPM$. Experiments at higher Ω would be needed to clarify this scaling. In this spinning flow, the linear scaling of the standard deviation can be explained using an energy balance. In such a steady state closed flow, the power injected by the propeller must be dissipated by the turbulent fluctuations: $\mathcal{P}_{inj} = \mathcal{P}_{diss}$. The latter can be easily expressed thanks to the energy dissipation rate ϵ:

$$\mathcal{P}_{diss} = \rho \mathcal{V} \epsilon \tag{4.5}$$

where $\mathcal{V}$ is the volume of fluid. On the other hand, the injected power is $\mathcal{P}_{inj} = \Gamma\Omega$, where Γ is the torque needed to sustain the propeller in motion. In a turbulent flow, this torque is proportional to the fluid velocity squared:

$$\Gamma = C_d \rho (L_p \Omega)^2 \mathcal{V} \tag{4.6}$$

where C_d is a dimensionless quantity known as the drag coefficient, and $L_p = 34mm$ is the radius of the propeller. Writing down the power budget leads to the following relation:

$$\begin{aligned} \epsilon =& C_d L_p^2 \Omega^3 \\ \implies \quad & \epsilon \propto \Omega^3 \end{aligned} \tag{4.7}$$

Additionally, the equation 1.5 states that $\epsilon = \frac{\sqrt{\langle v^2 \rangle}^3}{L}$, which demonstrates our point here:

$$\sqrt{\langle v^2 \rangle} \propto \Omega \tag{4.8}$$

Using the results from figure 4.23, it is possible to estimate a Reynolds number based on the propeller radius L_p, and the apparent helium II viscosity $\nu = 1.186 \times 10^{-8} m^2/s$ (at $P = 40mbar$) [23]. Moreover, a first order dissipation rate $\epsilon^{(1)} \propto \frac{\sqrt{\langle v^2 \rangle}^3}{L}$ can be estimated using equation 1.5. Each quantity can be computed with each velocity components, so we have:

$$\begin{aligned} Re_{Lr} = \frac{L_p \sqrt{\langle v_r^2 \rangle}}{\nu} \quad \& \quad Re_{Lz} = \frac{L_p \sqrt{\langle v_z^2 \rangle}}{\nu} \\ \epsilon_r^{(1)} = \frac{\left(\sqrt{\langle v_r^2 \rangle}\right)^3}{L_p} \quad \& \quad \epsilon_z^{(1)} = \frac{\left(\sqrt{\langle v_z^2 \rangle}\right)^3}{L_p} \end{aligned} \tag{4.9}$$

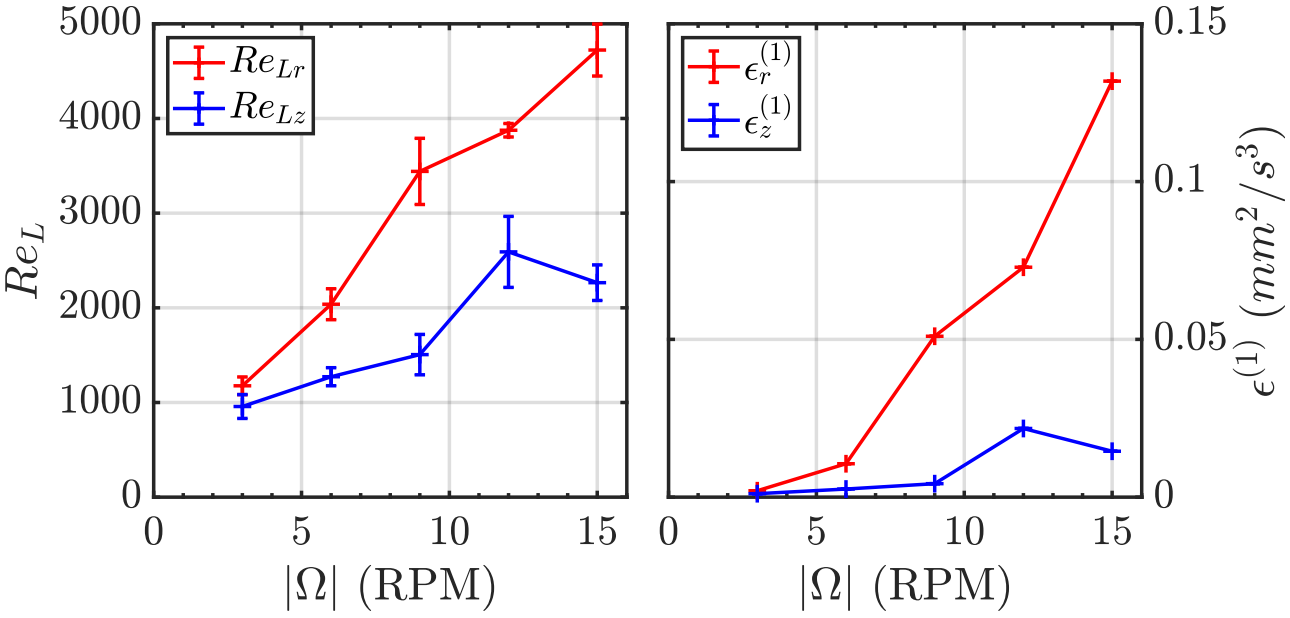

Figure 4.24: Reynolds numbers based on the propeller radius $L_p = 34mm$ (left) and dissipation rates (right) computed using the velocity standard deviations from figure 4.23, and the equations 4.9. The error bars come from the difference of std between the different movies ($< 10\%$) visible on fig. 4.23, top right. In the case of $\epsilon^{(1)}$, they are smaller than the size of the markers.

The results are given on figure 4.24. The Reynolds number scales linearly between 1200 and 4800 in the horizontal direction. These moderate Reynolds numbers suggest that turbulence should be observed at least for the highest values of Ω. In the vertical direction, the values are smaller: they are between 1000 and 2500.

These first order estimates only give orders of magnitude of the dissipation, and characterizing a turbulent cascade with them would not be relevant. However, these values are a good reference point for comparison in the higher-order calculations that will follow.

Experiments with a propeller in a rotating classical fluids have already been studied in the literature. In 2016, Campagne et al. [154] published an article in which several configurations are investigated, including the anticyclonic one ($Ro = \frac{\omega}{\Omega} < 0$) which is studied here ($Ro = -2$ here, as $\omega = -2\Omega$ in the rotating frame). Based on this work, and considering the fact that the field of view is far from the propeller, we should observe a rigid rotation of the fluid with an angular velocity $\beta \times \Omega$ ($\beta \in \mathbb{R}$), in the rotating frame of reference. This means that, in our configuration, the average velocity of the particle will be out of plane, hence not measurable directly.

At first sight, the observed particles trajectories are compatible with the observations of ref. [154] (fig. 4.25). There are long tracks in the middle of the image, and shorter ones at the edges. Thus, in order to quantify the out of plane velocity, the average residence time of the particles inside the laser sheet t_{res}, conditioned on their mean radial position r is computed. Based on the drawing on figure 4.26, we expect $t_{res} = \frac{2}{\beta\Omega} arcsin(\frac{e}{r})$ if $r > e$, the half thickness of the laser sheet. If $r < e$, we expect t_{res} to be infinite, which corresponds experimentally to $t_{res} \gg \frac{2\pi}{\Omega}$. Moreover, if $r \gg e$, it is possible to consider the following approximation:

$$t_{res} = \frac{2}{\beta\Omega} arctan(\frac{e}{r}) \tag{4.10}$$

This approximation has the advantage to be equivalent to the original expression for large r, while

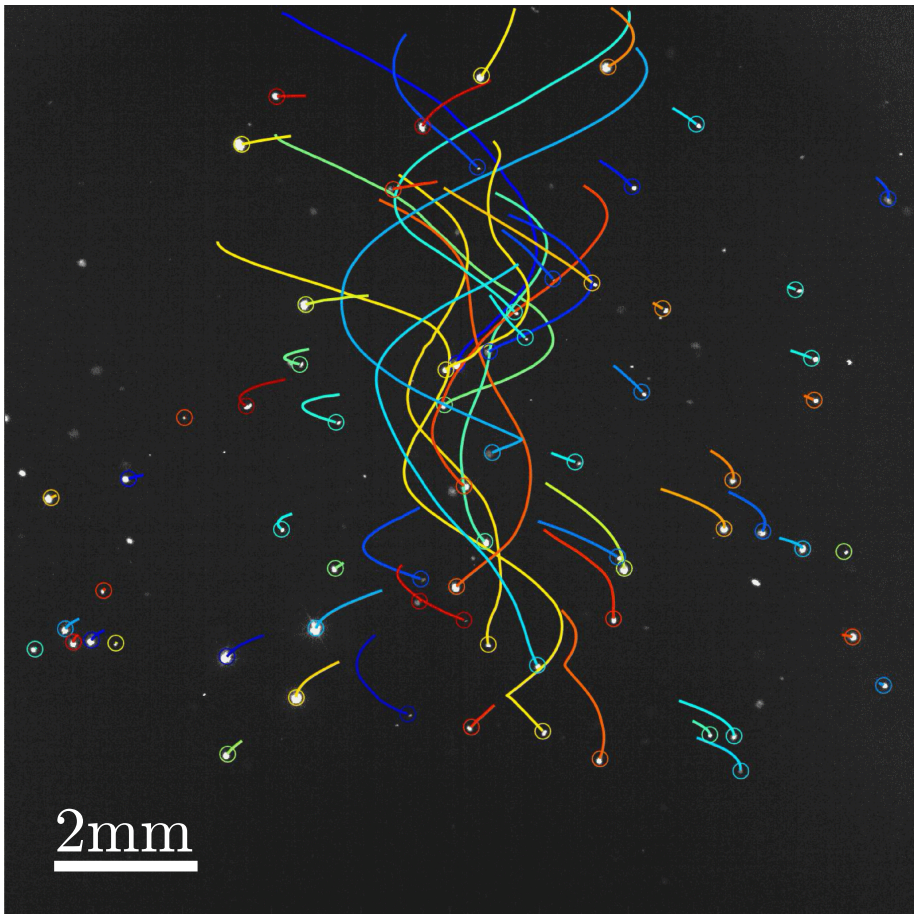

Figure 4.25: Image of particles in motion in helium II while the CryoLEM was rotating at $-15RPM$ and the motor at $15RPM$. The detected particles are circled, and the lines correspond to their past position. A color is randomly attributed to each detected particle.

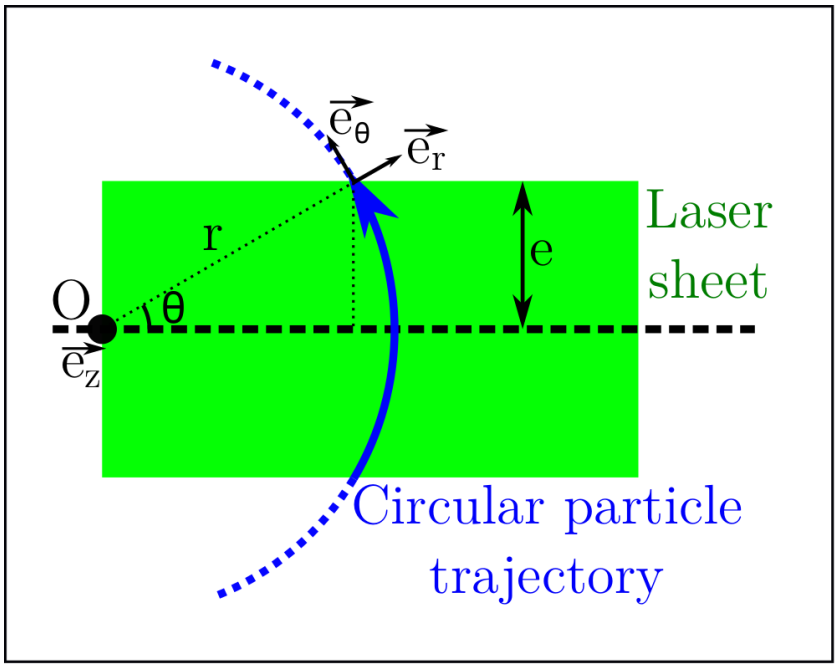

Figure 4.26: Drawing of a circular particle trajectory, crossing a laser sheet of half thickness e.

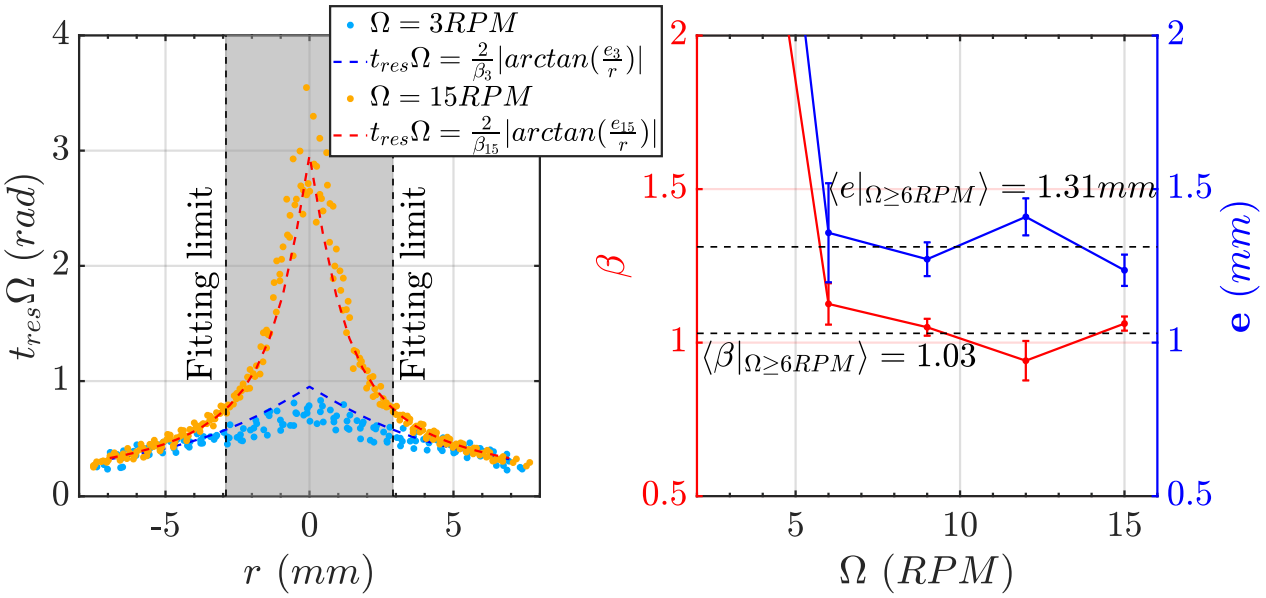

Figure 4.27: Left: example of normalized residence time as a function of the horizontal position for the data acquired at 3 and $15RPM$. The horizontal position in each movie has been shifted so that the peak of t_{res} stays at $r = 0$. The tails ($|r| > 2.9mm$) are fitted with an *arctan* function according to equation 4.10. The fit is also accurate in the non-fitted (grayed) interval. Right: Results of the free parameters of the fit. At $3RPM$, the period of rotation is too long to produce accurate results. At $6RPM$ and above, the results become consistent, and are averaged together (dashed line). The error bars represent the standard deviation of the results computed on each acquisition.

avoiding the discontinuity when $r < e$.

Besides, the value of e is not precisely known, especially at the center of the cryostat. This is why it will be set free in the fitting algorithm which will compute two parameters: β and e. In order to determine the optimal fitting range in r, the fitting algorithm has been run with different limits r_{min} between 1 and $5mm$, so that $|r| > r_{min}$. Then,the limit which provided the most consistent output value for e considering all the measurements has been chosen, since the laser sheet is unchanged. The value used is $r_{min} = 2.9mm$.

The results of this process are displayed in figure 4.27. The graph on the left shows a good agreement between the fit and the data. Note that these fits have been done on all acquisitions one by one. By doing so, we have noticed that the peak of residence time could be shifted from $r = 0$ by several millimeters on some movies. Thus, before fitting, the maximum residence time was detected, and shifted back to $r = 0$. This is why r varies between -8 and $8mm$ despite the field of view being $14.3mm$ wide.

The graph on the right shows that the fits return similar values of e and β, except at $\Omega = 3RPM$. At this low value, the rotation period ($20s$) is too long to produce relevant data. Indeed, the residence time of a particle is in fact the minimum between three time constants:

- The time during which a particle is "swept" by the laser sheet (eq. 4.10). This time depends directly on Ω.
- The time necessary for a settling particle to cross the height of the field of view H_{FoV} from top to bottom: $t_{settle} = \frac{H_{FoV}}{v_{settle}}$
- The average time at which a track is prematurely cut due to a misdetection of the algorithm.

Thus, we can assume that, at $3RPM$, the residence time is not dominated by the laser sheet sweeping, and other effects are involved. This leads to a residence time four times shorter than expected, with large discrepancies between the different acquisitions.

On the other hand, above $6RPM$, the results become consistent, and an average value of e and β can be computed. On average, $< e >= 1.31mm$ which is in good agreement with the laser sheet thickness measured at the entrance of the cryostat. The value of β is very close to 1, which indicates that the particles rotate at $\omega_p = \Omega$ in the rotating frame of reference. As our method using the time of residence only allows to estimate the absolute value of β, there are two possibilities in the laboratory frame: $\omega_p = (1 \pm \beta)\Omega$. As the motor is rotating at $\omega = -\Omega$, the option $\omega_p = 2\Omega$ is unlikely. It comes out that, in the laboratory frame, the particles, hence the fluid, are not spinning.

This means that, in the middle of the helium II bulk, the contribution of the motor, and the one of the cryostat rotation compensate for each other. It would be interesting in this case, to vary the ratio $Ro = \frac{\omega}{\Omega}$, and compute β again. This has been done in the article of Campagne et al. [154]. They have not reported the average radial profile in the case $Ro = -2$, but their figure 5 display the out-of-plane velocity profile in the cases $Ro = -3$ and $Ro = -12$. They also observe a cylindrical flow in which the average angular velocity differs from the forcing. An extrapolation of their data to $Ro = -2$ agrees with the value $\beta = 1$. The fact that the fluid is not spinning (on average) in the laboratory frame does not mean that turbulent dissipation processes do not occur. Thus, structure functions will now be used to investigate the energy distribution among scales, and the dissipation in this turbulent flow.

As in the section section 4.2.1, the 2D-scale dependent energy distribution will be studied. After checking the consistency of the data, the acquisitions of the same angular velocity Ω are merged, and the maps on figure 4.28 are computed according to equation 4.4.

These maps represent the amplitude of the second order structure function $\overline{E}$ as a function of the separation $\overrightarrow{ds} = dr\overrightarrow{e_r} + dz\overrightarrow{e_z}$. Obviously, the amplitude of $\overline{E}(dr, dz)$ increases with the forcing, as it reflects an energy per unit mass. Actually, for the same reasons that explain the linearity of the velocity standard deviation, we have $\langle \overline{E}(dr, dz) \rangle \propto \Omega^2$.

The amplitude of $\overline{E}(dr, dz)$ also increases with the distance. However, as in section 4.2.1, $\overline{E}(0, 0) \neq 0$ because of the width of the laser sheet. If particles are apparently separated by a distance $||\overrightarrow{ds}|| = 0$ on the camera sensor, they can actually be separated by up to $2e$ in the out of plane direction, hence having different velocities (more details in appendix B). Moreover, it is clear that the evolution of $\overline{E}(dr, dz)$ becomes anisotropic when Ω increases. Indeed, the vertical contour lines above $9RPM$ indicate that

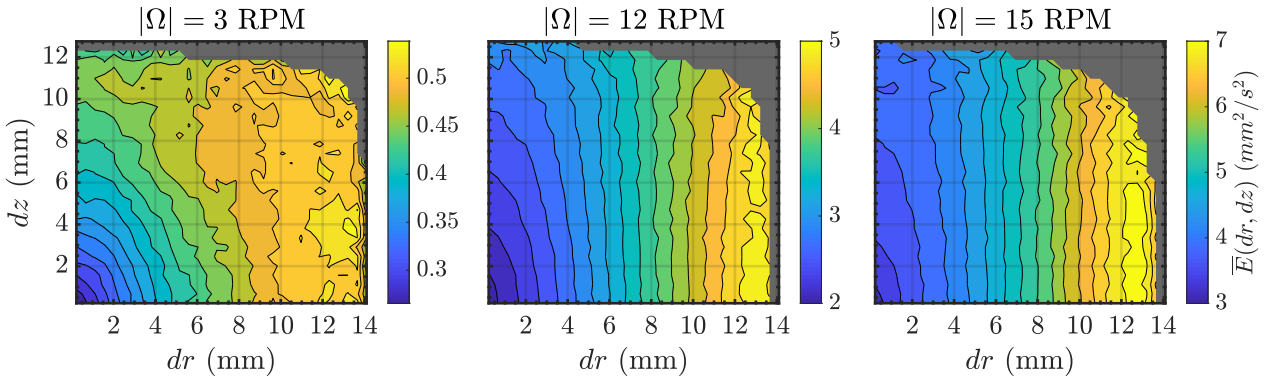

Figure 4.28: Second order structure function as a function of the separation between particles $\overline{E}(dr, dz)$. As in section 4.2.1, this map is computed from equation 4.4. As Ω increases, vertical lines appear, which is a sign of an increasing anisotropy.

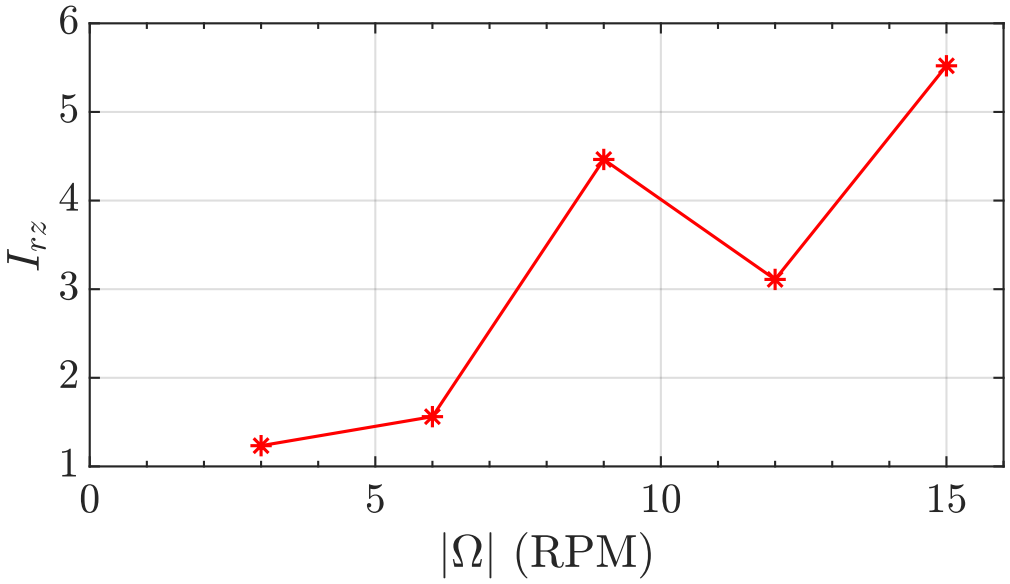

Figure 4.29: Evolution of the isotropy coefficient $I_{rz} = \frac{\overline{E}(8mm,0)-\overline{E}(2.6mm,0)}{\overline{E}(0,8mm)-\overline{E}(0,2.6mm)}$ as a function of Ω.

the energy increases faster with dr than with dz. This means that the correlation length is larger in the vertical direction. The rotation lengthen the turbulent structures, weakening the dependence of the dynamic quantities along the rotational axis. To quantify this phenomenon, the coefficient I_{rz}, defined in section 4.2.1, is used.

The evolution of I_{rz} as a function of Ω is depicted on figure 4.29. The anisotropy coefficient increases with Ω, in agreement with the Taylor-Proudmann theorem in a rotating flow. There is however a sudden increase between 6 and $9RPM$, which may correspond to the threshold to fully developed turbulence.

According to Kolmogorov's theory of homogeneous isotropic turbulence (HIT, see section 1.1.1), in the inertial range of the turbulent cascade, the second order structure function is strongly linked with the energy dissipation per unit mass ϵ (eq. 1.12):

$$S_2 \propto (\epsilon\ dr)^{2/3} \tag{4.11}$$

For the longitudinal second order structure function, the proportionality coefficient has been experimentally evaluated to be $C_2^{\parallel} = 2.0$ [9]. It is also possible to show, in the transverse direction that $S_2^{\perp} = \frac{4}{3}S_2^{\parallel}$. However, In this study, we used structure functions along the rotational axis (vertical direction), and the radial one (horizontal direction). We can then rewrite the decomposition of S_2 in both frames, and use the isotropy hypothesis:

$$S_2 = S_2^{\parallel} + 2S_2^{\perp} = \frac{11}{3}C_2^{\parallel}(\epsilon\ dr)^{2/3} \tag{4.12}$$

$$S_2 = S_2^{(r)} + S_2^{(\theta)} + S_2^{(z)} = 3S_2^{(r)} \tag{4.13}$$

Combining these two equations, we have, in HIT $S_2^{(r)} = S_2^{(z)} = \frac{11}{9}C_2^{\parallel}(\epsilon\ dr)^{2/3}$. Thus, ϵ can be expressed as:

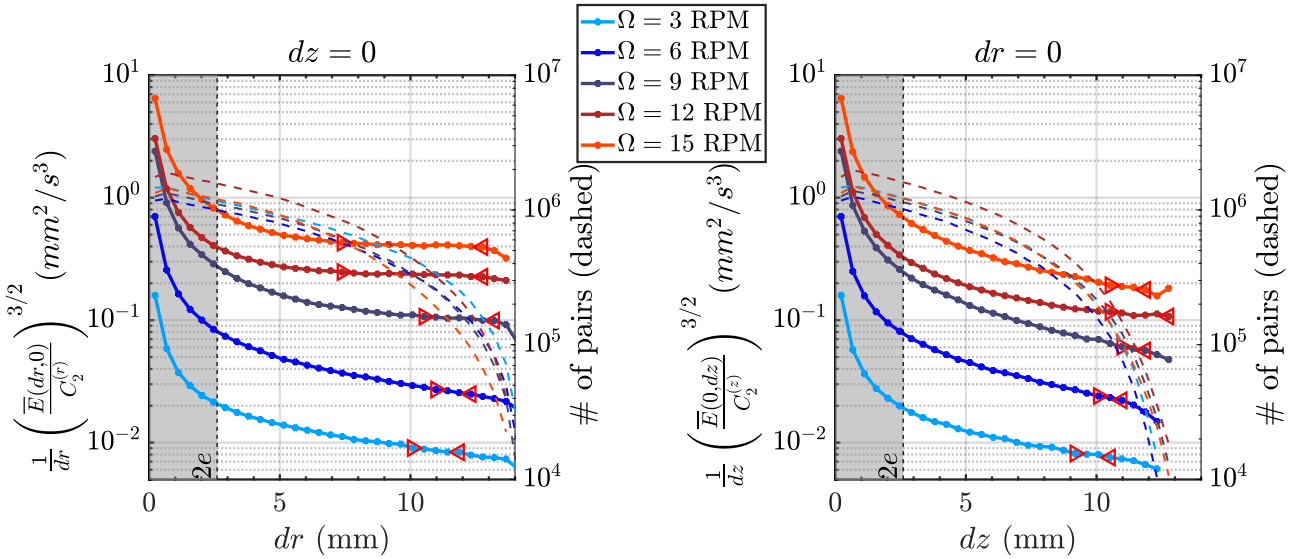

Figure 4.30: Left: the second order structure function conditioned on a null vertical separation ($\overline{E}(dr, 0)$) is used to compute the right hand side of equation 4.14. After a certain horizontal separation, this quantity becomes constant, in agreement with Kolmogorov's phenomenology of classical turbulence [5]. The red triangles (⋈) indicate the limits of the plateau. The dashed lines represent the number of particles pairs used to compute each value of $\overline{E}$. It decreases with the separation, due to the limited size of the acquired frames. Right: same process with a null horizontal separation: $\overline{E}(0, dz)$ is used.

$$\epsilon = \frac{1}{dr}\left(\frac{S_2^{(r)}}{C_2^{(r)}}\right)^{3/2} \tag{4.14}$$

where $C_2^{(r)} = C_2^{(z)} = \frac{11}{9}C_2^{\parallel}$. Thus, $S_2^{(r)} = \overline{E}(dr, 0)$ and $S_2^{(z)} = \overline{E}(0, dz)$ are used to compute the right hand side member of this equation. The figure 4.30 shows that above a certain separation, and when $\Omega \geq 9RPM$, $\frac{1}{dr}\left(\frac{\overline{E}(dr,0)}{C_2^{(r)}}\right)^{3/2}$ becomes constant. This means that, in this interval of separations, $\overline{E}(dr, 0)$ scales as $dr^{2/3}$, in good agreement with Kolmogorov's theory.

The limits of the plateaus are determined by an algorithm finding the largest sub-interval of a signal in which the values deviate less than 5% from their own average value in the sub-interval. In the case where several interval of same length fulfill this condition, the one with the lowest standard deviation is kept. The limits are highlighted by red triangles (⋈) on fig. 4.30, and define what we consider to be the inertial range. In the horizontal direction, the plateau hardly appears at 3 and $6RPM$. Therefore, we can argue that a transition to turbulence occurs between 6 and $9RPM$, corresponding to the sudden increase of anisotropy on fig. 4.29. In the vertical direction, a significant interval of 6 "constant" points is detected at $12RPM$, but the other graphs suggest that the inertial range does not appear here, or that the scaling exponent on the separation is smaller than $\frac{2}{3}$.

Using these results, the mean value of each detected plateau is used to compute a second order $\epsilon^{(2)}(\Omega)$. Following the same approach which was used with 1 point statistics, a value of dissipation $\epsilon^{(2)}$ is computed in the radial direction $\epsilon_r^{(2)}$, and in the axial direction $\epsilon_z^{(2)}$. The computed $\epsilon^{(2)}$ are then used to compute the characteristic properties of the turbulent cascade (fig. 4.31), according to Kolmogorov's phenomenology (section 1.1.1).

The value of $\epsilon_r^{(2)}$ is on average 3 times larger than $\epsilon_r^{(1)}$ and $\epsilon_z^{(2)}$ is 10 times larger than $\epsilon_z^{(1)}$. However, it must be kept in mind that the computed values of $\epsilon^{(1)}$ are only a first order estimate of the dissipation rate. A fundamental difference between $\epsilon^{(1)}$ and $\epsilon^{(2)}$ is the use of the propeller radius

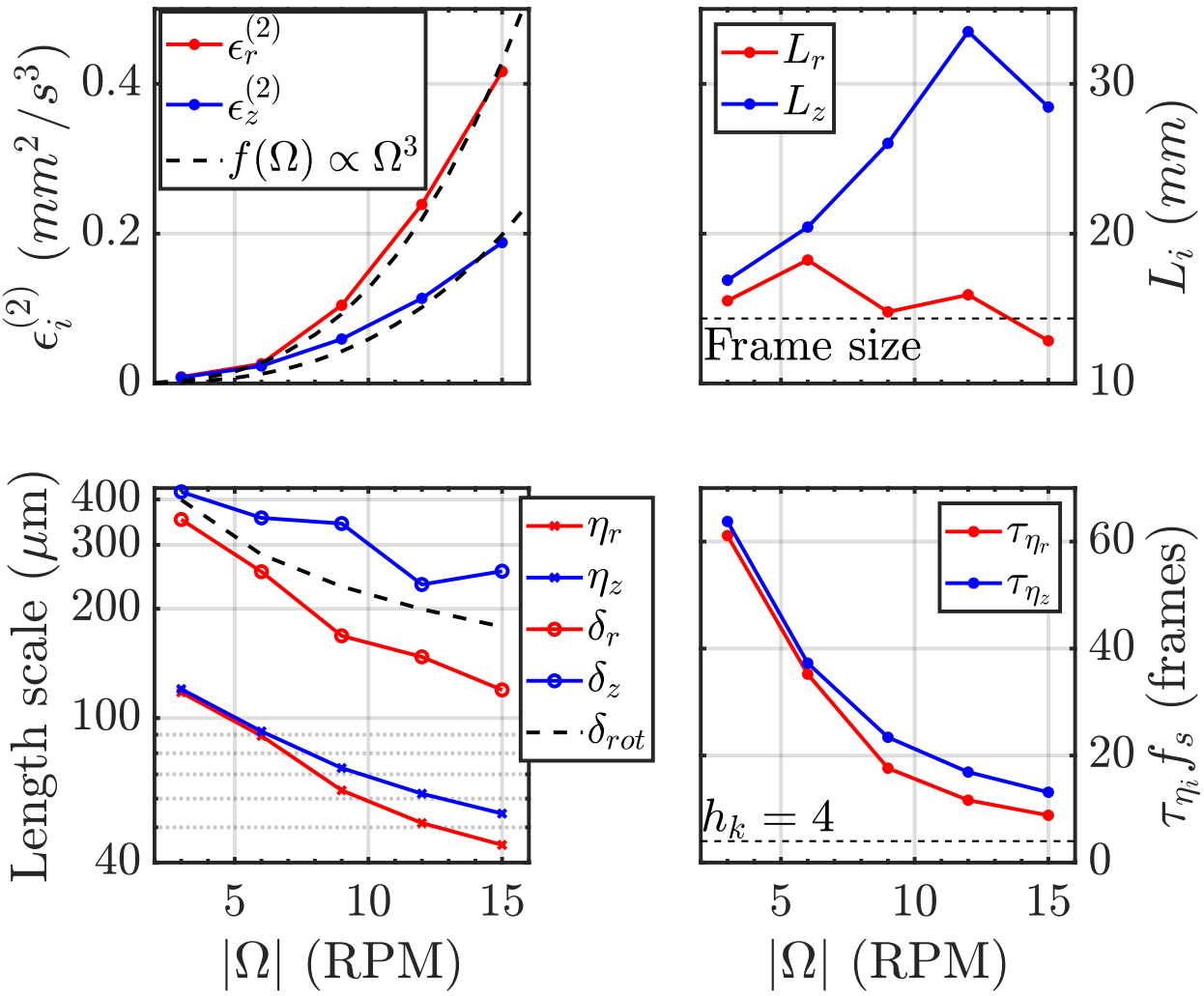

Figure 4.31: The value $\epsilon^{(2)}$ is directly extracted from the figure 4.30 as the mean of each plateau. Then, the equations 1.5, 1.7, and 1.9 are respectively used to compute $L_i = \frac{\left(\sqrt{\langle v^2 \rangle}\right)^3}{\epsilon_i}$, $\eta_i = \left(\frac{\nu^3}{\epsilon_i}\right)^{1/4}$ and $\tau_{\eta_i} = \sqrt{\frac{\nu}{\epsilon_i}}$ (where i is r or z).

L_p, which is different from the integral length scale L. Moreover, the measurements reported on figure 4.30 (left) are convincing enough to state that the scaling of $\overline{E}(dr, 0)$ as $\left(\epsilon_r^{(2)} dr\right)^{2/3}$ is relevant for this flow in the radial direction. Therefore the values of $\epsilon_r^{(2)}$ reported on figure 4.31 are trustworthy, at least for the "high" Re cases ($\Omega \geq 9RPM$). This is further demonstrated by the clear Ω^3 scaling, which is consistent with the energy balance previously reported (eq. 4.7).

Moreover, it is straightforward, using equation 1.5, to show that if $\sqrt{\langle v^2 \rangle} \propto \Omega$ and $\epsilon \propto \Omega^3$, then the integral length scale $L_i = \frac{\left(\sqrt{\langle v^2 \rangle}\right)^3}{\epsilon_i}$ should be constant. This is actually the case for L_r on the top right graph of figure 4.31. The vertical direction is less ideally described by the framework we developed though. First, the scaling of $\overline{E}(0, dz)$ as $\left(\epsilon_z^{(2)} dz\right)^{2/3}$ is highly questionable, if not wrong (fig. 4.30, right). Indeed, the inertial range found by our method is so small that it would be audacious to call it "a plateau". The 2/3 exponent is clearly too high. Therefore, the $\epsilon_z^{(2)}$ values measured this way

are more a function of the exponent we have chosen, than a reliable estimation of the dissipation rate. These remarks could be made about the $\Omega \leq 6RPM$ data sets in the radial direction as well. This naturally raise the question of exploring higher Reynolds numbers ($\Omega > 15RPM$), in order to discover if the 2/3 scaling can be reached in the vertical direction. We will nevertheless use these values as an ersatz, knowing their limits.

The first limit that we encounter is the $\epsilon_z^{(2)} \propto \Omega^3$ scaling. On the linear representation of figure 4.31, it looks reasonable, but if we look at it in a logarithmic plot, it is not well satisfied (see further, in fig. 4.36). A direct consequence is the trend of L_z (fig. 4.31, top right) which grows with Ω, while L_r is constant. This result goes in favor of our ersatz since we physically expect the vertical integral length to grow with Ω, according to the Taylor-Proudman theorem. We are actually able to grasp this trend with our processing method. However, we will not claim that the length scale L_z is the actual correlation length, as it is twice larger than our field of view. On the contrary, the computed value of L_r should be relatively accurate. Indeed, for horizontal separations dr larger than L_r, we observe that $\overline{E}(dr \geq L_r, dz)$ begins to decrease. For example, at $\Omega = 15RPM$, we find $L_r = 12.8mm$, and on the rightmost contour plot of fig. 4.28, we see that $\overline{E}$ starts to decrease when $dr \geq 13mm$. If this is not an artifact caused by a lack of data at large separations, the value of L_r computed from $\epsilon_r^{(2)}$ is consistent with the correlation length which can be observed on figure 4.28.

The dissipative scales (fig. 4.31, bottom left) in the horizontal direction are decreasing from $\eta_r = 118\mu m$ to $\eta_r = 45\mu m$. In the vertical direction the values are quite similar: they decrease from $\eta_z = 120\mu m$ to $\eta_z = 55\mu m$. In order to compare this small length scale with a quantity related to the quantum vortices distribution, we have plotted different values of the inter-vortex spacing. First, the black dashed line represents the inter-vortex spacing in a steadily rotating helium II bulk, given by Feynman's rule (eq. 1.32): $\delta_{rot} = \sqrt{\frac{\kappa}{2\Omega}}$, where κ is the quantum of circulation. Second, two quantities δ_r and δ_z have been computed adapting the equation 1.24 ($\frac{\delta}{L} = 0.5Re_\kappa^{-3/4}$):

$$\delta_i = \frac{L_i^{-1/4}}{2} \left(\frac{\sqrt{\langle v_i^2 \rangle}}{\kappa} \right)^{-3/4} \tag{4.15}$$

where i should be replaced by r or z. This expression gives the inter-vortex spacing in a turbulent flow.

All the graphs of this plot show a similar decreasing trend. An interesting fact is that the values of δ_r and δ_z are of the same order as δ_{rot}. The rotation of the propeller disorganizes the lattice which is theoretically aligned with the vertical rotational axis, and reduces the inter-vortex distance in the horizontal direction by an average factor 1.3. On the other hand, the radial Kolmogorov length scale η_r is on average 2.8 times smaller than the radial inter-vortex separation. In the vertical direction, this factor is about 4.1. Thus, comparing the dissipative length scale to the inter-vortex distance is relevant as they scale similarly, and have values of the same order of magnitude. However, the equation 1.24 has been tested in homogeneous and isotropic flows, which is not the case here. Thus, the accuracy of the anisotropic interpretation we used (eq. 4.15) still has to be demonstrated. In order to validate it, it would be interesting to perform the same experiments while equipping the CryoLEM with (at least) two second sound probes with different orientations.

The fastest time scale of the flow is normalized by the acquisition frame rate on the bottom right graph of figure 4.31. It varies between ~ 60 frames ($3RPM$) and 9 frames ($15RPM$), which means that each small eddy is measured by at least 9 points per turnover. This satisfies the Nyquist-Shannon sampling theorem, but we must keep in mind that the tracks have been low-pass filtered (section 3.2.3), with a time constant of $h_k = 4$ frames. Therefore, if larger values of Ω are investigated in the future, it will be necessary to increase the time resolution.

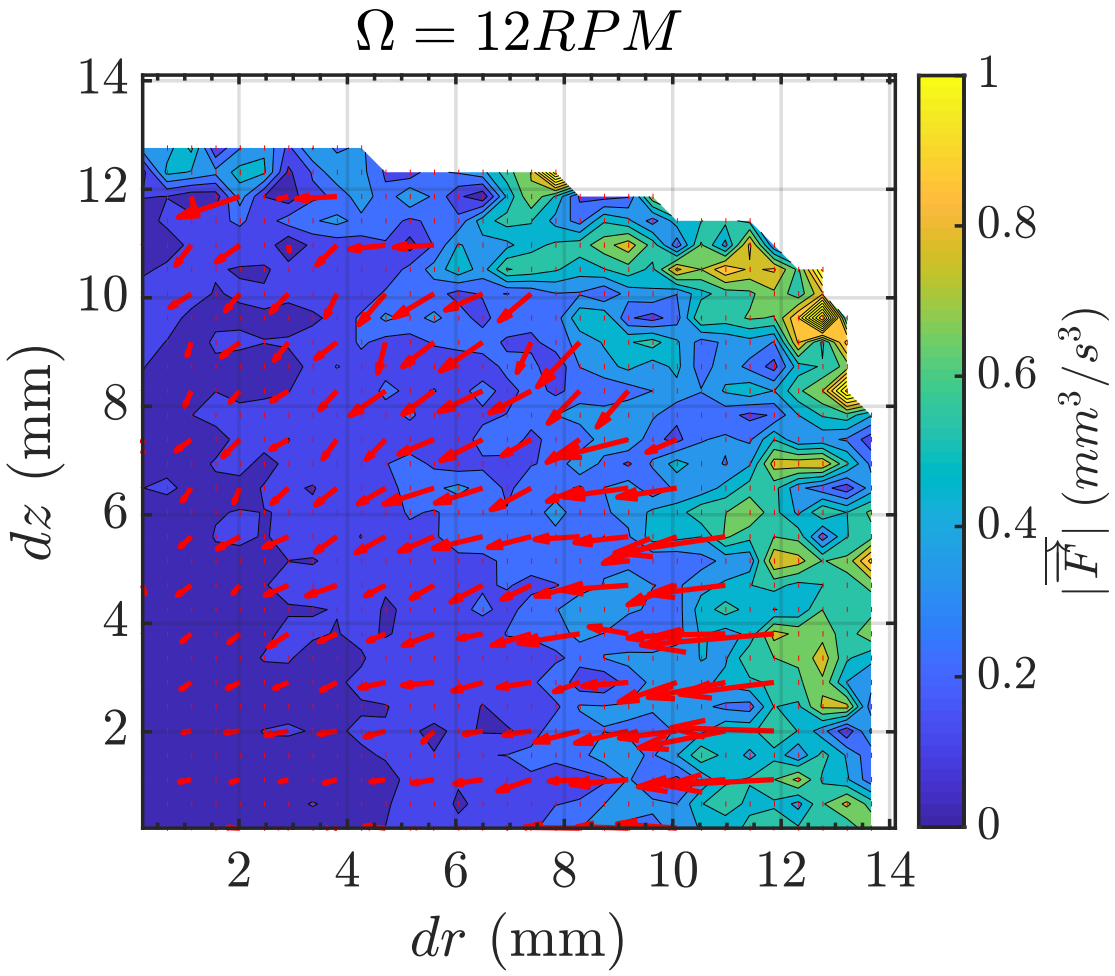

Figure 4.32: Time-averaged energy flux densities (eq. 4.17) computed with the acquisitions recorded at $\Omega = 12RPM$. It is under these conditions that the most data has been acquired, resulting in a better convergence of the results. As in figure 4.28, the number of particle pairs in the white areas was not considered sufficient ($< 10^4$) to produce relevant results. For a better readability, the arrows on the edge ($|\vec{ds}| > 12.5mm$) have been removed, and only one arrow in two is shown elsewhere. The $\vec{F}$ vector fields computed with the other data sets are shown in the appendix C.

Although the Kolmogorov's phenomenology has given very good results, it is only valid in isotropic flows, which is not our case. In an anisotropic flow, the tools detailed in section 1.1.2 can be used. The Karman-Howarth-Monin equation leads to the computation of third-order statistics. Indeed, as explained in section 1.1.2, in the inertial range, an exact derivation of the Navier-Stokes equation leads to:

$$\epsilon = -\frac{1}{4}\nabla\overrightarrow{F} \tag{4.16}$$

where $\overrightarrow{F}$ is the energy flux density in the space of separations $\overrightarrow{ds} = dr\overrightarrow{e_r} + dz\overrightarrow{e_z}$: $\overrightarrow{F}(\overrightarrow{ds}, t) = \delta\overrightarrow{v}(\delta\overrightarrow{v})^2$. As we are working with $2D$ measurements, the exact value of $\overrightarrow{F}$ will not be calculable. Thus, we will use $2D$ surrogates similar to the one used for the calculation of E:

$$\overrightarrow{F}(\overrightarrow{ds}) = \delta\overrightarrow{v}(\delta\overrightarrow{v_r}^2 + \delta\overrightarrow{v_z}^2) \tag{4.17}$$

This time-averaged quantity is shown on fig. 4.32 in the case $\Omega = 12RPM$. It has also been computed using all the other data sets (shown in appendix C), but the quantity of available data is

lower, and the turbulent regime is not fully established at low RPM. When the separation is smaller than $\sim 12mm$, the energy fluxes are predominantly oriented towards the smallest scales $dr = dz = 0$. This highlights the presence of an energy cascade from large to small scales, in agreement with Richardson's model. The fluxes norms are also larger at large scales than at small ones, which is also consistent with the figure 4.28 which showed that most of the energy is contained in the large scales. With these two observations, we can predict that the divergence of these fields will be negative, resulting in a positive dissipation rate according to the equation 4.16. At large separations, some vectors can be oriented randomly, which is due to the poorer amount of data in these areas.

The divergence of the vector fields of figure 4.32 is shown on figure 4.33. The boundaries of the plateaus determined with the second order structure functions are used here to highlight the inertial range. As we detected boundaries only in the horizontal ($dz = 0$) and vertical ($dr = 0$), we used ellipses to connect them and extrapolate the inertial range detection to all the directions. In the clear area of each figure, the divergence of $\overrightarrow{\overrightarrow{F}}$ is expected to be constant, and negative. However, the values are quite irregular and can double from a point to another, and reach positive values. This illustrates well the sensitivity of this data-intensive technique.

In order to obtain $\epsilon^{(3)}$ with equation 4.16, the values of $div(\overrightarrow{\overrightarrow{F}})$ are averaged together in the inertial range. Note that with this method, a single value of $\epsilon^{(3)}$ is obtained for all the directions. Considering the amount of data necessary, we decided not to restrict the calculation domain any further. The standard deviation is also computed in order to draw error bars.

On figure 4.34, the values of $\epsilon^{(3)}$ are an order of magnitude below the others, but with very large error bars. The error bars of $\epsilon^{(1)}$ and $\epsilon^{(2)}$ are not displayed, because they are below 5%, which is smaller than the marker size. The differences between $\epsilon^{(3)}$ and the others may come from the convergence of $\overrightarrow{F}$. Moreover, unlike E and $\sqrt{\langle v^2 \rangle}$, $\overrightarrow{F}$ is a signed vector, which makes it more sensitive to noise, and harder to average.

If the values of $\epsilon^{(3)}$ were used to characterize the turbulent cascade, as it has been done with $\epsilon^{(2)}$, the length scales, time scales, and Reynolds numbers would all increase by an order of magnitude. Then, the integral length scale would be larger than the size of the experimental cell, and the Kolmogorov length scale larger than the inter-vortex spacing of the steady rotating cases (which are laminar flows). Such low $\epsilon^{(3)}$ values lead to inconsistencies with our experimental setup. However, the scaling remains in good agreement with the Ω^3 prediction (eq. 4.7).

The expression 4.16 is certainly the closest to a proper definition of the energy dissipation rate in a turbulent flow. However, as we have just seen, it is very hard for experimental data to converge, especially in a cryogenic environment. Nevertheless, using the symmetries and invariances of the physical system studied, this expression can be dimensionally reduced. In homogeneous isotropic turbulence, this results in the celebrated $4/5^{th}$ law ($S_3^{\parallel} = -\frac{4}{5}\epsilon r$). In this case, because of the homogeneity and isotropy, the field of $\overrightarrow{F}$ is perfectly radial, and the computation of its divergence is doable analytically.

Solving this problem without assuming the isotropy (like in a rotating flow), is more complex though. In 2009, S. Galtier reported what could be considered as the equivalent of the $4/5^{th}$ law in the case of homogeneous rotating turbulence (eq. 54 in [16]):

$$\begin{aligned} \epsilon_r^{(3)} &= -\frac{1}{2}\frac{\langle \delta v_r \delta v_i^2 \rangle}{dr} = -\frac{1}{2}\frac{\langle \overrightarrow{F} \cdot \overrightarrow{dr} \rangle}{dr^2} = -\frac{1}{2}\frac{F_{rr}}{dr} \\ \epsilon_z^{(3)} &= -\frac{7}{16}\frac{\langle \delta v_z \delta v_i^2 \rangle}{dz} = -\frac{7}{16}\frac{\langle \overrightarrow{F} \cdot \overrightarrow{dz} \rangle}{dz^2} = -\frac{7}{16}\frac{F_{zz}}{dz} \end{aligned} \tag{4.18}$$

where $F_{ij} = \left\langle \frac{\overrightarrow{F} \cdot \overrightarrow{di}}{|\overrightarrow{di}|} \mid |\overrightarrow{dj}| \right\rangle$. In this case, $\epsilon^{(3)}$ remains a third order quantity, but it has the great advantage of averaging the components of $\overrightarrow{F}$ over the separation space (dr, dz). Therefore this quantity should converge with less data than eq. 4.16.

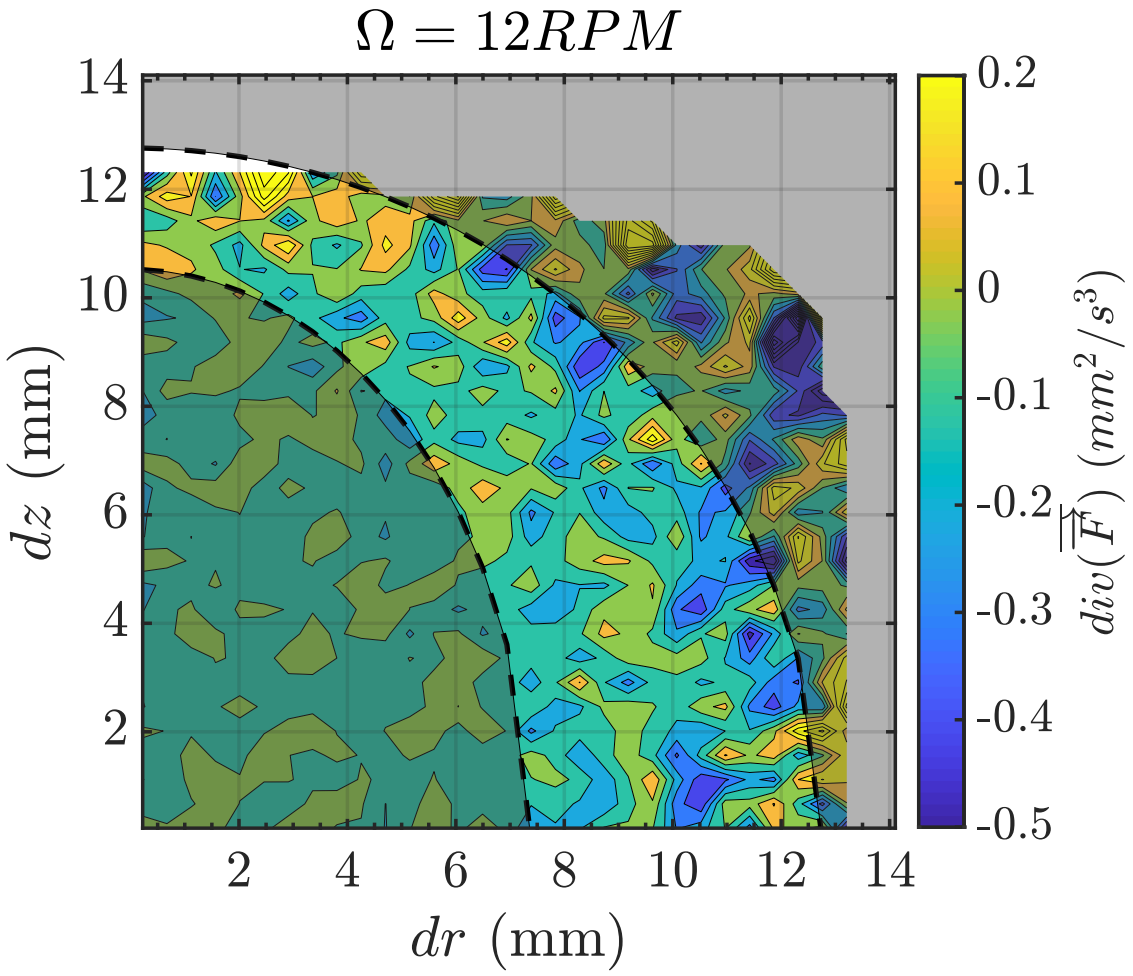

Figure 4.33: Divergence of the vector field displayed on figure 4.32. The scales corresponding to the plateau on figure 4.30 are used here to identify the inertial range. As these boundaries have been only measured in the horizontal and vertical directions, they have been extrapolated in every direction using ellipses. Thus, the non-grayed areas correspond to what we consider to be the inertial range. Note that a small white area (particle pairs $< 10^4$) is included in the inertial range, but it is an artifact from the Matlab contourf function representation. The divergence fields computed with the other data sets are shown in the appendix C.

The averages F_{ij} of our field $\overrightarrow{F}$ has been computed for all data sets (fig. 4.35). Galtier only makes predictions for F_{rr} and F_{zz} but we show the four projections for completeness. The graphs of F_{rr} have been linearly fitted (solid line) in the range detected on figure 4.30, left (highlighted by green triangles on fig. 4.35), which we still consider to be the inertial range. However, as no clear plateau is observed in the quantity $\frac{1}{dz}\left(\frac{\overline{E}(0,dz)}{C_2^{(z)}}\right)^{2/3}$ (fig. 4.30, right), the linear fit has been restricted to the range $dz \in [5:10]mm$. This choice is, of course, questionable, but fitting the whole range of dz had no physical meaning, and using the detected "plateau" of 4.30 would result in a fit where the values of F_{zz} suddenly increase, i.e. for $dz \geq 10mm$. This increase is due to a lack of data for large separations, and is observed on the four graphs of figure 4.35. Thus, the interval $dz \in [5:10]mm$ has been selected, as this is where a linear fit seems the most appropriated. On the other hand, the crossed projections F_{rz} and F_{zr} are negative and almost constant ($F_{rz} < F_{rr}$, and $F_{zr} < F_{zz}$). The diagonal terms F_{rr} and F_{zz} are:

- Negative, reflecting the direction of the energy fluxes from large to small scales without ambiguity.

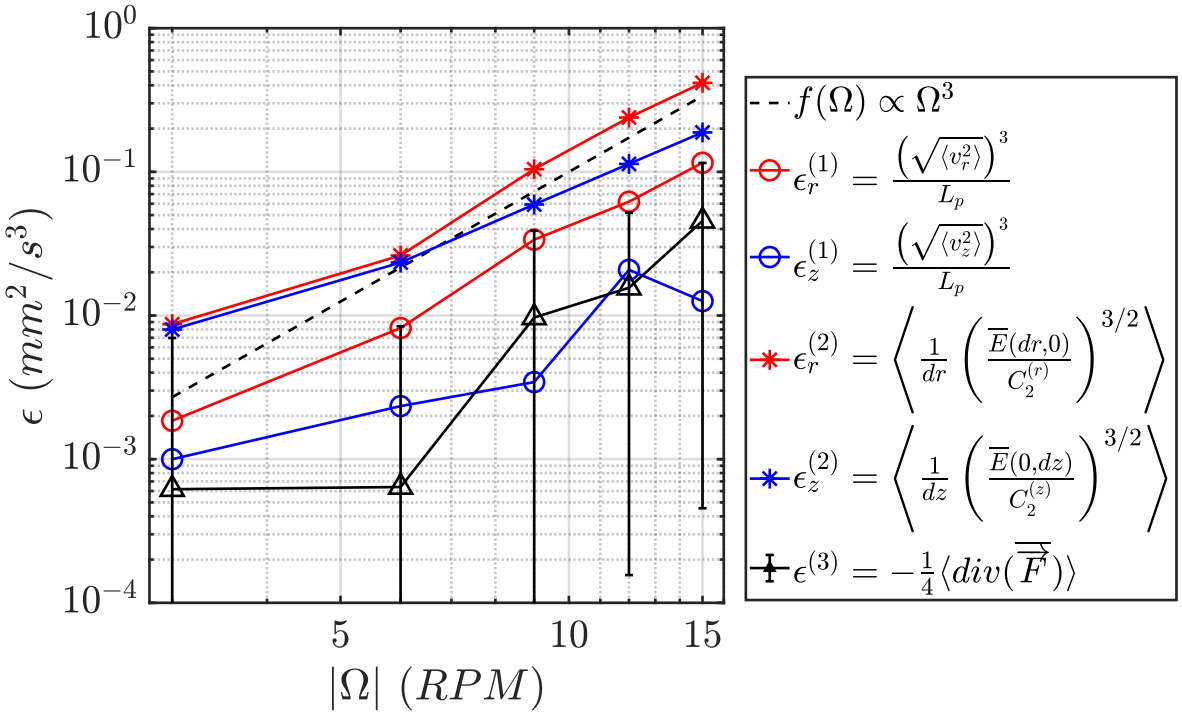

Figure 4.34: Summary of all the values of ϵ obtained with the different techniques, up to this point. The error bars on $\epsilon^{(3)}$ do not have a lower bound, as it is negative, hence non-representable on a logarithmic scale. The error bars of the other quantities are not represented as they would be smaller than the markers. The dashed line represents an Ω^3 scaling, which is predicted considering our power input (eq. 4.7).

- Linear with a negative slope.

This second point is not perfectly fulfilled, especially with F_{rr} at high RPM, which could be easily fitted with a dr^2. Despite the fact that this last observation breaks the validity of the model developed in [16], we applied the relations 4.18 to extract the two last values of the energy dissipation of this third order statistical analysis. Using the slopes of the linear fits of figure 4.35, we added the quantities $\epsilon_r^{(3)}$ and $\epsilon_z^{(3)}$ to the figure 4.34, and normalized it by $L_p^2\Omega^3$ to obtain the figure 4.36.

The values of $\epsilon_r^{(3)}$ are in good agreement with the values of $\epsilon^{(3)}$ computed using $div(\overrightarrow{\overline{F}})$. However, the values of $\epsilon_z^{(3)}$ are discontinue due to the fact that some fits have a positive slope, hence a negative dissipation. These values may be meaningless though, as they have not been computed on a clear inertial range, but on an arbitrarily fixed range ($dz \in [5:10]mm$).

An interesting point is that, whatever definition of ϵ we use, we always find a point after which the ratio $\frac{\epsilon_r}{L_p^2\Omega^3}$ is constant. For $\epsilon_r^{(1)}$ and $\epsilon_r^{(2)}$, it is reasonable to say that the Ω^3 scaling of ϵ_r is fulfilled for $\Omega \geq 6RPM$. This scaling is also reasonable for $\epsilon^{(3)}$ and $\epsilon_r^{(3)}$ if $\Omega \geq 9RPM$. Nevertheless, in the vertical direction, this scaling is not appropriated in the investigated range of Ω. As already mentioned, this is caused by the fact that we do not observe a turbulent behavior in the z direction, as already highlighted by the absence of a clear plateau on figure 4.30. We can also note that the vertical Froude number of our particles mentioned in section 2.3.1 indicated that our particles could not trace perfectly the vertical fluid motions. This issue must also play a role in the results observed in the vertical direction, especially with the third order estimates which are very sensitive.

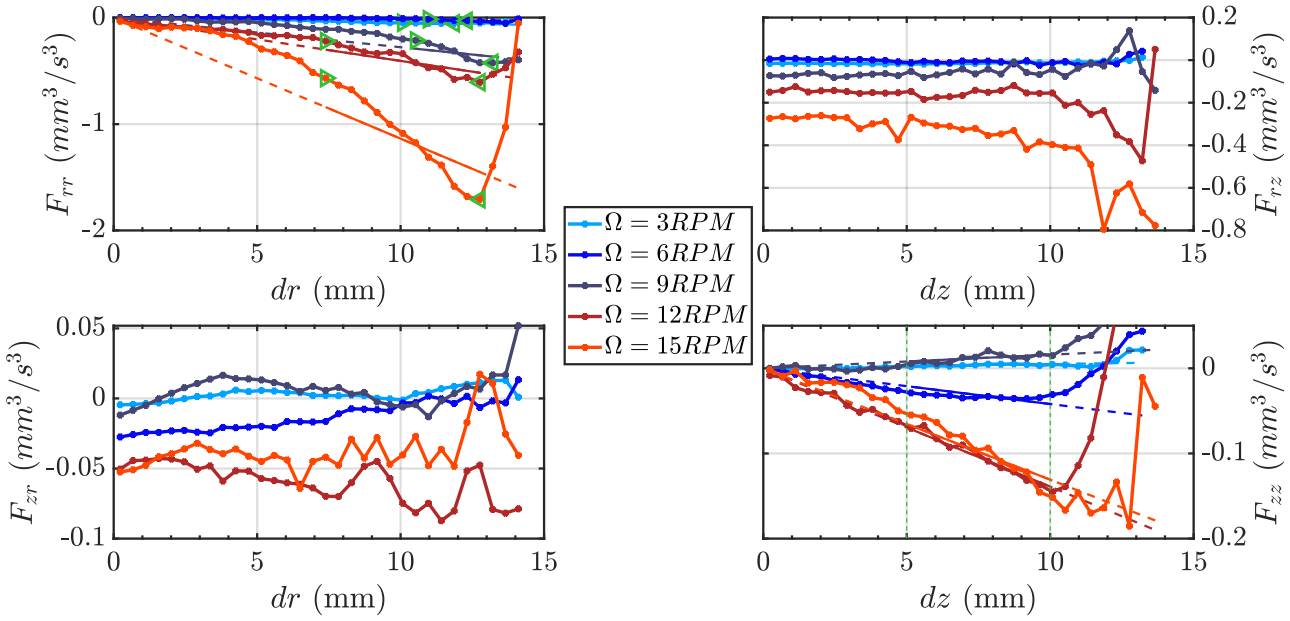

Figure 4.35: Averages of each component of the vector field $\overline{\vec{F}} = (Fr, Fz)$, conditioned on each separation vector $\vec{dr}$ and $\vec{dz}$. The diagonal terms F_{rr} and F_{zz} display a trend comparable with the linear scaling predicted by Galtier [16]. On the F_{rr} graph, the green triangles highlight the inertial range detected on figure 4.30. These ranges are used to fit the data linearly (solid line, extended with a dashed line out of the fitting range). The F_{zz} values have also been fitted linearly in the range $dz \in [5:10]mm$.

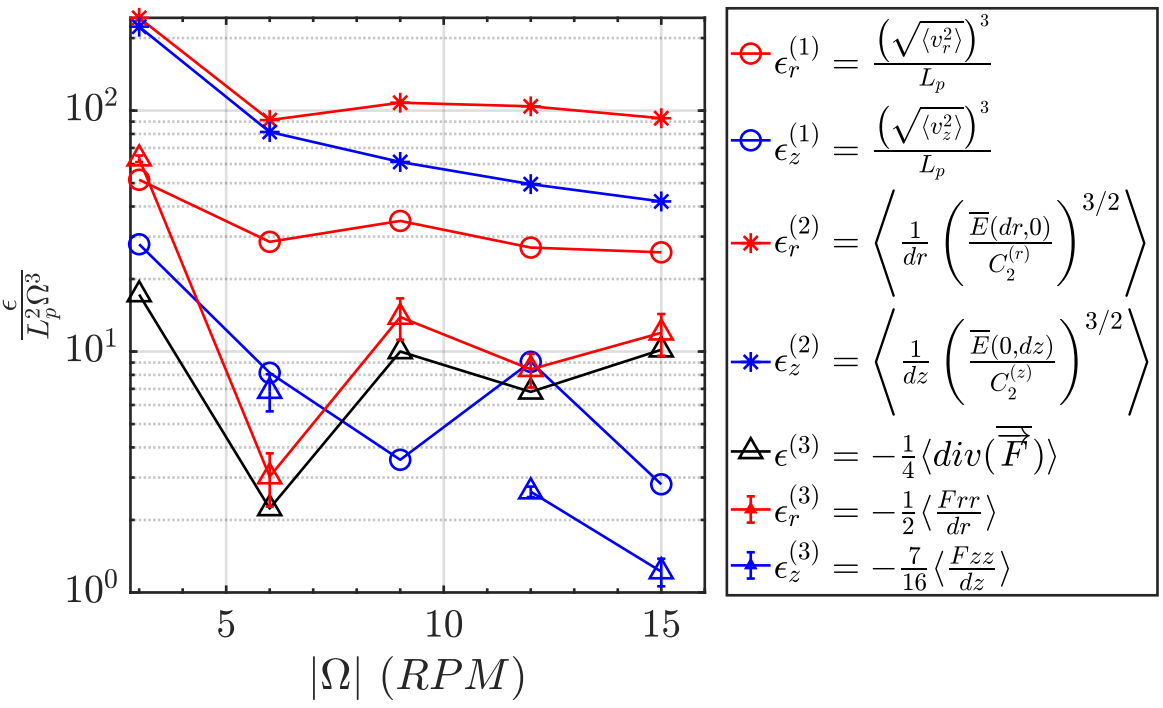

Figure 4.36: Summary of all the values of ϵ obtained with the different techniques used in this section. The values have been normalized by $L_p^2\Omega^3$ in order to check the validity of an Ω^3 scaling (relation 4.7). The error bars on $\epsilon^{(3)}$ have been removed here, for a better readability.

In conclusion, we have learnt a lot about this turbulent flow, which is well defined and relatively simple. We know that the average velocity in the laboratory frame of reference is 0. This encourages us to perform this experiment with different Rossby numbers. We know that the velocity fluctuations are gaussian, and that they overcome the oscillations of the particles witnessed when the cryostat was "simply" spinning.

The characteristic length and time scales have been computed. The radial length scale L_r is almost constant and about 2.2 times smaller than the propeller radius L_p. On the other hand, the axial length scale L_z increases with the rotation rate Ω. The evolution of both of these length scales is consistent with the evolution of the flow anisotropy, in agreement with the Taylor-Proudmann theorem. Our analysis also revealed an interesting link between the Kolmogorov length scale η, and the inter-vortex spacing δ. Both of these quantities follow the same trend, but a factor ~ 3 remains between them. The validity of our estimate of δ must be confirmed though, which is why the use of a second sound resonator will be of high interest in future experiments. The smallest time-scale of the flow also revealed that the investigation of higher Reynolds numbers will require the use of a higher time resolution. The use of the Phantom cameras will be mandatory, which will make the acquisition of such large data sets even harder.

The energy transfers of this anisotropic flow have also been investigated. The energy flows from the large to the small scales, as described by Richardson's cascade. However, the fluxes strongly depend on the direction: the radial transfers overcome the axial ones. But more importantly, we have thoroughly defined an applied different data-processing techniques which lead to 7 measurements of the energy dissipation rate ϵ. None of them are perfect:

- The order one estimate $\epsilon^{(1)}$ requires to arbitrarily choose an integral length scale. In our case, we chose $L = L_p$, the radius of the propeller.
- The order two estimate $\epsilon^{(2)}$ is weakened by the pollution of the small length scale by the laser sheet thickness. In the axial direction, the second order structure function did not display a real plateau for the computation of $\epsilon^{(2)}$. In fact, the velocity statistics in this direction did not display a turbulent behavior.
- The third order estimate $\epsilon^{(3)}$ requires a tow of data, which is hard to acquire in cryogenic conditions. The use of projections and averages of the field $\overrightarrow{F}$ along the each separation vector is useful to artificially increase the amount of statistics. However, a model which better fits our data in this case is needed.

Despite their weaknesses, they all obey to the simple energy balance scaling $\epsilon \propto \Omega^3$ in the radial direction. This evidences the fact that these results cannot be all wrong. Our goal here is not to say which estimate is the best, but it is to show what is doable experimentally with 2D particle imaging techniques. We focused on ϵ because it is a key quantity in turbulence: it is the core of the inertial range. Additionally, the fact that our fluid is a quantum one must not be forgotten. Besides the existence of quantum vortices, the main difference with a normal fluid resides in the energy dissipation processes. Therefore, in order to dig down this line, measuring ϵ is of tremendous importance.

We would also like to conjecture that this flow may be very different in helium I. Indeed, the velocity fluctuations we measured in helium II using a propeller are almost equal to the ones measured in helium I (using PIV, see fig. 4.19), when the cryostat was only spinning. This guess needs to be verified, but if it is true, the energy dissipation mechanism will be the best probe to understand this difference.

Last but not least, we would like to highlight the fact that this experiment of fully developed turbulence in a spinning cryostat using a quantum fluid is the first of its kind. It combines a lost of challenges, such as working in a rotating, and cryogenic frame, understanding frozen particles formation and dynamics, visualizing them, managing the acquired data, and process them... Most of these

challenges have been overcome. We hope that our results will be nice enough to arouse our colleagues interest, especially theoreticians. Their help would be valued in order to improve our ϵ surrogates, and understand in depth the processes of energy dissipation in a quantum fluid.

Conclusions

Summary of the different works presented

In this thesis, we presented a new innovative cryostat which will be used for the next decades to investigate quantum and classical turbulence. The main feature of this system is the ability to rotate while allowing the visualization of frozen particles. The modularity of the apparatus is another advantage, as several type of flows (grid turbulence, counterflow) will be investigated. Several experimental sessions have already been carried out, and were focused on different topics.

The formation of frozen deuterium particles by injecting a hot ($300K$) gaseous mixture directly in helium II ($< 2.17K$) with different flow rates has been studied. By regulating the injection pressure, the size of the particles can be reduced, and reach diameters as small as the ones produced by an injection in helium I. An empirical law of dependence of the particle size on the flow rate could not be established due to the influence of non-measured parameters on the particle formation. In order to obtain better results, it would be interesting to wrap the injection capillary in a heating wire, and to calibrate the helium level measurement gauge to have more precise information on the temperature gradients in the capillary. However, the current injection protocol is functional and produces micron-sized particles that can reliably trace the movement of the fluid, resulting in quality data.

Then, we studied the transient state caused by the injection of particles which uses the rotation of a propeller in order to homogenize the particle seeding. Actually, this corresponds to the investigation of the decay of the turbulence forced by the propeller in a rotating frame. However, this flow is not homogeneous, nor isotropic and it produces an anticyclonic large scale motion which is unstable. These instabilities perturb the clear power law ($\propto t^{-n}, n > 0$) decrease of the kinetic energy reported in the literature considering homogeneous isotropic decaying turbulent flows in rotation. Nevertheless, the trend of the energy dissipation process is respected, as we have shown that Ω^{-1} is the relevant time scale of this process. This allowed us to determine that a $200s$ wait was sufficient to recover a quiescent flow after a particle injection, and used this value in the experimental protocol to study steady flows. Note that the time constants we found were increasing linearly with the rotation rate of the system, which means that the value of $200s$ may not be sufficient if the system rotates faster than $\Omega = 15RPM$.

The other transient state we encountered was caused by the start and stop of the system rotation. In a classical fluid, this problem is characterized by the Ekman time. However, it does not apply to quantum fluids like helium II, as shown by several experiments of the 1950s-1980s. Among them, Tsakadze & Tsakadze proposed an empirical time constant for the recovery of their cryostat in decaying rotation after a sudden and spontaneous velocity increase (glitch). The order of magnitude of our results is in qualitative agreement with their time constant. However, the most striking fact is the observation of a delay before the decay of the velocity fluctuations in the spin-up case, whereas it does not occur in spin-down. An asymmetry between spin-up and spin-down was already reported by Hall in the 1950s. The delay we observed in the spin-up case is in agreement with his sentence: “acceleration begins

more slowly and finishes more rapidly than retardation". However, the second part of the sentence is incompatible with our results as the time constants in spin-up are longer than in spin-down. At last, considering the delay, the spin-up time constant is in good agreement with an Ekman time based on the quantum of circulation κ.

The experiments focusing on steady rotating helium II did not allow us to visualize the vortex lattice. We rather observed millimeter amplitude oscillations of the particles all together, in phase with the cryostat rotation. We think that they are caused by inertial waves amplified by the (very) small coaxiality fault between the cryostat rigid guide, and its rotational axis. These oscillations were not observed in normal fluid, highlighting the fact that the superfluid nature of helium II affects these waves. We doubt however that they could be the direct signature of Tkachenko waves, due to their large amplitude compared to the inter-vortex distance.

The last experiments made in this thesis were focused on the study of a counter-rotating propeller in a rotating frame of reference. The Rossby number studied is -2, with Reynolds numbers increasing from ~ 1000 to ~ 5000. This is a moderately turbulent flow, but which was still sufficient to overcome the particles oscillations which were not observed in it. We used different data processing techniques to measure the energy dissipation rate ϵ. At rotation rates above $\Omega \geq 9RPM$, we showed that second and third order structure functions display turbulent behaviors in agreement with Kolmogorov's phenomenology (K41). In these conditions, the measured values of ϵ scale as Ω^3, as predicted by a simple energy balance in the radial direction. Using these values to characterize the turbulent cascade led us to find an interesting link between the Kolmogorov length scale, and the estimated inter-vortex spacing. These two quantities scale similarly, but the exact factor between them must be clarified using a second sound resonator. This will be possible in future experiments, but for now, our goal was to experimentally approach ϵ using 2D visualization technique. This quantity is indeed the core of turbulent processes, and consequently a key to understand the energy dissipation in normal, as in quantum fluids.

Ongoing and future works

Several hints for future experiments have already been mentioned along the manuscript. First, it could be interesting to complete our study on the spin-up and spin-down of helium II by adding a second sound resonator in the cell. In addition to strengthening our visualization measurements, this would provide a close view on the vortex tangle. It would then help us to better understand the vortex pinning phenomena which may be the cause of the delay observed in spin-up. Second, digging down further into the turbulence decays in helium II is also of high interest. The use of a pulled grid produces homogeneous turbulence, which could then be compared to the t^{-n} $(n > 0)$ scaling of classical fluids. This experiment can be done in helium I as well, in order to compare both fluids. Indeed, decaying turbulence is a good way to measure the dissipation ϵ, which is why comparing both fluids would be of high interest to understand the dissipation mechanisms in helium II.

The behavior of the fluid reported in the last section of this manuscript is not very different from a classical one. This is a common observation of the literature, when the fluid is probed at scales larger than the inter-vortex distance. In order to investigate the particularities of the superfluid, it is necessary to increase the time resolution of our system. This is why, in future turbulent experiments, the Phantom cameras will be used. This is made possible by the fact that the transient states are now well characterized, which means that we do not need acquisitions of several minutes to be sure that we are observing statistically steady turbulent flows. Moreover, we evidenced reasons to think

that forcing helium I under rotation with a propeller would produce higher velocities than in helium II, which means a different behavior. Thus, performing the same experiment with helium I would be interesting to check this conjecture, and understand more about the differences between quantum and classical fluids. Finally, implementing 3D visualization in the CryoLEM would definitely benefit the study of all kinds of turbulent flows, including this one. This major improvement would allow the computation of actual values of E and $\overrightarrow{F}$, leading to a more accurate value of the dissipation, and a better characterization of the 3D turbulent cascade.

Still with the idea of focusing on the properties of the superfluid, it would be interesting to use the CryoLEM to study a counterflow in rotation. Indeed, counterflow experiments have no classical equivalent, and probing them with particles have produced interesting results in the recent literature. A collaboration with researchers on quantum turbulence from Prague (see appendix D) have already produced results on counterflows that encourage us to dig further in this direction. Indeed, the effect of rotation on this type of flow has not been tested experimentally, and we hope that it could help us to better understand this flow by polarizing the vortex tangle along the rotational axis. The initial plan was to perform it in 2019. However, a leak from the inner cell to the insulating vacuum at low temperatures ($\leq 5K$) prevented us from doing it. Indeed, once helium has come into the vacuum, the insulating property is lost, and helium can no longer remain liquid in the cell. The sealing of this leak is still in progress in July 2020. Once sealed, counterflow experiments in rotation will be performed using the channel shown on figure 2.15.

The analysis methods presented in this thesis were focused on statistical approaches. However, the Lagrangian framework also make possible to study each particle trajectory separately. In the counter-rotating propeller experiments, we observed that some particles could display unusual velocity oscillations (fig. 4.37). Their frequency is of the order of $\sim 3Hz$, reminding us a value already pointed out in [129]. La Mantia et al. reported the observation of the rotation of particles at frequencies of $\sim [1:10]Hz$ depending on their size. It is possible that our particles rotate, and their non-spherical shape leads to oscillations of their centroid position, hence velocity. The question is now: what is the source of these oscillation/rotation? Recent numerical studies [134, 155] report the fact that the Magnus force could produce similar excitations on particles trapped in one or several quantum vortices. In other words, these oscillations would be the first (indirect) observation of quantum vortices in the CryoLEM. Of course, this work is still in progress in order to evidence a quantitative agreement between both studies.

Another sign of the interactions between particles and quantum vortices has probably been observed earlier. As reported several times in the literature [122, 129, 130], hydrogen aggregates in filaments in helium II. These hydrogen filaments have also been observed in the CryoLEM (fig. 4.38). This shape reminds that of the quantum vortices, which is why Gordon [144, 156] studied the possibility of a catalytic character of the quantum vortices in hydrogen particles aggregation. However, this study did not provide irrefutable evidences on the role of quantum vortices in the filaments aggregation. In conclusion, we cannot be sure that the quantum vortices have been observed in the CryoLEM at this moment. However, there is no doubt that increasing the acquisition rate of our images will allow us to observe their signature in turbulent flows.

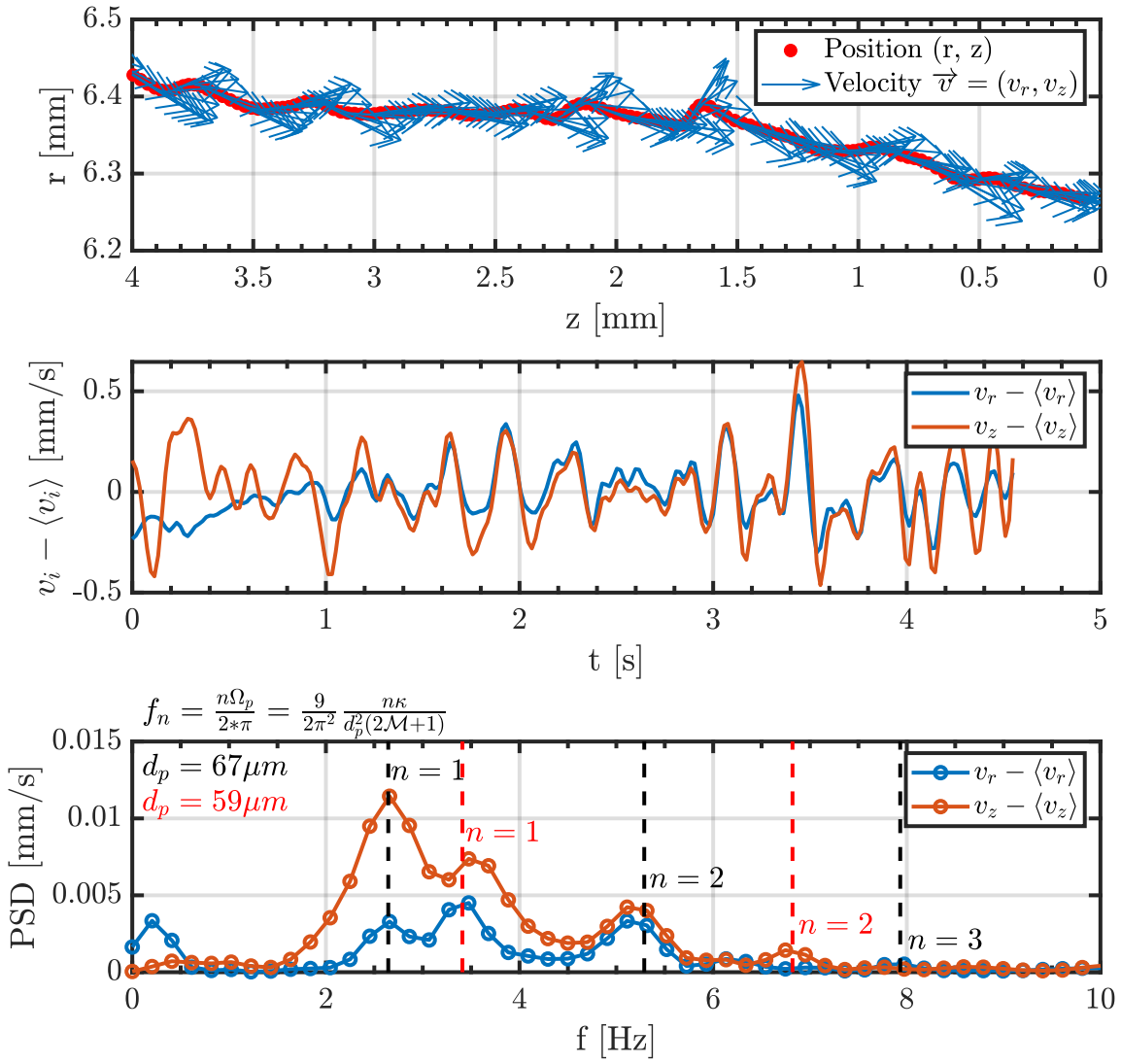

Figure 4.37: Observation of a single particle trajectory in the same flow as in section 4.3 (with $\Omega = 9RPM$). Unusual oscillations are observed. They are visible on both components of the velocity, with a slightly larger amplitude in the vertical direction (z). A spectral analysis reveals a first peak around $2.5Hz$, and a second one around $3.5Hz$. The Magnus frequency reported in [134] to be $f_n = \frac{9}{2\pi^2}\frac{n\kappa}{d_p^2(2\mathcal{M}+1)}$ can be used to identify the peaks. In this expression, n is the mode κ is the quantum of circulation, d_p is the particle diameter, and $\mathcal{M} = \frac{\rho_p}{\rho_f}$ is the density ratio between the particle and the fluid. On this track, the peaks correspond to different particle sizes ($d_p = 59\mu m$ and $67\mu m$), and are spread. This is expected as the model is made for spherical particles, which is not the case here. Note that the size of this particle measured using light scattering returns $d_p \sim 110\mu m$. This phenomenon has only been observed for several "large" particles up to now.

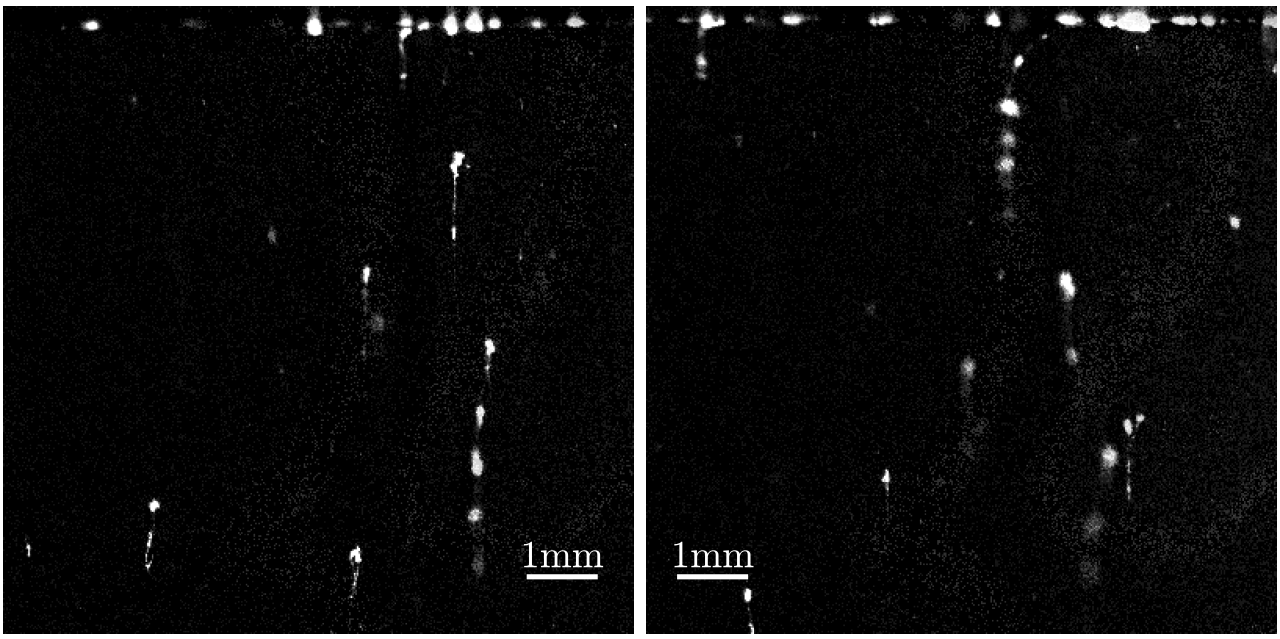

Figure 4.38: Particles of hydrogen in suspension in rotating helium II. The background of the image has been subtracted for better contrasted particles. The particles are slowly settling to the surface of the superfluid bulk. They have aggregated as filaments, maybe because of the quantum vortices. Both images have been recorded within the same minute. When the vertically oriented hydrogen filaments approach the surface, they bend and lay horizontally on it.

Appendix A

Lists of data sets used in chapter 4

Movie #	**Duration (s)**	**Ω (RPM)**	**Pressure (mbar)**	**Kinematic viscosity ($\times 10^{-8}$m^2/s)**	**Time constant (s)**
1	573	−5	40	1.18	40
2	573	−10	40	1.18	152
3	573	−15	40	1.18	202
4	573	−5	40	1.18	30
5	573	−5	40	1.18	32
6	558	−15	40	1.18	154
7	573	−15	17	0.895	127
8	573	−10	17	0.895	176
9	539	−15	17	0.895	111
10	541	−15	27	0.961	122
11	539	−15	40	1.18	176
12	382	0	40	1.18	227
13	382	0	40	1.18	143
14	573	−3	40	1.18	54
15	573	−5	40	1.18	111
16	438	−8	40	1.18	608
17	573	−10	40	1.18	231
18	573	−13	40	1.18	196
19	573	−15	40	1.18	124
20	382	−5	40	1.18	47
21	382	0	40	1.18	270

Table A.1: Experimental conditions of the movies studying the decay of the motion of deuterium particles after stopping the stirring turbine. At $t = 0$, the stirring turbine velocity is suddenly stopped from $\omega = 57RPM$ to 0. Ω is negative as the cryostat was spinning in the clockwise direction, viewed from the top. The last column displays the results of the analysis done in section 4.1.1.

Movie #	**Duration (s)**	**Ω (RPM)**	**Particle nature**	**Time constant (s)**	**Delay (s)**
22	573	−15	D_2	58	90
23	573	−10	D_2	169	90
24	573	−8	D_2	240	101
25	573	−5	D_2	139	336
26	573	−3	D_2	197	10
27	573	−12	D_2	172	110
28	573	−15	Air	63	110

Table A.2: Experimental conditions of the movies studying the helium spin up. At $t = 0$, the cryostat starts spinning at Ω. In these movies, the pressure is constant at $40mbar$, which corresponds to a viscosity of $1.18 \times 10^{-8} m^2/s$. The injection of deuterium particles (with associated stirring) has been done $200s$ before the beginning of the recording. Ω is negative as the cryostat was spinning in the clockwise direction, viewed from the top. The results of the analysis done in section 4.1.2 are displayed in the last column.

Movie #	**Duration (s)**	**Ω (RPM)**	**Particle nature**	**Time constant (s)**
29	513	−15	D_2	133
30	273	−10	D_2	426
31	273	−5	D_2	327
32	273	5	D_2	41
33	273	10	D_2	224
34	273	15	D_2	140
35	182	5	H_2	69
36	573	−15	D_2	109

Table A.3: Experimental conditions of the movies studying the helium spin down. In these movies, the pressure is constant at $40mbar$, which corresponds to a viscosity of $1.18 \times 10^{-8} m^2/s$. The injection of deuterium particles (with associated stirring) has been done $200s$ before the beginning of the recording while the cryostat was spinning at Ω. Ω is positive when spinning in the anti-clockwise direction, viewed from the top. The results of the analysis done in section 4.1.2 are displayed in the two last columns.

Movie #	**Duration of steady state (s)**	**Ω (RPM)**	**Pressure (mbar)**	**Particle nature**
1	285	−5	40	D_2
4	538	−5	40	D_2
5	521	−5	40	D_2
15	365	−5	40	D_2
20	297	−5	40	D_2
2	441	−10	40	D_2
17	260	−10	40	D_2
23	314	−10	40	D_2
3	377	−15	40	D_2
6	363	−15	40	D_2
19	450	−15	40	D_2
22	425	−15	40	D_2
11	385	−15	40	D_2
28	400	−15	40	*Air*
37	210	−15	40	D_2 & *Air*

Table A.4: Experimental conditions of the movies studying the steady rotation of the cryostat. Ω is negative as the cryostat was spinning in the clockwise direction, viewed from the top. The steady part of some movies listed in the previous sections are used. The movies in which the steady part was shorter than $300s$ have been removed. Moreover, only the movies recorded at $40mbar$, with $\Omega = \{-5; -10; -15\}RPM$ have been kept.

Movie #	**Duration (s)**	**Ω (RPM)**	**Pressure (mbar)**	**Particle nature**
38	573	−15	[72 : 93]	D_2 & *Air*

Table A.5: Experimental conditions of the movie studying helium I in steady rotation. To record this movie, the pressure is decreased below $50mbar$ (He II transition), and a sudden repressurization is made to move away from the saturated vapor pressure curve, in order to avoid bubbles in the field of view. While repressurizing, some air is injected, and particles of D_2 or H_2 can be added once air particles have settled. Then, the PTV algorithm can be used to track them.

Movie #	**Number of acquisitions**	**Total number of frames**	**Omega (RPM)**
39	3	45 000	−3
40	3	45 000	−6
41	3	45 000	−9
42	6	90 000	−12
43	6	90 000	−15
44	2	30 000	3
45	2	30 000	6
46	3	45 000	9
47	2	30 000	12
48	2	30 000	15

Table A.6: Experimental conditions of the data sets studied in section 4.3. The cryostat rotating at Ω contains a propeller rotating at $\omega = -\Omega$ in the laboratory frame. Each movie is composed of several data sets of 15 000 frames each. With a frame rate of $52.3Hz$, this corresponds to $286.6s$. The pressure is always stabilized at $40mbar$, corresponding to $T = 2.087K$ and $\nu = 1.186 \times 10^{-8} m^2/s$ [23].

Appendix B

Impact of a laser sheet thickness on the second order structure function in PTV

In this thesis, the computation of the second order structure function in the space of differences is often used. Let's assume a 2D plane $(\overrightarrow{e_r};\overrightarrow{e_z})$ in which two particles are separated by a vector $\overrightarrow{ds} = dr.\overrightarrow{e_r} + dz.\overrightarrow{e_z}$. The second order structure function is $E(\overrightarrow{ds},t) =< (\delta\overrightarrow{v})^2 >$ where $\delta\overrightarrow{v}$ is the difference of velocity between the particles. If the two particles are faithful tracers, and if they are very close together ($\overrightarrow{ds} \rightarrow \overrightarrow{0}$), then their velocity difference must be $\overrightarrow{0}$ as well by continuity of the velocity field. Thus, $E(\overrightarrow{0},t) = 0$.

Now, let's consider that the 2D plane is a real laser sheet, commonly used in experimental fluid dynamics, with a thickness $2e$. The particles enlightened by this laser sheet are observed with a single camera whose optical axis is orthogonal to the sheet, which (a priori) makes it impossible to collect any information in this direction. In other words, two particles detected at the same position by the camera can actually be separated by a distance of up to $2e$ along the optical axis. In this case, it is possible to find $E(\overrightarrow{0},t) > 0$.

In a nutshell, the thickness of a laser sheet used in a 2D2C measurement can lead to abnormal value of $E(\overrightarrow{ds},t)$ at small scales. In this section, we will try to evaluate the scale at which the value of $E(\overrightarrow{ds},t)$ becomes relevant, depending on the sheet thickness $2e$. In order to do this, we used the result of a 3D3C simulation of 1279 neutrally buoyant particles in a homogeneous isotropic turbulent (HIT) flow (used in [157]). The mesh grid has a size of 512^3 with periodic boundary conditions.

In order to simulate the laser sheet, the information related to the third component have been removed. The space has been divided in slices along the third direction. The number of slices varies from 2^0 ($2e = 512$) to 2^7 ($2e = 4$). We end up with 8 sets of 2D data, each with a virtual sheet thickness. The routine used in sections 4.2.1 and 4.3 to compute $\overline{E}(dr,dz)$ is applied to each data set. Note that we kept the same notations: dr is the horizontal separation, and dz the vertical one.

The simulated data of HIT should obey Kolmogorov's phenomenology of turbulence [5]. Thus, we expect $\overline{E}(dr,0)$ to scale as $dr^{2/3}$, and $\overline{E}(0,dz)$ to scale as $dz^{2/3}$. As the data is isotropic, this verification will only be done on the horizontal direction.

The figure B.1 displays the results of this process. On the left, the quantity $G(dr,2e) = \frac{\overline{E}(dr,0)}{dr^{2/3}}$ is represented. If we focus on the $2e = 4$ graph, we see the typical shape of a graph that would be obtained in HIT: there is a short growth at low scales after which a plateau is reached until it collapses at large scales. The plateau corresponds to the inertial range of the turbulent cascade. This pattern is also observed when $2e \leq 16$. Indeed, when e increases, the initial value of $\overline{E}(0,0)$ increases for the reasons mentioned above. Thus, the plateau appears at larger and larger separation values. At some point, e is so large that the plateau no longer appears: the whole inertial range is masked by the slice thickness.

In order to check the validity of the results, we will consider $G(dr,2e = 4)$ to be accurate, and it

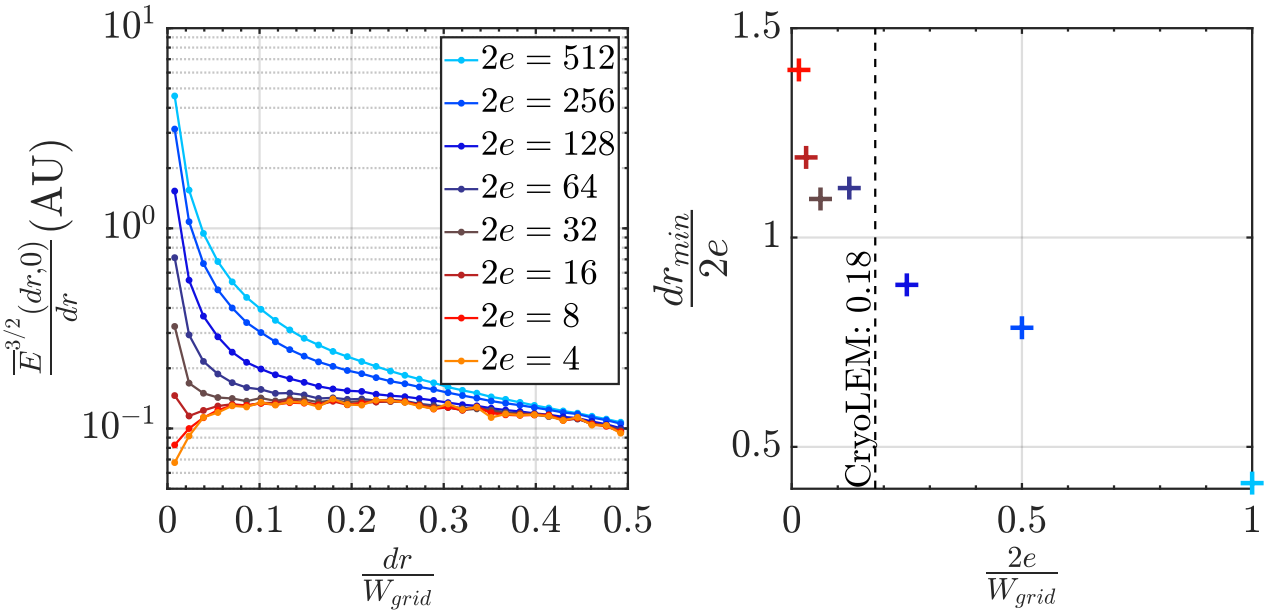

Figure B.1: Left: Evolution of $\frac{\overline{E}(dr,0)}{dr^{2/3}}$ as a function of the horizontal separation dr, normalized by the width of the simulation grid ($W_{grid} = 512$). This quantity has been computed with different values of $2e$, and it will be noted $G(dr, 2e)$. As the boundary conditions are periodic, the maximum horizontal separation between two particles is $W_{grid}/2$. Right: On the left hand side graph, the plot with $G(dr, 2e = 4)$ is used as a reference. The relative difference $K(2e) = \frac{G(dr,2e)-G(dr,4)}{G(dr,4)}$ is computed for the 7 other plots. The separation noted dr_{min} corresponds to the value of dr above which $K(2e)$ is below 10%.

will be used as a reference. Then, we compute the relative difference of the 7 other graphs with the reference: $K(2e) = \frac{G(dr,2e)-G(dr,4)}{G(dr,4)}$. At large separation ($dr \gtrsim 0.4 W_{grid}$), all the graphs $G(dr, 2e)$ are superimposed. This means that there exists a value dr_{min} above which the relative difference $K(2e)$ is below 10%. On the graph on the right, the value of dr_{min} is reported as a function of e. On the abscissa axis, $2e$ is normalized by the width of the simulation mesh grid W_{grid}. The values of $\frac{dr_{min}}{2e}$ are distributed around 1, with a decreasing trend. This value is a bit larger than 1 (up to 1.4) for small thicknesses, and a bit lower (down to 0.4) for large ones. In the CryoLEM setup used in this thesis, the ratio $\frac{2e}{W_{Frame}}$ is about 18% (black dashed line), which is moderated. In this range, the values of $\frac{dr_{min}}{2e}$ are very close to 1. This means that our computations of E becomes valid for scales dr larger than the thickness of the laser sheet $2e$. This rule will then be applied to the data processed in chapter 4.

Appendix C

Additional figures on the energy flux density obtained in section 4.3

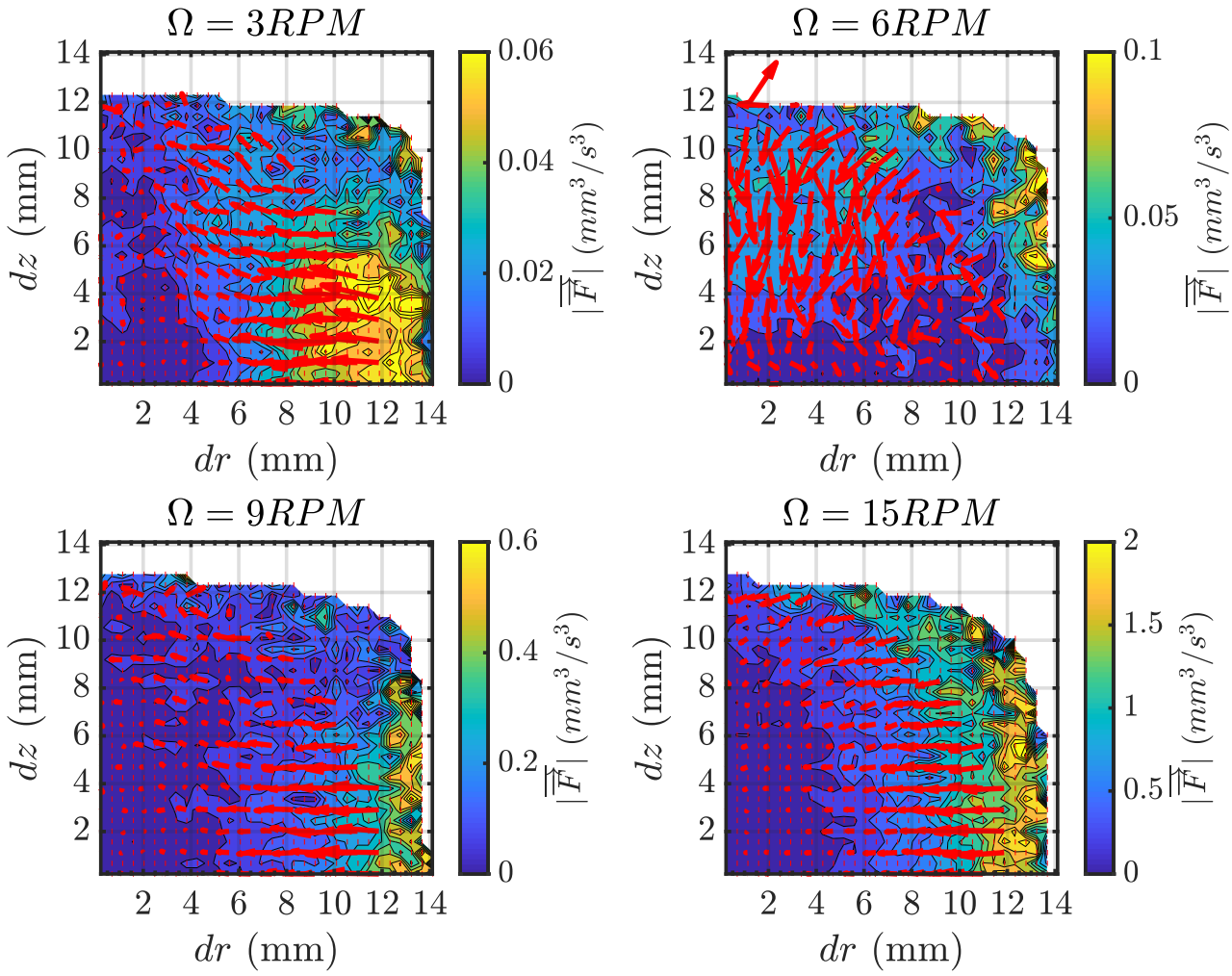

Figure C.1: Additional graphs of the vector field $\vec{F}$ used in section 4.3. These graphs have been respectively computed for the data acquired at 3, 6, 9 and $15RPM$. The $12RPM$ graph is in figure 4.32.

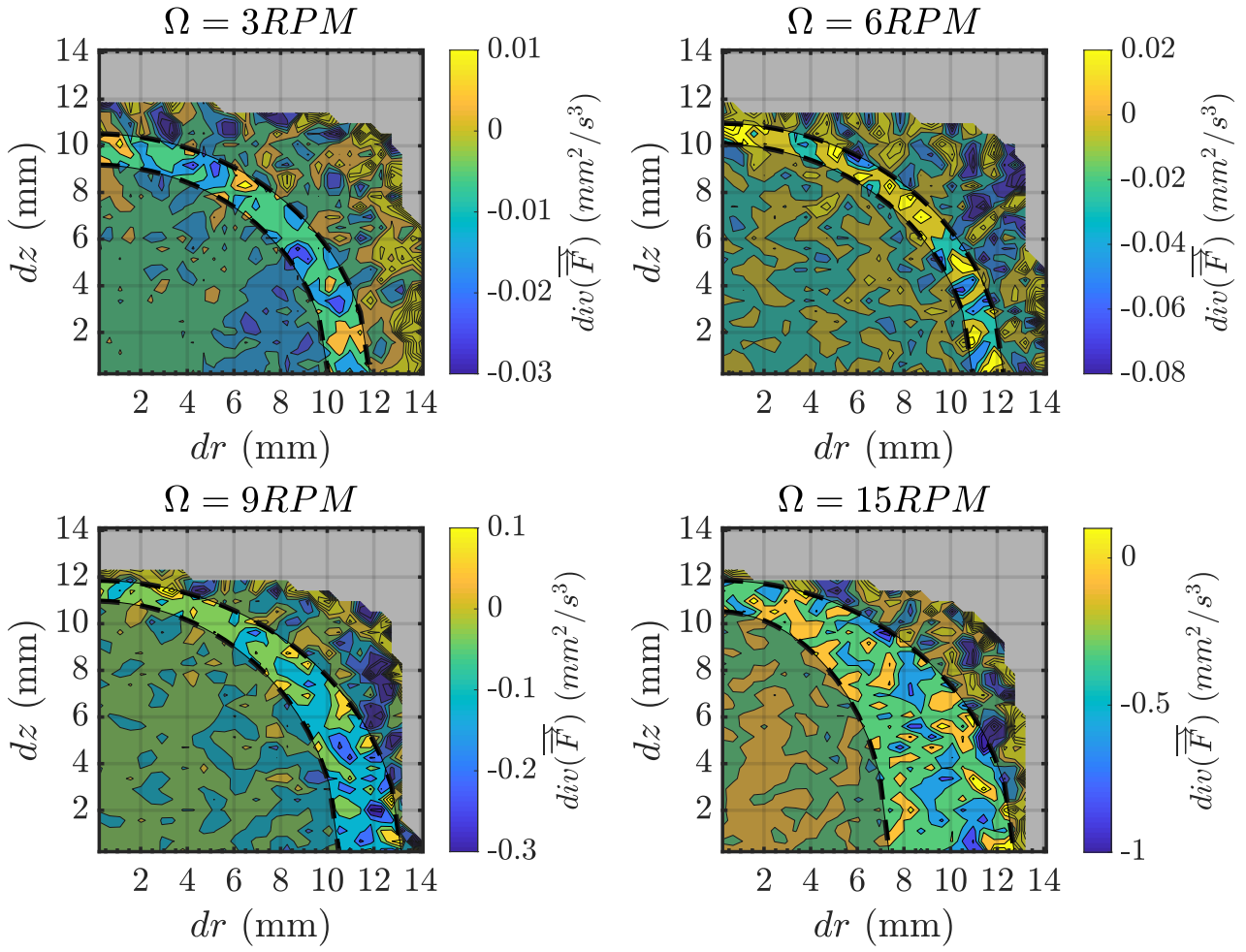

Figure C.2: Additional graphs of the divergence of the field $\vec{F}$, used in section 4.3. These graphs have been respectively computed for the data acquired at 3, 6, 9 and $15RPM$. The $12RPM$ graph is in figure 4.33.

Appendix D

Particle-vortex interactions in a turbulent counterflow

During this thesis, a collaboration with the Charles University (Prague, Czech Republic) took place. In February 2017, M. Gibert, P. Diribarne, B. Rousset and M. Bourgoin went to Prague, and performed counterflow experiments in the Prague cryogenic visualization setup, together with P. Švančara, D. Duda, P. Hrubcova, M. Rotter, L. Skrbek, and M. La Mantia. The data have been processed in Grenoble, in July 2017, 2018 and 2019 during the visits of respectively D. Duda and P. Švančara (twice). During their visits, they worked and interacted with M. Gibert, and me. This collaboration resulted in the article below, which has recently been submitted to the Journal of Fluid Mechanics, and is still under revision. I also presented the results in Lyon, on October 24^{th} 2019, during the 2019 GDR Turbulence meeting.

Ubiquity of particle-vortex interactions in turbulent counterflow of superfluid helium

P. Švančara[1], D. Duda[1]†, P. Hrubcová[1]‡, M. Rotter[1], L. Skrbek[1], M. La Mantia[1]¶, E. Durozoy[2], P. Diribarne[3], B. Rousset[3], M. Bourgoin[4] and M. Gibert[2]

[1]Faculty of Mathematics and Physics, Charles University, Prague, Czech Republic

[2]Université Grenoble Alpes, CNRS, Institut Néel, Grenoble, France

[3]DSM/DRFMC/SBT, CEA, Grenoble, France

[4]Université Lyon, ENS de Lyon, Université Claude Bernard, CNRS, Laboratoire de Physique, Lyon, France

(Received xx; revised xx; accepted xx)

Thermal counterflow of superfluid ^{4}He is investigated experimentally, by employing the Particle Tracking Velocimetry technique. A flat heater, located at the bottom of a vertical channel of square cross-section, is used to generate this unique type of thermally driven flow. Micronic solid particles, made *in situ*, probe this quantum flow and their time-dependent positions are collected by a digital camera, in a plane perpendicular to the heat source, away from the channel walls. The experiments are performed at relatively large heating powers, resulting in fluid velocities exceeding 10 mm/s, to ensure the existence of sufficiently dense tangles of quantized vortices. Within the investigated parameter range, we observe that the particles intermittently switch between two distinct motion regimes, along their trajectories, that is, a single particle can experience both regimes while traveling upward. The regimes can be loosely associated to fast particles, which are moving away from the heat source along almost straight tracks, and to slow particles, whose erratic upward motion can be said to be significantly influenced by quantized vortices. We propose a separation scheme to study the properties of these regimes and of the corresponding transients between them. We find that particles in both regimes display non-classical, broad distributions of velocity, which indicate the relevance of particle-vortex interactions in both cases. At the same time, we observe that the fast particles move along straighter trajectories than the slow ones, suggesting that the strength of particle-vortex interactions in the two regimes is notably different.

Key words:

1. Introduction

The superfluid phase of liquid ^{4}He is often called He II and can be regarded as an easily accessible quantum fluid, compared to other systems, such as superfluid ^{3}He (see,

† Present address: Faculty of Mechanical Engineering, University of West Bohemia, Plzeň, Czech Republic

‡ Present address: Department of Physics, Royal Holloway University of London, Egham, Surrey, United Kingdom

¶ Email address for correspondence: lamantia@mbox.troja.mff.cuni.cz

for example, Barenghi *et al.* 2014; Mongiovì *et al.* 2018). He II is usually obtained from the normal liquid phase, known as He I, by evaporative cooling below the transition temperature T_λ, equal to 2.17 K at the saturated vapour pressure, and its extraordinary physical properties, such as the extremely small kinematic viscosity, allow to study highly turbulent flows in relatively compact setups (Skrbek & Sreenivasan 2012).

The most popular phenomenological description of the large-scale hydrodynamics of He II postulates that the liquid consists of two components, with temperature-dependent relative densities (Barenghi *et al.* 2014). In the close proximity of T_λ, He II is made solely of the normal component, which behaves similarly to a classical fluid possessing finite viscosity. As the temperature decreases, the corresponding relative density decreases and the superfluid component – inviscid and of zero entropy – becomes more abundant. Eventually, below 1 K, He II can be, for many practical purposes, regarded as a pure superfluid.

Additionally, it follows from the quantum mechanical description of He II that the flow of the superfluid component is potential. Yet vortical flows may occur in this unique system due to the presence of quantized vortices, which are one-dimensional topological defects – holes – within the superfluid component. The core size of these vortex lines is of the order of 0.1 nm and their circulation quantum κ is equal to $h/m_4 \approx 10^{-7}$ m^2/s, where h is the Planck constant and m_4 denotes the mass of the ^{4}He atom. Typically, these vortices arrange themselves in a dynamic tangle, interacting with the fluid flow via the mutual friction force, and represent the main ingredient of what is usually called quantum turbulence. A relevant intensity measure of quantum turbulence then becomes the vortex line density L, defined as the total length of quantized vortex lines per unit volume.

When heat is dissipated in He II, the fluid is set into motion and, in the standard semi-closed channel geometry, with the heat source located at the closed end, the normal component flows away from the heater. In the steady state, the normal component will flow, on average, at a constant velocity, whose magnitude v_n can be written as

$$v_n = \frac{q}{\rho S T}, \tag{1.1}$$

where q denotes the applied heat flux, ρ is the He II density, S indicates the fluid specific entropy and T is the liquid temperature. The superfluid component flows in the opposite direction, i.e., toward the heater, with the average velocity magnitude v_s, in such a way that the net mass flow equals to zero, that is, $\rho_n \vec{v}_n + \rho_s \vec{v}_s = 0$, where the subscripts n and s denote the normal and superfluid components, respectively. This flow, called thermal counterflow, has no direct classical analogue, especially if one considers that the liquid is characterized by an extremely large thermal conductivity, which actually depends on the heat flux (Mongiovì *et al.* 2018). The magnitude of the flow characteristic velocity, which is called the counterflow velocity v_{ns}, is defined as

$$v_{ns} = |\vec{v}_n - \vec{v}_s| = \frac{q}{\rho_s S T}. \tag{1.2}$$

Channel counterflow represents the hallmark of both experimental and numerical studies of quantum turbulence (Skrbek & Sreenivasan 2012). Here, we investigate its properties experimentally, by flow visualization. Specifically, we observe the motions of relatively small solid particles dispersed in the liquid, which proved their usefulness as probes of both classical and quantum features of He II flows (Guo *et al.* 2014). Indeed, the interactions between flow-probing particles and quantized vortices can be observed as events of extremely large particle velocity and it was shown that the corresponding

statistical distributions display power-law tails at sufficiently small scales (La Mantia *et al.* 2016).

In order to appreciate the latter remark, two principal scales are introduced. The smallest, experimentally resolved scale, which we call here the scale s_p probed by the particles, is defined as the mean particle displacement between two consecutive positions and can be written as

$$s_p = \langle v \rangle \, t_p, \tag{1.3}$$

where $\langle v \rangle$ is the mean particle velocity, obtained at the corresponding time scale t_p (the typical particle size is usually smaller than or of the same order of s_p). The characteristic scale of the flow, which we call here the quantum scale s_q, is the mean distance between quantized vortices. The latter can be obtained from the flow vortex line density – as discussed, for example, by Sergeev *et al.* (2006) – because, at large enough v_{ns}, in the steady state, one can write

$$s_q = \frac{1}{\sqrt{L}} = \frac{1}{\gamma v_{ns}}, \tag{1.4}$$

where γ is an empirical scaling constant depending not only on the liquid temperature (Babuin *et al.* 2012) but also on the channel geometry (Hrubcová *et al.* 2018), that is, on how close the channel boundaries are to the investigated flow region.

If the experimental resolution falls significantly behind the quantum scale, that is, if the probed scale s_p is appreciably smaller than the mean distance s_q between quantized vortices, the tails of the particle velocity statistical distribution are well visible, with distinctive power-law scaling (La Mantia *et al.* 2016). As the probed scale increases, the tails become less visible, but are still noticeable, and, when $s_p > s_q$, the tails disappear and we observe that the particle velocity distribution shape is almost Gaussian, resembling therefore classical turbulence (Švančara & La Mantia 2017) and indicating the averaged result of multiple interactions between particle and quantized vortices (Švančara & La Mantia 2019).

To date, distinctive motion features have been observed in experiments involving particles probing thermal counterflow in vertical channels, with the heat source located at the channel bottom. At relatively small heat fluxes, a significant amount of particles move, on average, toward the heater (Paoletti *et al.* 2008; La Mantia 2016), that is, downward, in the direction of the superfluid component. As q increases, the portion of particles moving upward, away from the heater, in the normal fluid direction, increases, indicating that, at relatively large heat fluxes, the particles tend to follow, on average, the normal fluid flow, although the corresponding tracks become less straight than at smaller q values (La Mantia 2016). Additionally, it was found that the mean particle velocity in the counterflow direction is approximately equal to v_n (Paoletti *et al.* 2008; Chagovets & Van Sciver 2011) or to $v_n/2$ (Zhang & Van Sciver 2005; Chagovets & Van Sciver 2011), with the latter occurring at larger heat fluxes – a similar decrease of the mean particle velocity was obtained in numerical simulations and attributed to the stronger interactions between particles and quantized vortices at larger L values (Kivotides 2008*a*).

Recently, Mastracci & Guo (2018) further investigated the occurrence of these particle motion features, by using a square channel of 16 mm sides, and confirmed the above mentioned experimental findings. Additionally, they found that, at the largest q values probed in their experiments, the statistical distributions of the particle velocity in the vertical direction (i.e., the normal fluid direction) are characterized by a single peak centered near $v_n/2$. As the applied heat flux decreases, another peak, centered near v_n, appears in these velocity distributions and, for even smaller q values, the peak at the smaller velocity is centered near v_s, which is taken with the negative sign, as the superfluid

and normal fluid components move in opposite directions. The outcome indicates that, at small heat fluxes, particles can be trapped onto quantized vortices for relatively long times and move therefore downward, in the superflow direction, with the vortex tangle – see, e.g., Sergeev & Barenghi (2009) for a discussion on particle trapping. For larger v_{ns} values, the Stokes drag of the normal component forces instead most particles to move upward, away from the heater, that is, the probes tend to stay trapped onto vortices for shorter times.

In this work, we focus on the intermediate range of counterflow velocity, occurring when the vast majority of particles move upward, in the normal fluid direction, away from the heat source, with the corresponding streamwise (vertical) velocity distributions characterized by two peaks centered near $v_n/2$ and v_n. We specifically observe frequent velocity changes along individual particle trajectories and, as detailed below, we propose a separation scheme that allows us to neatly identify two motion regimes. Our results clearly show that the flow-induced motion of single particles can be associated to the low velocity peak of the velocity distribution, when it can be said that the particle motion is significantly influenced by quantized vortices (slow regime), or to the high velocity peak, when it appears that the particle motion is greatly affected by the imposed normal fluid velocity (fast regime).

However, before proceeding, it is important to remark that a direct, quantitative comparison between our results and those reported by Mastracci & Guo (2018) is currently not possible because our square channel is larger (it has 25 mm sides) and, as discussed, for example, by Babuin *et al.* (2012), the transition to the turbulent state occurs at smaller fluid velocities in larger channels – see also La Mantia (2016). It follows that in our channel a single-peaked velocity distribution can be obtained at q values corresponding to double-peaked distributions in the channel used by Mastracci & Guo (2018). Additionally, in the latter case, the investigated flow region included the channel walls, where quantized vortices tend to preferentially concentrate, as discussed, for example, by Baggaley & Laizet (2013) and La Mantia (2017), while the present results are obtained away from the walls, in the channel bulk region, but also at a distance from the heat source smaller than in the case reported by Mastracci & Guo (2018) – see, e.g., Bertolaccini *et al.* (2017) and Švančara *et al.* (2018*b*) for discussions on the role of the entrance length in thermal counterflow. Consequently, at the same heat flux, the actual L values of the regions experimentally probed are not expected to be equal. On the other hand, the features of particle motion introduced above have been identified in both channels, although at different q values, indicating therefore that their occurrence is not qualitatively influenced by the flow geometry.

More importantly, we show here that the interactions between quantized vortices and flow-probing particles appear to be relevant not only for the slow particles, as claimed in the past, for example, by Mastracci & Guo (2018), but also for the fast ones, at least in the range of investigated parameters, that is, for sufficiently dense vortex tangles, in turbulent counterflow. Specifically, we find that both slow and fast particles display non-classical, broad distributions of velocity, which are characterized by heavy tails and indicate the occurrence of particle-vortex interactions in both regimes. This can be regarded as the work main scientific result, obtained by applying the just mentioned separation scheme.

The paper is organized as follows. In §2 we describe our visualization setup and in §3.1 we use the statistical distributions of the streamwise particle velocity to estimate the normal fluid velocity for our experiments. We then show how the different velocity regimes of particle motion can be separated (§3.2) and investigate their properties (§3.3 to 3.6), before concluding in §4.

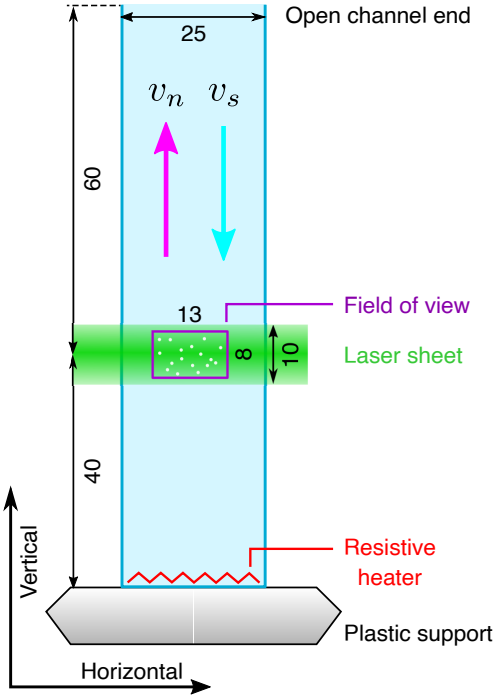

FIGURE 1. Schematic view of the channel, see La Mantia (2016) for a relevant picture; dimensions are in millimeters. The glass channel (light blue) has a square cross-section and its top is open to the surrounding helium bath. The channel glass walls are mounted on a frame and touch each other at the channel corners. The frame bottom (shaded grey) is slightly smaller than the experimental volume cross-section and the heater is located in its middle, inside the channel. The laser sheet (green) is about 1 mm thick (in the direction perpendicular to the scheme). The magenta and cyan arrows indicate the directions of the normal fluid velocity $\vec{v}_n$ and of the superfluid velocity $\vec{v}_s$, respectively. The horizontal and vertical directions used in the text are marked by black arrows.

2. Methods

The Prague cryogenic visualization setup was employed for data acquisition, see, e.g., Švančara *et al.* (2018*b*) and references therein for detailed descriptions. In brief, it consists of a low-loss helium cryostat with the experimental volume located at its bottom; the latter has a square cross-section, of 51 mm sides, and is 300 mm high. The optical access to the volume is provided by multi-layered windows, of 25 mm diameter, located 100 mm above the volume bottom, in the middle of each side. Two windows are used for the laser sheet (approximately 10 mm high and 1 mm thick) and one for the camera.

Thermal counterflow is investigated in a semi-closed glass channel of square cross-section, see figure 1, vertically mounted inside the experimental volume. The flow source is a planar resistive heater located at the bottom of the channel. As mentioned above, when the heater is switched on, the normal component flows upward, i.e., in the positive vertical direction, while the superfluid component flows toward the heater.

We seed liquid helium with solid deuterium particles in order to visualize its flow. The particles are made *in situ* by abrupt solidification from the gaseous phase (about 2% of deuterium gas diluted into helium gas is introduced into the bath by several short pulses). We capture the particle motions by using a CMOS camera, sharply focused on the plane illuminated by the laser sheet. The camera field of view is 13×8 mm^2, with 1 Mpix spatial resolution.

Each acquired movie is characterized by the temperature T of the He II bath, the heat flux q supplied by the heater and the camera frame rate f, and consists of hundreds of frames (up to a few thousands). In order to obtain large data sets, we collected between 5

and 105 movies for each experimental condition. Individual camera frames were processed by employing a custom-made tracking algorithm, providing sets of particle positions linked to the respective trajectories. Raw tracks were smoothed and differentiated to obtain time-dependent velocities and accelerations.

Following Mordant *et al.* (2004), we estimated the particle velocities and accelerations by convolving their positions with Gaussian kernels, denoted below as G_1 and G_2, which are obtained as time derivatives of the Gaussian filter G_0, employed to smooth the trajectories. From $G_0(t) \sim \exp\left[-\left(\frac{t}{\alpha\tau}\right)^2\right]$ we obtain, for the particle velocities, $G_1(t) \sim -\left(\frac{t}{\alpha\tau}\right) G_0(t)$ and, for their accelerations, $G_2(t) \sim \left[2\left(\frac{t}{\alpha\tau}\right)^2 - 1\right] G_0(t)$, where t indicates the time and $\tau = 1/f$ (the relations are only proportional because the kernels have to be adequately normalized).

The non-dimensional parameter α controls the level of smoothing and here we use 1.7 for G_0 and G_1, and 5.0 for G_2. We specifically studied the influence of this parameter on the standard deviations of the particle velocity and acceleration, and chose the α values resulting in relatively small standard deviation changes, following a procedure analogous to that outlined by Švančara *et al.* (2018*a*). Similarly, the convolution with discretely sampled positions was carried out in a finite sliding time window of width $2\beta\tau$, that is,

$$x_i(t) = \sum_{t'=t-\beta\tau}^{t+\beta\tau} x(t')G_i(t'-t), \tag{2.1}$$

where x_i, with $i \in \{0, 1, 2\}$, indicates the position, velocity and acceleration, respectively, and x denotes the raw position obtained from the tracking software; we set the parameter β equal to 3 for particle positions and velocities, and to 10 for accelerations, that is, $\beta > \alpha$.

The finite width of the kernels is linked to the loss of time resolution because multiple raw positions are taken into account to obtain a smooth single position (velocity, acceleration). We can estimate the effective time resolution of the kernels to be $\tau' \approx 2\sqrt{2}\alpha\tau$, which is analogous to the 95% (two-sigma) confidence interval of the normal distribution. For the velocity estimate we obtain $\tau_1' \approx 5\tau$ and, in the case of the particle accelerations, $\tau_2' \approx 14\tau$.

It then follows that the latter time resolutions can be used in equation (1.3) as the characteristic time scale t_p needed for the estimation of the scale s_p probed by our particles, which consequently can be influenced by the specific feature (velocity, acceleration) one is trying to measure. Note also that the choice of the α and β parameters depends in general on the experimental conditions and that here we chose values satisfying the standard deviation criterion mentioned above (Mordant *et al.* 2004; Švančara *et al.* 2018*a*).

3. Results and discussion

Experiments were carried out at temperatures ranging from 1.3 to 1.7 K. The temperature was kept constant by stabilizing the pressure of helium vapour (this was done by using a PC-controlled butterfly valve mounted between the cryostat and the pumping unit). To generate thermal counterflow, a power up to 2.5 W was applied to our planar heater. Since the walls and frame of our experimental channel are pressed against each other, we assume here, as in previous studies performed with the same setup, that the applied heat leaks out of the channel and thermal counterflow occurs also outside the channel, within the experimental volume. Heat is therefore transported over an area larger than the channel cross-section and, as a first step, we set this area equal to the cross-section of our experimental volume (51×51 mm^2). It then follows from equation (1.1)

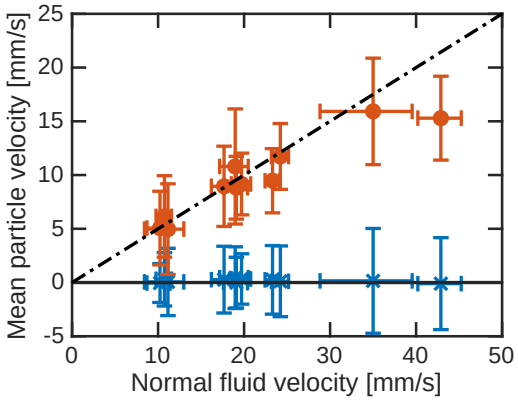

FIGURE 2. Mean horizontal (blue crosses) and vertical (red circles) particle velocities as a function of the normal fluid velocity v_n, computed from equation (1.1) by using the experimental volume cross-section (51×51 mm^2). Solid black line: null velocity; dot-dashed black line: $v_n/2$ scaling. The error bars correspond to the measurement standard deviation on the vertical axis and, on the horizontal axis, to the variation of v_n due to the (relatively small) temperature changes occurring during each experimental run, associated to each point; results obtained from 11 data sets, containing at least 0.5 million velocity points each, are displayed in the figure.

that the corresponding range of normal fluid velocities is from 10 to 45 mm/s, which can therefore be regarded as a conservative estimate of the actual v_n values. Note in passing that for the present channel the transition to the turbulent state was reported to occur for $v_{ns} \gtrsim 1$ mm/s (La Mantia 2016).

Figure 2 displays the systematic dependence of the mean particle velocity on v_n calculated from equation (1.1). We observe that the horizontal component (blue crosses) remains around zero, while the mean vertical velocity scales as $v_n/2$, up to approximately 25 mm/s, and deviates from this scaling for larger v_n values. The outcome confirms therefore that the majority of our particles flow in the normal fluid direction, away from the heat source (see the above discussion on the features of particle motion in thermal counterflow).

The result also justifies, at least to a first approximation, our choice of assuming that the applied heat is transported over an area equal to that of the experimental volume cross-section because the mean particle velocity in the vertical direction scales as $v_n/2$ which is the value one would expect in the range of investigated parameters, that is, at sufficiently small values of heat flux – note in passing that the mean particle velocity can also be significantly smaller than $v_n/2$ in dense vortex tangles (Kivotides 2008*a*). Additionally, as discussed below, see figure 11, particle trajectories do not show any prominent deviation from the vertical direction.

However, one cannot in principle exclude that inhomogeneous parasitic flows, due to the heat leak from the channel, may affect the observed particle dynamics. These flows may occur (i) in the close proximity of the heat source, where the channel walls are pressed against its bottom support, and (ii) at the corners where the vertical walls are pressed against each other, see figure 1. We also note that a small part of the heat supplied by the planar heater is conducted through the bottom structure to the bulk helium and convected by a counterflow around the channel, because the bottom structure temperature, due to the finite conductivity of the heater and support, and to Kapitza resistance, is always slightly higher than that of the surrounding liquid. Considering that our field of view – 13×8 mm^2 – is located approximately 40 mm away from the heater, in the middle of the channel, of 25 mm sides, and approximately 14 mm away from the corners of the channel, along the corresponding diagonals, one may say that the field of view is relatively far away from the just mentioned problematic spots.

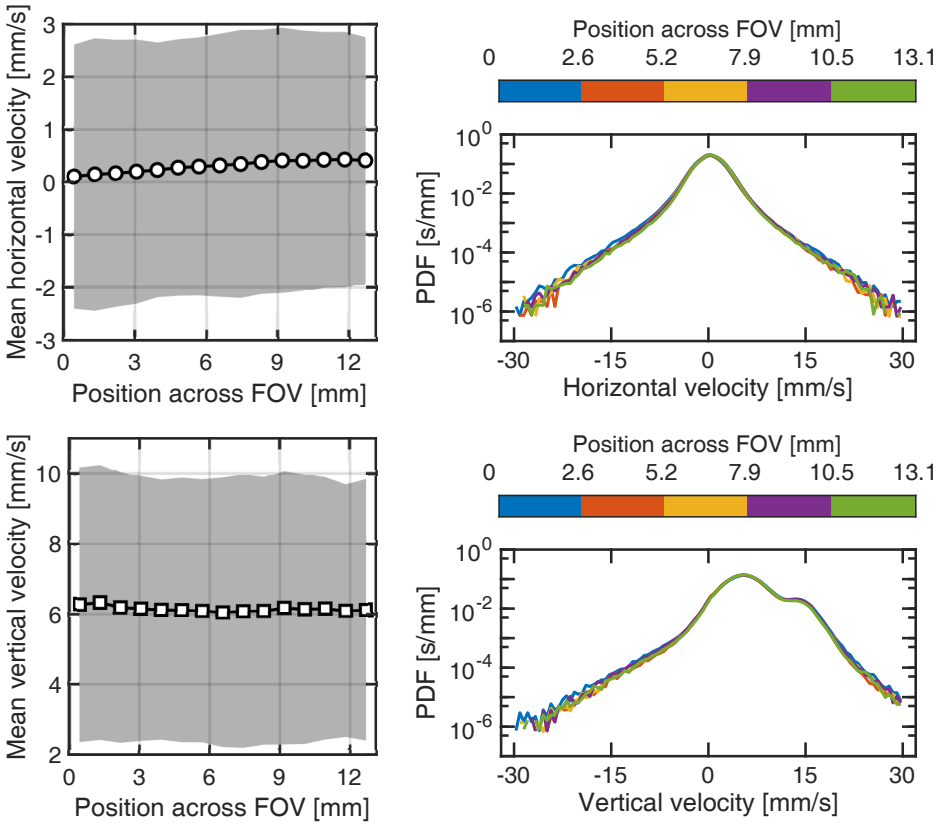

FIGURE 3. Uniformity of the particle velocity across the field of view (FOV). Left column: mean values of the horizontal (circles) and vertical (squares) velocities of the particles, calculated by splitting the FOV into 15 vertical regions; grey areas: corresponding velocity standard deviation. Right column: probability density function (PDF) of the horizontal (top) and vertical (bottom) velocities of the particles, calculated by splitting the FOV into 5 vertical regions, indicated by the colour map. Data set collected at 1.36 K, with an applied heat power $P = 0.61$ W.

In order to quantitatively check if this is far enough, that is, in order to further justify our assumption that the applied heat is transported over an area larger than that of the channel cross-section, we divided the field of view into rectangular regions, and computed for each of them the mean particle velocity, in all probed experimental conditions. We found that the latter velocity is always directed upward, i.e., away from the heat source, with negligible side component and approximately constant magnitude, regardless of the number of regions in which the field of view is divided. Specifically, the mean value of the horizontal velocity is always close to zero and substantially smaller than the corresponding standard deviation (it is also much smaller than the mean value of the vertical velocity).

The outcome is shown explicitly in figure 3 for a large data set containing more than 8 million particle positions, obtained at 1.36 K, with an applied heat power $P = 0.61$ W. The left column displays the particle velocity components as a function of the particle position across the field of view, split into 15 vertical regions. It can be seen that the mean horizontal velocity is slightly larger on the right side of the field of view, but its magnitude is close to zero and much smaller than the corresponding standard deviation, plotted in the panel as the grey area (other data sets display similar features but with less evident systematic behaviour of the mean horizontal velocity). More importantly, relevant statistical distributions of the particle velocity, computed after splitting the field of view into 5 vertical regions, are plotted in the right column of the same figure and neatly overlap (the velocity statistical distributions of the particles are discussed below

#	T [K]	P [W]	f [fps]	N [10^6]	v_n [mm/s]	v_{ns} [mm/s]
1	1.39 ± 0.02	1.22	800	1.4	18.7	20.2
2	1.36 ± 0.02	0.61	800	8.6	10.9	11.6
3	1.52 ± 0.03	1.23	250	1.1	10.2	11.7

TABLE 1. Experimental conditions for the data sets displaying bimodal behaviour, see also figure 4; T: temperature of the He II bath; P: applied heat power; f: camera frame rate; N: number of particle positions in the data set; v_n: normal fluid velocity computed from equation (1.1) by using the experimental volume cross-section; v_{ns}: counterflow velocity computed from equation (1.2) by using the experimental volume cross-section; note that the velocity values reported here can be regarded as conservative estimates of the actual values, see the text for details.

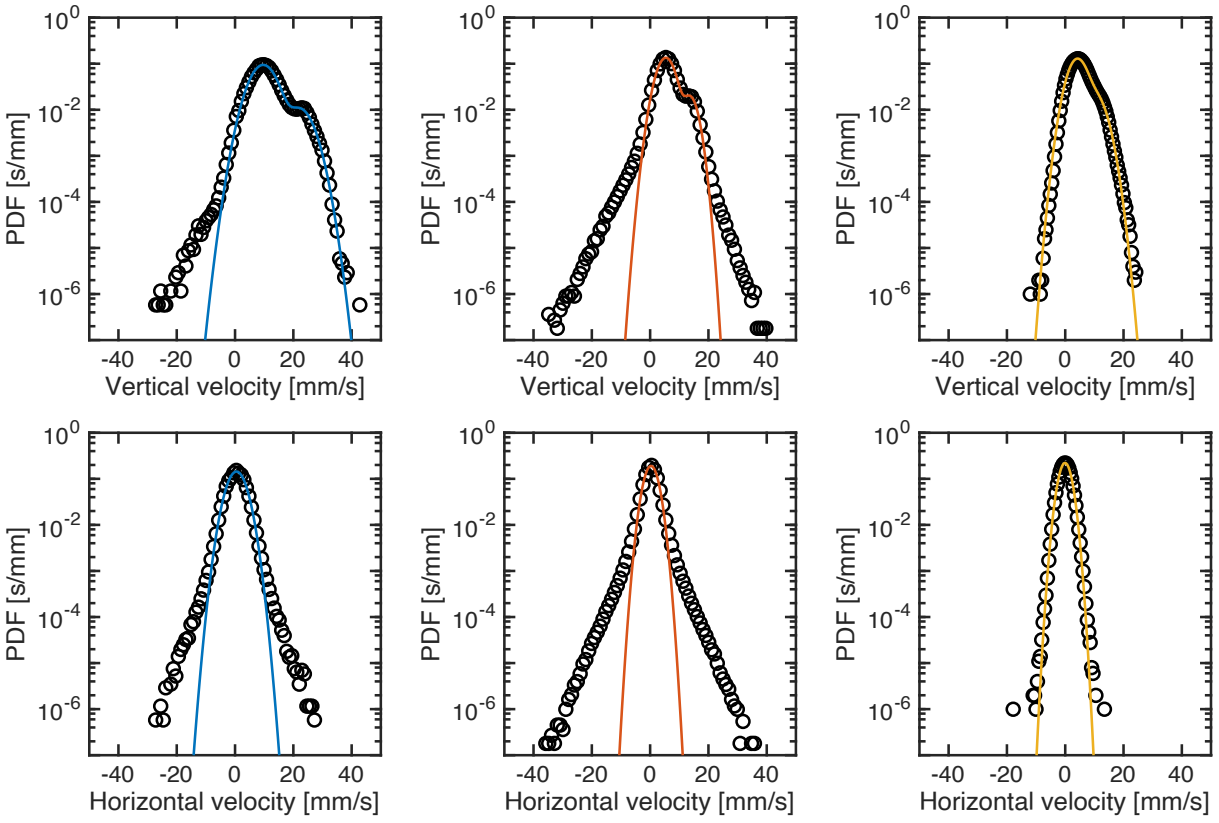

FIGURE 4. PDF of the particle velocity. Top row: distributions of the vertical component (black circles) with their double-peaked Gaussian fits (colour lines). Bottom row: distributions of the horizontal component with their single-peaked Gaussian fits. Columns correspond to data sets #1, #2 and #3, respectively, see table 1 for relevant experimental conditions.

in detail). The latter result clearly demonstrates that the observed particle dynamics does not depend appreciably on the particle position within the field of view, that is, no evidence of significant parasitic flows is found in our data.

3.1. *Statistical distributions of the particle vertical velocity*

As mentioned above, the probability distribution functions (PDFs) of the particle vertical velocity display either one or two local maxima. From now on we focus on three data sets that are characterized by two neat distribution maxima which are well separated from each other and centered near $v_n/2$ and v_n, that is, the vertical velocity distributions

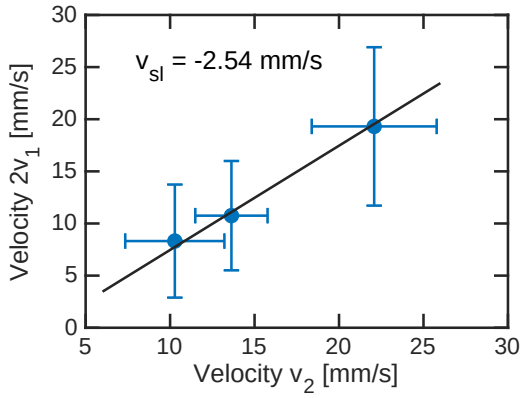

FIGURE 5. Scaling of the peak velocities, obtained from double-peaked Gaussian fits of the considered vertical velocity PDFs. Blue circles: experimental data, see table 1 for relevant experimental conditions. The error bars indicate the standard deviation of the velocities. Black line: equation (3.1) with $v_{sl} = -2.54$ mm/s.

of the other data sets considered for figure 2 display only one prominent peak; see table 1 for relevant experimental conditions.

The first step of the analysis is to fit the vertical velocity distributions with a double-peaked Gaussian function, see the top row of figure 4. The fits neatly follow the experimental data in the distributions cores (the tails are discussed below) and the peak velocities, $v_1 < v_2$, with the respective standard deviations, $\sigma(v_1)$ and $\sigma(v_2)$, can be obtained from the fits. Following Mastracci & Guo (2018) the peak velocities are expected to scale as $v_1 = v_n/2 + v_{sl}$ and $v_2 = v_n + v_{sl}$, where v_{sl} denotes the non-zero slip velocity due to the density difference between He II and solid deuterium – note that Mastracci & Guo (2018) set arbitrarily the v_1 offset to approximately 2 mm/s.

It then follows that v_1 and v_2 obey the scaling relation

$$2v_1 = v_2 + v_{sl}, \tag{3.1}$$

which allows us to verify the origin of the two peaks and to determine v_{sl}. We plot this dependence in figure 5 (circles), with a linear fit of unit slope (line). The scaling is clearly verified and we can hence estimate the slip velocity v_{sl} to be approximately equal to -2.5 mm/s. The negative sign indicates that our particles are heavier than He II and, indeed, solid deuterium is heavier than He II.

If we assume that v_{sl} is equal to the terminal velocity of a freely falling spherical particle, we can estimate the corresponding particle radius r from the Stokes formula

$$r = \sqrt{\frac{9}{2}\frac{\mu v_{sl}}{g(\varrho_p - \varrho)}}, \tag{3.2}$$

where μ and ρ denote the temperature-dependent dynamic viscosity and density of He II, respectively, tabulated by Donnelly & Barenghi (1998), g indicates the acceleration due to gravity and $\rho_p = 200$ kg/m^3 is the density of solid deuterium, estimated from its crystal structure (Bostanjoglo & Kleinschmidt 1967). For $T = 1.40$ K, we obtain $r \approx 5$ μm, which agrees with the typical size of the used particles, see, for example, Švančara & La Mantia (2017).

It is consequently possible to compute the normal fluid velocity v_n, the superfluid velocity v_s and the counterflow velocity v_{ns} following the just outlined procedure, see table 2 for relevant results. Specifically, we set the normal fluid velocity magnitude v_n equal to $v_2 - v_{sl} = 2(v_1 - v_{sl})$, by using equation (3.1) and the corresponding values of peak and slip velocities, estimated from the probability density functions of the particle vertical

#	v_n [mm/s]	v_s [mm/s]	v_{ns} [mm/s]	s_q [μm]	s_p [μm]	R
1	24.6	1.9	26.5	35	70	2.0
2	16.2	1.1	17.3	58	45	0.8
3	12.8	1.9	14.7	48	110	2.3

TABLE 2. Characteristic flow velocities and scales, estimated from the slip and peak velocities, see the text for details; $v_n = v_2 - v_{sl} = 2(v_1 - v_{sl})$: normal fluid velocity magnitude, see also equation (3.1); $v_s = v_n\rho_n/\rho_s$: superfluid velocity magnitude; $v_{ns} = v_n + v_s$: counterflow velocity magnitude, see also equation (1.2); note that the velocity values reported here are larger than those listed in table 1; s_q: mean distance between quantized vortices, equation (1.4), note that relevant γ values were obtained as discussed by Švančara *et al.* (2018*b*); s_p: scale probed by the particles, equation (1.3), with $t_p = 5/f$; $R = s_p/s_q$: non-dimensional scale ratio.

velocity. We then take into account that, in thermal counterflow, the mass flow rate is null and, consequently, we set the superfluid velocity magnitude v_s equal to $v_n\rho_n/\rho_s$, where, as mentioned above, the fluid density ratio depends on temperature. Finally, we obtain v_{ns} from equation (1.2), that is, we set the counterflow velocity magnitude equal to $v_n + v_s$. Note that the v_n values obtained from equation (1.1) by using the experimental volume cross-section, reported in table 1, are of the same order of (and consistently smaller than) the values of normal fluid velocity listed in table 2, with the largest relative difference observed for data set #2 and approximately equal to 50% (the same applies when one compares the corresponding counterflow velocities).

Additionally, we can now calculate the scale s_p probed by our particles and, to this end, we set $t_p = 5/f$ in equation (1.3) because, as discussed in §2, the time resolution imposed by the chosen velocity estimation algorithm is equal to approximately 5τ, where $\tau = 1/f$. We can also compute the mean distance s_q between quantized vortices from equation (1.4) by using the v_{ns} values listed in table 2, that is, those derived from the statistical distributions of the particle vertical velocity – relevant γ values were obtained following Švančara *et al.* (2018*b*). The scales estimated in such a way are also reported in table 2, together with the corresponding ratio R.

We find that, for the chosen data sets, the smallest resolved scale is of the same order of the mean distance between quantized vortices. The outcome does not change appreciably, if, for the estimation of s_q, we employ the thermal counterflow velocities derived from equation (1.2) by using the experimental volume cross-section, see table 1. Indeed, the obtained R values are still of order one, although slightly smaller than those listed in table 2, that is, the corresponding scale ratios are equal to 1.5, 0.5 and 1.8 for data sets #1, #2 and #3, respectively.

It then follows that, for the present statistical distributions of the particle velocity, the most significant deviations from the Gaussian shape should be observed for data set #2. This is indeed the case, as shown in figure 4. The outcome is consistent with the fact, mentioned in §1, that neat power-law tails are usually observed solely for R values appreciably smaller than 1.

3.2. *Bimodal dynamics and trajectory segmentation*

A striking observation of this paper is apparent from the time evolution of the vertical position of some particles, see the left panel of figure 6. Two characteristic slopes can be easily spotted, corresponding to the peak velocities v_1 and v_2. Let us follow the highlighted trajectory. We plot its vertical velocity and acceleration as a function of time in the right panel of the same figure. Note that rapid velocity changes between

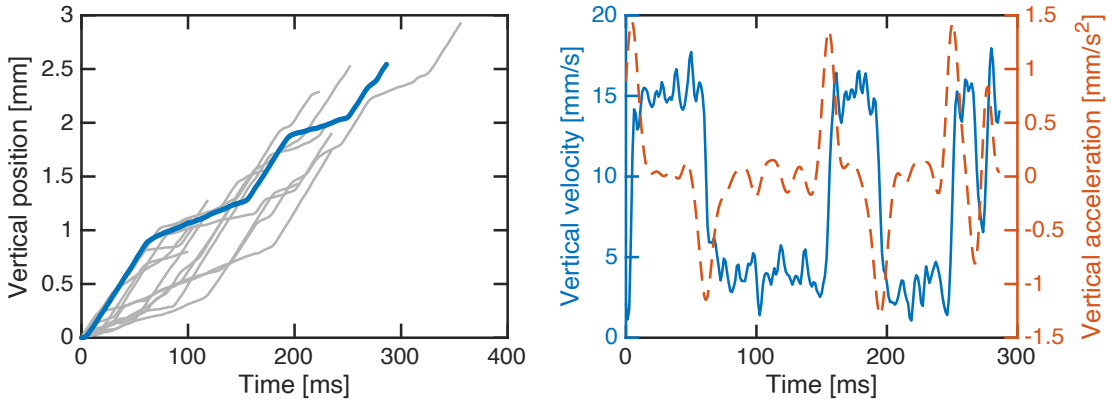

FIGURE 6. Left: typical particle trajectories collected from data set #2. Right: vertical velocity (blue solid line) and acceleration (red dashed line) of the particle track highlighted in the left panel.

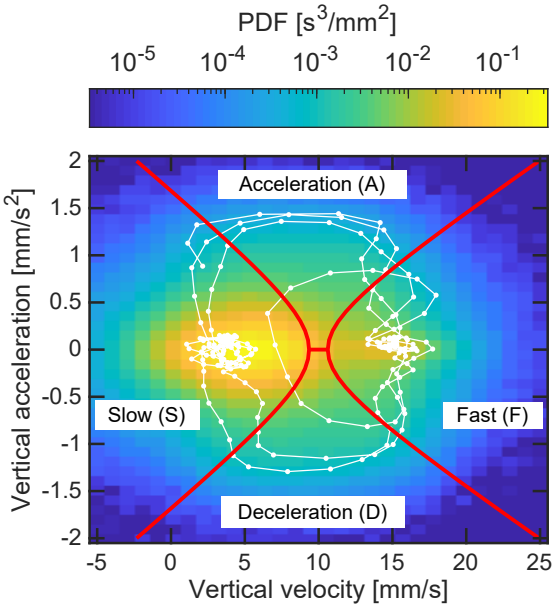

FIGURE 7. Separation scheme for data set #2. Colour-coded map: bivariate PDF of the measured velocity-acceleration pairs. White points: trajectory highlighted in figure 6. Two hyperbolas and a segment (red lines) divide the phase space into four motion types, see the text for details.

two roughly constant values are clearly visible and consistent with the corresponding acceleration changes.

The behaviour allows us to develop a separation scheme in the velocity-acceleration phase space, shown in figure 7 for data set #2. The trajectory highlighted in figure 6 takes the form of several loops (white points) and the areas of higher density of points, near the line of zero acceleration, represent the two peak velocities (note the bivariate PDF plotted as the colour-coded background).

Our separation scheme is based on that developed by Mastracci & Guo (2018), but, while they separated motion regimes solely on the basis of the particle vertical velocity, here we divide the two-dimensional phase space into four subspaces (or motion types), labelled throughout the paper as Slow (S), Fast (F), Acceleration (A) and Deceleration (D).

We define the respective separating curves as (i) a slow hyperbola, with focus in $[v_1, 0]$ and semi axes of lengths $2\sigma(v_1)$ and $2\sigma(a_y)$, (ii) a fast hyperbola, with focus in $[v_2, 0]$ and semi axes of lengths $2\sigma(v_2)$ and $2\sigma(a_y)$, and (iii) a segment between the points

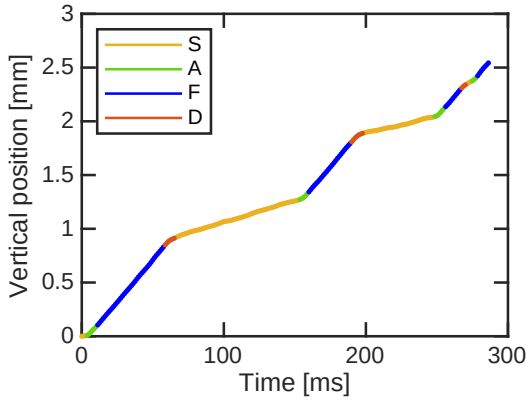

FIGURE 8. Trajectory highlighted in figure 6 separated into segments according to the scheme discussed in the text.

$[v_1 + 2\sigma(v_1), 0]$ and $[v_2 - 2\sigma(v_2), 0]$. The values v_i and $\sigma(v_i)$, with $i \in \{1, 2\}$, are obtained from Gaussian fits, and $\sigma(a_y)$ denotes the standard deviation of the particle vertical acceleration (its mean value is very close to zero in all considered cases). These curves are plotted as thick red lines in figure 7.

The segmentation of the exemplary trajectory, plotted in figure 8, indicates that the proposed scheme correctly identifies different motion regimes and can be used to split other trajectories. Note that spurious short segments of type A or D, consisting of less than three points, are sometimes observed in the segmentation scheme results. They usually precede and follow much longer segments of type S or F, and most likely indicate false transitions between regimes of the same type, that is, they are due to the noise level of the computed particle acceleration. In order to prevent excessive trajectory fragmentation, we decided to merge these short segments with their respective neighbours. This choice led to the softening of the separation scheme, but, at the same time, it helped to retrieve long segments of type S or F, which are discussed in the following section.

3.3. *Segment length distributions*

We define the segment length as the physical distance separating its first and last point (segments consisting of a single point have zero length). Typical distributions of segment lengths of different types are plotted in the top row of figure 9. Although the PDFs of Slow and Fast segments (top left panel) are highly peaked near zero, we see that the distributions are fairly broad and segments of lengths appreciably exceeding the mean distance between quantized vortices, about 0.06 mm for the displayed data set, are relatively common. We summarize the mean values and standard deviations of segment lengths in table 3.

The lengths of segments of type F, associated to fast particles, indicate that the latter can often travel long distances without changing their motion regime, i.e., without being significantly disturbed by quantized vortices during their upward journey. The outcome suggests therefore that the vortex tangle is likely not distributed uniformly in the considered flow region; this, by the way, is consistent with our current understanding of counterflow in vertical channels – see, for example, Švančara *et al.* (2018*b*) and Varga & Skrbek (2019). Note also that Kivotides (2008*b*) observed a similar depletion of particle-vortex interactions in relevant numerical simulations.

The length distributions obtained in different conditions collapse if we normalize the segment length by its standard deviation, see the bottom panels of figure 9. This may indicate that the distribution shape is not significantly influenced by the vortex line

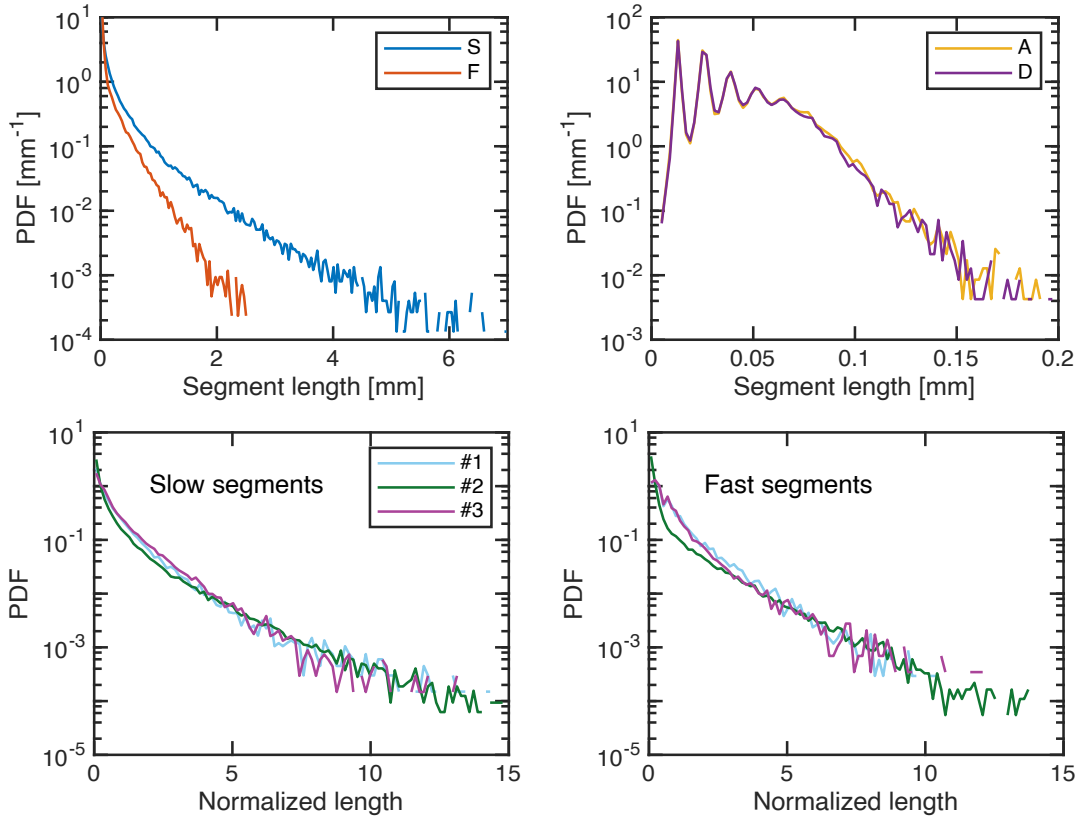

FIGURE 9. PDFs of segment lengths. Top row: PDFs of different types obtained from data set #2. Bottom row: comparison of different data sets; lengths are here normalized by their standard deviations. The segment type is specified in each panel.

#	μ_S [μm]	σ_S [μm]	μ_F [μm]	σ_F [μm]
1	279	425	108	137
2	221	415	86	178
3	90	123	170	230

TABLE 3. Characteristic lengths of trajectory segments; μ: mean; σ: standard deviation. The subscripts S and F denote slow and fast trajectory segments, respectively; see the text for details.

density. However, we do not observe any clear relation between the mean segment length and the mean distance between quantized vortices.

The lengths of transition segments – A and D, see the top right panel of figure 9 – display much narrower PDFs, with typical lengths comparable to the mean distance s_q between quantized vortices. It is very tempting to conclude that these abrupt events of large acceleration (deceleration) occur in the vicinity of quantized vortices, but, unfortunately, the time resolution of the present measurements does not allow such a strong claim. Indeed, we mentioned in §2 that the effective time resolution of our acceleration measurements is appreciably larger than that of the velocity estimates. It then follows that the former scale ratios are about three times larger than the latter ones, which are reported in table 2. Our results therefore suggest that the observed events of large acceleration (deceleration) may occur in the proximity of quantized vortices, but, in order to make a stronger statement, we would need to access smaller scales, i.e., to improve our time resolution, which, by the way, is technically feasible (see, for example,

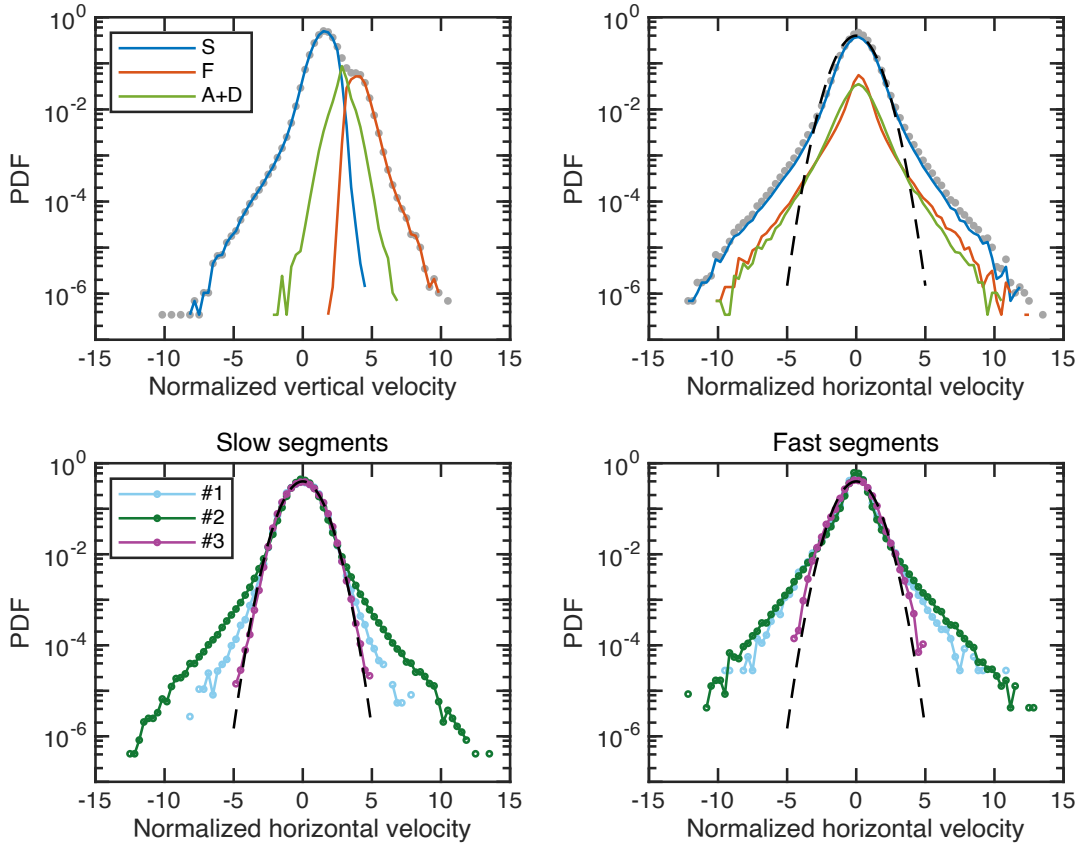

FIGURE 10. PDFs of Cartesian velocities, conditioned by the motion regime. Top row: PDFs of the horizontal and vertical components obtained from data set #2 (A+D corresponds to the merged data of types A and D); grey points denote unconditioned velocity distributions, scaled to unit area (dimensional velocities are normalized by using the standard deviation of unconditioned data). Black dashed line: Gaussian distribution. Bottom row: PDFs of the horizontal component obtained from the chosen data sets and conditioned by segments of type S and F; all distributions are scaled to unit area.

Voth *et al.* 2002). Note also that the oscillations seen in this panel at small length are an experimental artefact, due to the finite camera frame rate, because the individual peaks represent the contributions of trajectory segments containing the same number of particle positions.

3.4. *Conditioned velocity distributions*

The PDFs of vertical and horizontal velocities, obtained from data set #2, are plotted in the top row of figure 10. While the grey points indicate the unconditioned PDFs, scaled to unit area, the colour lines denote the respective contributions of different motion types (types A and D are merged together, for the sake of clarity). Note that all the physical velocities are normalized by the standard deviation of the unconditioned data and that the areas under the PDFs reflect the relative abundance of individual motion types.

The PDFs of the particle vertical velocity (top left panel) clearly show that motion types S and F are well separated (the small overlap is due to the removal of very short segments, mentioned above). For the PDFs in the horizontal direction, displayed in the top right panel of figure 10, we observe that, at large enough velocities, the distributions of all motion types neatly deviate from the Gaussian shape, displayed as the black dashed line. The trends for all the three data sets considered here are displayed in the bottom row of figure 10, where we plot the PDFs conditioned by the motion type S (bottom left panel) and F (bottom right panel). Note that shapes close to the Gaussian one are

observed only for data set #3, which is characterized by the largest ratio between the scale probed by the particles and the quantum scale, see table 2.

This result contradicts the findings of Mastracci & Guo (2018). They reported that the horizontal velocity distributions of particles belonging to their group G2, loosely corresponding to our motion type F, strictly display a Gaussian form. Based on this observation, they claimed that these particles behave as if the vortex tangle were absent, but our results suggest a different physical picture, that is, both fast and slow particles appear to interact with the vortex tangle, at least in the range of investigated parameters – several arguments supporting the close relation between velocity distribution heavy tails and particle-vortex interactions are presented by La Mantia *et al.* (2016). Additionally, the latter interactions could be influenced by the the normal fluid vortical structures observed in numerical simulations (Idowu *et al.* 2000; Yui *et al.* 2020), in the close proximity of moving quantized vortices. However, these wake structures were observed at relatively small fluid velocities, that is, their topology in dense vortex tangles, which are specifically relevant for the present study, is currently unknown.

The disagreement between our measurements and those reported by Mastracci & Guo (2018) is most likely due to the relatively small sizes of the data sets they discussed, which are at least one order of magnitude smaller than ours – this is apparent if one compares PDFs plotted in logarithmic-linear scale – and which consequently do not allow to resolve events of large velocity occurring at small scales and with much smaller probability.

Mastracci & Guo (2018) also reported velocity fluctuations of particles belonging to their group G2 – fast particles – and, consistently with the corresponding velocity distribution shapes, these fluctuations were interpreted solely as an effect of the normal fluid flow on the particle dynamics, see also Mastracci *et al.* (2019). They specifically found that horizontal and vertical velocity fluctuations of fast particles are qualitatively different, with the latter larger than the former, but this is not apparent from our data, that is, we do not see any consistent dependence of velocity fluctuations on experimental parameters. This might be related once more to the relatively small size of the data sets collected in the past and/or to the fact that these studies were performed at relatively small heat fluxes (Yui *et al.* 2020).

We may therefore say that, at sufficiently large heat fluxes, particle-vortex interactions cannot be neglected, but this could possibly be the case at heat fluxes smaller than those considered in the present study, that is, in the laminar regime for the normal fluid component. Additionally, as shown in the following section, the particle trajectories for motion types S and F appear to have different topologies, that is, the strength of the corresponding particle-vortex interactions does not seem to be the same in the two cases.

3.5. *Distributions of the velocity orientation angle*

The idea of different interaction strengths came to us by studying the appearance of the particle trajectories. We observed that segments of type F are considerably straighter than those of type S and, additionally, we found similar observations in the literature (Chagovets & Van Sciver 2011; La Mantia 2016). It was specifically argued that the erratic, wiggly paths of some particles may be related to frequent interactions between the particles and quantized vortices. In contrast, fast particles are expected to follow the more uniform flow field of the normal component. Here, we study the behaviour quantitatively, by evaluating how straight the individual trajectory segments are, focusing mostly on motion types S and F.

In order to quantify the trajectory shape, we employ the velocity orientation angle θ, which can be evaluated along the trajectory, for each point, and is defined, following

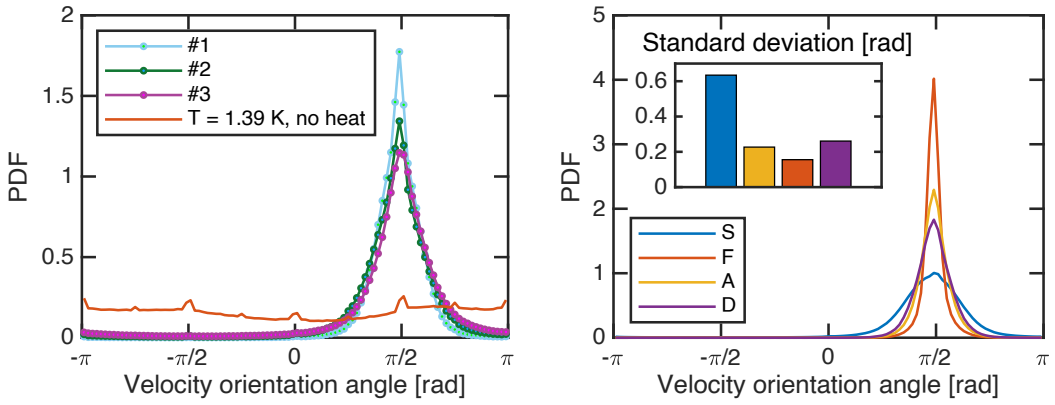

FIGURE 11. PDFs of the velocity orientation angle θ, see equation (3.3). Left panel: comparison of the chosen data sets with a residual flow with no applied heat flux. Right panel: PDFs corresponding to the individual motion types, from data set #2; inset: standard deviation of the distributions, displayed in the order corresponding to a typical time evolution of particle motion, that is, S $\rightarrow$ A $\rightarrow$ F $\rightarrow$ D.

Paoletti *et al.* (2008), as

$$\theta = \arctan\left(\frac{v_y}{v_x}\right), \tag{3.3}$$

where v_y and v_x indicate the particle velocities in the vertical and horizontal directions, respectively. Note that θ can be evaluated in the full angular range, yielding values $-\pi \leqslant \theta \leqslant \pi$. The direction of the normal fluid flow corresponds to $\theta = \pi/2$ and that of the superflow to $\theta = -\pi/2$.

We plot the PDFs of the unconditioned orientation angle in the left panel of figure 11, where we compare the distributions obtained in thermal counterflow with a control data set measured when the heater was switched off (red line). We observe that the latter distribution is relatively constant, indicating that the corresponding velocity vectors do not have a preferred orientation. The small equidistant peaks are experimental artefacts due to the finite spatial resolution, almost equivalent to the bias known as peak-locking in Particle Imaging Velocimetry (Raffel *et al.* 2018). Indeed, it is impossible to achieve sub-pixel resolution with a one-pixel particle. Therefore this particle will move to one of the eight pixels around it in the next frame (the average velocity being zero in this case), and induce a small bias for θ, equal to $\pi/4$. Instead, in thermal counterflow, we observe a strong preferential orientation of the velocity vectors in the direction of the normal component. This confirms that our data belong to the intermediate range of counterflow velocity discussed in §1 and, additionally, means that most particles follow relatively straight vertical trajectories.

Deviations from straight trajectories, that is, particle tracks with constant θ, can be quantified by using the width of the corresponding distribution peaks. We plot PDFs of different motion types in the right panel of figure 11, and, as expected, segments of type S display a significantly broader distribution – i.e., of larger standard deviation (see inset) – than that of type F. The result indicates not only that slow particles are, on average, slower than fast ones but also that their trajectories are subjected to larger deviations, as they seem to strongly interact with nearby vortices.

3.6. *Particle accelerations*

A number of previous experimental studies (La Mantia *et al.* 2013; La Mantia & Skrbek 2014; La Mantia 2017; Švančara & La Mantia 2017) showed that information

obtained from the accelerations of particles probing turbulent flows of superfluid ^{4}He may contribute to our understating of the underlying physics. It was reported, for example, that the statistical distributions of the particle acceleration display classical-like shapes at sufficiently large scales, regardless of the flow type (La Mantia *et al.* 2013; Švančara & La Mantia 2017) and of the boundary proximity (La Mantia 2017). Additionally, experimentally obtained mean values of the particle acceleration were used to test relevant models of particle dynamics, taking especially into account added mass effects (La Mantia *et al.* 2013; La Mantia & Skrbek 2014).

Similarly, the present results suggest that not only particle velocities but also their accelerations may bring useful information for the identification of the two motion regimes corresponding to fast and slow particles. However, the just mentioned works (La Mantia *et al.* 2013; La Mantia & Skrbek 2014; La Mantia 2017; Švančara & La Mantia 2017) focused on general features of the observed particle dynamics, that is, they were less concerned by the investigation of single particle trajectories, which is instead the focus of the present study. We therefore decided to employ here the smoothing scheme described in §2, considering that one should be aware that experimental noise – due, for example, to the imprecise location of the particles – can be greatly amplified by common differentiation schemes, especially in the case of accelerations, usually computed as the second time derivative of the particle positions (see, for example, Voth *et al.* 2002; Lawson *et al.* 2018).

The drawback of our choice is the loss of time resolution in comparison with the data processing schemes used in the past, which, nevertheless, gave results consistent with the proposed physical description of the problem. Indeed, as mentioned above, the effective time resolution for the calculated accelerations is approximately three times larger than that associated to the particle velocities – note, for example, that the acceleration of the exemplary trajectory shown in figure 6 is a smoother function of time than the corresponding velocity. On the other hand, the advantage of our choice is that, in comparison to previous studies, we are confident that the chosen data processing scheme is less prone to noise amplification, that is, we believe that our separation scheme is robust enough to detect the occurrence of motion types S and F.

The idea that acceleration estimates may be important for the present analysis can also be supported by the pattern of the mean particle acceleration, conditioned by both velocity components, displayed in figure 12. The mean acceleration is indicated in the figure by white arrows and the colour map shows the bivariate PDF of the particle velocity. It seems that, on average, particles accelerate, that is, break free from the slow state and start to follow the normal component, when their horizontal velocity is close to zero. In contrast, we observe that events corresponding to particle deceleration in the vertical direction are coupled to non-zero horizontal velocity. It then appears that particle deceleration and acceleration events do not share the same features. The former events seems to be more abrupt than the latter, as they apparently increase the particle velocity in the direction perpendicular to the mean flow. Possibly, these events may be related to Kelvin waves generated on the vortex lines when particles are in their close proximity (Kivotides 2008*b*; Giuriato & Krstulovic 2019).

Additionally, from the figure it is apparent that the obtained mean accelerations are smaller than 0.1 mm/s^2. In order to physically interpret the latter value, one could start from the fact that the pressure gradient force, per unit of mass, attracting a spherical particle to a quantized vortex core is proportional to κ^2/d^3, where d indicates the distance between the particle and vortex core, see, for example, La Mantia *et al.* (2013) for the exact expression. A pressure gradient force of 0.1 mm/s^2 is obtained for a distance equal to approximately 120 μm, which is comparable to the scale probed by our particles, about

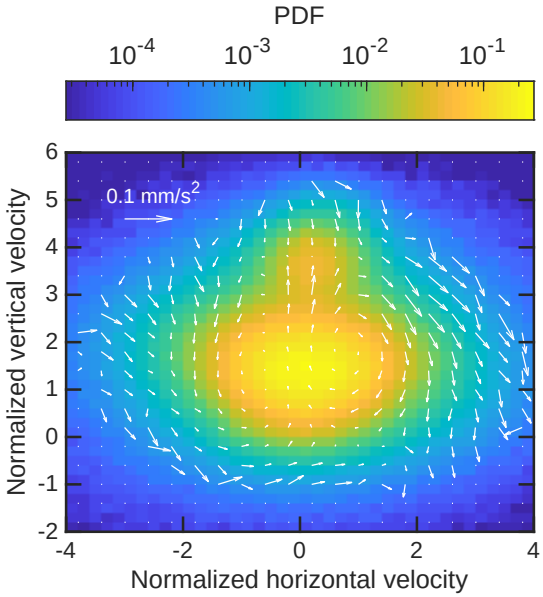

FIGURE 12. Mean particle acceleration conditioned by the particle velocity. Colour map: bivariate PDF of the particle velocity; both velocity components are normalized by their standard deviations. White arrows: mean acceleration map; accelerations are computed on a mesh two times coarser than the velocity PDF and are shown only if the corresponding bin counts more than 500 samples. The results are obtained from data set #2.

150 μm in the case of accelerations. On the other hand, if we set $d = 50$ μm, which is comparable to the estimated quantum scale s_q, see table 2, we find that the pressure gradient force is 1.5 mm/s^2, a value much larger than the mean accelerations shown in figure 12, but of the same order of the peak accelerations displayed in figure 6.

The reader should, nevertheless, keep in mind that the latter considerations on particle accelerations are rather speculative mainly because no obvious pattern in this phase space was observed for individual trajectories. Additionally, other experimental conditions should be investigated and data sets appreciably larger than the present ones should be collected. A clearer picture may also be achieved with better time resolution, which can be obtained, for example, with higher camera frame rates, i.e., by reducing the scale probed by the particles. Indeed, precise measurements of particle acceleration were achieved in classical flows with very fast pixel detectors originally developed for high energy physics (Voth *et al.* 2002; Mordant *et al.* 2004).

4. Conclusions

The behaviour of relatively small solid particles displays multiple regimes in thermal counterflow of superfluid ^{4}He. Within the investigated range of experimental parameters, we observe a clear bimodal dynamics along particle trajectories. These two regimes can be associated to fast particles, moving in the direction of the normal fluid along almost straight tracks, and to slow particles, whose erratic upward motion appears to be significantly influenced by quantized vortices. The regimes, together with the corresponding transition events, were identified by using a custom-made separation scheme, based on the identification of specific trajectory patterns in the two-dimensional velocity-acceleration phase space. It is important to stress that a single particle can explore both regimes during its motion away from the heat source.

Particle trajectories, split into individual segments according to the motion regimes, were then studied separately. We observed the occurrence of very long segments, meaning that particles can be fast or slow on macroscopic length scales, appreciably larger than

the mean distance between quantized vortices. We found that fast particles move, on average, with velocities close to the normal fluid velocity v_n, once the density mismatch between particle and fluid is accounted for, and that the trajectories of these particles are relatively straight. The slow particles seem instead to be influenced by stronger interactions with the vortex tangle. Their mean velocity is reduced to about $v_n/2$ and their tracks are considerably more erratic. We also observed that the particle velocity PDFs reveal extreme events (heavy tails) in both cases but with different strengths that may be related to their different interaction with the underlying vortex tangle.

It then follows that the interactions between quantized vortices and flow-probing particles are ubiquitous in thermal counterflow of superfluid helium. They appear to be relevant not only for the slow particles, as claimed in the past, for example, by Mastracci & Guo (2018), but also for the fast ones, at least at sufficiently large heat fluxes, in turbulent counterflow. This can be regarded as the work main scientific result, obtained by applying the proposed separation scheme.

In summary, we believe that this work not only gives a significant contribution to our current understanding of particle-vortex interactions in quantum turbulence but also presents a data processing scheme that could be used to interpret particle dynamics in other flows. Additionally, retrieving patterns in the four-dimensional velocity-acceleration phase space, as outlined in §3.6, may be useful for the neat identification of particle deceleration and acceleration events, that is, to study the still largely unknown dynamics of particles trapped onto quantized vortices, once adequate time resolution is achieved. We also envisage that these patterns could be detected by using contemporary computational methods, such as neural networks and machine learning, following, for example, Dosset *et al.* (2016), and that seeking similar behavioural patterns in numerical simulations could also be a feasible line of future research, if one considers, for example, the recent work by Polanco & Krstulovic (2020).

The visits to Prague of P. Diribarne, B. Rousset, M. Bourgoin and M. Gibert were supported by the EuHIT project QuantumPC. The visits to Grenoble of P. Švančara and D. Duda were supported by the French Barrande program, the Czech Mobility program, the Charles University Mobility Fund and the Czech Science Foundation. The latter also supported the experiments discussed here. M. Gibert acknowledges the support of grants ANR-11-PDOC-0001 (3D-QuantumV) and ANR-10-LABX-0051 (LANEF). P. Švančara, M. Rotter, L. Skrbek and M. La Mantia acknowledge the support of GAČR grant 19-00939S.

Declaration of Interests. The authors report no conflict of interest.

REFERENCES

Babuin, S., Stammeier, M., Varga, E., Rotter, M. & Skrbek, L. 2012 Quantum turbulence of bellows-driven ^{4}He superflow: Steady state. *Phys. Rev. B* **86**, 134515.

Baggaley, A. W. & Laizet, S. 2013 Vortex line density in counterflowing He II with laminar and turbulent normal fluid velocity profiles. *Phys. Fluids* **25**, 115101.

Barenghi, C. F., Skrbek, L. & Sreenivasan, K. R. 2014 Introduction to quantum turbulence. *Proc. Natl. Acad. Sci. U. S. A.* **111**, 4647–4652.

Bertolaccini, J., Lévêque, E. & Roche, P.-E. 2017 Disproportionate entrance length in superfluid flows and the puzzle of counterflow instabilities. *Phys. Rev. Fluids* **2**, 123902.

Bostanjoglo, O. & Kleinschmidt, R. 1967 Crystal structure of hydrogen isotopes. *J. Chem. Phys.* **46**, 2004–2005.

Chagovets, T. V. & Van Sciver, S. W. 2011 A study of thermal counterflow using particle tracking velocimetry. *Phys. Fluids* **23**, 107102.

Donnelly, R. J. & Barenghi, C. F. 1998 The observed properties of liquid helium at the saturated vapor pressure. *J. Phys. Chem. Ref. Data* **27**, 1217–1274.

Dosset, P., Rassam, P., Fernandez, L., Espenel, C., Rubinstein, E., Margeat, E. & Milhiet, P.-E. 2016 Automatic detection of diffusion modes within biological membranes using back-propagation neural network. *BMC Bioinformatics* **17**, 197.

Giuriato, U. & Krstulovic, G. 2019 Interaction between active particles and quantum vortices leading to Kelvin wave generation. *Sci. Rep.* **9**, 4839.

Guo, W., La Mantia, M., Lathrop, D. P. & Van Sciver, S. W. 2014 Visualization of two-fluid flows of superfluid helium-4. *Proc. Natl. Acad. Sci. U. S. A.* **111**, 4653–4658.

Hrubcová, P., Švančara, P. & La Mantia, M. 2018 Vorticity enhancement in thermal counterflow of superfluid helium. *Phys. Rev. B* **97**, 064512.

Idowu, O. C., Willis, A., Barenghi, C. F. & Samuels, D. C. 2000 Local normal-fluid helium II flow due to mutual friction interaction with the superfluid. *Phys. Rev. B* **62**, 3409–3415.

Kivotides, D. 2008*a* Motion of a spherical solid particle in thermal counterflow turbulence. *Phys. Rev. B* **77**, 174508.

Kivotides, D. 2008*b* Normal-fluid velocity measurement and superfluid vortex detection in thermal counterflow turbulence. *Phys. Rev. B* **78**, 224501.

La Mantia, M. 2016 Particle trajectories in thermal counterflow of superfluid helium in a wide channel of square cross section. *Phys. Fluids* **28**, 024102.

La Mantia, M. 2017 Particle dynamics in wall-bounded thermal counterflow of superfluid helium. *Phys. Fluids* **29**, 065102.

La Mantia, M., Duda, D., Rotter, M. & Skrbek, L. 2013 Lagrangian accelerations of particles in superfluid turbulence. *J. Fluid Mech.* **717**, R9.

La Mantia, M. & Skrbek, L. 2014 Quantum turbulence visualized by particle dynamics. *Phys. Rev. B* **90**, 014519.

La Mantia, M., Švančara, P., Duda, D. & Skrbek, L. 2016 Small-scale universality of particle dynamics in quantum turbulence. *Phys. Rev. B* **94**, 184512.

Lawson, J. M., Bodenschatz, E., Lalescu, C. C. & Wilczek, M. 2018 Bias in particle tracking acceleration measurement. *Exp. Fluids* **59**, 172.

Mastracci, B., Bao, S., Guo, W. & Vinen, W. F. 2019 Particle tracking velocimetry applied to thermal counterflow in superfluid ^{4}He: Motion of the normal fluid at small heat fluxes. *Phys. Rev. Fluids* **4**, 083305.

Mastracci, B. & Guo, W. 2018 Exploration of thermal counterflow in He II using particle tracking velocimetry. *Phys. Rev. Fluids* **3**, 063304.

Mongiovì, M. S., Jou, D. & Sciacca, M. 2018 Non-equilibrium thermodynamics, heat transport and thermal waves in laminar and turbulent superfluid helium. *Phys. Rep.* **726**, 1–71.

Mordant, N., Crawford, A. M. & Bodenschatz, E. 2004 Experimental Lagrangian acceleration probability density function measurement. *Physica D* **193**, 245–251.

Paoletti, M. S., Fiorito, R. B., Sreenivasan, K. R. & Lathrop, D. P. 2008 Visualization of superfluid helium flow. *J. Phys. Soc. Jpn.* **77**, 111007.

Polanco, J. I. & Krstulovic, G. 2020 Inhomogeneous distribution of particles in coflow and counterflow quantum turbulence. *Phys. Rev. Fluids* **5**, 032601(R).

Raffel, M., Willert, C. E., Scarano, F., Kähler, C. J., Wereley, S. T. & Kompenhans, J. 2018 *Particle Image Velocimetry – A Pratical Guide*. Springer.

Sergeev, Y. A. & Barenghi, C. F. 2009 Particles-vortex interactions and flow visualization in ^{4}He. *J. Low Temp. Phys.* **157**, 429–475.

Sergeev, Y. A., Barenghi, C. F. & Kivotides, D. 2006 Motion of micron-size particles in turbulent helium II. *Phys. Rev. B* **74**, 184506.

Skrbek, L. & Sreenivasan, K. R. 2012 Developed quantum turbulence and its decay. *Phys. Fluids* **24**, 011301.

Varga, E. & Skrbek, L. 2019 Thermal counterflow of superfluid ^{4}He: Temperature gradient in the bulk and in the vicinity of heater. *Phys. Rev. B* **100**, 054518.

Voth, G. A., La Porta, A., Crawford, A. M. & Bodenschatz, E. 2002 Measurement of particle accelerations in fully developed turbulence. *J. Fluid Mech.* **469**, 121–160.

Švančara, P., Hrubcová, P. & La Mantia, M. 2018*a* Estimation of Lagrangian velocities in thermal counterflow of superfluid helium by a multi-point algorithm. In *WDS'18 Proceedings of Contributed Papers – Physics* (ed. J. Pavlů & J. Šafránková), pp. 168–173. Prague, Czech Republic: Matfyzpress.

Švančara, P., Hrubcová, P., Rotter, M. & La Mantia, M. 2018*b* Visualization study of thermal counterflow of superfluid helium in the proximity of the heat source by using solid deuterium hydride particles. *Phys. Rev. Fluids* **3**, 114701.

Švančara, P. & La Mantia, M. 2017 Flows of liquid ^{4}He due to oscillating grids. *J. Fluid Mech.* **832**, 578–599.

Švančara, P. & La Mantia, M. 2019 Flight-crash events in superfluid turbulence. *J. Fluid Mech.* **876**, R2.

Yui, S., Kobayashi, H., Tsubota, M. & Guo, W. 2020 Fully coupled two-fluid dynamics in superfluid ^{4}He: Anomalous anisotropic velocity fluctuations in counterflow. *Phys. Rev. Lett.* **124**, 155301.

Zhang, T. & Van Sciver, S. W. 2005 The motion of micron-sized particles in He II counterflow as observed by the PIV technique. *J. Low Temp. Phys.* **138**, 865–870.

Bibliography

[1] G. G. Stokes, "On the theories of the internal friction of fluids in motion, and of the equilibrium and motion of elastic solids", in *Mathematical and Physical Papers vol.1*, 75–129 (Cambridge University Press) (1845).

[2] O. Reynolds, "XXIX. an experimental investigation of the circumstances which determine whether the motion of water shall be direct or sinuous, and of the law of resistance in parallel channels.", Philosophical Transactions of the Royal Society of London **174**, 935–982 (1883).

[3] O. Reynolds, "On the dynamical theory of incompressible viscous fluids and the determination of the criterion.", Proceedings of the Royal Society A: Mathematical, Physical and Engineering Sciences **451**, 5–47 (1885).

[4] L. F. Richardson, *Weather prediction by numerical process* (Cambridge University Press) (1922).

[5] A. N. Kolmogorov, "The local structure of turbulence in incompressible viscous fluid for very large reynolds numbers", Proceedings of the Royal Society A: Mathematical, Physical and Engineering Sciences **434**, 9–13 (1941).

[6] A. N. Kolmogorov, "On the degeneration of isotropic turbulence in an incompressible viscous fluid", in *Doklady Akademii Nauk*, 319–323 (Doklady Akademii Nauk) (1941).

[7] A. N. Kolmogorov, "Dissipation of energy in the locally isotropic turbulence", Proceedings of the Royal Society A: Mathematical, Physical and Engineering Sciences **434**, 15–17 (1941).

[8] A. N. Kolmogorov, "Equations of turbulent motion in an incompressible fluid", in *Doklady Akademii Nauk*, 328–330 (Doklady Akademii Nauk) (1941).

[9] S. B. Pope, *Turbulent flows* (Cambridge University Pr.) (2000).

[10] T. de Karman and L. Howarth, "On the statistical theory of isotropic turbulence", Proceedings of the Royal Society of London. Series A - Mathematical and Physical Sciences **164**, 192–215 (1938).

[11] G. I. Taylor, "Motion of solids in fluids when the flow is not irrotational", Proceedings of the Royal Society of London. Series A, Containing Papers of a Mathematical and Physical Character **93**, 99–113 (1917).

[12] J. Proudman, "On the motion of solids in a liquid possessing vorticity", Proceedings of the Royal Society of London. Series A, Containing Papers of a Mathematical and Physical Character **92**, 408–424 (1916).

[13] A. S. Monin, A. M. Yaglom, and J. L. Lumley, *Statistical fluid mechanics: mechanics of turbulence, vol. 2* (The MIT Press) (1975).

[14] C. Lamriben, P.-P. Cortet, and F. Moisy, "Direct measurements of anisotropic energy transfers in a rotating turbulence experiment", Physical Review Letters **107** (2011).

[15] C. Lamriben, "Transferts anisotropes d'énergie en turbulence en rotation et excitation de modes d'inertie", Ph.D. thesis, Université Paris Sud (2012).

[16] S. Galtier, "Exact vectorial law for homogeneous rotating turbulence", Physical Review E **80** (2009).

[17] H. K. Onnes, "The liquefaction of helium", Communications of the Physical Laboratory of the University of Leiden, 108 (1908).

[18] G. P. Bewley, "Using frozen hydrogen particles to observe rotating and quantized flows in liquid helium", Ph.D. thesis, Yale University (2006).

[19] D. Duri, "Mise en évidence expérimentale de l'intermittence dans un jet cryogénique turbulent d'hélium normal et superfluide", Ph.D. thesis, Grenoble INP (2012).

[20] J. J. Niemela, L. Skrbek, K. R. Sreenivasan, and R. J. Donnelly, "Turbulent convection at very high rayleigh numbers", Nature **404**, 837–840 (2000).

[21] A. Bezaguet, J. P. Dauvergne, S. Knoops, P. Lebrun, M. Pezzetti, O. Pirotte, J. L. Bret, B. Chabaud, G. Garde, C. Guttin, B. Hébral, S. Pietropinto, P. Roche, J. P. Barbier-Neyret, C. Baudet, Y. Gagne, C. Poulain, B. Castaing, Y. Ladam, and F. Vittoz, "A cryogenic high-Reynolds turbulence experiment at CERN", in *AIP Conference Proceedings* (AIP) (2002).

[22] B. Rousset, P. Bonnay, P. Diribarne, A. Girard, J. M. Poncet, E. Herbert, J. Salort, C. Baudet, B. Castaing, L. Chevillard, F. Daviaud, B. Dubrulle, Y. Gagne, M. Gibert, B. Hébral, T. Lehner, P.-E. Roche, B. Saint-Michel, and M. B. Mardion, "Superfluid High REynolds von Kármán experiment", Review of Scientific Instruments **85**, 103908 (2014).

[23] R. J. Donnelly and C. F. Barenghi, "The observed properties of liquid helium at the saturated vapor pressure", Journal of Physical and Chemical Reference Data **27**, 1217–1274 (1998).

[24] W. H. Keesom and A. P. Keesom, "New measurements on the specific heat of liquid helium", Physica **2**, 557–572 (1935).

[25] J. O. Wilhelm, A. D. Misener, and A. R. Clark, "The viscosity of liquid helium", Proceedings of the Royal Society of London. Series A, Mathematical and Physical Sciences **151**, 342–347 (1935).

[26] J. F. Allen, R. Peierls, and M. Z. Uddin, "Heat conduction in liquid helium", Nature **140**, 62–63 (1937).

[27] J. F. Allen and A. D. Misener, "Flow of liquid helium II", Nature **141**, 75–75 (1938).

[28] P. L. Kapitza, "Viscosity of liquid helium below the λ-point", in *Nature*, 99–102 (Nature) (1938).

[29] F. London, "The λ-phenomenon of liquid helium and the Bose-Einstein degeneracy", Nature **141**, 643–644 (1938).

[30] L. Tisza, "Transport phenomena in helium II", Nature **141**, 913–913 (1938).

[31] L. D. Landau, "The theory of superfluidity of helium II", in *Journal of Physics, USSR 5, 71*, 191–233 (Journal of Physics, USSR) (1941).

[32] C. F. Barenghi, L. Skrbek, and K. R. Sreenivasan, "Introduction to quantum turbulence", Proceedings of the National Academy of Sciences **111**, 4647–4652 (2014).

[33] R. P. Feynman, "Application of quantum mechanics to liquid helium", in *Progress in Low Temperature Physics*, 17–53 (Elsevier) (1955).

[34] J. Maurer and P. Tabeling, "Local investigation of superfluid turbulence", Europhysics Letters (EPL) **43**, 29–34 (1998).

[35] J. Salort, C. Baudet, B. Castaing, B. Chabaud, F. Daviaud, T. Didelot, P. Diribarne, B. Dubrulle, Y. Gagne, F. Gauthier, A. Girard, B. Hébral, B. Rousset, P. Thibault, and P.-E. Roche, "Turbulent velocity spectra in superfluid flows", Physics of Fluids **22**, 125102 (2010).

[36] V. Shukla, A. Gupta, and R. Pandit, "Homogeneous isotropic superfluid turbulence in two dimensions: inverse and forward cascades in the Hall-Vinen-Bekharevich-Khalatnikov model", Physical Review B **92** (2015).

[37] J. Salort, B. Chabaud, E. Lévêque, and P.-E. Roche, "Energy cascade and the four-fifths law in superfluid turbulence", EPL (Europhysics Letters) **97**, 34006 (2012).

[38] J. Salort, "Turbulence quantique versus classique", Ph.D. thesis, Université Grenoble Alpes (2011).

[39] M. S. Paoletti, M. E. Fisher, K. R. Sreenivasan, and D. P. Lathrop, "Velocity statistics distinguish quantum turbulence from classical turbulence", Physical Review Letters **101** (2008).

[40] M. L. Mantia and L. Skrbek, "Quantum, or classical turbulence?", EPL (Europhysics Letters) **105**, 46002 (2014).

[41] J. Gao, W. Guo, S. Yui, M. Tsubota, and W. F. Vinen, "Dissipation in quantum turbulence in superfluid ^4He above 1K", Physical Review B **97** (2018).

[42] S. K. Nemirovskii and W. Fiszdon, "Chaotic quantized vortices and hydrodynamic processes in superfluid helium", Reviews of Modern Physics **67**, 37–84 (1995).

[43] G. P. Bewley, "The generation of particles to observe quantized vortex dynamics in superfluid helium", Cryogenics **49**, 549–553 (2009).

[44] H. E. Hall and W. F. Vinen, "Mutual friction in a heat current in liquid helium II i. experiments on steady heat currents", Proceedings of the Royal Society of London. Series A. Mathematical and Physical Sciences **240**, 114–127 (1957).

[45] H. E. Hall and W. F. Vinen, "Mutual friction in a heat current in liquid helium II. II. experiments on transient effects", Proceedings of the Royal Society of London. Series A. Mathematical and Physical Sciences **240**, 128–143 (1957).

[46] H. E. Hall and W. F. Vinen, "Mutual friction in a heat current in liquid helium II III. theory of the mutual friction", Proceedings of the Royal Society of London. Series A. Mathematical and Physical Sciences **242**, 493–515 (1957).

[47] M. Tsubota, "Quantum turbulence: from superfluid helium to atomic Bose-Einstein condensates", Contemporary Physics **50**, 463–475 (2009).

[48] C. F. Barenghi, R. J. Donnelly, and W. F. Vinen, "Friction on quantized vortices in helium ii. a review", Journal of Low Temperature Physics **52**, 189–247 (1983).

[49] L. D. Landau, "Theory of the superfluidity of helium II", Physical Review **60**, 356–358 (1941).

[50] S. Babuin, M. Stammeier, E. Varga, M. Rotter, and L. Skrbek, "Quantum turbulence of bellows-driven ^4He superflow: Steady state", Physical Review B **86** (2012).

[51] C. T. Lane, H. A. Fairbank, and W. M. Fairbank, "Second sound in liquid helium II", Physical Review **71**, 600–605 (1947).

[52] H. E. Hall and W. F. Vinen, "The rotation of liquid helium ii i. experiments on the propagation of second sound in uniformly rotating helium ii", Proceedings of the Royal Society of London. Series A. Mathematical and Physical Sciences **238**, 204–214 (1956).

[53] J. T. Tough, "Classical and quantum-mechanical turbulence in He II heat flow", Physical Review **144**, 186–195 (1966).

[54] P. Hrubcová, P. Švančara, and M. L. Mantia, "Vorticity enhancement in thermal counterflow of superfluid helium", Physical Review B **97** (2018).

[55] K. W. Schwarz, "Three-dimensional vortex dynamics in superfluid ^4He: homogeneous superfluid turbulence", Physical Review B **38**, 2398–2417 (1988).

[56] Y. A. Sergeev, C. F. Barenghi, and D. Kivotides, "Motion of micron-size particles in turbulent helium II", Physical Review B **74** (2006).

[57] H. Adachi, S. Fujiyama, and M. Tsubota, "Steady-state counterflow quantum turbulence: simulation of vortex filaments using the full Biot-Savart law", Physical Review B **81** (2010).

[58] K. P. Martin and J. T. Tough, "Evolution of superfluid turbulence in thermal counterflow", Physical Review B **27**, 2788–2799 (1983).

[59] J. Gao, E. Varga, W. Guo, and W. F. Vinen, "Energy spectrum of thermal counterflow turbulence in superfluid helium-4", Physical Review B **96** (2017).

[60] T. V. Chagovets and L. Skrbek, "On flow of He II in channels with ends blocked by superleaks", Journal of Low Temperature Physics **153**, 162–188 (2008).

[61] W. Guo, S. B. Cahn, J. A. Nikkel, W. F. Vinen, and D. N. McKinsey, "Visualization study of counterflow in superfluid ^4He using metastable helium molecules", Physical Review Letters **105** (2010).

[62] D. Schmoranzer, M. Rotter, J. Šebek, and L. Skrbek, "Experimental setup for probing a von-karman type flow of normal and superfluid helium", in *International Conference Experimental Fluid Mechanics 2009* (2009).

[63] B. Saint-Michel, E. Herbert, J. Salort, C. Baudet, M. B. Mardion, P. Bonnay, M. Bourgoin, B. Castaing, L. Chevillard, F. Daviaud, P. Diribarne, B. Dubrulle, Y. Gagne, M. Gibert, A. Girard, B. Hébral, T. Lehner, and B. Rousset, "Probing quantum and classical turbulence analogy in von Kármán liquid helium, nitrogen, and water experiments", Physics of Fluids **26**, 125109 (2014).

[64] S. R. Stalp, L. Skrbek, and R. J. Donnelly, "Decay of grid turbulence in a finite channel", Physical Review Letters **82**, 4831–4834 (1999).

[65] N. F. I. Sy, "Turbulence de grille oscillante à basses températures", Ph.D. thesis, Université Grenoble Alpes (2016).

[66] B. Mastracci and W. Guo, "An apparatus for generation and quantitative measurement of homogeneous isotropic turbulence in he ii", Review of Scientific Instruments **89**, 015107 (2018).

[67] M. Murakami and N. Ichikawa, "Flow visualization study of thermal counterflow jet in He II", Cryogenics **29**, 438–443 (1989).

[68] D. Duri, C. Baudet, P. Charvin, J. Virone, B. Rousset, J.-M. Poncet, and P. Diribarne, "Liquid helium inertial jet for comparative study of classical and quantum turbulence", Review of Scientific Instruments **82**, 115109 (2011).

[69] D. V. Osborne, "The rotation of liquid helium II", Proceedings of the Physical Society. Section A **63**, 909–912 (1950).

[70] E. J. Yarmchuk, M. J. V. Gordon, and R. E. Packard, "Observation of stationary vortex arrays in rotating superfluid helium", Physical Review Letters **43**, 214–217 (1979).

[71] H. P. Greenspan and L. N. Howard, "On a time-dependent motion of a rotating fluid", Journal of fluid mechanics **17**, 385–404 (1963).

[72] H. E. Hall and W. F. Vinen, "The rotation of liquid helium II II. the theory of mutual friction in uniformly rotating helium II", Proceedings of the Royal Society of London. Series A. Mathematical and Physical Sciences **238**, 215–234 (1956).

[73] W. F. Vinen, "Detection of single quanta of circulation in rotating helium II", Nature **181**, 1524–1525 (1958).

[74] E. L. Andronikashvili and Y. G. Mamaladze, "Chapter III rotation of helium II", in *Progress in Low Temperature Physics*, 79–160 (Elsevier) (1967).

[75] C. E. Chase, "Thermal conduction in liquid helium II. I. Temperature dependence", Physical Review **127**, 361–370 (1962).

[76] G. Careri, W. D. McCormick, and F. Scaramuzzi, "Ions in rotating liquid helium II", Physics Letters **1**, 61–63 (1962).

[77] T. A. Kitchens, W. A. Steyert, R. D. Taylor, and P. P. Craig, "Flow visualization in He II: direct observation of Helmholtz flow", Physical Review Letters **14**, 942–945 (1965).

[78] W. A. Steyert, R. D. Taylor, and T. A. Kitchens, "Direct measurements of multiple quantization in He II", Physical Review Letters **15**, 546–549 (1965).

[79] V. K. Tkachenko, "Stability of vortex lattices", Soviet Journal of Experimental and Theoretical Physics (1966).

[80] F. Pobell, W. Schoepe, and W. Veith, "The λ-point, entropy and density of rotating HeII", Physics Letters A **25**, 209–210 (1967).

[81] W. I. Glaberson, W. W. Johnson, and R. M. Ostermeier, "Instability of a vortex array in He II", Physical Review Letters **33**, 1197–1200 (1974).

[82] F. Vidal and D. Lhuillier, "Second-sound velocity in rotating superfluid helium", Physical Review B **13**, 148–168 (1976).

[83] C. E. Swanson, C. F. Barenghi, and R. J. Donnelly, "Rotation of a tangle of quantized vortex lines in He II", Physical Review Letters **50**, 190–193 (1983).

[84] E. B. Sonin, "Vortex oscillations and hydrodynamics of rotating superfluids", Reviews of Modern Physics **59**, 87–155 (1987).

[85] E. B. Sonin, "Tkachenko waves", JETP Letters **98**, 758–768 (2014).

[86] C. A. van Eysden, "Oscillatory superfluid Ekman pumping in helium II and neutron stars", Journal of Fluid Mechanics **783**, 251–282 (2015).

[87] M. Ruderman, "Long period oscillations in rotating neutron stars", Nature **225**, 619–620 (1970).

[88] A. B. Migdal, "Superfluidity and the moments of inertia of nuclei", Nuclear Physics **13**, 655–674 (1959).

[89] J. S. Tsakadze and S. J. Tsakadze, "Superfluidity in pulsars", Soviet Physics Uspekhi **18**, 242–250 (1975).

[90] S. D. Tsakadze, "Oscillations of a vortex system in rotating He II", Soviet Journal of Experimental and Theoretical Physics **44** (1976).

[91] E. N. Sonin, "Vortex–lattice vibrations in a rotating helium II", Soviet Journal of Experimental and Theoretical Physics **43** (1976).

[92] J. S. Tsakadze and S. J. Tsakadze, "Properties of slowly rotating helium II and the superfluidity of pulsars", Journal of Low Temperature Physics **39**, 649–688 (1980).

[93] A. Hewish, S. J. Bell, J. D. H. Pilkington, P. F. Scott, and R. A. Collins, "Observation of a rapidly pulsating radio source", Nature **217**, 709–713 (1968).

[94] M. A. Alpar, "Relaxation of rotating He II following a spin-up of its container: A superfluid Ekman time?", Journal of Low Temperature Physics **31**, 803–815 (1978).

[95] Z. S. Nadirashvili and D. S. Tsakadze, "Metastable state of rotating helium II when its rotary speed is suddenly changed", JETP letters (1973).

[96] L. J. Campbell and Y. K. Krasnov, "Transient behavior of rotating superfluid helium", Journal of Low Temperature Physics **49**, 377–396 (1982).

[97] A. Reisenegger, "The spin-up problem in helium II", Journal of Low Temperature Physics **92**, 77–106 (1993).

[98] C. A. van Eysden and A. Melatos, "Spin down of superfluid-filled vessels: Theory versus experiment", Journal of Low Temperature Physics **165**, 1–14 (2011).

[99] V. Graber, N. Andersson, and M. Hogg, "Neutron stars in the laboratory", International Journal of Modern Physics D **26**, 1730015 (2017).

[100] J. S. Tsakadze and S. J. Tsakadze, "Relaxation phenomena at accelaration of rotation of a spherical vessel with helium II and relaxation in pulsars", Physics Letters A **41**, 197–199 (1972).

[101] H. E. Hall, "The angular acceleration of liquid helium II", Philosophical Transactions of the Royal Society A: Mathematical, Physical and Engineering Sciences **250**, 359–385 (1957).

[102] R. Blaauwgeers, S. Boldarev, V. B. Eltsov, A. P. Finne, and M. Krusius, "Superfluid He in rotation: single-vortex resolution and requirements on rotation", Journal of Low Temperature Physics **132**, 263–279 (2003).

[103] K. L. Chopra and J. B. Brown, "Suspension of particles in liquid helium", Physical Review **108**, 157–157 (1957).

[104] M. J. Fear, P. M. Walmsley, D. A. Chorlton, D. E. Zmeev, S. J. Gillott, M. C. Sellers, P. P. Richardson, H. Agrawal, G. Batey, and A. I. Golov, "A compact rotating dilution refrigerator", Review of Scientific Instruments **84**, 103905 (2013).

[105] S. Oguri, H. Ishitsuka, J. Choi, M. Kawai, and O. Tajima, "Sub-kelvin refrigeration with dry-coolers on a rotating system", Review of Scientific Instruments **85**, 086101 (2014).

[106] T. Makiuchi, S. Murakawa, and K. Shirahama, "A compact rotating 1K cryostat for helium 4 studies", Journal of Low Temperature Physics **187**, 633–638 (2016).

[107] M. J. Fear, P. M. Walmsley, D. E. Zmeev, J. T. Mäkinen, and A. I. Golov, "No effect of steady rotation on solid ^{4}He in a torsional oscillator", Journal of Low Temperature Physics **183**, 106–112 (2015).

[108] D. Duda, "Quantum turbulence in superfluid helium studied by particle tracking velocimetry visualization technique", Ph.D. thesis, Universitas Carolina Facultas Mathematica Physicaque (2017).

[109] D. Y. Chung and P. R. Critchlow, "Motion of suspended particles in turbulent superflow of liquid helium II", Physical Review Letters **14**, 892–894 (1965).

[110] G. G. Stokes, *On the effect of the internal friction of fluids on the motion of pendulums*, volume 9 (Pitt Press Cambridge) (1851).

[111] D. R. H. Craig F. Bohren, *Absorption and scattering of light by small particles* (Wiley-VCH Verlag GmbH & Co. KGaA) (2008).

[112] T. Xu and S. W. V. Sciver, "PIV application in He II forced flow research", Cryogenics **49**, 535–542 (2009).

[113] E. Fonda, K. R. Sreenivasan, and D. P. Lathrop, "Sub-micron solid air tracers for quantum vortices and liquid helium flows", Review of Scientific Instruments **87**, 025106 (2016).

[114] R. J. Adrian and C.-S. Yao, "Pulsed laser technique application to liquid and gaseous flows and the scattering power of seed materials", Applied Optics **24**, 44 (1985).

[115] F. Toschi and E. Bodenschatz, "Lagrangian properties of particles in turbulence", Annual Review of Fluid Mechanics **41**, 375–404 (2009).

[116] N. Yoshimura, *Vacuum technology* (Springer-Verlag GmbH) (2007).

[117] L. Thomas Flynn (Cryoco Inc and U. Colorado, *Cryogenic engineering, revised and expanded* (Taylor & Francis Inc) (2004).

[118] G. Stamm, F. Bielert, W. Fiszdon, and J. Piechna, "Counterflow-induced macroscopic vortex rings in superfluid helium: visualization and numerical simulation", Physica B: Condensed Matter **193**, 188–194 (1994).

[119] T. Zhang, D. Celik, and S. W. V. Sciver, "Tracer particles for application to PIV studies of liquid helium", Journal of Low Temperature Physics **134**, 985–1000 (2004).

[120] M. Murakami, M. Hanada, and T. Yamazaki, "Flow visualization study on large-scale vortex ring in he II", Japanese Journal of Applied Physics **26**, 107 (1987).

[121] G. P. Bewley, M. S. Paoletti, K. R. Sreenivasan, and D. P. Lathrop, "Characterization of reconnecting vortices in superfluid helium", Proceedings of the National Academy of Sciences **105**, 13707–13710 (2008).

[122] G. P. Bewley, D. P. Lathrop, and K. R. Sreenivasan, "Visualization of quantized vortices", Nature **441**, 588–588 (2006).

[123] B. Mastracci and W. Guo, "Exploration of thermal counterflow in he ii using particle tracking velocimetry", Physical Review Fluids **3** (2018).

[124] E. Fonda, K. R. Sreenivasan, and D. P. Lathrop, "Reconnection scaling in quantum fluids", Proceedings of the National Academy of Sciences **116**, 1924–1928 (2019).

[125] P. Švančara and M. L. Mantia, "Flows of liquid ^4He due to oscillating grids", Journal of Fluid Mechanics **832**, 578–599 (2017).

[126] M. S. Paoletti, M. E. Fisher, and D. P. Lathrop, "Reconnection dynamics for quantized vortices", Physica D: Nonlinear Phenomena **239**, 1367–1377 (2010).

[127] M. S. Paoletti, R. B. Fiorito, K. R. Sreenivasan, and D. P. Lathrop, "Visualization of superfluid helium flow", Journal of the Physical Society of Japan **77**, 111007 (2008).

[128] T. V. Chagovets and S. W. V. Sciver, "A study of thermal counterflow using particle tracking velocimetry", Physics of Fluids **23**, 107102 (2011).

[129] M. L. Mantia, T. V. Chagovets, M. Rotter, and L. Skrbek, "Testing the performance of a cryogenic visualization system on thermal counterflow by using hydrogen and deuterium solid tracers", Review of Scientific Instruments **83**, 055109 (2012).

[130] W. Kubo and Y. Tsuji, "Lagrangian trajectory of small particles in superfluid he II", Journal of Low Temperature Physics **187**, 611–617 (2017).

[131] D. P. Meichle and D. P. Lathrop, "Nanoparticle dispersion in superfluid helium", Review of Scientific Instruments **85**, 073705 (2014).

[132] C. F. Barenghi, D. Kivotides, and Y. A. Sergeev, "Close approach of a spherical particle and a quantised vortex in helium II", Journal of Low Temperature Physics **148**, 293–297 (2007).

[133] D. Kivotides, C. F. Barenghi, and Y. A. Sergeev, "Interactions between particles and quantized vortices in superfluid helium", Physical Review B **77** (2008).

[134] U. Giuriato, G. Krstulovic, and S. Nazarenko, "How trapped particles interact with and sample superfluid vortex excitations", Physical Review Research **2** (2020).

[135] "Orange cryostats on the ILL website: https://www.ill.eu/users/support-labs-infrastructure/sample-environment/services-for-advanced-neutron-environments/history/cryogenics/orange-cryostats/", .

[136] M. Melich, R. Boltnev, F. Bonnet, L. Guyon, and P. E. Wolf, "On the efficiency of infrared filters in optical cryostats", Journal of Low Temperature Physics **162**, 740–747 (2010).

[137] B. Bach, E. C. Linnartz, M. H. Vested, A. Andersen, and T. Bohr, "From newton's bucket to rotating polygons: experiments on surface instabilities in swirling flows", Journal of Fluid Mechanics **759**, 386–403 (2014).

[138] R. E. Packard, "Vortex photography in liquid helium", Physica B+C **109-110**, 1474–1484 (1982).

[139] M. R. Smith, R. J. Donnelly, N. Goldenfeld, and W. F. Vinen, "Decay of vorticity in homogeneous turbulence", Physical Review Letters **71**, 2583–2586 (1993).

[140] M. L. Mantia, "Particle trajectories in thermal counterflow of superfluid helium in a wide channel of square cross section", Physics of Fluids **28**, 024102 (2016).

[141] T. Xu and S. W. V. Sciver, "Particle image velocimetry measurements of the velocity profile in HeII forced flow", Physics of Fluids **19**, 071703 (2007).

[142] M. H. Edwards, "The index of refraction of liquid helium", Canadian Journal of Physics **34**, 898–900 (1956).

[143] M. L. Mantia, D. Duda, M. Rotter, and L. Skrbek, "Lagrangian accelerations of particles in superfluid turbulence", Journal of Fluid Mechanics **717** (2013).

[144] E. B. Gordon, R. Nishida, R. Nomura, and Y. Okuda, "Filament formation by impurities embedding into superfluid helium", JETP Letters **85**, 581–584 (2007).

[145] N. T. Ouellette, H. Xu, and E. Bodenschatz, "A quantitative study of three-dimensional Lagrangian particle tracking algorithms", Experiments in Fluids **40**, 301–313 (2005).

[146] N. Mordant, A. M. Crawford, and E. Bodenschatz, "Experimental lagrangian acceleration probability density function measurement", Physica D: Nonlinear Phenomena **193**, 245–251 (2004).

[147] R. Volk, N. Mordant, G. Verhille, and J.-F. Pinton, "Laser Doppler measurement of inertial particle and bubble accelerations in turbulence", EPL (Europhysics Letters) **81**, 34002 (2007).

[148] D. Gale and L. S. Shapley, "College admissions and the stability of marriage", The American Mathematical Monthly **69**, 9 (1962).

[149] N. Machicoane, P. D. Huck, A. Clark, A. Aliseda, R. Volk, and M. Bourgoin, "Recent developments in particle tracking diagnostics for turbulence research", in *Soft and Biological Matter*, 177–209 (Springer International Publishing) (2019).

[150] C. Morize and F. Moisy, "Energy decay of rotating turbulence with confinement effects", Physics of Fluids **18**, 065107 (2006).

[151] F. Moisy, C. Morize, M. Rabaud, and J. Sommeria, "Decay laws, anisotropy and cyclone–anticyclone asymmetry in decaying rotating turbulence", Journal of Fluid Mechanics **666**, 5–35 (2010).

[152] P. G. Saffman, "Note on decay of homogeneous turbulence", Physics of Fluids **10**, 1349 (1967).

[153] K. Squires, J. Chasnov, N. Mansour, and C. Cambon, "Investigation of the asymptotic state of rotating turbulence using large-eddy simulation", Annual research briefs of the center for turbulent research **-1**, 157–170 (1993).

[154] A. Campagne, N. Machicoane, B. Gallet, P.-P. Cortet, and F. Moisy, "Turbulent drag in a rotating frame", Journal of Fluid Mechanics **794** (2016).

[155] A. Griffin, V. Shukla, M.-E. Brachet, and S. Nazarenko, "Magnus-force model for active particles trapped on superfluid vortices", Physical Review A **101** (2020).

[156] E. B. Gordon and Y. Okuda, "Catalysis of impurities coalescence by quantized vortices in superfluid helium with nanofilament formation", Low Temperature Physics **35**, 209–213 (2009).

[157] E. Calzavarini, R. Volk, M. Bourgoin, E. Lévêque, J.-F. Pinton, and F. Toschi, "Acceleration statistics of finite-sized particles in turbulent flow: the role of Faxén forces", Journal of Fluid Mechanics **630**, 179–189 (2009).